4

Analyzing the derecho system over Poland on 11 August 2017.

Preface to the topical issue

Mateusz Taszarek
Adam Mickiewicz University, Department of Meteorology and Climatology

Michał Z. Ziemiański
Institute of Meteorology and Water Management – National Research Institute

On the evening of 11 August 2017, a well organized mesoscale convective system (MCS: Houze 2018) moved through western and northern parts of Poland and produced a widespread wind damage. With peak wind gusts exceeding 150 km/h this storm had a remarkable intensity and resulted in 6 fatalities, 58 injuries and 79700 ha of forest being destroyed. In terms of both induced damage and social impacts, it was one of the most impactful convective storms observed in the modern era of radar measurements in Poland (Surowiecki, Taszarek 2020).

This storm rapidly intensified in the late afternoon hours over southwestern Poland when discreet convective cells organized into a squall line consisting of an embedded mesocyclone. In the later stages, the latter evolved into a mesoscale convective vortex (MCV; Bartels, Maddox 1991), which had a major contribution in the production of the most significant surface winds. In the mature stage, a strong cold pool lead to the formation of a large bow-echo (Klimowski et al. 2004). Nearly 1200 severe wind reports on the distance exceeding 450 km associated with this storm allowed to classify it as a derecho (a long-lived convective windstorm producing a widespread straight-line wind damage), consistent with definition provided by Johns and Hirt (1987).

Squall lines with bow-echo occur in Poland on average 10 times per year while those reaching a derecho criteria are much rarer with an average frequency of 1 per year (Celiński-Mysław, Matuszko 2014; Celiński-Mysław, Palarz 2017). However, the extreme intensity of derecho on 11 August 2017 appears to be very unique not only for Poland, but also in comparison with other derecho events across Europe and the United States (Guastini, Bosart 2016; Gatzen et al. 2020, Chernokulsky et al. 2022).

Due to immensely large social impact produced by this storm, it has become increasingly important to better understand how it developed, why it reached such intensity, how it was registered by observational systems, and finally, whether numerical weather models were able to predict such intensity? Providing answers to these questions may allow operational forecasters to better predict similar storms in the future while lessons learned from the outcome of 11 August 2017 may also provide future guidance to emergency managers.

Addressing aforementioned questions was the main motivation for this topical issue in Meteorology Hydrology and Water Management. The collection of articles elaborated by employees of the Polish Institute of Meteorology and Water Management – National Research Institute (IMGW-PIB) extends the findings of the initial work by Taszarek et al. (2019) by analyzing in greater detail the derecho event of 11 August 2017. The collection responds mainly to the vital need to further develop and improve the capabilities to effectively forecast and warn against such devastating convective storms. That includes an improvement in their understanding on the level of operational forecasters but also research scientists. The way toward that goal is to extensively document such cases using information from available observing systems. It is essential to consider the atmospheric environment supporting the existence of the systems, and study their development, evolution, and internal dynamics. On the other side, it is also essential to analyze and document the capabilities of the state-of-the-art operational numerical weather prediction tools and their ability to represent the basic dynamical processes associated with such convective systems. The observational and numerical studies, published in this collection, use the tools and products currently available at the time of writing (some even developed in the aftermath of the 2017 derecho), but many of them were not available at the time the event took place.

The opening article by Wrona et al. (2022) analyzes the synoptic and mesoscale conditions characterizing the atmospheric environment of the derecho system. The study confirms the presence of essential synoptic-scale ingredients for severe weather outbreak, including strong upper winds and large thermodynamic instability. It also shows a large-scale ascent known to dynamically force the development of the mesoscale convective systems. On the mesoscale, it indicates that the linear convective system, forming the derecho later, developed and propagated along the eastern edge of the vast cold pool resulting from the earlier deep convective development over southwest Poland.

The following two studies analyze the remote sensing observations of the derecho. Łuszczewski and Tuszyńska (2022) use reflectivity and Doppler radar data to study the evolution of the derecho's main convective features, especially the mesocyclone and rear inflow jet. The analysis revealed the details of the evolving structure of these interacting flows which decisively affected the intensity of the storm. Łapeta et al. (2021) present a collection of satellite products characterizing the environmental susceptibility for convection and its development, followed by the variety of products visualizing the convection, itself, and allowing to analyze its evolution, organization and strength.

The final set of studies analyzes the results of various numerical weather prediction tools. Figurski et al. (2021) use the WRF model to analyze the dependence of the forecasts on the source of the initial and boundary conditions, forecast initiation time, and model resolution. Kolonko et al. (2023) compare the results of the ALARO and AROME models for varying initiation times. They also present the models' representations of the mesoscale structure of low tropospheric flow and its vorticity. A work from Mazur and Duniec (2023) use the COSMO model to investigate to what extent increasing model resolution affected quality of the forecast for 11 August 2017. They found that the reduction of horizontal grid size from 7 km to 2.8 km increased the forecasts' value much more than the further grid size reduction from 2.8 km to 0.7 km.

We hope that articles available in this topical issue contribute to better understanding of derecho storms, will be of interest for scientists working in the area, and can serve as a future guidance for operational forecasters and emergency managers. The question is not whether storm of similar intensity to that of 11 August 2017 will occur again, but rather when and where.

REFERENCES

- Bartels D. L., Maddox R.A., 1991, Midlevel cyclonic vortices generated by mesoscale convective systems, Monthly Weather Review, 119 (1), 104-118, DOI: 10.1175/1520-0493(1991)119<0104:MCVGBM>2.0.CO;2.

- Celiński-Mysław D., Matuszko D., 2014, An analysis of selected cases of derecho in Poland, Atmospheric Research, 149, 263-281, DOI: 10.1016/j.atmosres.2014.06.016.

- Celiński-Mysław D., Palarz A., 2017, The occurrence of convective systems with a bow echo in warm season in Poland, Atmospheric Research, 193, 26-35, DOI: 10.1016/j.atmosres.2017.04.015.

- Chernokulsky A., Shikhov A., Bykov A., Kalinin N., Kurgansky M., Sherstyukov B., Yarinich Y., 2022, Diagnosis and modelling of two destructive derecho events in European Russia in the summer of 2010, Atmospheric Research, 267, DOI: 10.1016/j.atmosres.2021.105928.

- Figurski M.J., Nykiel G., Jaczewski A., Baldysz Z., Wdowikowski M., 2021, The impact of initial and boundary conditions on severe weather event simulations using a high-resolution WRF model. Case study of the derecho event in Poland on 11 August 2017, Meteorology, Hydrology and Water Management, DOI: 10.26491/mhwm/143877.

- Gatzen C., Fink A.H., Schulz D.M., Pinto J.G., 2020, An 18-year climatology of derechos in Germany, Natural Hazards and Earth System Sciences, 20 (5), 1335-1351, DOI: 10.5194/nhess-20-1335-2020.

- Guastini C.T., Bosart L.F., 2016, Analysis of a progressive derecho climatology and associated formation environments, Monthly Weather Review, 144 (4), 1363-1382, DOI: 10.1175/MWR-D-15-0256.1.

- Houze R.A., 2018, 100 years of research on mesoscale convective systems, [in:] A Century of Progress in Atmospheric and Related Sciences: Celebrating the American Meteorological Society Centennial, G. McFarquhar (ed.), Meteorological Monographs, 59, 17.1-17.54, DOI: 10.1175/AMSMONOGRAPHS-D-18-0001.1.

- Johns R.H., Hirt W.D., 1987, Derechos: Widespread convectively induced windstorms, Weather and Forecasting, 2 (1), 32-49, DOI: 10.1175/1520-0434(1987)002<0032: DWCIW>2.0.CO;2.

- Klimowski B.A., Hjelmfelt M.R., Bunkers M.J., 2004, Radar observations of the early evolution of bow echoes, Weather and Forecasting, 19 (4), 727-734, DOI: 10.1175/1520-0434 (2004)019<0727:ROOTEE>2.0.CO;2.

- Kolonko M., Szczęch-Gajewska M., Bochenek B., Stachura G., Sekuła P., 2023, Using ALARO and AROME numerical weather prediction models for the derecho case on 11 August 2017, Meteorology, Hydrology and Water Management, DOI: 10.26491/mhwm/156260.

- Łapeta B., Kuligowska E., Murzyn P., Struzik P., 2021, Monitoring the 11 August 2017 storm in central Poland with satellite data and product, Meteorology, Hydrology and Water Management, DOI: 10.26491/mhwm/144590.

- Łuszczewski H., Tuszyńska I., 2022, Derecho radar analysis of August 11, 2017, Meteorology, Hydrology and Water Management, DOI: 10.26491/mhwm/152504.

- Mazur A., Duniec G., 2023, Influence of computational grid resolution on the quality of forecasts of dangerous convection phenomena: a case study of August 11, 2017, Meteorology, Hydrology and Water Management, DOI: 10.26491/mhwm/159068.

- Surowiecki A., Taszarek M., 2020, A 10-Year Radar-Based Climatology of Mesoscale Convective System Archetypes and Derechos in Poland, Monthly Weather Review, 148 (8), 3471-3488, DOI: 10.1175/MWR-D-19-0412.1.

- Taszarek M., Pilguj N., Orlikowski J., Surowiecki A., Walczakiewicz S., Pilorz W., Piasecki K., Pajurek Ł., Półrolniczak M., 2019, Derecho evolving from a mesocyclone – A study of 11 August 2017 severe weather outbreak in Poland: event analysis and high-resolution simulation, Monthly Weather Review, 147 (6), 2283-2306, DOI: 10.1175/MWR-D-18-0330.1.

- Wrona B., Mańczak P., Woźniak A., Ogrodnik O., Folwarski M., 2022, Synoptic conditions of the derecho storm. Case study of the event passed over Poland on August 11, 2017, Meteorology, Hydrology and Water Management, DOI: 10.26491/mhwm/152798.

Synoptic conditions of the derecho storm. Case study of the derecho event over Poland on August 11, 2017

8

Barbara Wrona, Piotr Mańczak, Anna Woźniak, Michał Ogrodnik, Michał Folwarski
Institute of Meteorology and Water Management – National Research Institute

ABSTRACT. This study presents a comprehensive synoptic analysis of one of the most violent storms recorded in recent years in the north-western part of Poland, which occurred on August 11, 2017. Its development took place ahead of a waving cold front in the tropical air mass, downstream of the upper-level trough. The thunderstorms formed over Lower Silesia in the afternoon and moved towards Gdańsk Pomerania to occur over the Baltic Sea after midnight on August 12, 2017, where they gradually disappeared. As the thunderstorms moved through this area, they ranged from single convective cells and unorganized multicell storms through supercell thunderstorms to mesoscale convective systems in the form of bow echo squall lines and the mesoscale convective vortex (MCV). The convective system, evolving over time, fulfilled the derecho criteria. Its development was related to the presence of both the upper and mid-level jet stream, which supported the formation of a strong rear inflow jet (RIJ) in the rear part of the convective system, being one of the main factors generating the formation of a bow echo squall line with strong wind gusts. The maximum wind gusts recorded on August 11, 2017, are among the highest in the history of Polish measurements and amounted to 42 m/s in Elbląg, 36 m/s in Chrząstów, 35 m/s in Gniezno, and around 30 m/s at several other stations.

1. INTRODUCTION

In Poland, thunderstorms are a frequent, almost daily phenomenon during the warm season (from May to September). Statistically, there are about 150 days with storms in Poland (Bielec-Bąkowska 2003; Taszarek et al. 2015). However, storm structures capable of generating strong wind gusts and having the characteristic appearance of bow-shaped lines, based on which they are called "bow echo," are less common. It is estimated that, on average, the bow echo occurs about 10 times a year in Poland (Celiński-Mysław et al. 2019). The period of occurrence of these events is also shorter and generally limited to the warmest months of the year, i.e., from May to August (Celiński-Mysław, Palarz 2017). On the other hand, derecho phenomena, which are the more intense type of bow echo in terms of the strength of wind gusts and their spatial and temporal extent, are less frequent. Derecho phenomena, on average, are recorded once a year in Poland, although sometimes they do not occur at all in a given year (Celiński-Mysław, Matuszko 2014; Surowiecki, Taszarek 2020). The mechanisms of the formation and development of both phenomena are similar. Bow echo is classified as a derecho; when characterized by an appropriate evolutionary cycle, it meets the conditions allowing for development and persistence in the environment for several hours, reaches certain spatial dimensions, affects a specific area, and is accompanied by wind gusts exceeding certain thresholds (Fujita 1978; Johns, Hirt 1987; Evans, Doswell 2001; Coniglio et al. 2004).

Most relevant publications in European literature described a derecho as a case study, with comprehensive analysis from an environmental point of view, which often plays a decisive role in the development of this phenomenon (Punkka et al. 2006; Lopez 2007; Gatzen et al. 2011; Hamid 2012; Gospodinow et al. 2015; Taszarek et al. 2019; Sipos et al. 2021; Chernokulsky et al. 2022). Fewer studies from Europe present climatological characteristics of long time series derechos (Gatzen et al. 2020). In this context, two Polish publications, which examine the derecho phenomenon in annual series, starting in 2007, are relatively well presented (Celiński-Mysław, Matuszko 2014; Surowiecki, Taszarek 2020). The derecho which occurred in 2017 near Suszek village was subject of a higher number of studies because it seems to be the most violent windy phenomenon which appeared in Poland during the last decade (Taszarek et al. 2019; Figurski et al. 2021; Łapeta et al. 2021; Łuszczewski, Tuszyńska 2022). This article presents a comprehensive synoptic analysis of this case and constitutes a part of a derecho monograph, together with two recent publications on radars and satellites.

The violent storm that occurred on August 11, 2017, met the derecho criteria (Johns, Hirt 1987; Celiński-Mysław, Matuszko 2014; Taszarek et al. 2019), although not those proposed by Corfidi et al. (2017), and was the most hazardous, recently recorded one in Poland. The wind gusts were some of the strongest in the history of Polish measurements, with a speed of 42 m/s in Elbląg, 36 m/s in Chrząstów, 35 m/s in Gniezno, and 31 m/s in Chojnice and Lębork. The storm zone covered almost the entire north-western part of the country, extending from 200 to 400 km. Analysis of radar data and atmospheric lightning indicated that the thunderstorms, which took the form of an organized convective system over time, had begun to develop over the Sudetes in the afternoon (14-16 UTC) and moved towards NNE. On the border of Lower Silesia and Wielkopolska, a supercell (a thunderstorm with rotating updraft) was formed, from which a bow-shaped line (bow echo) was generated in the evening (19-20 UTC). The system moved further through Kujawy and Gdańsk Pomerania, where the mesoscale convective vortex (MCV) developed. Then, crossing the region of Żuławy Wiślane, it moved over the Baltic Sea at night (23-00 UTC). Six people died, including two children, and several dozen people were injured as a result of broken trees and buildings de-

stroyed by the squall. According to media reports, the scale of forest damage on the path of the storm passed reached almost 80,000 hectares.

2. PURPOSE OF THE STUDY AND SOURCE DATA

The purpose of this study is to perform a detailed synoptic analysis and documentation of the conditions in which the storm occurred over Poland's western and northern parts on August 11, 2017. A detailed examination of the environment in which the derecho occurred, a rare phenomenon in Polish conditions, the causes of its formation, and the stages of its development are important not only from a scientific perspective but can also be applied in practice in short-range forecasting.

Based on archive charts and data used in the operational work of the Polish Meteorological Service, we analyzed the synoptic conditions. Precisely, we used surface and upper-level (850, 700, 500, and 300 hPa) synoptic charts at 00 and 12 UTC, Stüve diagrams and hodographs based on atmospheric soundings generated in Wrocław, Łeba, and Legionowo at 00 and 12 UTC, hourly SYNOP data from Polish synoptic stations, and meteorological data from the automatic stations of the Meteorological Measurement and Observation Network of the IMGW-PIB.

In addition, for the analysis, we used Stüve diagrams and hodographs based on atmospheric soundings carried out in Lindenberg, Prague, Prostejov, Lviv, and Vienna, obtained from the Univ. of Wyoming database available at http://weather.uwyo.edu/upperair/sounding.html; atmospheric sounding data and isobaric charts from the Plymouth State Weather Center archive from the website https://vortex.plymouth.edu/myowxp/upa/ovr-map-a.html; reanalysis from the GFS model http://www1.wetter3.de/archiv_gfs_dt.html; KNMI surface synoptic charts (from 00, 06, 12, 18 UTC) available on the website https://www.knmi.nl/nederland-nu/klimatologie/daggegevens/weerkaarten; DWD surface synoptic charts (00, 06, 12, 18 UTC) available on the website http://www1.wetter3.de/archiv_dwd_dt.html; reports on dangerous meteorological phenomena from the European Severe Weather Database (ESWD) from https://www.eswd.eu/.

The POLRAD radar network data and the MSG satellite images were used to retrace thunderstorm evolution and movement in high spatial and temporal resolution. General thunderstorm organization was determined based on the radar data.

3. METHODOLOGY

There are various definitions and approaches to "synoptic analysis" (Łozowicki 1991; Kalkstein et al. 1996; Niedźwiedź 2003; Lackmann 2011). Nowadays, complex numerical models are used to simulate and study the state of the atmosphere as well as the causes and development of the examined phenomenon. However, this study follows the classic synoptic analysis used in the operational work of the Polish Meteorological Forecast Offices. Its definition is simple and states that synoptic analysis is based on studying the state of the atmosphere over a large area, using synoptic charts (surface synoptic charts and isobaric upper-level charts) and other available material (Niedźwiedź 2003; AMS 2021). However, this simple identification of the "state of the atmosphere" requires a detailed analysis of the type of air masses and their physical properties, the determination of the location of the atmospheric fronts, as well as the vertical and horizontal air movements occurring in the atmosphere, and the dependencies between them, generating conditions for the emergence of complex weather phenomena.

The first stage of the research was the analysis of the isobaric upper level with reference to surface synoptic charts. This provided an insight into the general distribution of air masses and their properties, also considering the vertical structure of the atmosphere over Europe on August 11, 2017,
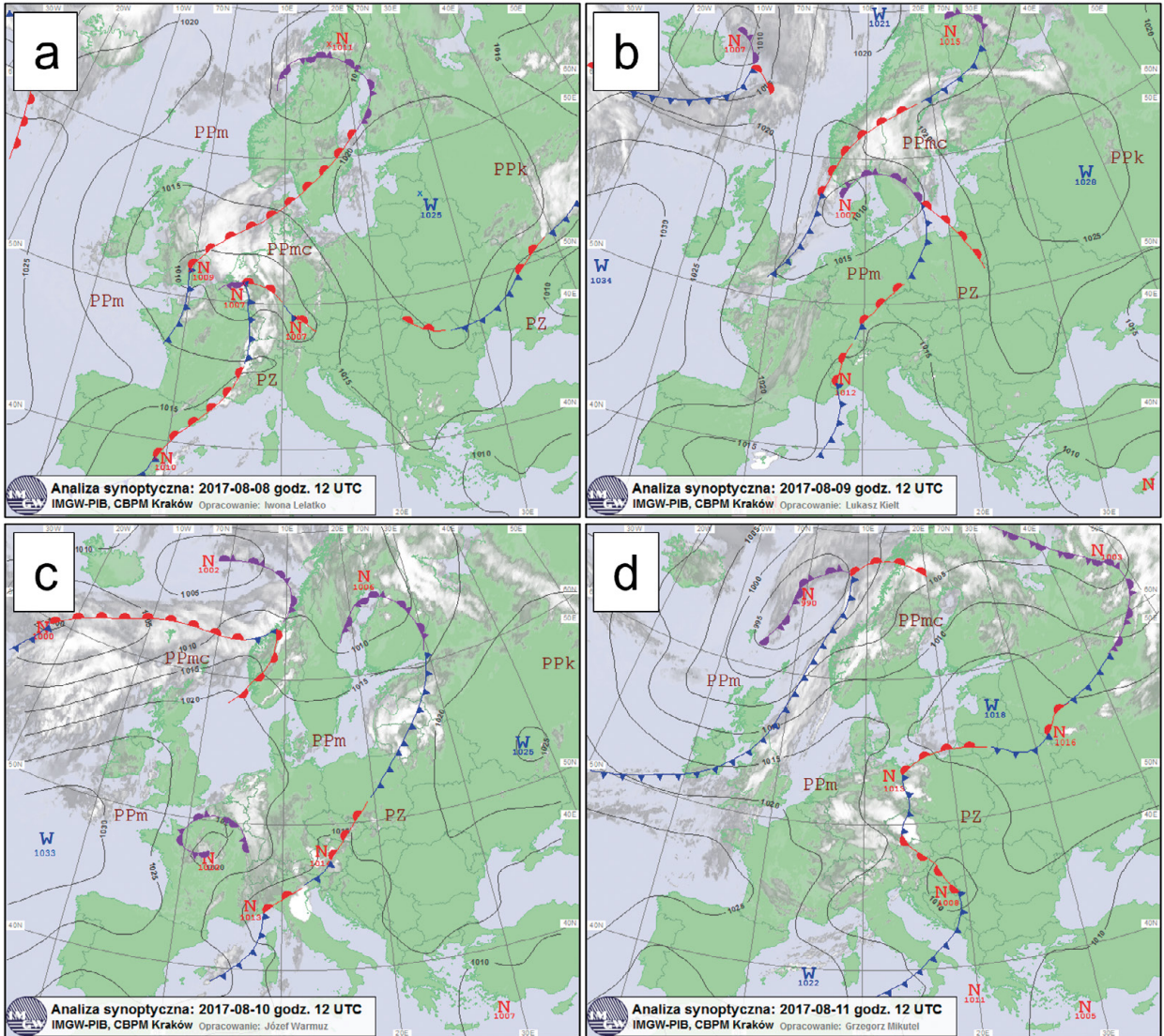
Fig. 1. Surface analysis, 12 UTC on August 8-11 (a-d), 2017. N – low, W – high, PPm – polar maritime airmass, PPmc – warm polar maritime airmass, PPk – polar continental airmass, PZ – tropical airmass.

and in the days preceding the occurrence of violent thunderstorms. The source areas of the air masses, the direction of their inflow, and the frontal zones separating them were analyzed. The influences of the upper- and mid-troposphere airflow on the development of the situation in the lower troposphere was also studied in detail.

In the following stage, the physical parameters of air masses in the frontal zone and in the warm tropical air mass were analyzed. Based on the aerological sounding data, the vertical profiles of temperature, humidity, and wind changes were determined. However, it should be emphasized that the sounding data have low spatial and temporal resolution and therefore do not fully reflect the evolution of the discussed situation. The aerological soundings from Legionowo characterized the conditions east of the developed thunderstorms. On the other hand, the vertical structure of the atmosphere over Wrocław was influenced by the convective cloudiness forming ahead of the cold front in the period preceding the violent storm development. When analyzing the atmospheric soundings from Łeba, located closest to the derecho occurrence, it should be kept in mind that at 12 UTC on August 11, 2017, the sounding was influenced by a sea breeze, and at 00 UTC on August 12, 2017, the storm system was already present in Łeba. Sound-

ings from Prostojev, Prague, and Vienna helped to characterize the tropical air mass that inflowed over the western part of Poland on August 11, 2017, because the same air mass had been present over Austria and the Czech Republic the day before, where violent thunderstorms, including bow echo, also occurred.

The following convective indices were used to assess the stratification of the atmosphere: SBCAPE (Surface-Based Convective Available Potential Energy) – the potential energy available to a parcel of air lifted from the surface; MLCAPE (Mixed Layer Convective Available Potential Energy) – the potential energy available to parcels representing the well-mixed lowest 500-m-thick atmospheric layer; CIN (Convective Inhibition) – a measure of the vertically integrated negative buoyancy of a rising parcel; LI (Lifted Index) – the difference between the temperature of a parcel lifted with average temperature and dewpoint of the layer 500 m above the surface to the level of 500 hPa and the temperature of the surrounding (Lelątko, Ziemiański 2004; Bąkowski 2005).

To determine the vertical humidity distribution, the following indices were used, calculated based on aerological soundings: TPW (Total Precipitation Water), relative and specific humidity, surface mixing ratio.
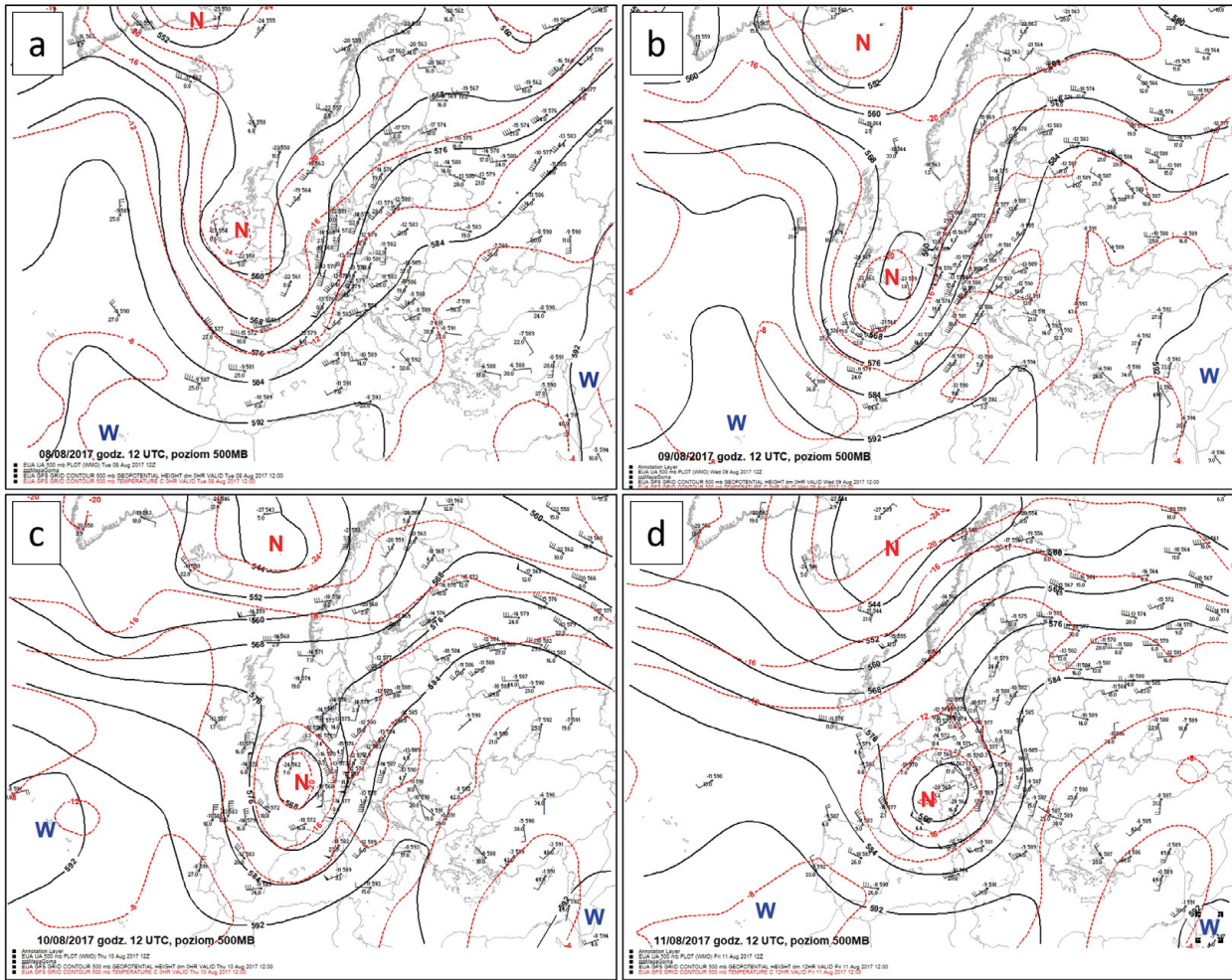
Fig. 2. Absolute topography map of the 500-hPa surface, 12 UTC on August 8-11 (a-d), 2017. N – low, W – high (source: IMGW-PIB).

Hodograph analysis was performed to determine the wind shear vectors in the 0-3-km and 0-6-km layers and the mean wind vector in the 0-6-km layer as well as to determine the relation between these vectors, which affects the structure of developing thunderstorm systems.

4. ANALYSIS OF THE SYNOPTIC SITUATION IN THE PERIOD PRECEDING THE SQUALL

The genesis of the mesoscale convective system that developed over Poland on August 11, 2017, was related to the evolution of the synoptic situation that had started a few days earlier. On August 8, 2017, eastern and partly central Europe was covered by a surface anticyclone and upper-level ridge. (Fig. 1a, 2a). This high-pressure system brought relatively warm but dry continental polar air from the east toward central and northern Europe. However, in the afternoon, it began to move eastwards, followed by the trough approaching from the west towards central Europe. This initiated a change in circulation over Poland to the southerly regions, with an inflow of warmer and more humid polar maritime air. An extensive trough (Rossby Wave) was observed over the North Atlantic and western Europe in the upper and middle troposphere (Fig. 2a), which gradually evolved into a cut-off low over England throughout the day. Along its leading part, a waving cold front stretched from Scandinavia to the Iberian Peninsula (Fig. 1a). Ahead of the front, warm, moist tropical air was lying over southern Europe, and polar maritime, warm air over central Europe, separated from the much colder and more humid polar maritime air approaching from the Atlantic.

On the following day, i.e., 09.08.2017, there was a relatively small but significant reconstruction of the thermobaric field. All main surface pressure systems moved slowly eastwards, and the frontal system covered the northern and western parts of Poland (Fig. 1b). The middle- and upper-tropospheric low, located over Great Britain the previous day, moved toward France, simultaneously elongating meridionally. A deep trough developed through the entire depth of the troposphere, separating the ridges over the Atlantic and southeast Europe (Fig. 2b). Such pressure distribution intensified the advection of warm and moist tropical air from the south-west to central Europe, including Poland.

On August 10, 2017, the synoptic situation further changed, seemingly insignificantly but in fact essentially for the evolution of the conditions for convective activity on that day, especially over the Czech Republic and Austria, and over Poland on the following day. The extensive upper-level trough, with the cut-off low over France, began to change its orientation from SW-NE to S-N direction (Fig. 2c). Such a pattern strengthened the direct, meridionally oriented tropical air mass advection from the Mediterranean basin over central Europe, including south-eastern Poland (Fig. 1c). Colder and moist polar maritime air advected over western Europe at the same time. The large thermal contrast of air masses in the front zone and the evolution of the upper-level trough created a favorable environment for frontogenesis and cyclogenesis, as well as a large-scale rising motion supporting the de-

11
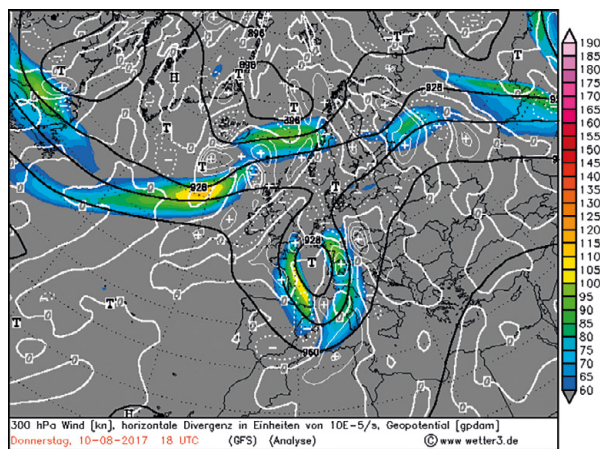
Fig. 3. Absolute topography map of the 300-hPa surface (GFS analysis), August 10, 2017, 18 UTC; jet streams (color scale) and horizontal divergence field (white isolines) are marked (source: www.wetter3.de).

velopment of deep convection in the warm air mass ahead of the front line. There was a significant horizontal divergence in the forward part of the upper trough, reaching its maximum over the Czech Republic (Fig. 3). This favored convergence at the surface, where the maximum convective activity occurred in the evening. The path of extreme phenomena, among which strong wind gusts were the most hazardous, was recorded in the area from Slovenia to southern Poland and marked the line of the maximum storm activity (Fig. 4a).

5. DETAILED ANALYSIS OF THE DERECHO STORM
5.1. SYNOPTIC SITUATION

As a consequence of the described favorable conditions in the upper troposphere, on the night of August 10/11, 2017, a wave on the atmospheric front over the western Czech Republic developed into a shallow low in the Rudawy region and moved towards Brandenburg (NE Germany) in the morning and during the day on August 11, 2017. The frontal zone stretched along the northern and western border of Poland at 12 UTC, and the tropical airmass advected over the whole country (Fig. 1d). The location of the main pressure systems in the middle and upper troposphere on August 11, 2017, did not differ much from that of the previous day. However, their shape changed, which affected the further development of the situation. Western Europe was covered by an extensive upper trough, with a cut-off low in its southern part, moving from France towards the Alps (Fig. 2d). In this way, the axis of the upper trough was slightly directed to the northwest, which generated an advection of tropical air from the eastern part of the Mediterranean basin, through the Adriatic Sea, over Poland. Simultaneously, the frontal waves and surface lows in the frontal zone were moving in the same direction. On an isobaric surface of 850 hPa, a ridge of warm air covered most of Poland, exceeding the temperature of 20°C in the southeast of the country. At the same time, there was polar maritime air, colder by about 10°C (Fig. 5), over Germany.

5.2. THE PROCESS OF FRONTOGENESIS

The temperature gradient increased over time in the west of the country and over eastern Germany, indicating frontogenesis. The process of frontogenesis in this area could be traced over time by analyzing the magnitude of the vector -Qn (Fig. 6). This vector is a component of the Q-vector, which describes the evolution of the horizontal potential temperature gradient vector due to changes in the geostrophic wind. The vector -Qn is the Q-vector's component perpendicular to the isotherms on a given isobaric surface. If -Qn > 0, frontogenesis occurs; if -Qn < 0, frontolysis occurs (Kurz 1992). The maximum value of the -Qn-vector, indicating frontogenesis, moved from Austria through the Czech Republic to western Poland on August 11, 2017.

The increase in the horizontal temperature gradient in the lower troposphere resulted in the isobaric surfaces becoming more inclined. This led to an intensification of the horizontal pressure gradient and an increase in the geostrophic wind speed above due to the thermal wind principle. Changes in the vertical wind profile could be noticed by analyzing data from the soundings, carried out in the frontal zone or its vicinity (Fig. 7). Prague was located closest to the waving cold front or directly in its zone in the period from August 10 to August 12, 2017. The maximum wind speeds of 30-38 m/s were maintained there in the upper troposphere (at an altitude of 10-12 km), proving the presence of an upper-level jet stream in the frontal zone. There was also a clear increase in wind speed in the mid-troposphere (at an altitude of 3.5-7 km). In Wrocław, located ahead of the cold front on August 10-11, 2017, two distinct wind speed maxima were measured: the first one in the upper troposphere, related to the jet stream, and the second one in the middle troposphere. In a layer of 3.5-6 km, the wind speed increased significantly from around 15 to around 28 m/s from August 10 to August 11, 2017. The changes in wind speed with altitude and time were the largest but the least regular ones in Prostejov, located also ahead of the cold front. However, there was also a noticeable increase in wind speed in the lower and middle troposphere. The maximum speed of 35 m/s was recorded on August 11, 2017, at 00 UTC, at an altitude of approximately 4 km.

5.3. PROCESSES GENERATING LARGE-SCALE RISING MOTIONS OVER CENTRAL EUROPE

The evolution of the upper cut-off low of an ellipsoidal shape significantly influenced the atmosphere dynamics in central Europe on August 11, 2017. The longer axis of the low changed its orientation from N-S to W-E during the slow movement from France to northwest Italy and further turned to the S-N orientation (180° in total), which took place in the afternoon. Such a rotation enabled a strong cyclonic vorticity advection, covering the area from northern Italy through Austria to the Polish-Czech-German border (Fig. 8). Simultaneously, this area coincided with a jet stream which generated a clear divergence in its exit region (Fig. 9). These processes were conducive to forming the aforementioned low-level low over the western Czech Republic and eastern Germany throughout the day.

The development of large-scale rising motion related to the evolution of the upper-level low took place in the zone of the waving atmospheric front, i.e., from Austria through the western Czech Republic and the Polish-German border. However, also ahead of the front, i.e., in the broader area from the Balkans to Poland, a large-scale lifting was supported by changes in the geopotential field. The axis of the high-pressure ridge moved from Poland to the northeast. The geopotential field in the upper and middle troposphere was transforming from anticyclonic to cyclonic, which generated cyclonic vorticity advection. In the evening on August 11, 2017, this cyclonic vorticity advection was visible in the zone extending from the South Baltic to south-eastern Poland, with a slight maximum near the coast (Fig. 8c), slowly moving away to the northeast. This indicated the dynamic support of large-scale lifting in the central part of northern Poland during the convective system development.

Another factor contributing to the occurrence of large-scale vertical movements was warm air advection, which can be expressed, among
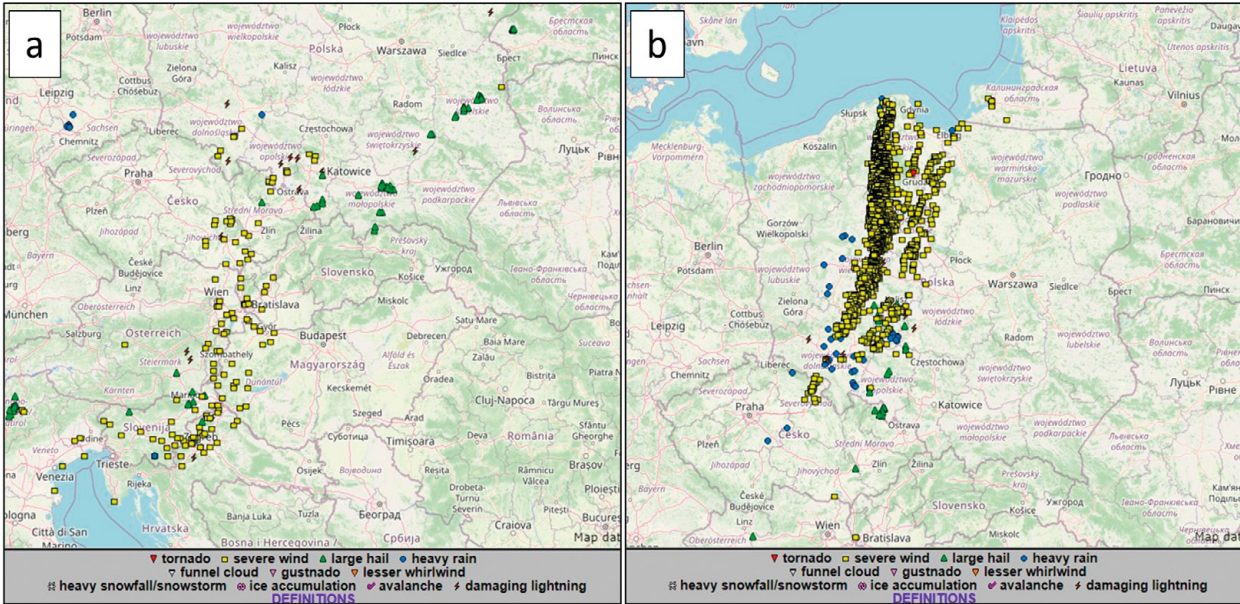
Fig. 4. Reports on hazardous meteorological phenomena from August 10, 2017, 09 UTC to August 11, 2017, 03 UTC (a) and from August 11, 2017, 06 UTC to 24 UTC (b) (source: www.eswd.eu).

others, in 1,000- to 500-hPa layer thickness changes. A summary of changes in the thickness of this layer, based on selected aerological soundings on August 11, 2017, indicates that the layer was the thickest and, therefore, the warmest in Legionowo, Prostejov, and Wrocław and on August 10, 2017, also in Prague (Fig. 10). There was a tropical air mass at that time in those locations. The layer thickness was smaller in Łeba and Lindenberg. Lindenberg was in the polar maritime air mass, whereas Łeba was in the tropical air mass only on August 11, 2017, at 12 UTC. The changes in the 1,000- to 500-hPa layer thickness over time were significant: in the period from 00 to 12 UTC on August 11, 2017, the thickness was increasing in Legionowo, Prostejov, and Łeba, showing warm air advection, while it began to decrease in Wrocław, Lindenberg, and, especially, in Prague, which already indicated cold air advection. Analyses from the GFS model may help diagnose a temperature advection in space and time. The maximum warm air advection in the 1,000 to 500-hPa layer moved from the eastern Czech Republic (12 UTC) over Wielkopolska (18 UTC) and then to the north and northeast on August 11, 2017 (Fig. 11). The maximum warm air advection occurred in the area of the mesoscale convective system passage, i.e., from Wielkopolska through the Kuyavian-Pomeranian and Pomeranian voivodeships in the evening on August 11, 2017.

Warm air advection, indicated by veering of upper wind, with height in the lower and middle troposphere, was confirmed by atmospheric sounding data. It was most clearly visible in Łeba at 12 UTC on August 11, 2017, where the veering wind was observed with slight deviations in the layer from the ground surface (SE) to about 600 hPa (SW) and in Wrocław from about 900 to 650 hPa (Fig. 12).

The described processes, i.e., cyclonic vorticity advection in the upper and middle troposphere and warm air advection in its lower and middle part, are factors forcing large-scale air rising, as described by quasi-geostrophic omega equations (Lackmann 2011). Air rising on the synoptic scale favors the development of deep convection (Lackmann 2011; Bechtold 2019). Analysis of large-scale vertical motions using the GFS model (Fig. 13) shows that there was strong lifting over western Poland, reaching maximum values of 40 hPa/h in the evening of August 11, 2017.

<div style="page-number">13</div>
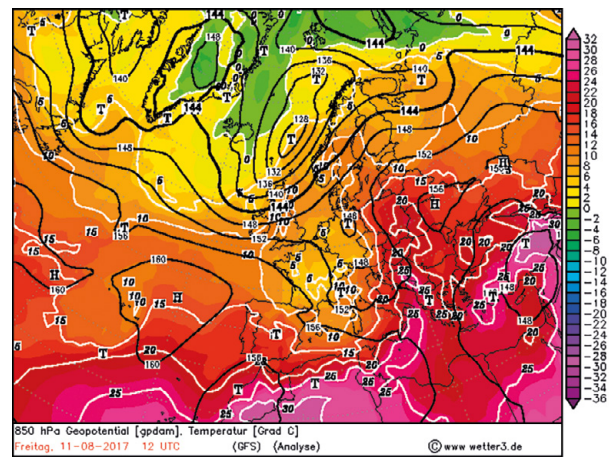
Fig. 5. Absolute topography map of the 850-hPa surface (GFS analysis), August 11, 2017, 12 UTC (source: www.wetter3.de).

5.4. ASSESSMENT OF CONVECTIVE CONDITIONS

The key components for the development of deep convection, including MCS systems with bow echo, are as follows: a large amount of moisture in the boundary layer, a steep temperature lapse rate in the middle troposphere, which indicates a rapid temperature drop with altitude, mechanisms that initiate and maintain convection, and wind changes in the vertical profile, which determine the wind shear.

The tropical air mass over Poland on August 11, 2017, differed in terms of physical properties in the western and eastern half parts of the country. In the southeast, the air was noticeably warmer. The air temperature at 850 hPa was 19-22°C at noon, and the maximum temperature at 2 m in that area reached 35°C (Figs. 5 and 14). In the west, the temperature at 850 hPa was significantly lower, from 14 to 18°C, and the maximum temperature at the surface was 22-26°C.

The air in the southeast of the country was relatively dry. Total Precipitation Water (TPW) in the southeast was below 30 mm. Due to the strong subsidence inversion, humidity was low from the surface up to 600 hPa, resulting in cloudless weather. On the other hand, humidity was larger and reached 45-48 mm
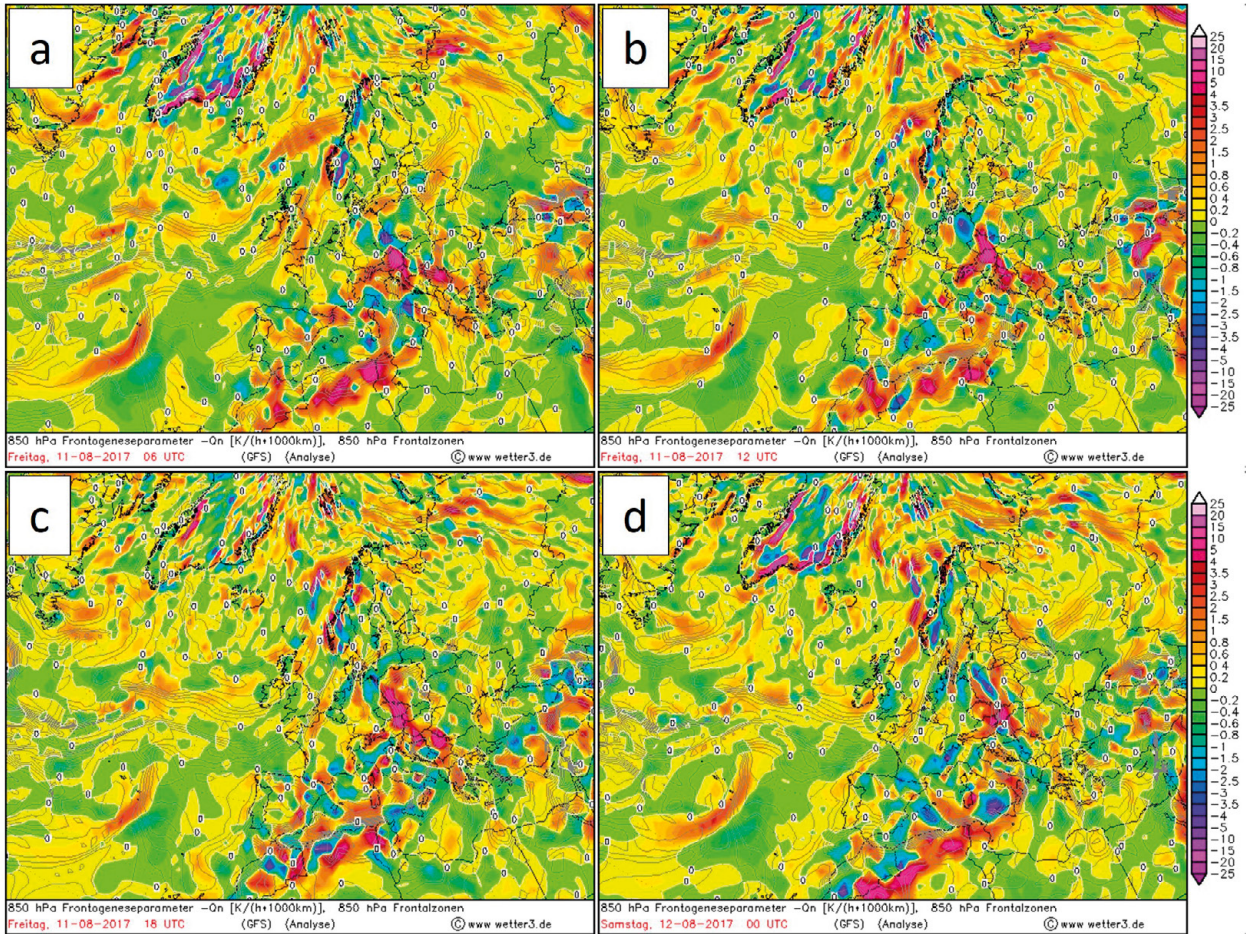
Fig. 6. Frontogenesis on the surface of 850 hPa (GFS analysis, description in the text), August 11, 2017, 06 UTC (a), 12 UTC (b), 18 UTC (c), and August 12, 2017, 00 UTC (d) (source: www.wetter3.de).
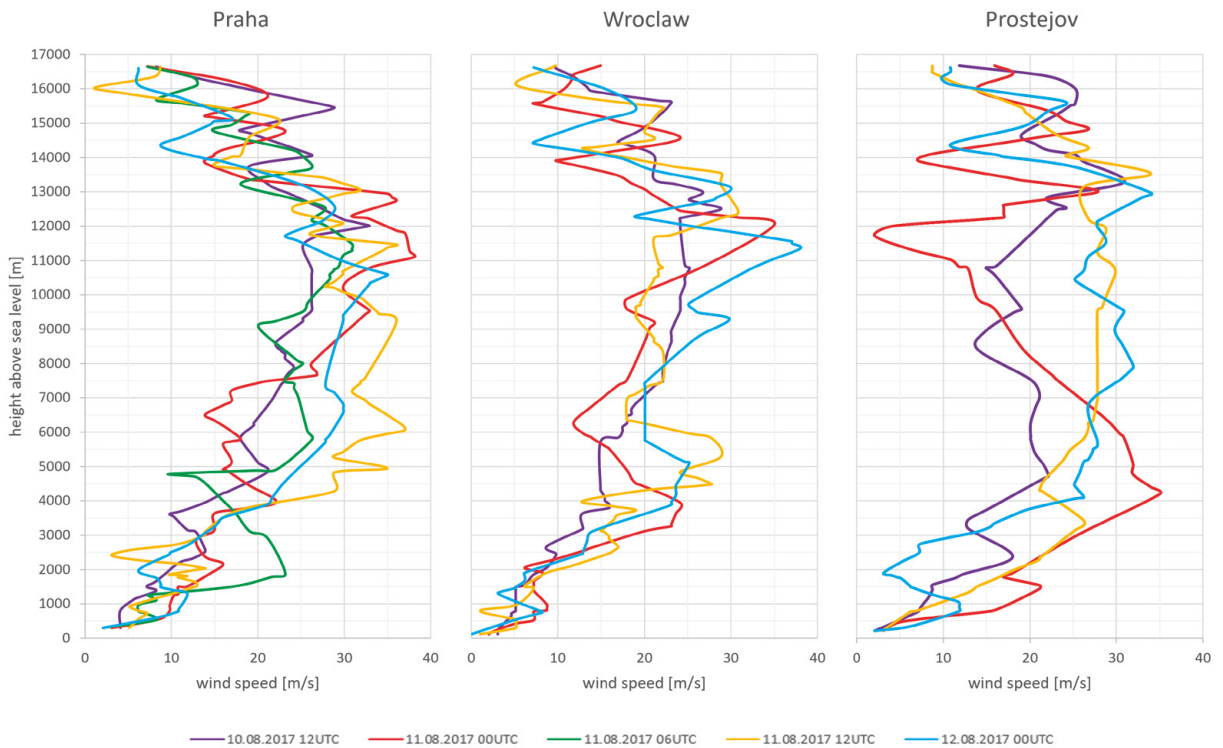
Fig. 7. Vertical wind speed profiles in Prague, Wrocław, and Prostejov from August 10, 2017, at 12 UTC to August 12, 2017, at 00 UTC (source: IMGW-PIB).
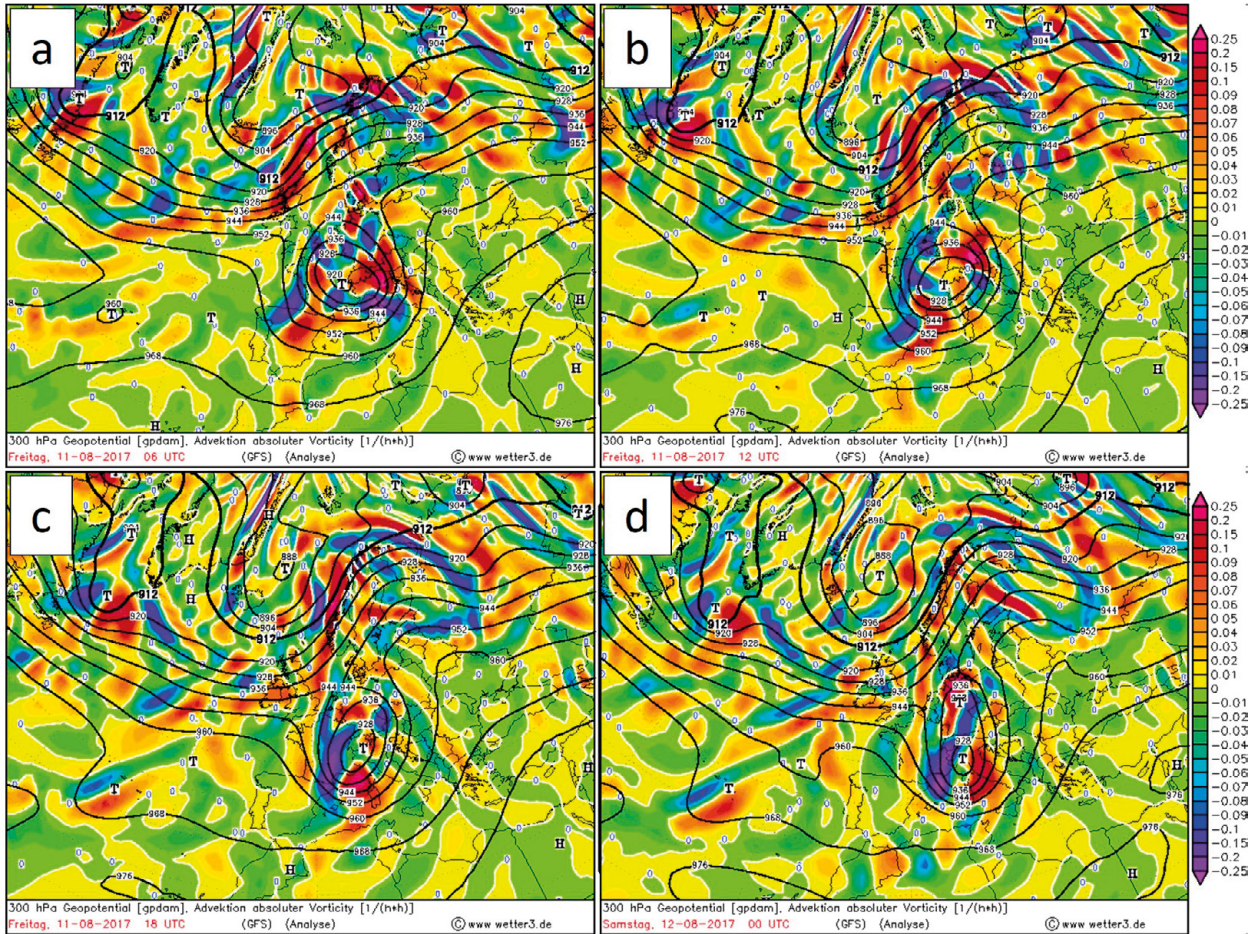
Fig. 8. Absolute topography maps of the 300-hPa surface with total vorticity advection (GFS analysis), August 11, 2017, 06 UTC (a), 12 UTC (b), 18 UTC (c), and August 12, 2017, 00 UTC (d) (source: www.wetter3.de).
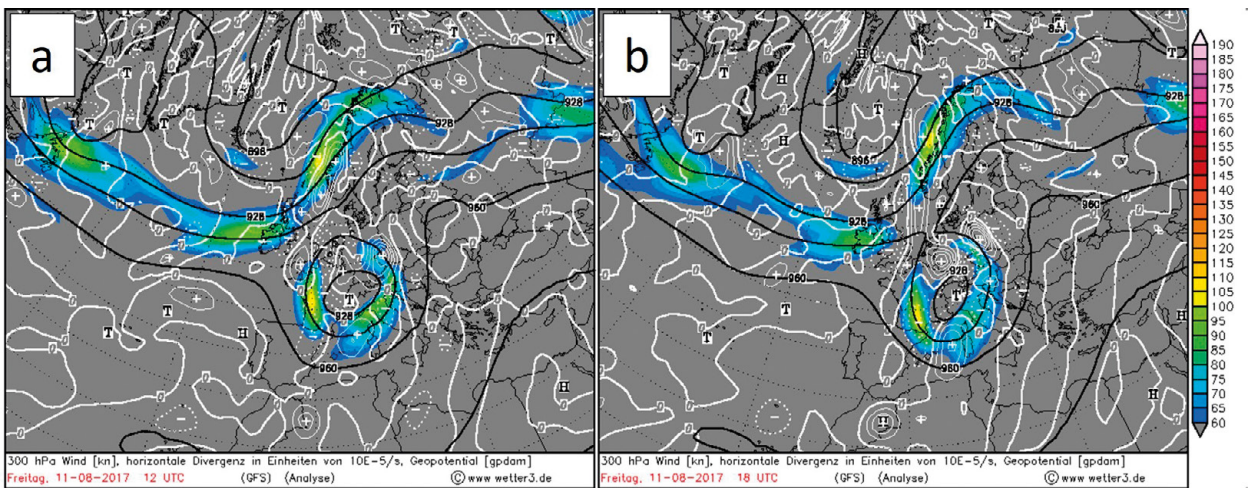
Fig. 9. Absolute topography maps of the 300-hPa surface (GFS analysis), August 11, 2017, 12 UTC (a), and 18 UTC (b); jet streams (color scale) and horizontal divergence field (white isolines) are marked (source: www.wetter3.de).

15

in the west of Poland, in the frontal zone and the line of convergence ahead of it, and in the northern part of the country (about 45 mm in Wrocław on August 11, 2017). Humidity was accumulated mainly in a layer from about 700 to 400 hPa. The day before, TPW was also significant over Austria and the Czech Republic – on August 10, 2017, at 00 UTC, it reached 46 mm in Vienna and 30-40 mm over the Czech Republic, where significant humidity was also accumulated in the 700- to 400-hPa layer. In addition to the increased humidity

in the middle troposphere, humidity was concentrated at the surface, to the isobaric level of about 900 hPa. The water vapor mixing ratio in the boundary layer was 11-14 g/kg in western Poland at noon, slightly to the east of the front, and in the northern part of the country, it reached 15-17 g/kg. The lowest values were observed in the southeast – from 8 to 11 g/kg. For comparison, the surface mixing ratio was 14 g/kg on August 10, 2017, at 12 UTC in Prostojev.
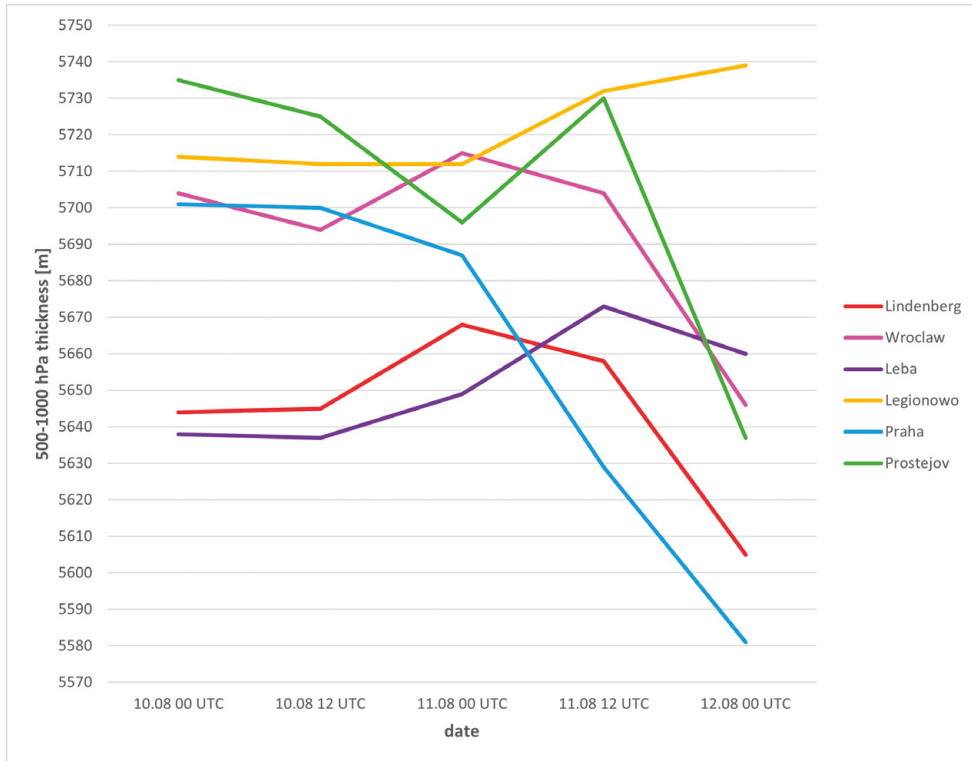
Fig 10. Thickness changes in the layer of 500-1,000 hPa from August 10, 2017, at 00 UTC to August 12, 2017, at 00 UTC in selected locations based on aerological measurements (source: IMGW-PIB).
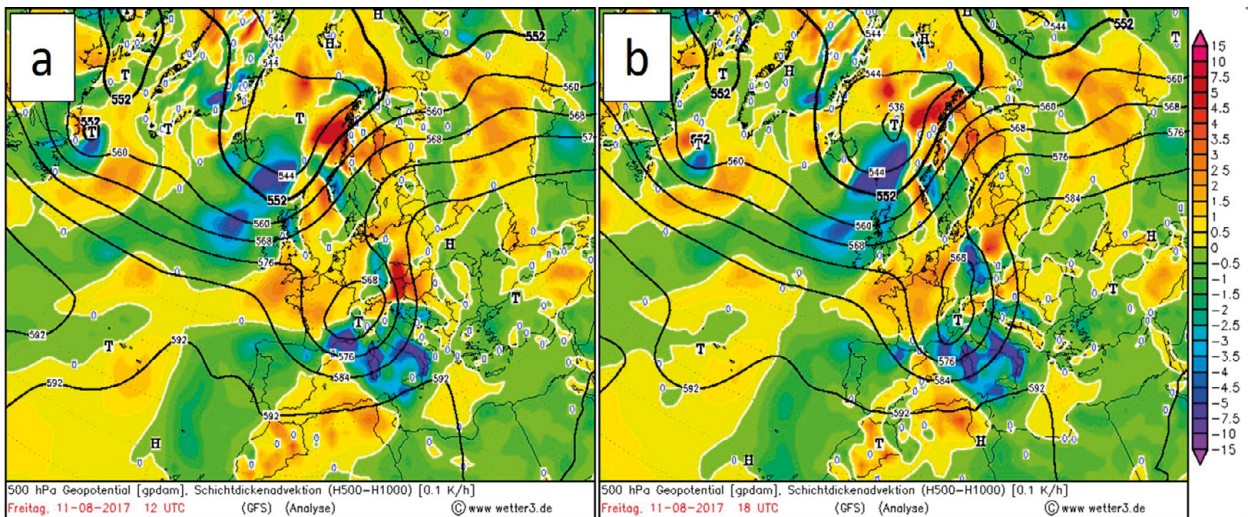
Fig. 11. Temperature advection in the 500-1,000 hPa layer (GFS analysis) on August 11, 2017, 12 UTC (a) and 18 UTC (b) (source: www.wetter3.de).

Such a humidity distribution in the vertical profile, with drier air in the 900- to 700-hPa layer (Fig. 15), indicates the possibility of intensifying strong wind gusts at the surface via acceleration of the downdrafts.

In addition to the spatial distribution of humidity, it is also necessary to consider its changes over time. The increase in the mixing ratio and water vapor content in the vertical column of air between August 10, 2017, and August 11, 2017, was best visible in Wrocław and Legionowo. A similar increase took place during the night on August 11/12, 2017, in Łeba (Tab. 1), indicating the presence of moist air advection.

Apart from the significant humidity, the air mass in which the most severe thunderstorms developed was characterized by unstable stratification. In the 800-600-hPa layer, the vertical thermal gradient was around

8.0°C/km in Legionowo on August 11, 2017, at 00 UTC and 12 UTC, and about 7.4 and 6.0°C/km in Wrocław, respectively. For comparison, this gradient was about 8.5°C/km on August 10, 2017, at 12 UTC in Prostejov.

The Lifted Index (LI) can also be used to determine mass instability. Here, LI, calculated for a parcel lifted with average temperature and dewpoint of the layer 500 m above the surface, was approximately −1°C in Wrocław at 00 UTC but 2.6°C at 12 UTC on August 11, 2017, while in Legionowo, it was even −8°C at 12 UTC. On the other hand, this air mass over Austria and the Czech Republic was characterized by LI values from −4 to −7°C on the previous day and was therefore moderately and strongly unstable (Lelątko, Ziemiański 2004). It should
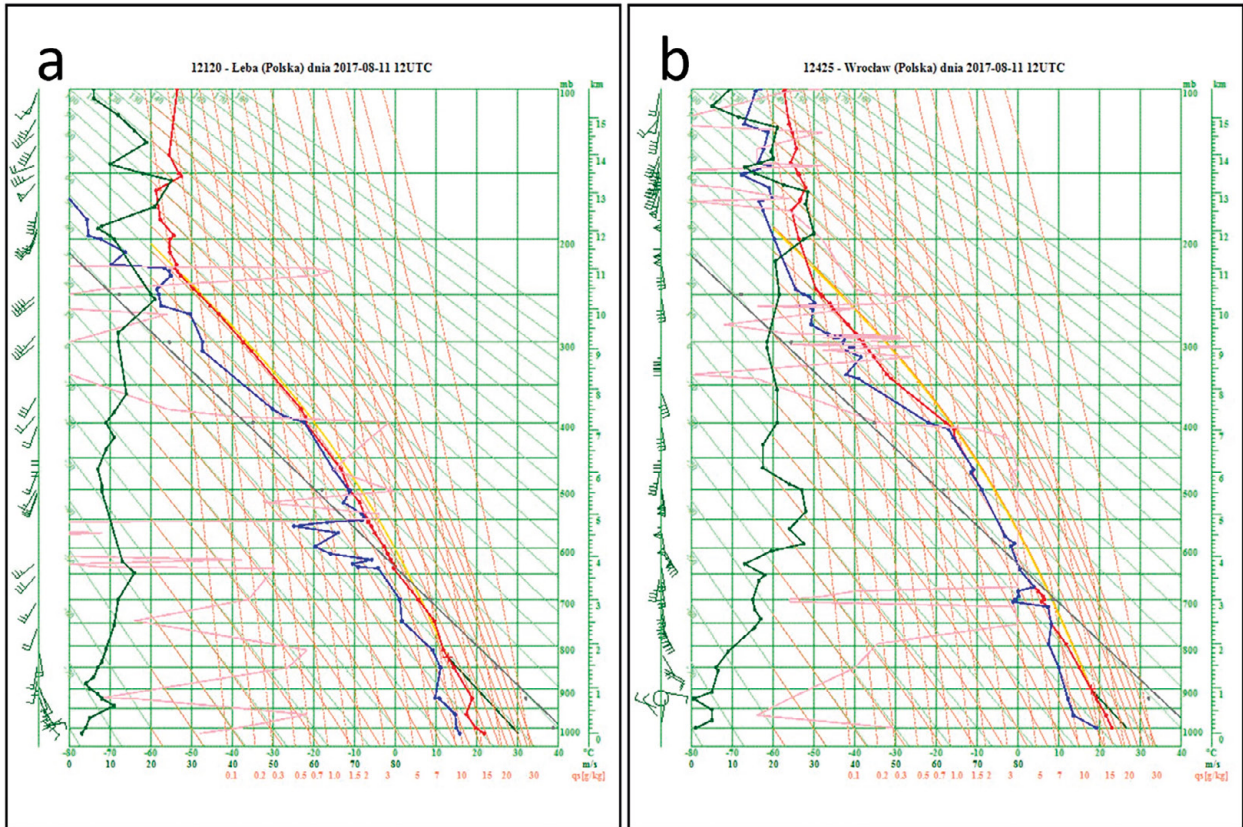
Fig. 12. Aerological soundings from Łeba (a) and Wrocław (b), August 11, 2017, 12 UTC (source: IMGW-PIB).

be mentioned that LI, calculated for the most unstable parcel, dropped to –4°C at 00 UTC and to –1°C at 12 UTC in Wrocław. According to GFS analyses, the highest instability measured by LI, from –6 to –8°C, occurred in the east of the country, whereas in the west, LI ranged from –1 to –3°C, decreasing to –6°C in the afternoon.

Such a large amount of humidity and instability resulted in a significant amount of potential energy available for convection. The SBCAPE (Surface-Based Convective Available Potential Energy), reaching 2,500-3,000 J/kg, was observed in central and north-eastern Poland, whereas it was 200-800 J/kg in the west of the country. The previous day, an SBCAPE of 1,500-2,200 J/kg was recorded in the air mass moving over from Austria and the Czech Republic towards Poland. According to GFS analyses, the MLCAPE (Mixed Layer Convective Available Potential Energy) reached 1,800 J/kg over the Czech Republic and Austria on August 10, 2017, and it increased in the afternoon from 100-700 J/kg to 300-1,100 J/kg (Fig. 16) over western Poland on August 11, 2017. These values indicate the low and moderate intensity of convection (Lelątko, Ziemiański 2004).

It should be added that from the level of 900 hPa to about 750-650 hPa, a stable stratification was observed on some aerological soundings.The CIN (Convective Inhibition) values reached about –180 J/kg in Prostejov on August 10, 2017, at 12 UTC, and –280 J/kg in Wrocław on August 11, 2017, at 00 UTC. Therefore, moisture and temperature advection in the boundary layer as well as the kinematic conditions and dynamic factors that force convection initiation were important.

The above analysis shows that the convective instability over Poland increased from west to east, in contrast to humidity, which was highest in the west of the country. Therefore, optimal conditions for the devel-
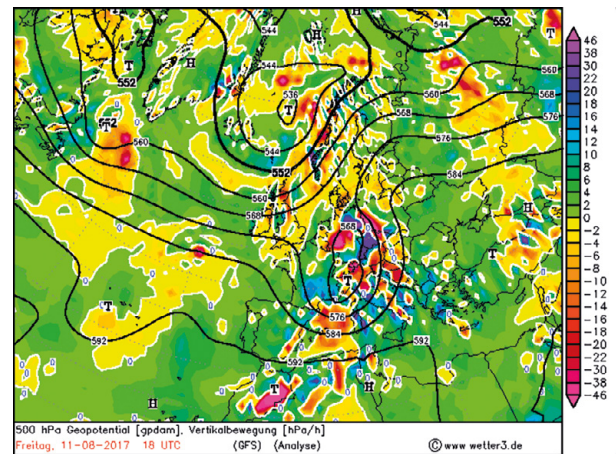
Fig. 13. Vertical movements on the surface of 500 hPa (GFS analysis), August 11, 2017, 18 UTC (source" www.wetter3.de).

opment of deep convection should have been expected in the central belt of Poland.

The dynamic factors that supported the initiation and sustaining of the upward movements on August 11, 2017, were the orography and the surface wind convergence zones in the southwest of the country. Over the Sudetes and in the area from Poznań through Leszno to Wrocław (Fig. 17a), thunderstorms were already developing in the morning and before noon. These phenomena were not violent and intense but gave rise to cold pool development in the southwest of Poland. A distinct horizontal thermal gradient and a wind convergence zone were formed; two zones of wind convergence were noticeable at 13 UTC (Fig. 17b). The thermal differences were amplified by daily heating, especially on the eastern convergence line,

Temperatury ekstremalne:
2017-08-11 18UTC
godzina 20:00 czasu urzędowego

od 13.9 Resko
do 24.4 Kozienice
od 21.2 Jelenia Góra
do 35.3 Kraków

TX   RRR
TG
TN   RRR24

TX - T. maks. RRR - Wys. opadu w mm
TG - Temperatura gruntu
TN - T. min. RRR24 - Suma opadu za 24H
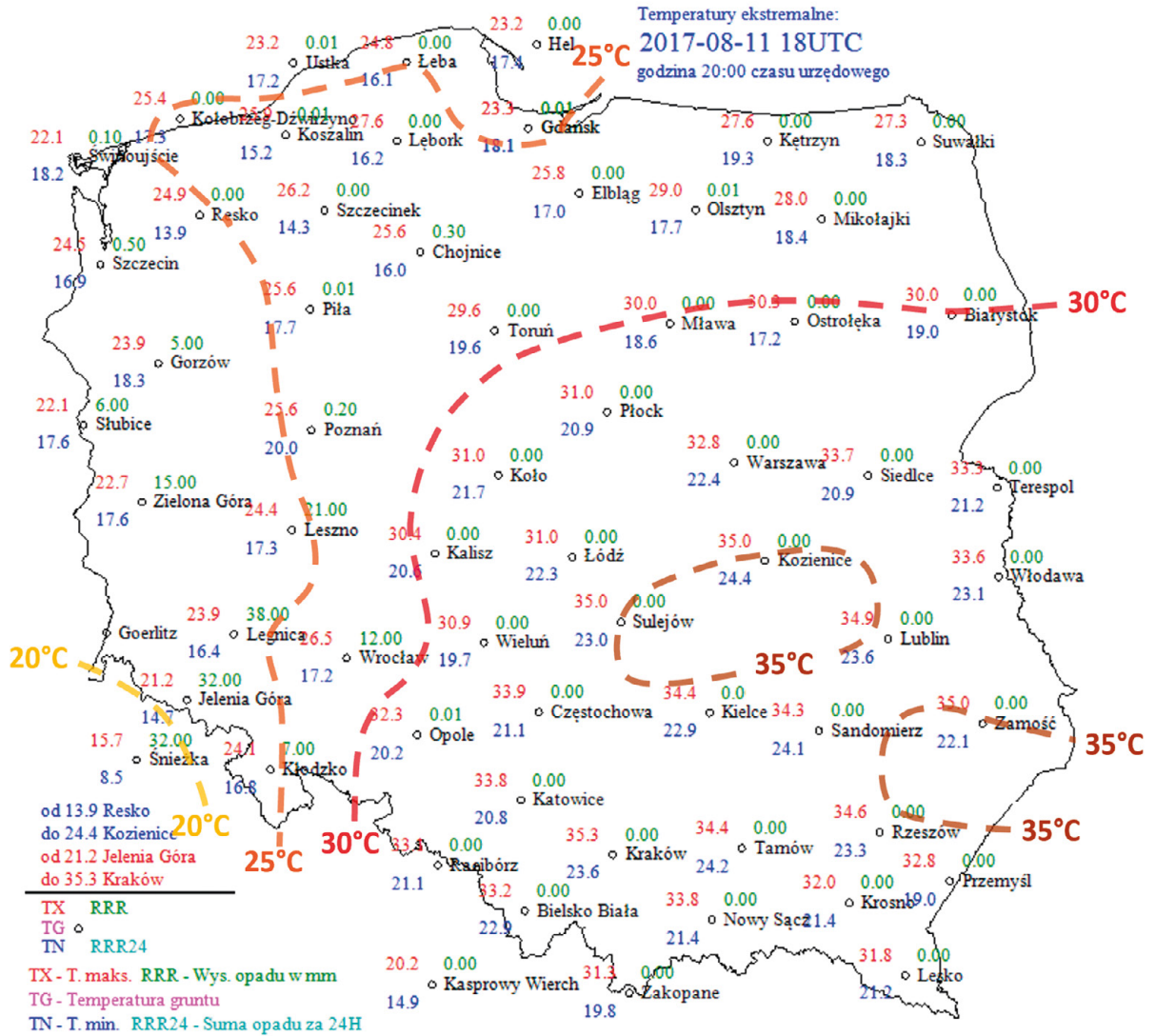
Fig. 14. Maximum temperature distribution in Poland on August 11, 2017, 18 UTC (source: IMGW-PIB).

Table 1. Mixing ratio and water vapor in the vertical air column from August 10, 2017, at 12 UTC to August 12, 2017, at 00 UTC, based on aerological measurements.

	Surface mixing ratio [g/kg]				Water vapor content in the vertical air column (TPW) [mm]			
	10.08 12 UTC	11.08 00 UTC	11.08 12 UTC	12.08 00 UTC	10.08 12 UTC	11.08 00 UTC	11.08 12 UTC	12.08 00 UTC
Wrocław	13.5	13.7	14.2	11.8	35.4	45.0	44.4	33.8
Łeba	12.8	9.1	11.2	13.3	32.9	28.5	37.9	40.8
Legionowo	12.9	13.9	15.7	13.2	31.6	41.0	40.7	36.1
Prostejov	14.2	12.8	14.1	11.8	35.6	35.1	35.3	31.5

where the cloudiness changed from fine to the east of this line to cloudy, post-convective to the west. The first afternoon thunderstorms were formed over the Sudetes. Following the mean wind direction in the troposphere, they moved to the north, into the zone of the western line of wind convergence, where a further rapid development of convection occurred in the following hours. The convergence lines approached each other at 17 UTC, and the horizontal thermal gradient in this zone increased, particularly over the Opole region (Fig. 17c). According to the radar data, thunderstorms had the form of a mesoscale convective system at that time, in which the line of the most active thunderstorm cells was divided into the one located more zonal and the other located meridionally. The entire system was moving north and northeast and was gaining in intensity. Kinematic factors (mainly appropriate wind shear) ultimately led to the formation of the bow echo structure (between 18:30 UTC and 19 UTC) in the zonal part of the MSC (perpendicular to the direction of airflow on the higher levels). Maximum thunderstorm activity took place between 19 and 22 UTC (Fig. 17d), after which the intensity of the phenomena decreased, and the system moved away to the Baltic Sea.

5.5. IMPORTANCE OF WIND SHEAR
In addition to the appropriate convective instability and humidity in the lower troposphere, a wind shear also occurred in the atmospheric en-

11747 - Prostejov (Czechy) dnia 2017-08-10 12UTC

Fig. 15. Atmospheric sounding from Prostejov, August 10, 2017, 12 UTC (source: IMGW-PIB).

Table 2. Wind gusts or maximum wind speeds ≥20 m/s from 10-minute intervals measured by the measurement and observation network of the IMGW-PIB within the range of the mesoscale convective system moving through Poland on August 11, 2017.

Time [UTC]	Wind gust/ maximum wind [m/s]	Location	Voivodeship
16:50	21.9	CHWAŁKOWICE	Lower Silesia
16:50	22.5	WROCŁAW	Lower Silesia
18:10	20.7	KÓRNIK	Wielkopolskie
18:30	22.7	KALISZ	Wielkopolskie
18:30	26.1	SŁUPCA	Wielkopolskie
18:50	34.8	GNIEZNO	Wielkopolskie
19:10	20.0	KOŁO	Wielkopolskie
19:50	20.7	TORUŃ	Kuyavian-Pomeranian
20:00	36.0	CHRZĄSTOWO	Kuyavian-Pomeranian
20:30	28.6	GRUDZIĄDZ	Kuyavian-Pomeranian
20:50	31.2	CHOJNICE	Pomeranian
21:00	20.0	PRABUTY	Pomeranian
21:00	22.6	STAROGARD GDAŃSKI	Pomeranian
21:10	20.6	RADOSTOWO	Pomeranian
21:20	21.8	KOŚCIERZYNA	Pomeranian
21:20	22.9	OSTRZYCE-BRODNICA GÓRNA	Pomeranian
21:30	24.7	KMIECIN	Pomeranian
21:40	42.2	ELBLĄG-MILEJEWO	Warmian-Mazurian
21:50	25.0	FROMBORK	Warmian-Mazurian
21:50	25.0	GDAŃSK-PORT PÓŁNOCNY	Pomeranian
21:50	23.8	GDYNIA	Pomeranian
22:00	24.6	HEL	Pomeranian
22:00	27.7	NOWA PASŁĘKA	Warmian-Mazurian
22:10	31.0	LĘBORK	Pomeranian
22:10	20.3	ROZEWIE	Pomeranian

Table 3. 1-hour precipitation ≥20 mm, determined by the measurement and observation network of the IMGW-PIB within the range of the mesoscale convective system, moving through Poland on August 11, 2017.

Time [UTC]	1-hour precipitation [mm]	Location	Voivodeship
16:00	22.3	JAKUSZYCE	Lower Silesia
17:00	21.4	BORÓW	Lower Silesia
17:00	35.6	DOBROGOSZCZ	Lower Silesia
17:00	22.7	TWARDOCICE	Lower Silesia
17:00	27.9	CHWAŁKOWICE	Lower Silesia
17:00	24.4	OTMUCHÓW	Opolskie
18:00	36.9	BIERUTÓW	Lower Silesia
19:00	23.9	OSTRÓW WIELKOPOLSKI	Wielkopolskie
19:00	30.5	SIEMIANICE	Wielkopolskie
19:00	23.0	WRZEŚNIA	Wielkopolskie
19:00	23.7	NOWA WIEŚ PODGÓRNA	Wielkopolskie
20:00	24.5	ZBIERSK	Wielkopolskie
20:00	26.1	MIRKÓW	Łódzkie
20:00	27.6	JANOWIEC WIELKOPOLSKI	Kuyavian-Pomeranian
21:00	28.3	SYPNIEWO	Kuyavian-Pomeranian
21:00	20.0	TORUŃ	Kuyavian-Pomeranian
22:00	21.4	NIEZABYSZEWO	Pomeranian
22:00	20.9	KOŚCIERZYNA	Pomeranian
22:00	22.3	TOLKMICKO	Warmian-Mazurian
23:00	23.2	NOWA PASŁĘKA	Warmian-Mazurian
23:00	21.1	ROGITY	Warmian-Mazurian
23:00	38.5	LĘBORK	Pomeranian

vironment, allowing thunderstorms to be organized into a mesoscale convective system in the form of bow echo, visible on radars and persisting for several hours. When analyzing the hodographs from the aerological stations located near the MCS path (Wrocław, Łeba) and in the direction of air-mass advection (Prostejov), it could be noticed that bulk shear in the 0-3-km layer was either strong or very strong (15-25 m/s) on August 11, 2017, at 00 and 12 UTC. (Fig. 18). The 0-6-km wind shear differed from the 0-3-km shear by no more than 5 m/s. Only in Wrocław at 12 UTC, it was stronger by about 10 m/s, which indicated the existence of conditions favorable for the development of a supercell thunderstorm on the border of Lower Silesia and Wielkopolska. If we calculate the maximum wind shear in the lower and middle troposphere, not considering the 0-3-km and 0-6-km layers, it was about 29 m/s from the surface to 4.5 km at 12 UTC in Wrocław and about 19 m/s to 4 km in Łeba. The presence of wind shear of at least 15 m/s in a layer up to 2.5-5 km above the ground level confirms the favorable conditions for the development of multi-cellular convection in a linear form, with a high probability of bow echo, mainly when the shear is concentrated to a height of 2.5-3 km (Weisman 1993). Analysis of upper-air soundings shows that the atmospheric conditions met the criteria needed for the development of such intense convective phenomena.

Attention should also be paid to the orientation of the wind shear vector relative to the mean wind vector. At 12 UTC on August 11, 2017, the mean wind speed in the 0-6-km layer was about 20 m/s and the direction about 170° in Prostejov, 14 m/s and 170° in Wrocław, respectively, and 8 m/s and 200° in Łeba. Thus, the mean wind and the 0-3-km wind shear vectors' directions were similar in individual cases. According to the RKW theory (Rotunno et al. 1988), the formation of a new thunderstorm cell in a multicell convective system, in an environment with a significant wind shear in the layer up to several kilometers, usually takes place at the cold pool edge, moving in the same direction as the wind shear vector (downshear flank). It is the place where the strongest convergence occurs. The vector

of the movement of the entire system, at least in a homogeneous external environment and for linear hodographs, is the sum of the wind shear vector, determining the place of new cell formation, and the mean wind vector, determining the movement of a single convective cell. The more

19
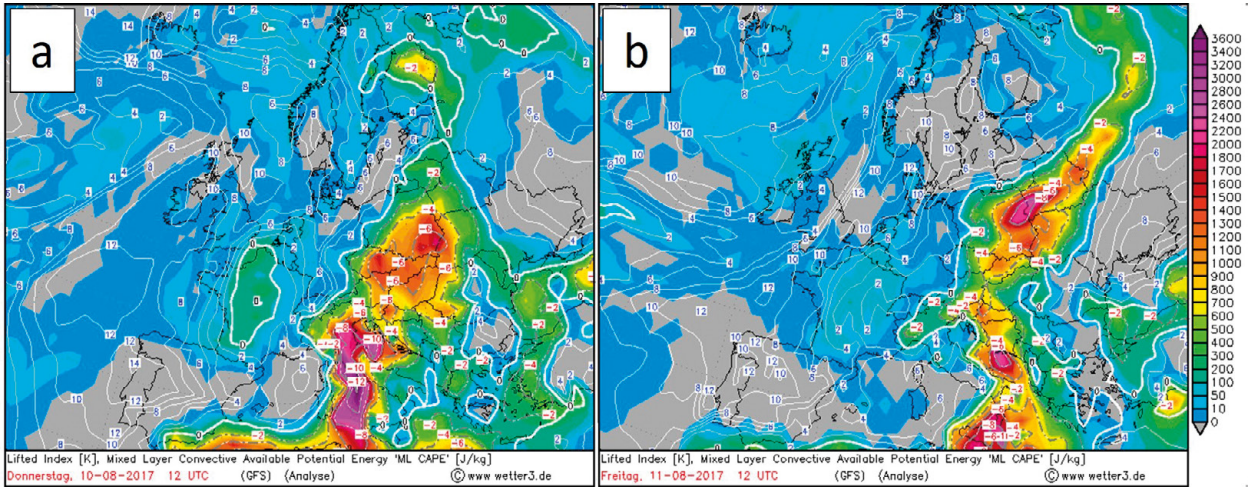
Fig 16. Lifted Index and MLCAPE (GFS analysis), August 10, 2017, 12 UTC (a) and August 11, 2017, 12 UTC (b) (source: www.wetter3.de).
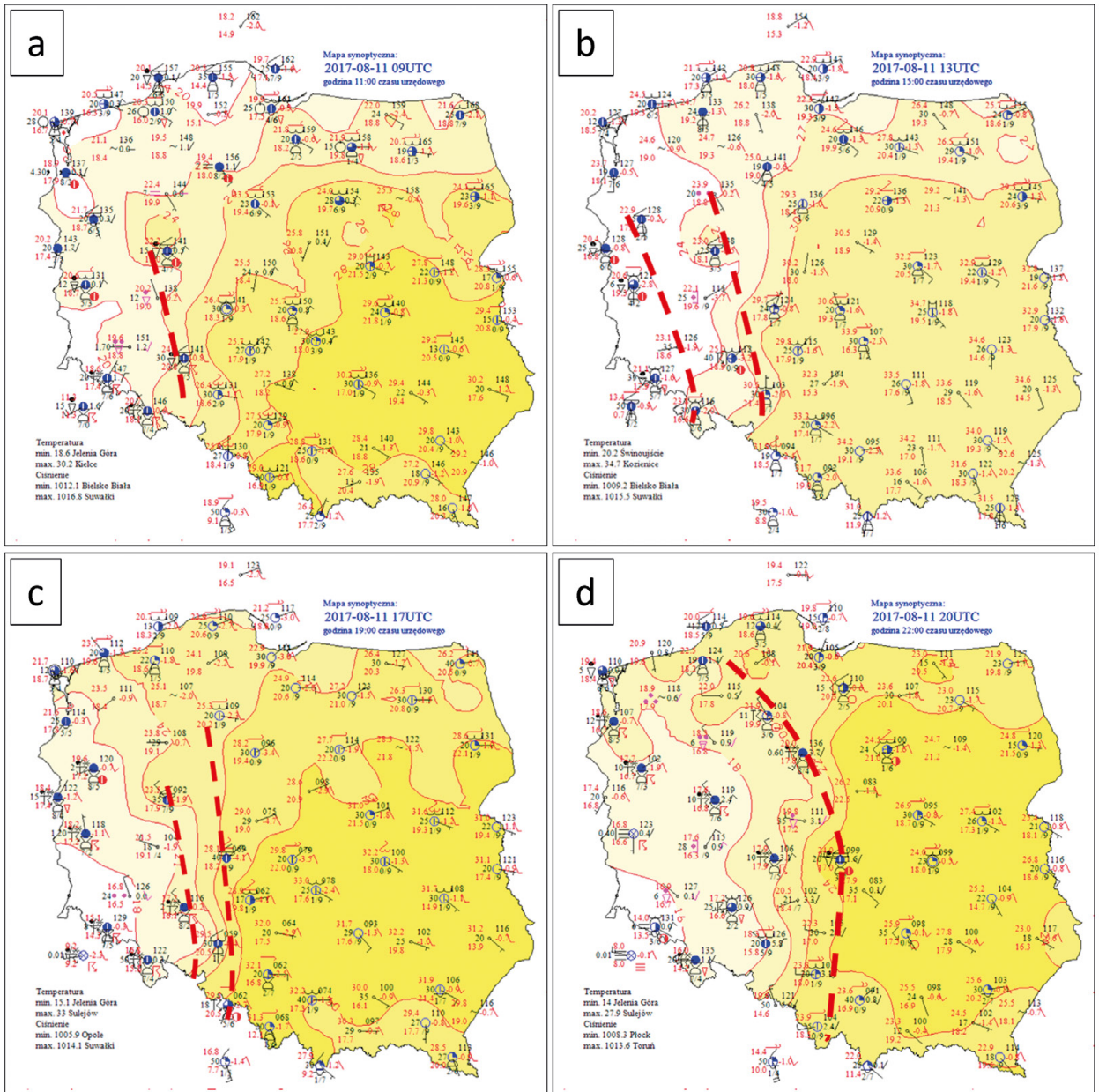
Fig. 17. Location of the convergence lines over Poland at 9 UTC (a), 13 UTC (b), 17 UTC (c), and 20 UTC (d) on Au-gust 11, 2017 (source: IMGW-PIB).
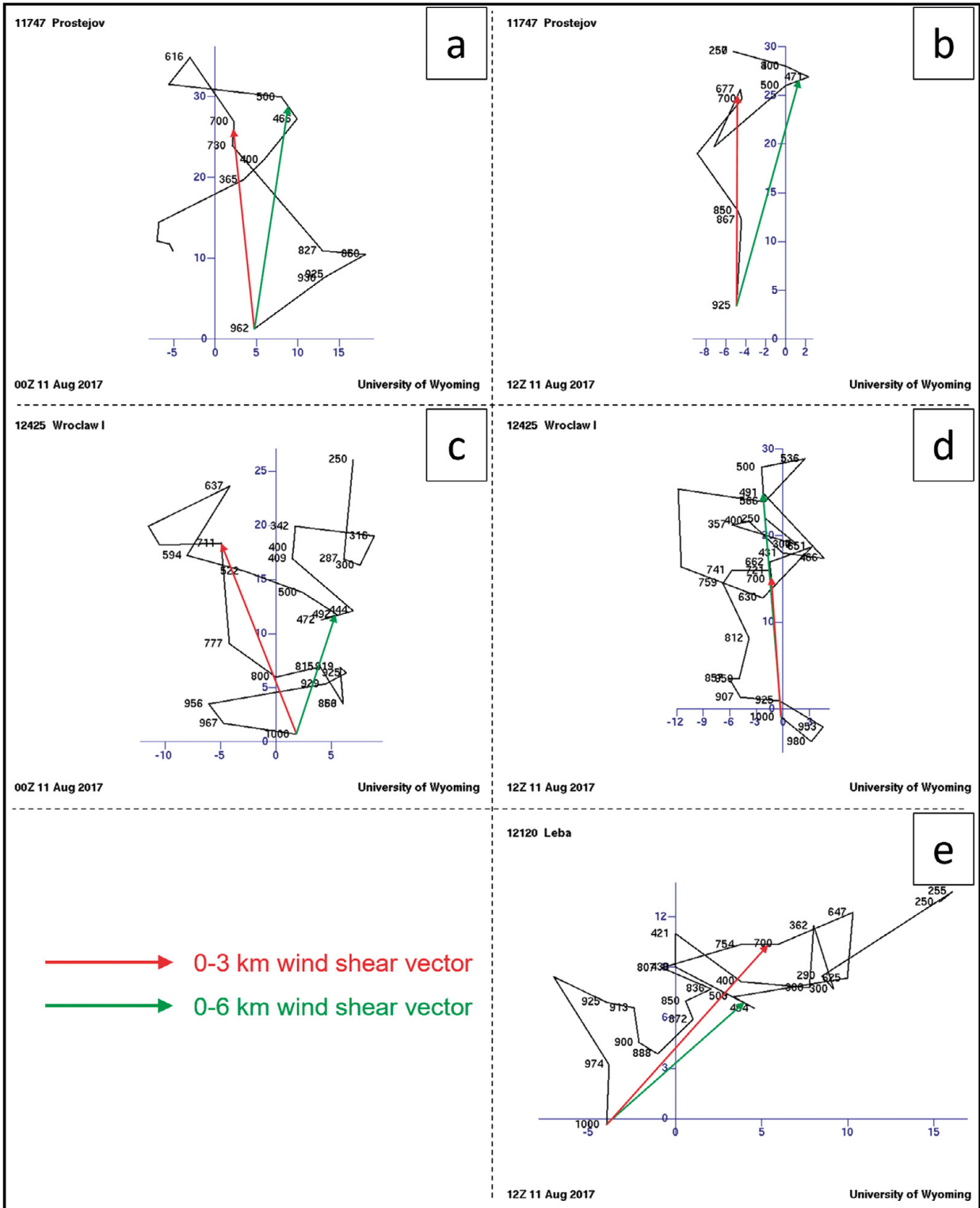
Fig. 18. Hodographs on August 11, 2017, from Prostejov at 00 UTC (a) and 12 UTC (b), Wrocław at 00 UTC (c) and 12 UTC (d), and Łeba at 12 UTC (e) (source: www.weather.uwyo.edu).

the directions of these vectors coincide, the more likely it is that a linear forward-propagating MCS will develop (Corfidi 2003). The sum of these vectors for Prostejov at 12 UTC on August 11, 2017, indicates the movement of the potential system northwards, in Wrocław to the north with a slight deviation to the west and in Łeba towards NNE and NE. In fact, the system was moving through Poland in the direction from SSW to NNE, with a mean speed of about 20 m/s. The deviation of the movement towards the east, different from that determined based on data from Prostejov and Wrocław, could have resulted from the heterogeneity of thermodynamic conditions over Poland. New convective cells tend to form towards the highest instability areas, and this increased towards the east, deflecting the vector of the entire convective system movement in this direction. Hodographs in Wrocław and Łeba
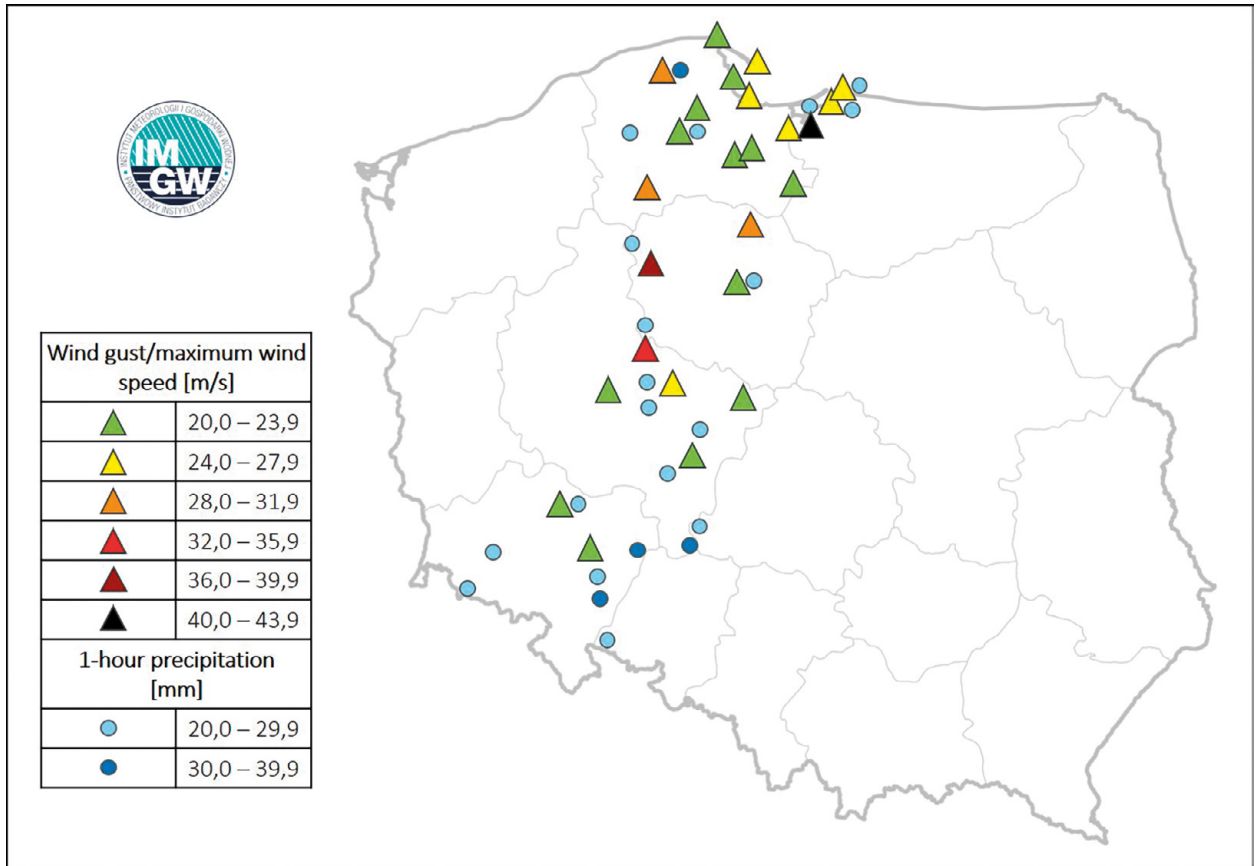
Fig. 19. Wind gusts or maximum wind speeds ≥20 m/s and 1-hour precipitation ≥20 mm within the range of the mesoscale convective system moving through Poland on August 11, 2017 (source: IMGW-PIB).
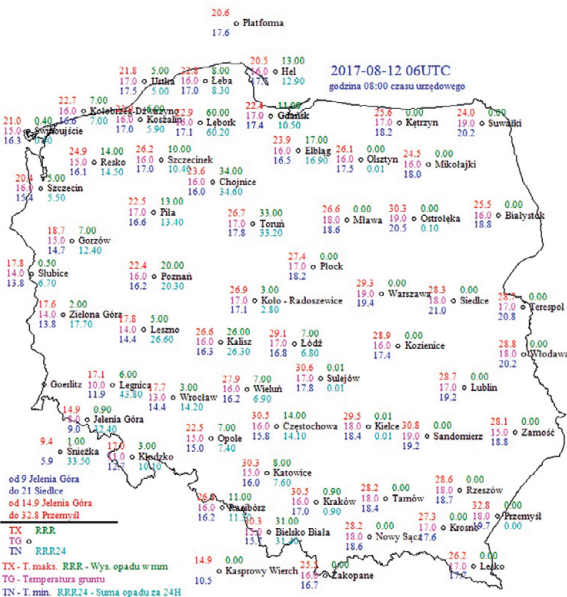
Fig. 20. Meteorological situation in Poland from 06 UTC on August 11, 2017, to 06 UTC on August 12, 2017 (source: IMGW-PIB).

were also bended up to the 650-hPa level (above 900 hPa in Wrocław), showing the wind veer in this layer. Consequently, the storm-relative wind in the lower troposphere had an NNE to E direction, increasing convergence at the cold pool edge in this sector. It could also have contributed to the easterly deviation of the movement vector of the entire mesoscale system.

In addition to good conditions for the development of convection in the form of a multi-cell linear system, the sounding from Wrocław on August 11, 2017, at 12 UTC, indicated the possibility of a super-cell development. Wind shear in the 0-6-km layer was about 26 m/s. The maximum wind speed at about 540 hPa was 28 m/s, and the wind was veering in the lower troposphere, which is reflected in the hook shape of the hodograph (Fig. 18d). The development of the supercell was observed on the border of Lower Silesia and Wielkopolska in the initial stage of the formation of the MCS system.

The previously demonstrated increase in wind speed from the surface to the middle troposphere, where its maximum values were recorded in all analyzed soundings (Fig. 7), contributed to the increase in the dynamics of the thunderstorm system and the intensity of wind gusts. One of the factors that influence the strength of convective gusts is the transport of momentum from the middle troposphere to the surface by the downdraft in the Cumulonimbus cloud. The wind speed reached 35 m/s at 4,200 m (at 00 UTC on August 11, 2017) in Prostejev, 28 m/s at 5,300 m (at 12 UTC) in Wrocław, and 16 m/s at 3,800 m (at 12 UTC) in Łeba, where the pressure gradient was the weakest. This indicates suitable conditions to transfer significant wind speeds from the middle troposphere to the surface in the air mass flowing from the south.

Besides the direct transfer of momentum, the jet stream in the middle troposphere, or even a slight increase in wind speed at these heights, favors the development and intensification of the cold pool itself, which increases the dynamics of the entire convective system. A stronger wind

at an altitude of several kilometers facilitates the inflow of drier air behind the system. Thus, the higher evaporation of precipitation from the trailing stratiform cloud occurs, lowering the air temperature (Punkka et al. 2006; Goulet 2015). The low humidity content was clearly visible in the 2,500- to 4,000-m layer on the sounding from Prostejov at 12 UTC on August 11, 2017. The intensification of the cold pool directly resulted in an increase in gust front speed and the magnitude of associated wind gusts.

The southern wind with maximum speed in the middle troposphere observed on August 11, 2017, could eventually be a significant element in the development of the rear inflow jet (RIJ). The rear inflow jet arises from the formation of a meso-low, where the convective cloud slopes over the cold pool and turns into layered cloudiness. However, an increased ambient wind speed at the height of several kilometers may accelerate this process (Goulet 2015; Crossett 2017). The presence of the rear inflow jet potentially increases the speed of the wind gusts as it descends to the surface near the downshear side of the cold pool.

6. PHENOMENA ACCOMPANYING THE DERECHO

The most hazardous phenomena accompanying the thunderstorms on August 11, 2017, were wind gusts. The ESWD reports, among which strong wind gust events were the most numerous, clearly mark the thunderstorm activity area on that day from south-western to northern Poland (Fig. 4b). Table 2 and Figure 19 summarize the values of maximum wind gusts or maximum wind speed from 10-minute intervals, with a speed of 20 m/s or more, based on the measurement and observation network of the IMGW-PIB. The highest wind speeds, above 30 m/s, were recorded in the northern part of the Wielkopolskie Voivodeship, in the Kuyavian-Pomeranian and Pomeranian Voivodeships, and in the north-western part of the Warmian-Masurian Voivodeship, where the maximum wind gust of 42.2 m/s was measured in Elbląg. The convective system had already moved as a bow echo through these areas.

Downpour or heavy showers occurred in many parts of the country. Table 3 and Figure 19 summarize the 1-hour precipitation for a full hour, with 20 mm or higher, from the locations over which the analyzed thunderstorm zone was formed and passed. The highest precipitation intensities were recorded in Lębork (38.5 mm/h), Bierutów (36.9 mm/h), Dobrogoszcz (35.6 mm/h), and Siemianice (30.5 mm/h). The 24-hour precipitation sum exceeded 30 mm in many places at 06 UTC on August 12, 2017. However, it should be noted that in south-western Poland, before the formation of the analyzed convective system, several precipitation and thunderstorm zones were passing in the first half of the day. Rainfall and thunderstorms associated with a cold front occurred from the Opole region to Gdańsk Pomerania after midnight on August 12, 2017. However, in Lębork, where the highest daily precipitation among all synoptic stations was recorded, 60.2 mm (Fig. 20), practically all rainfall occurred within about 3 hours, i.e., during a passage of the mesoscale convective system in this region.

7. CONCLUSIONS

This study profoundly analyzed the synoptic conditions preceding the development of the mesoscale convective system on 11 August 2017 and during its passage over Poland from the southwest to the north of the country. This article was planned as a common part of two other publications that analyzed this violent phenomenon from satellite and radar points of view (Łapeta et al. 2021; Łuszczewski, Tuszyńska 2022). We found that synoptic-scale mechanisms and appropriate

thermodynamic, humidity, and kinematic conditions were favorable for developing a mesoscale convective system, classified as a derecho. A comprehensive analysis of one of the most violent windy events has been performed by other authors (Taszarek et al. 2019; Figurski et al. 2021). However, the investigation of the synoptic situation was not the main purpose of these publications.

The analyzed derecho fulfilled most of the criteria, which is common for warm season European derechos. It was embedded in the convergence zone of the MCS ahead of the waving cold front, downstream of the extensive upper-level trough over western Europe. This is similar to the occurrence of other derechos in Europe (Gatzen 2004; Celiński-Mysław, Palarz 2017; Ryva 2019).

The formation of the derecho evolved in an environment that featured the three necessary requirements for the occurrence of deep moist convection (Johns, Doswell 1992).

The derecho of August 11, 2017, was connected with the surface trough under a southwestern flow in low- and mid-levels, supported by an upper-level jet. The presence of a left jet stream exit over the convergence zone generated the upper divergence and the increase of large-scale lifting. They were a consequence of the strong cyclonic vorticity advection in the upper and middle troposphere, associated with the evolution of the cut-off low. Warm air advection in the lower and middle troposphere was one of the essential components causing rising air on a synoptic scale, generating an adequate environment for the formation of mesoscale vortex structures.

Vertical wind shear is a crucial ingredient for linearly organized MCSs (Weisman, Klemp 1982; Rotunno et al. 1988; Bryan et al. 2006). The increase in speed, generating moderate and strong wind shear (15-25 m/s) in the 0-3-km layer and an equally high shear in the 0-6-km layer, enabled the formation of both supercell thunderstorms and organized linear convection. The wind shear vectors in the 0-3-km layer were oriented almost parallel to the mean wind vectors, favoring the development of a forward-propagating MCS. The maximum wind speed at the height of several kilometers (4-6 km) favored the development of the rear inflow jet within the linear convective system, which contributed to the formation and intensification of the derecho. The strong wind in the middle troposphere in the air mass flowing from the south created the conditions for the transfer of momentum from the middle troposphere to the surface by the downdrafts in the cumulonimbus clouds, increasing the wind gusts. Moreover, a drier layer of air was observed above the humid boundary layer in the incoming mass, which contributed to the intensification of downdrafts in cumulonimbus clouds and, consequently, to the intensification of surface wind gusts.

Concerning the thermal condition, a tropical warm, humid air mass was advected over Poland. Warm air advection in the lower and middle troposphere was one of the essential components causing rising air on a synoptic scale. This constituted a good condition for high instability, which decreased from the west to the east of the country. The steep vertical temperature gradients in the middle troposphere and the high humidity in the boundary layer generated the atmospheric instability with moderate to high SBCAPE levels (600-3,000 J/kg), whereas the maximum occurred in the central part of Poland, where the convergence zone started to reactivate.

The documentation and analysis of such an impressive, rare weather phenomenon can help understand the underlying mechanism leading to the formation of the derecho and facilitates the prediction of similar events in the future.

23

REFERENCES

- AMS, 2021, Glossary of Meteorology, American Meteorological Society, available at: https://glossary.ametsoc.org/wiki/Welcome.

- Bąkowski R., 2005, Wybrane analityczne i prognostyczne wskaźniki chwiejności atmosfery, [in:] Hydrologia, meteorologia, klimatologia – badania naukowe i prognozy w erze informatyzacji, M. Ozga-Zielińska, D. Limanówka (ed.), Polskie Towarzystwo Geofizyczne, IMGW, Warszawa, 209-218.

- Bechtold P., 2019, Atmospheric moist convection, ECMWF Meteorological Training Course Lecture Series, available at: https://www.ecmwf.int/en/elibrary/16953-atmospheric-moist-convection (data access 16.08.2022).

- Bielec-Bąkowska Z., 2003, Long-term variability of thunderstorm occurrence in Poland in the 20th century, Atmospheric Research, 67-68, 35-52, DOI: 10.1016/S0169-8095(03)00082-6.

- Bryan G.H., Knievel J.C., Parker M.D., 2006. A multimodel assessment of RKW theory's relevance to squall-line characteristics. Monthly Weather Review, 134 (10), 2772-2792, DOI: 10.1175/MWR3226.1.

- Celiński-Mysław D., Matuszko D., 2014, An analysis of the selected cases of derecho in Poland, Atmospheric Research, 149, 263-281, DOI: 10.1016/j.atmosres.2014.06.016.

- Celiński-Mysław D., Palarz A., 2017, The occurrence of convective systems with a bow echo in warm season in Poland, Atmospheric Research, 193, 26-35, DOI: 10.1016/j.atmosres.2017.04.015.

- Celiński-Mysław D., Palarz A., Łoboda Ł., 2019, Kinematic and thermodynamic conditions related to convective systems with a bow echo in Poland, Theoretical and Applied Climatology, 137, 2109-2123, DOI: 10.1007/s00704-018-2728-6.

- Chernokulsky A., Shikhov A., Bykov A., Kalinin N., Kurgansky M., Sherstyukov B., Yarinich Y., 2022, Diagnosis and modelling of two destructive derecho events in European Russia in the summer of 2010, Atmospheric Research, 267, DOI: 10.1016/j.atmosres.2021.105928.

- Coniglio M.C., Stensrud D.J., Richman M.B., 2004, An observational study of derecho-producing convective systems, Weather and Forecasting, 19 (2), 320-337, DOI: 10.1175/1520-0434(2004)019<0320:AOSODC>2.0.CO;2.

- Corfidi S.F., 2003, Cold pools and MCS propagation: forecasting the motion of downwind-developing MCSs, Weather and Forecasting, 18 (6), 997-1017.

- Corfidi S.F., Evans J.S., Johns R.H., 2017, About derechos, Storm Prediction Center.

- Craven J.P., Brooks H.E., 2004, Baseline climatology of sounding derived parameters associated with deep moist convection, National Weather Digest, 28, 13-24.

- Crossett C., 2017, An examination of the dynamics of a rear-inflow-jet associated with an idealized mesoscale convective system, Theses and Dissertations, University of Wisconsin Milwaukee, 1458, available at https://dc.uwm.edu/etd/1458 (data access 16.08.2022).

- Evans J.S., Doswell III C.A., 2001, Examination of derecho environments proximity soundings, Weather and Forecasting, 16, 329-342.

- Figurski M.J., Nykiel G., Jaczewski A., Baldysz Z., Wdowikowski M., 2021, The impact of initial and boundary conditions on severe weather event simulations using a high-resolution WRF model. Case study of the derecho event in Poland on 11 August 2017, Meteorology, Hydrology and Water Management, DOI: 10.26491/mhwm/143877

- Fujita T.T., 1978, Manual of downburst identification for project NIMROD, SMRP Research Paper 156, The University of Chicago, 104 pp.

- Gatzen C., 2004, A derecho in Europe: Berlin, 10 July 2002, Weather and Forecasting, 19 (3), 639-645, DOI: 10.1175/1520-0434(2004)019<0639:ADIEBJ>2.0.CO;2.

- Gatzen C., Pucik T., Ryva D., 2011, Two cold-season derechoes in Europe, Atmospheric Research, 100 (4), 740-748, DOI: 10.1016/j.atmosres.2010.11.015.

- Gatzen C.P., Fink A.H., Schultz D.M., Pinto J.G., 2020, An 18-year climatology of derechos in Germany, Natural Hazards and Earth System Sciences, 20 (5), 1335-1351, DOI: 10.5194/nhess-20-1335-2020.

- Gospodinov I., Dimitrova T., Bocheva L., Simeonov P., Dimitrov R., 2015, Derecho-like event in Bulgaria on 20 July2011, Atmospheric Research, 158-159, 254-273, DOI: 10.1016/j.atmosres.2014.05.009.

- Goulet L., 2015, Bow Echoes: Conceptual Schemes and European Relevance, The European Forecaster – Newsletter of the Working Group for the Cooperation between European Forecasters, 20, available at http://www.euroforecaster.org/newsletter20/meteofr2.pdf (data access 16.08.2022).

- Hamid K., 2012, Investigation of the passage of the derecho in Belgium, Atmospheric Research, 107, 86-105, DOI: 10.1016/j.atmosres.2011.12.013.

- Johns R.H., Doswell C.A. III, 1992, Severe local storms forecasting, Weather and Forecasting, 7 (4), 588-612, DOI: 10.1175/1520-0434(1992)007<0588:SLSF>2.0.CO;2.

- Johns R.H., Hirt W., 1987, Derechos: Widespread convectively induced windstorms, Weather and Forecasting, 2 (1), 32-49, DOI: 10.1175/1520-0434(1987)002<0032:DWCIW>2.0.CO;2.

- Kalkstein L.S., Nichols M.C., Barthel C.D., Greene J.S., 1996, A new spatial synoptic classification: application to air-mass analysis, International Journal of Climatology, 16 (9), 983-1004, DOI: 10.1002/(SICI)1097-0088(199609)16:9<983::AID-JOC61>3.0.CO;2-N.

- Kurz M., 1992, Synoptic diagnosis of frontogenetic and cyclogenetic processes, Meteorology and Atmospheric Physics, 48, 77-91, DOI: 10.1007/BF01029560.

- Lackmann G., 2011, Midlatitude Synoptic Meteorology: Dynamics, Analysis, and Forecasting, American Meteorological Society, 345 pp.

- Łapeta B., Kuligowska E., Murzyn P., Struzik P., 2021 Monitoring the 11 August 2017 storm in central Poland with satellite data and product, Meteorology, Hydrology and Water Management, DOI: 10.26491/mhwm/144590.

- Lelątko I., Ziemiański M., 2004, Niewielki przewodnik po wybranych wskaźnikach konwekcji, Operational Manual of the IMGW-PIB Weather Service.

- Lopez J.M., 2007, A Mediterranean derecho: Catalonia (Spain), 17th August 2003, Atmospheric Research, 83 (2-4), 272-283, DOI: 10.1016/j.atmosres.2005.08.008.

- Łozowicki L. (ed.), 1991, Meteorologia synoptyczna, Dowództwo Wojsk Obrony Powietrznej Kraju.

- Łuszczewski H., Tuszyńska I., 2022, Derecho radar analysis of August 11, 2017, Meteorology, Hydrology and Water Management, DOI: 10.26491/mhwm/152504.

- Mathias L., Ludwig P., Pinto J, 2019, Synoptic-scale conditions and convection-resolving hindcast experiments of a cold-season derecho on 3 January 2014 in western Europe, Natural Hazards and Earth System Sciences, 19 (5), 1023-1040, DOI: 10.5194/nhess-19-1023-2019.

- Niedźwiedź T., 2003, Extreme precipitation in Central Europe and its synoptic backgrounds, Papers on Global Change, 10, 15-29.

- Punkka A-J., Teittinen J., Johns R.H., 2006, Synoptic and mesoscale analysis of a high-latitude derecho-severe thunderstorm outbreak in Finland on 5 July 2002, Weather and Forecasting, 21 (5), 752-763, DOI: 10.1175/WAF953.1.

- Rotunno R., Klemp J.B., Weisman M.L., 1988, A theory for strong, long-lived squall lines, Journal of the Atmospheric Sciences, 45 (3), 463-485, DOI: 10.1175/1520-0469(1988)045<0463:ATFSLL>2.0.CO;2.

- Ryva D., 2019, Preliminary climatology of derechos in Czechia, ECSS Conference, DOI:10.13140/RG.2.2.30202.85448.

- Sipos Z., Simon A., Csirmaz K., Lemler T., Manta R., Kocsis Z., 2021, A case study of a derecho storm in dry, high-shear environment, Quarterly Journal of the Hungarian Meteorological Service, 125 (1), DOI: 10.28974/idojaras.2021.1.1.

- Surowiecki A., Taszarek M., 2020, A 10-year radar-based climatology of mesoscale convective system archetypes and derechos in Poland, Monthly Weather Review, 148 (8), 3471-3488, DOI: 10.1175/MWR-D-19-0412.1.

- Taszarek M., Czernecki B., Kozioł A., 2015, A cloud-to-ground lightning climatology for Poland, Monthly Weather Review, 143 (11), 4285-4304, DOI: 10.1175/MWR-D-15-0206.1.

- Taszarek M., Piguj N., Orlikowski J., Surowiecki A., Walczakiewicz S., Pilorz W., Piasecki K., Pajurek Ł., Półrolniczak M., 2019, Derecho evolving from a mesocyclone – a study of 11 August 2017 severe weather outbreak in Poland: event analysis and high-resolution simulation, Monthly Weather Review, 47 (6), 2283-2306, DOI: 10.1175/MWR-D-18-0330.1

- Weisman M.L., 1993, The genesis of severe, long-lived bow echoes, Journal of the Atmospheric Sciences, 50 (4), 645-670, DOI: 10.1175/1520-0469(1993)050<0645:TGOSLL>2.0.CO;2.

- Weisman M.L., Klemp J.B., 1982, The dependence of numerically simulated convective storms on vertical wind shear and buoyancy, Monthly Weather Review, 110 (6), 504-520, DOI: 10.1175/1520-0493(1982)110<0504:TDONSC>2.0.CO;2.

Derecho radar analysis of August 11, 2017

Hubert Łuszczewski, Irena Tuszyńska
Institute of Meteorology and Water Management – National Research Institute

ABSTRACT. This paper presents an analysis of the derecho phenomenon that occurred over Poland on August 11, 2017. The storm caused 6 fatalities, 39 injuries (Wrona et al. 2022), and some of the greatest damage in the history of Polish forestry. Our study is based on radar meteorology and measurements from the Polish POLRAD radar network, and intended for advanced meteorologists with good knowledge of radar measurements. The research used both standard and specialized radar products as well as classic and Doppler scan data. The Doppler velocity products were especially useful for showing the characteristics of the storm. The analysis was mainly based on data from two radars: Poznań and Gdańsk, but the composite maps, consisting of data from more than one radar, were also analyzed. The derecho complex developed from unorganized thunderstorm cells over SW Poland and moved toward the NE. The various stages of the evolution of the system are presented and analyzed, accounting for the formation of a SC, the development of a rear inflow jet (RIJ), the split of the entire system, and the appearance of the bow echo signature. Significant factors affecting the scale of the wind damage were: (1) the extensive mesocyclone which evolved to the mesoscale convective vortex (MCV), and (2) a strong rear flank downdraft interacting with the rear inflow jet (RIJ).

KEYWORDS: Meteorology, derecho, bow echo, mesocyclone, analysis, radar, Doppler.

1. INTRODUCTION

Gustavus Hinrichs (1888), an American scientist, first proposed the term derecho ("straight" in Spanish) in meteorology as a designation for an extensive convective system with long-lived convective straight-line windstorms, unlike the formation of vortical wind systems.

There are several approaches for derecho identification, one of them proposed by Johns and Hirt (1987). The first criterion requires the main axis of the damage area (wind gusts over 26 m/s) to reach 400 km. The damage reports must show the chronological progression. Moreover, there must be at least three reports of F1 damage or gusts over 33 m/s within the area, separated by 64 km and with no more than 3 h elapsed between them.

Initially, it was postulated that the development of the derecho was strongly correlated with high CAPE (Convective Available Potential Energy >2000 J·kg^{-1}) and the occurrence of strong vertical wind shear in the lower troposphere (>20 m·s^{-1}, at an altitude of 2.5-5 km) (Weisman 1993, 2001). The studies of Duke and Rogash (1992), Bentley and Mote (1998), Evans and Doswell (2001), and Ashley et al. (2005) proved that derechos could occur at any time of the year, also at significantly lower vertical wind shear, in various environmental conditions with much less instability.

The causes of derecho cases in Europe were analyzed by: Schmid et al. (2000), Punkka et al. (2006), Lopez (2007), Putsay et al. (2009), Walczakiewicz and Ostrowski (2010), Gatzen (2011), Pucik et al. (2011), Simon et al. (2011), and Hamid (2012). An analysis of long-term derecho occurrence in Europe was carried out by Gatzen et al. (2011).

The term precisely associated with a derecho is the characteristic radar echo pattern called bow echo. This bowing convective line segment is often associated with swaths of damaging downburst winds and is sometimes accompanied by tornadoes that may reach a violent rating of F4. Occurring singly, it is called progressive derecho, in contrast to serial derecho, where there are multiple bowing segments (Przybylinski 1995).

Most available articles deal with the bow echoes generally, without pointing out significant vortex structures (Weisman 1993); however, there are some studies that examine the storm development as affected by an embedded supercell (SC) or bookend vortex signatures (Wolf 1998; Atkins, Laurent 2009; Atkins et al. 2004).

Przybylinski (1995) as well as Forbes and Wakimoto (1983) have shown that the strongest damaging wind gusts usually occur along the apex of bowing line segments. Nevertheless, in some cases, an embedded mesocyclone or mesoscale convective vortex (MCV) (Davies, Weisman 1994) can significantly strengthen the potential of damaging wind gusts, both tornadic and downburst-related (Funk et al. 1994) as it was in the case described in this paper.

The first study of derecho cases in Poland was undertaken by Celiński-Mysław and Matuszko (2014). They examined derecho phenomena that occurred between 2007 and 2012 (6 cases). They confirmed that the long-lasting and extensive convective systems causing the derecho often elicit damage comparable to that caused by F0-F2 tornadoes (Celiński-Mysław, Matuszko 2014) and that the damage was caused by the straight-line wind. Whereas, if we consider the frequency of derecho-producing MCSs (mesoscale convective systems) (Zipser 1982) with embedded MCV, this phenomenon is quite rare over Poland (3.5% cases of MCSs in a 10-yr study) (Surowiecki, Taszarek 2020).

In the case of the extensive wind storm that took place over western Poland on August 11, 2017, the damage was generally not generated by vortical winds, but by straight-line winds, except for one report of a possible tornado. This finding contributed, among others, to investigating the case as a derecho.

2. AIM OF THE STUDY

This paper documents the storm system that occurred over Poland on August 11, 2017, using radar data from the POLRAD network. This case study was made specifically to determine the genesis of the system, the development of an embedded storm SC, the interaction between essential system features, and their impact on the mechanisms responsible for the greatest damage. This article does not provide a detailed analysis of the synoptic and meteorological situation accompanying the formation of the phenomenon (which was provided by Taszarek et al. 2019 and with greater detail by Wrona et al. 2022). Nor does it deliver the standard nowcasting and warning procedures for weather forecasters, but analyses the event in detail, using solely the radar data provided by the IMGW-PIB system. The results of the analyses are presented on the basis of non-standard POLRAD products specifically developed and implemented for this study, which are not available for operational forecasters.

One of the factors influencing the intense dynamics of the derecho was the development of a SC from one of the numerous storm cells formed in the vicinity of the waving atmospheric front in Lower Silesia. This type of thunderstorm is characterized by a deep and persistent rotating updraft (Klemp, Rotunno 1983). To detect the SC on the classic radar scan images, we were looking for basic SC features such as a high-reflectivity compact core on the CMAX product and raised maximum reflectivity on the EHT product (early stage, outside of the Doppler scan), along different movement patterns (Davies, Johns 1993), as well as an inflow notch on the PPI scans, a bounded weak echo region (BWER) on the vertical cross-section Doppler reflectivity scan, and finally the velocity couplet on radial velocity data (later stage, close to radar).

The rear inflow jet (RIJ) was the second important factor responsible for severe wind damage caused by the storm which played a significant role in the formation of bow echo-type storms. It is formed due to the pressure difference between the area of rapid ascent and condensation (low) and the area cooled by rainfall (high) (Rotunno et al. 1988). The strong release of the latent heat is mainly responsible for the pressure difference. Consequently, the strength of the RIJ is primarily influenced by the power of updrafts associated with CAPE as well as the range and potential of the cold pool, i.e. the area of cool air at the surface caused by heavy rainfall. The lower the temperature, the higher the pressure in the cold pool area, and the deeper the local low within the strong updrafts, the stronger the RIJ flow (Lemon, Doswell 1979; Johns, Hirt 1987; Weisman 1992). The RIJ might be so strong that it starts to push a fragment of the storm cell forward, which is marked as bow echo on radar products. Under favorable conditions, strong downdrafts of storm cells can bring a part of the RIJ momentum to the surface, generating heavy squall winds with speeds above 150 km/h (Fujita, Wakimoto 1981).

3. RADAR DATA

The analysis of the phenomenon was based on data from the network of eight POLRAD meteorological radars located in: Legionowo (LEG), Rzeszów-Jasionka (RZE), Brzuchania (BRZ), Ramża (RAM), Pastewnik (PAS), Poznań (POZ), Świdwin (SWI), and Gdańsk (GDA). All devices are Doppler radars, three of which (Rzeszów, Ramża, Pastewnik) have dual polarization measurement functionality. The entire radar network was put into service in 2004.

Each radar operating in the POLRAD network takes two measurements in a 10-minute cycle. The first is a classic scan (operational range is 250 km), otherwise known as the rainfall scan (only a reflectivity measurement is made). The second measurement is a Doppler scan (range 125 km), called a wind scan, the parameters of which are set to obtain the best possible infor-

Table 1. The radar products used to analyze the phenomenon.

Name of product	Scan type	Data type		Definition of products obtained and possible to obtain from a specific scan
		Input data	Output data	
PPI(dBZ) **PPI(V)** Plan Position Indicator (conical section)	K D	dBZ V W	dBZ V	Distribution of: • radar reflectivity, • radial velocity, • radial velocity spectrum for a localized meteorological structure obtained from one antenna rotation.
MAX(dBZ)	K D	dBZ V W	dBZ V W	Maximum values of display: • radar reflectivity, • radial velocities, • radial velocities spectrum in projection on three planes.
CMAX(dBZ) **CMAX(V)** Maximum Display (maximum values of radar measurements)	K D	dBZ V	dBZ V	Maximum values of display: • radar reflectivity, • radial velocities in projection only on the horizontal plane.
EHT(height): • Echo Top • Height of Max Reflectivity • Layer Thickness • Echo Base	K	dBZ	Height	Height of display: • echo tops, • maximum reflectivity, • layer thickness, • echo base within a localized meteorological structure in [km].
SRV Storm Relative Velocity	D	V	V	Mapping: • radial velocity reduced/increased by mean radial velocity.
VCUT Vertical Cut	K D	dBZ V	dBZ V	Vertical distribution: • radar reflectivity, • radial velocity for vertical cut.
MLVCUT Multiple-Line Vertical Cut	K D	DBZ V	dBZ V	Vertical distribution: • radar reflectivity, • radial velocity for multi-vertical cut.
PCAPPI(dBZ) **PCAPPI(V)** Pseudo Constant Altitude PPI	K D	dBZ V W	dBZ V	Distribution of: • radar reflectivity, • radial velocity, • radial velocity spectrum for an altitude of 1 km above sea level

Key: **D** = Doppler scan with spatial resolution of the products 0.5 km × 0.5 km; **K** = Classic scan (standard) with spatial resolution of the products 1 km × 1 km; **Z** = reflectivity [dBZ]; **V** = radial velocity [m/s]; **W** = radial spectrum width [m/s].

mation on radial velocities, radial velocity spectrum, and reflectivity.

After considering the location of the event, it was decided to use data from the Poznań and Gdańsk single polarization radars for the research.

This paper presents analysis of the original radar data (3-dimensional recorded in spherical coordinates) processed into radar products defined in the 2-dimentional Cartesian system (Tuszyńska 2011). Non-standard products (non-operationally generated) and their combinations were used to study the convective system (Table 1).

The products of the radial velocity distribution, such as PPI (V), SRV (V), and CMAX (V) played a special role in the assessment of the nature of the event. They helped to choose the instants for performing more detailed analyses of the system. The flexibility in the definitions of radar products, including the data threshold values, allowed us to develop additional products such as EHT (Height Max Z).

4. METHODOLOGY OF WORKING WITH DATA

The analysis of the processes taking place in the derecho area based on radar data was made particularly difficult by the extreme nature of meteorological events, which also affected the measurement data. Therefore, because of interpretation difficulties and radar measurement errors (Szturc et al. 2010, Jurczyk et al. 2020), the limitations and uncertainty of results had to be kept in mind.

While considering the origin of the phenomenon and its evolution, many problematic issues related to the interpretation of the radar measurements were encountered. The specificity of radar sounding required determining the measurement geometry depending on the location of the phenomenon, and filtering out data from non-meteorological echoes.

The composite maps, integrating observations from the entire radar network via selection of the maximum reflectivity, have shown great usefulness for interpretation of the event along its entire route. Despite the signal dumping in heavy rainfall and during its passage over the Poznań and Gdańsk radar stations, the composite maps properly reflected the course of the event and the migration of the mesoscale convective system.

In the analysis of the Doppler scanning of radial velocity, data gaps occurred in some areas. The gaps were mainly related to high values of the radial velocity spectrum (W), which meant that for a given voxel (3D pixel of data) the system received velocity measurements with large uncertainty.

The POLRAD system configuration, oriented towards eliminating many disturbances hindering the operation of the radar, was set in such a way that voxels with high values of W, i.e. places of disturbances or high turbulence, were treated as incorrect data and discarded. Visible clear gaps in velocity data (Fig. 1b) on the PPI (V) scan coincide with the areas of higher values of the velocity spectrum (Fig. 1a) on the PPI (W).

Another problem was the convective system's location relative to radar stations. When the system reached its greatest strength, it was out of the Doppler scanning range of the Poznań radar. At the same time, it was also too far from the Gdańsk radar to enable continuous analysis of near-surface wind distribution.

Despite these difficulties, a reliable qualitative derecho analysis was carried out. Reflectivity (dBZ) on composite maps was used to illustrate the overall course of the event. More detailed elements of the storm system were analyzed using radial velocity (V) data, usually in a pair of high-resolution reflectivity PPI products. Also VCUT or MLVCUT vertical sections were performed on properly configured products.

Key radar signatures related to the SC and bow echo were searched. In the early stage of the system we were generally looking for SC signatures, especially the high reflectivity core and BWER. When the system entered the Doppler scanning range of POZ radar, velocity couplets were observed in the area of exploration as evidence of a mesocyclone. While the system was passing the POZ radar, we looked in detail at the radial velocity data in order to detect and estimate the RIJ (rear inflow jet). Many cross-sections were made to find the interaction between this jet and the mesocyclone, especially with the rear flank downdraft (RFD) of the SC. When the system reached GDA radar Doppler range, the radial velocity data were analyzed, directly over the area of the greatest damage. The goal was to show the most devastating bowing segments and the position of the mesovortex. At the end of the analysis we focused on the MCV pattern, showing its details on the SRV product.

The RIJ analysis was conducted in two variants. The first used vertical cuts VCUT (V) to visualize its vertical extent, the interaction with the SC circulation, and the estimation of maximum velocities in the core. The vertical cuts were made manually. In each case they ran along with the RIJ core towards the storm movement. The second variant is an analysis using the SRV (V) product from three different elevations. It was considered that this product would be preferable to CAPPI (V) at a given altitude, due to the lack of data interpolation; the product configuration was chosen to visualize the horizontal range of the RIJ. The analysis of horizontal characteristics of the RIJ using the SRV (V) product was carried out based on POZ radar. The 1.7-degree elevation was used when the storm system was far away from the radar. Then, as the storm approached the radar station and passed directly over it, data from the 3.6-degree elevation were analyzed. These elevations were selected to avoid ground clutter and to analyze the data from approximately constant altitude. A wind vector of 15 m/s parallel to the RIJ direction was added to the product configuration to better visualize the RIJ pattern.
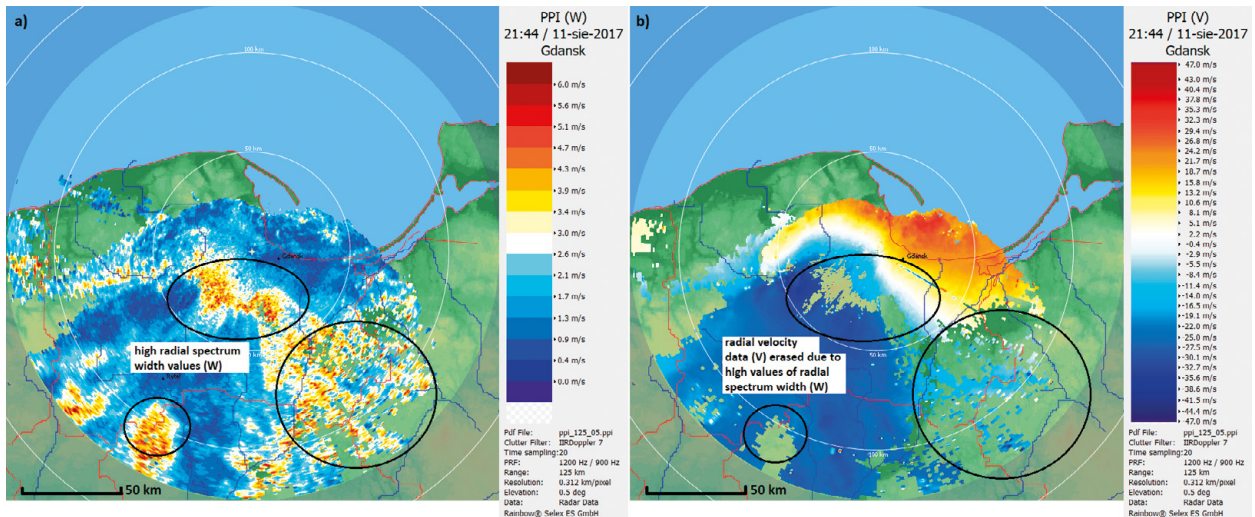
Fig. 1. The distribution of (a) radial spectrum PPI(W); (b) radial velocity PPI(V) for 0.5 degree elevation – GDA radar.
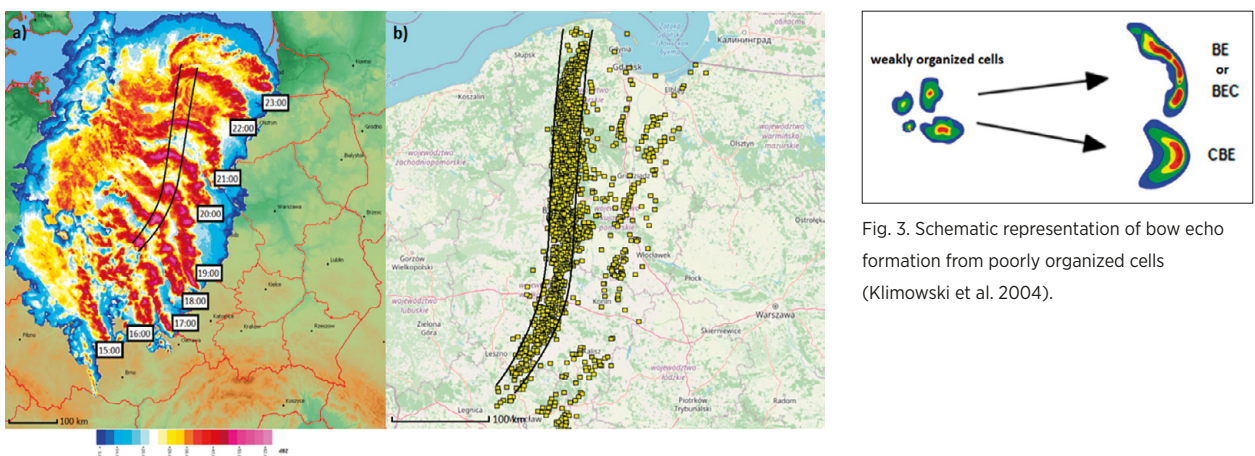

Fig. 2. CMAX composite map with 1-h steps (a) with marked SC and (later) MCV track; (b), severe wind gust reports with marked SC and (later) MCV track (source: eswd.eu).

Fig. 3. Schematic representation of bow echo formation from poorly organized cells (Klimowski et al. 2004).

5. GENERAL EVOLUTION OF THE CONVECTIVE SYSTEM

The whole derecho evolution process is shown in Figure 2 using the 1-h step composite maps. The main, wide path of damage was detected along the track of the SC (early stage) and MCV (later stage) (Fig. 2). In this chapter we have presented a brief chronological overview of this event.

The derecho day was stormy over Poland from early morning. The convection, which developed in Lower Silesia from morning until noon, generated a surface outflow boundary and influenced the evolution of local wind convergence. These dynamics, in turn, enabled the development of a much stronger afternoon convection (Wrona et al. 2022).

The development of storm cells in the Czech Republic and on the Czech-Polish border in the early afternoon can be considered as the beginning of the evolution of the convective system responsible for derecho development. In the environment of high CAPE values and strong wind shear, storms moving towards the NNE were characterized by high reflectivity through the entire vertical extent. The reflectivity demonstrated highly dynamic hydrometeor movement inside storm cells, due to the strong downdrafts and updrafts.

Storm cells intensified after entering Poland. On the composite maps of maximum reflectivity it was possible to observe their increasingly better organization and clustering, ahead of the dynamically waving atmospheric front (Wrona et al. 2022). After 16 UTC the formation of the mesoscale convective system (MCS) was complete.

At around 16:10 UTC the first radar signatures (distinctive, high reflectivity core) appeared, indicating the possible presence of an embedded SC, which played a key role in the evolution of the storm system to the derecho category. This SC is likely to have existed previously in the Czech Republic, but it was disorganized when crossing the Sudetes Mountain range (Taszarek et al. 2019). Then, in Lower Silesia, the strong updraft of this storm began to rotate again. At that time the first reports of damage caused by strong winds, which overlapped the SC route, began to appear. Large hail was also recorded in the area of Kalisz (Taszarek et al. 2019).

After 18:30 UTC on radar scans, the signature of the SC began to overtake the entire system, forming a more and more distinct bowing segment. At 19:10 UTC a well-formed bowing segment was present at the head of the system. Subsequently, the mesoscale convective system, initially formed from poorly organized storm cells (Fig. 3), took the form of a bow echo with the embedded SC (bow echo complex) (Moller et al. 1990; Klimowski et al. 2000, 2004).

Between 20:00 and 21:00 UTC a bow echo with active mesovortex caused the greatest wind damage (Taszarek et al. 2019), passing over the area of Bory Tucholskie. In the radar images we can distinguish one vast bow-type segment at the leading edge of the storm.

Later, the bookend vortex signature is visible in the western part of the system on the scan from 21:30 UTC, indicating the occurrence of a mesovortex caused by the evolution of the mesocyclone. The MCS weakens after passing over the Baltic Sea, and the radar echo system indicates the formation of a mesoscale low, surrounded by precipitation areas. The radar analysis of the event ends when the storm leaves the classic scan area of the radar in Gdańsk.

6. SUPERCELL AND REAR INFLOW JET INTERACTION

The detailed analysis began when the mesocyclone was likely to redevelop within a previously existing cell in the Czech Republic. Additionally, in the southern part of the system, one more embedded structure with a rotating updraft, visible on PPI (V) scans of the POZ radar as the velocity couplet, has developed. However, it did not have a direct impact on the path of the greatest damage. The first symptoms of SC formation can be seen on radar scans from 16:10 UTC (not shown). However, the most visible signatures of a storm with rotating updraft begin to appear around 16:30 UTC (Fig. 4).

The vertical sections VCUT show (Fig. 4) a visible, bounded weak echo region (BWER) associated with a strong updraft lifting the hydrometeors to a significant height, which may be a mesocyclone precursor (Lemon, Doswell 1979). In turn, the EHT (HeightMaxZ) product, which in this case presents a reflectivity above 30 dBZ, which can be a precursor of the mesocyclone at 16:30 UTC, highlights the areas where the updraft keeps the hydrometeor particles high above the surface. It is clearly visible within the developing storm SC.

In subsequent observations the mesocyclone starts to be visible on the SRV (V) product of the POZ radar, where the velocity couplet signature appears, indicating the vortex area (Fig. 5). Unfortunately, due to high noise from WiFi transmitters and the high filtering threshold, there are gaps in radial data, especially in the period when the system was in the immediate vicinity of the radar. After 17:00 UTC the inflow notch, i.e. the area of reflectivity gap at the point of intense air inflow into the mesocyclone, is well outlined on the PPI (dBZ) product from the lowest elevation (not shown).

At 17:13 the first scans clearly indicating the presence of RIJ were performed. They show the area of elevated radar-towards velocity on the VCUT made on the radial data along the direction of the system moving towards the POZ radar, at an altitude of about 4 km (Fig. 6). The velocity measured by the radar is in the range of 30 m/s. Still, due to the specificity of the Doppler measurement, when the axis of the air stream is not parallel to the signal beam, we get information only about the component to or from the radar. Therefore, we are unable to measure the real wind velocity at the RIJ core. The area of air inflow towards the storm is also well-distinguished and the Mid-Altitude Radial Convergence (MARC) signature appears (Fig. 6); (Rasmussen, Rutledge 1993; Moller 2001; Markowski 2002). The horizontal scans, starting from 17:33 UTC, show the RIJ as an area of increased radial velocity ~40-50 km wide with undefined length (Fig. 7).

After 17:53 UTC the velocity in the RIJ stream starts to rise, while the altitude of the leading part of the jet core drops below 2 km, which indirectly indicates the intensification of the influence of the updrafts and downdrafts (Fig. 6). At the same time, the mesocyclone of the embedded SC continues to move NNW relative to the movement of the system, slowly approaching the area of the RIJ core, entering the area of the illustrated cross-sections. This is the first time the strong air current associated with the RFD of the storm SC becomes visible (Fig. 8).

The signature of the mesocyclone along with the inflow area is also visible on the cuts. The RIJ stream continues to descend and the velocity in its core increases as well. The gust front associated with the rear downdraft of the SC

becomes increasingly visible, as the winds within it lie in the direction parallel to the axis of the signal beam (Fig. 8).

The horizontal observations from 18:03 to 18:23 UTC reveal that the high-speed area increases to a width of about 70 km. The RIJ structure on the scan at 18:23 UTC is slightly disturbed because it is passing directly over the radar and a there is a strong directional wind shear with the altitude (Fig. 9).

During the passage of the storm over the POZ radar, the signal was significantly muffled by the wet dome, which made it difficult to observe the signatures typical of the SC. As the phenomenon moved away from the radar, the reflectivity data decreased in quality due to the damping caused by precipitation. Therefore, the signatures at the forehead of the storm were not visible. Contrastingly, on the radial data, the SRV (V) product still showed a distinct vortex signature. Moreover, typical of SC forward flank downdraft (FFD) and rear flank downdraft (RFD) have emerged. Additionally, the range of the RIJ and the mesocyclone of the SC located in the northern part of the system are visible on the vertical section VCUT (V) (Fig. 10).

Over time, the RIJ and the RFD began to cover an increasing area; especially as the RFD began to encircle the mesocyclone more and more, which in turn continued to move along the forehead of the mesoscale system towards the NNW, constantly increasing its diameter (Fig. 11). The presence of the RIJ became increasingly apparent.

After 18:33 UTC the forehead of the RIJ begins to move away from the POZ radar, and its range becomes increasingly distinguishable. The wind speed in the RIJ core measured by the radar starts to rise. The core width is already more than 100 km, and further estimation of its spatial extent becomes impossible due to the specificity of Doppler measurements (Fig. 12).

About 19:10 UTC, on the EHT (HeightMaxZ) product (Fig. 13), a split of the system was observed within the SC storm, probably forced by the influence of the mesocyclone. In turn, the RFD, surrounding the mesocyclone, divided the updraft area into two sectors, i.e. the northwestern one associated with the mesocyclone and the southeastern one not associated with its circulation. The whole process clearly shows the mesocyclone role in the long duration of the storm. Figure 14 clearly shows the gradual disorganization of the raised strong echo not related to the mesocyclone. In contrast, the echo in the area where the hydrometeors are held at high altitudes by the rotating updraft is still significant.

At approximately 19:13 UTC one can notice the aforementioned moment when the RIJ was catching up with the air stream associated with the RFD of the SC. Both air currents are visible while comparing data from two different radar elevations for the same observation (Fig. 14). A strong air current powered by the RFD of an embedded SC is visible on the 0.5-degree elevation data, showing the wind field distribution in the lowest measurable layers. At the same time the RIJ, which is located higher, is not visible at this altitude. It is clearly visible only on the 3.6-degree elevation data, where only a small section of the flow forced by RFD is seen. In the following observations the forehead of RIJ starts to accelerate together with an increase of wind velocity in its area. At the same time the signatures proving the presence of the mesocyclone are poorly visible in that elevation, which confirms its most significant impact in the lower atmospheric layers (Fig. 15).

After 19:13 UTC a crucial moment in the derecho evolution occurs. The RIJ continues to catch up with the area of heavy winds associated with the SC RFD. The vertical cross-section VCUT from 19:13 UTC also shows that the RIJ and RFD cores are separated, while on the cross-section from 19:23 UTC they already present a single compact stream that continues to descend (Fig. 16).

Based on radar data, the moments between 19:23 UTC and 19:43 UTC can be considered the beginning of the bow echo. We can classify it as BEC
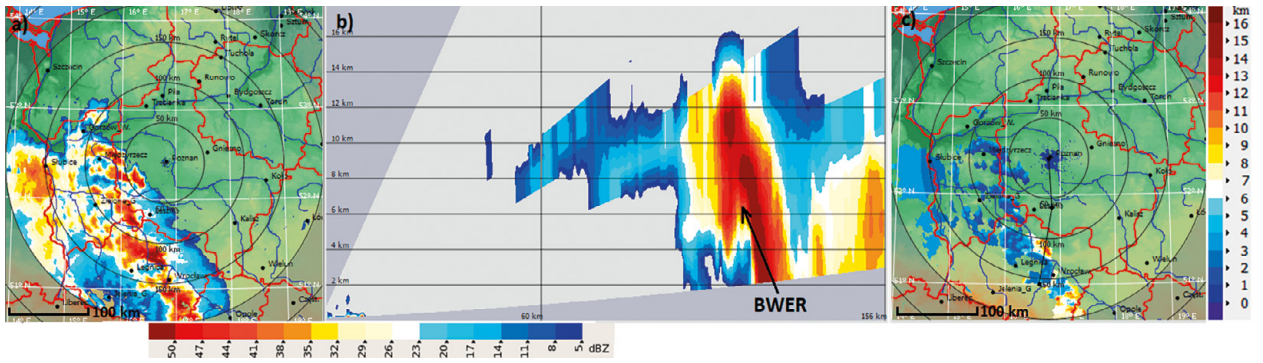
Fig. 4. Products: (a) MAX (dBZ); (b) vertical cut VCUT (dBZ) through a SC; and (c) EHT (HeightMaxZ) – POZ radar from 16:30 UTC.
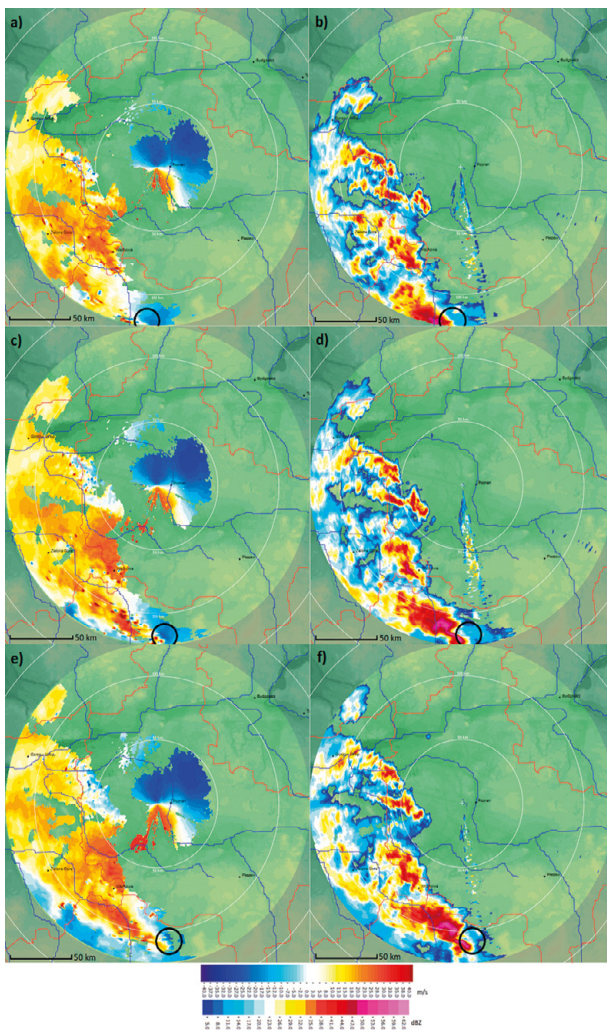

Fig. 5. SRV (V) (left), PPI (dBZ) (right) scans from 1.7-degree elevation showing the location of the mesocyclone at: (a, b) 16:23 UTC; (c, d) 16:33 UTC; (e, f) 16:43 UTC – POZ radar.


Fig. 6. Vertical section VCUT(V) from POZ radar presenting the evolution of RIJ at: (a)17:13 UTC; (b) 17:33 UTC; (c) 17:53 UTC with the corresponding 4 km CAPPI (V) scans with marked vertical section line (d, e, f).
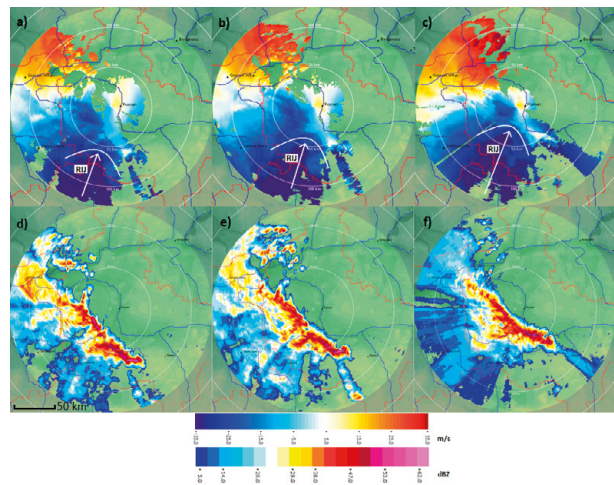

Fig. 7. SRV (V), PPI (dBZ) products, POZ radar, 1.7-degree elevation from 17:33 (a, d) to 17:43 UTC (b, e) and 3.6-degree elevation at 17:53 UTC (c, f). RIJ direction and range are marked.

31

because the mesocyclone still existed. Later, due to the split of the SC, a new branch of the RIJ is formed. Its direction further deviates toward the northeast (Fig. 17). The downbursts associated with this RIJ may be responsible for some damage east of the main path of damage.

After 20:00 UTC the most significant wind damage occurred, the trail of which coincided with the path of the eastern flank of the SC (Taszarek et al. 2019). By analyzing the radar data, it can be concluded that the overlap of RFD and RIJ in the storm was the crucial factor in generating such strong

winds, which reached the surface. (Taszarek et al. 2019). In turn, such a long trail of destruction was possible because of the constantly active, expanding mesocyclone, the local circulation of which ensured a good separation of updrafts and downdrafts, and thus, contributed to the long life of the storm.

At 20:44 UTC, at the edge of the Doppler scan range, the data from the POZ radar were already strongly attenuated and distorted. Therefore, the mesocyclone analysis was continued using data from the GDA radar. Despite problems with the interpretation of data related to noise and the sec-
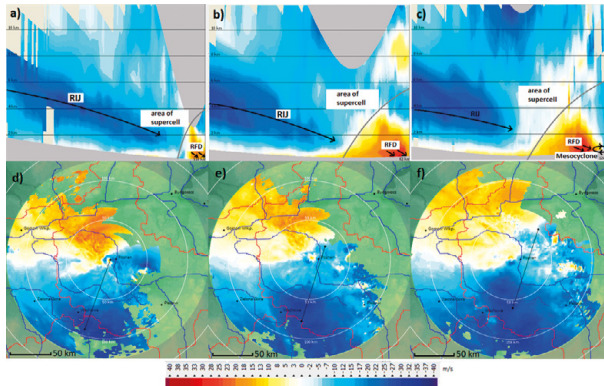
Fig. 8. Vertical section VCUT(V) from POZ radar showing further stages of RIJ evolution and a part of SC area at: (a) 18:13 UTC; (b) 18:33 UTC; (c) 18:53 UTC; with the corresponding 4 km CAPPI (V) scans with marked vertical section lines (d, e, f).
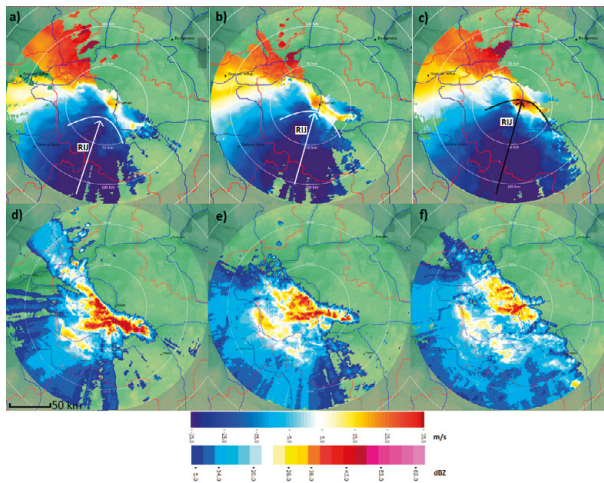

Fig. 9. SRV(V), PPI (dBZ) products, POZ radar, 3.6-degree elevation, at: 18:03 UTC (a, d), 18:13 UTC (b, e), 18:23 UTC (c, f). RIJ direction and range are marked.
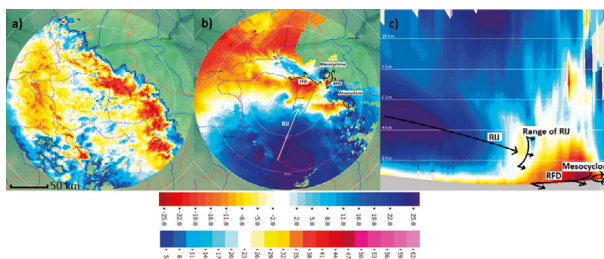
Fig. 10. (a) PPI (dBZ); (b), SRV (V) scans from 1.7-degree elevation and vertical cut VCUT (V) from 18:53 UTC (c) – POZ radar.
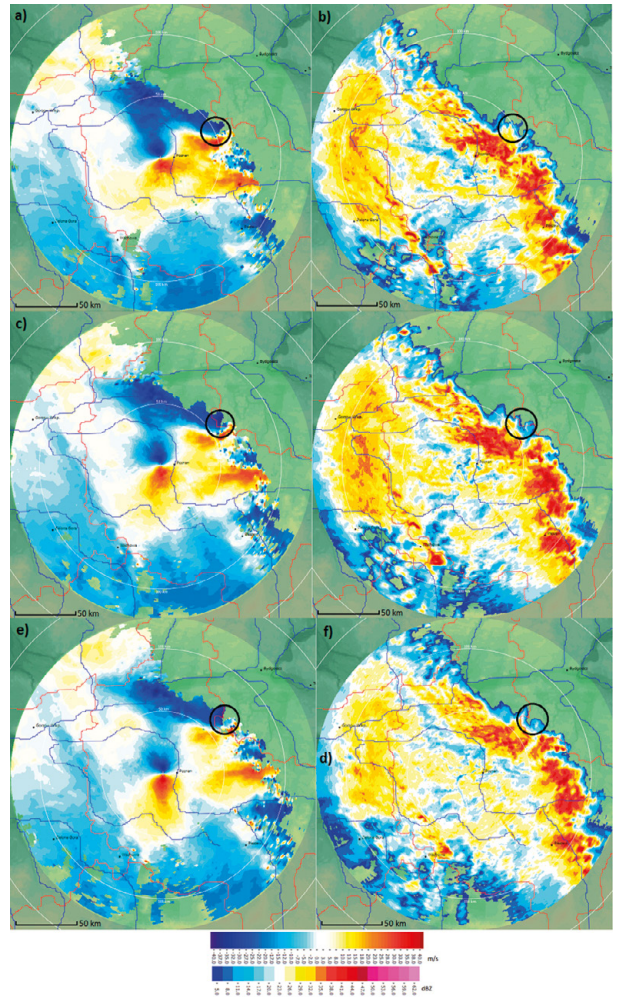
Fig. 11. SRV (V) (left), PPI (dBZ) (right) scans from 1.7-degree elevation showing the location of the mesocyclone at: 18:43 UTC (a, b), 18:53 UTC (c, d), and 19:03 UTC (e, f) – POZ radar.
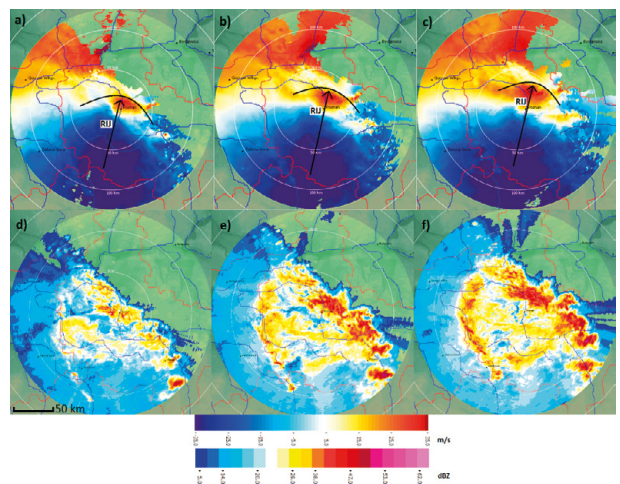
Fig. 12. SRV(V), PPI (dBZ) products, POZ radar, 3.6-degree elevation, at: 18:33 UTC (a, d), 18:43 UTC (b, e), and 18:53 UTC (c, f); RIJ direction and range are marked.
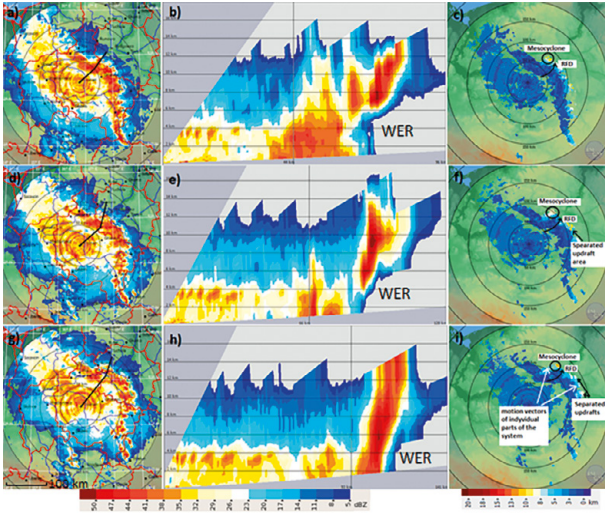
Fig. 13. Products: (a, d, g) MAX (dBZ); (b, e, h) vertical section VCUT (dBZ) through a SC; and (c, f, i) EHT (HeightMaxZ) – POZ radar at 19:10 UTC (a, b, c), 19:30 UTC (d, e, f), 19:50 UTC (g, h, i).

Fig. 15. SRV (V), PPI (dBZ) products, POZ radar, 3.6-degree elevation, at: 19:03 UTC (a, d), 19:13 UTC (b, e), 19:23 UTC (c, f); RIJ direction and range are marked.
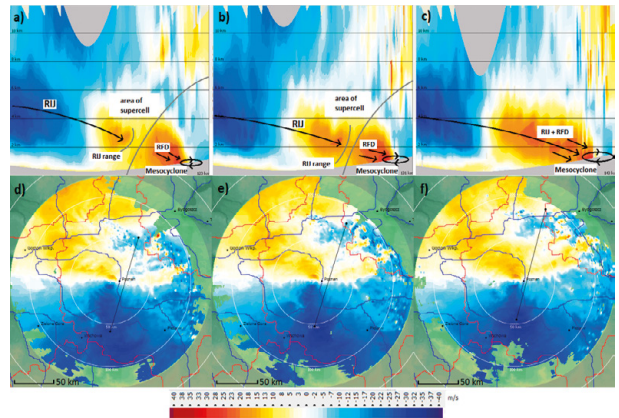

Fig. 16. Vertical section VCUT(V) from POZ radar presenting interaction of RIJ with RFD SC at: 19:13 UTC (a), 19:23 UTC (b), and 19:33 UTC (c) with the corresponding 4 km CAPPI (V) scans with marked vertical section line (d, e, f).


Fig. 14. SRV(V), PPI (dBZ) products, POZ radar, at 19:13 UTC: (a, c) 3.6-degree elevation; (b, e) 0.5-degree elevation.
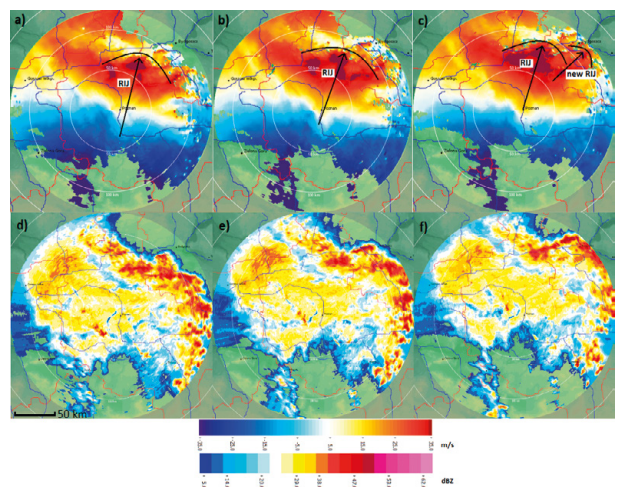

Fig. 17. SRV (V), PPI (dBZ) products, POZ radar, 1.7-degree elevation, at: 19:33 UTC (a, d), 19:43 UTC (b, e), and 19:53 UTC (c, f). RIJ direction and range are marked.

33
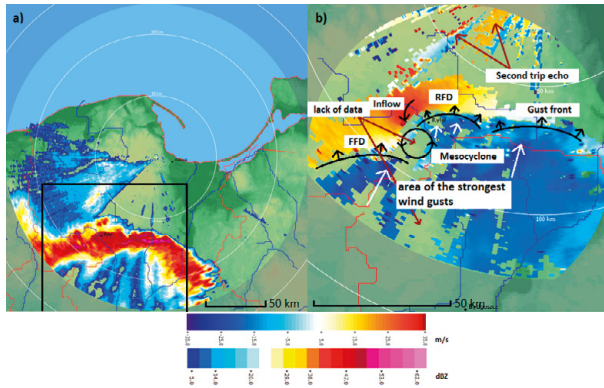
Fig. 18. (a) PPI (dBZ); (b) SRV (V) products from 0.5-degree elevation at 20:44 UTC with the essential elements of the storm system indicated – GDA radar.
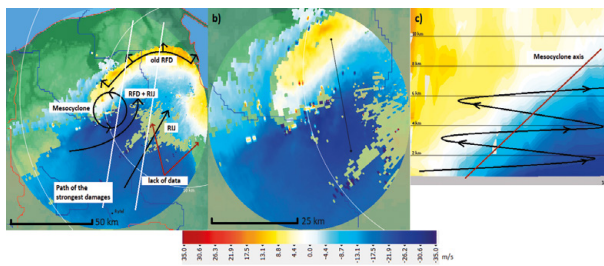

Fig. 19. (a, b) SRV(V) product from GDA radar at 21:44; and (c) the vertical section VCUT(V). The area between white lines is path of the greatest damage.
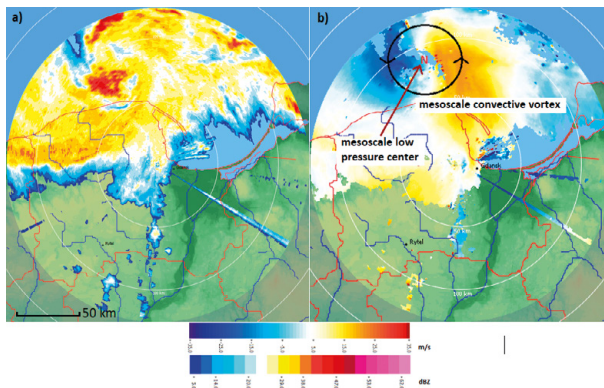
Fig. 20. (a) PPI (dBZ); (b) SRV (V) products from 0.5-degree elevation at 23:14 UTC with visible mesoscale vortex formed around the local low – GDA radar.

ond trip echo phenomenon, the SRV (V) product clearly shows the effects of further transformation that the system underwent while moving between the Doppler range of the POZ and GDA radar. The RFD on the eastern flank of the mesocyclone overtook the FFD and became the main bow segment additionally powered by the descending RIJ. The mesocyclone distinctly increased its diameter, still moving along the forehead, to the west of the system axis (Fig. 18).

Unfortunately, due to the poor quality of data from the GDA radar between 20:00-21:00 UTC, the RIJ analysis was abandoned for that period. However, this is already the stage where the direction of the RIJ and of the near-surface flow associated with the weakening RFD of the pre-existing SC are diverging. Although the RIJ is relatively low, there is no longer such strong transfer of the RIJ momentum

to the surface. This fact reveals why no such extensive wind damage has been recorded in the coastal area.

After 21:00 UTC the MCS takes the form of a compact bow echo with one large bowing segment associated with transformed RFD, along with the MCV signature formed at the mesocyclone site. Unfortunately the precise time of the MCV forming can't be determined due to poor data quality just before 21:00 UTC. The vertical section VCUT clearly shows the MCV axis inclined from north to south and its eastern flank with high-velocity values at lower elevation, additionally powered by the RIJ (Fig. 19). The presence of the mesoscale low resulting from the evolution of the mesocyclone was distinctly visible in the SRV (V) scans after passing over the shore of the Baltic Sea. A cyclonic circulation of air masses developed around the mesocyclone low, which is confirmed by the twisting motion of hydrometeors (Fig. 20).

7. CONCLUSION

This paper presents a case study of a derecho based on radar observations. In particular, the origin of the phenomenon and the various stages of its development were determined, important components of the storm were identified, and their role in the formation of the damaging winds was shown.

The analysis shows formation of a bow echo complex (classified on the grounds of the inflicted damage as a derecho) (Taszarek et al. 2019; Wrona et al. 2022), which developed from unorganized storm cells. The decisive role in the system evolution was played by one of the storm SCs embedded into the system, the local circulation of which intensified the processes taking place therein.

The study has focused on the development and the evolution of the mesocyclone, RIJ activity, and their interaction. The main objective was to verify the hypothesis formulated by Taszarek et al. (2019) that the overlapping of wind vectors within the RFD SC and the RIJ vectors was responsible for such significant wind damage. Our analysis of radial wind observations confirms the presence of characteristic gust fronts associated with mesocyclone circulation and their interactions with RIJ.

Despite some data discontinuities, it was confirmed that the areas of the most significant damage coincide in time and space with radar observations showing the convergence of wind vectors related to RFD and RIJ. Later divergence of these wind directions explains why the storm did not cause so much damage in the northern part of Pomerania.

In conclusion, this study presents a detailed qualitative analysis of the elements of the storm system responsible for extreme anemological phenomena: the interaction between the RFD of the SC and the RIJ. More accurate quantitative analysis was hindered because of the system's distance from the radars during the key moments of its evolution and the difficulties in the data interpretation, including contamination by strong precipitation. Nevertheless, the key question was answered: what mechanisms acting within the convective system led to development of such strong winds and damages? In addition, this paper provides evidence that mesoscale convective systems, in which intense SCs are embedded, could be extremely dangerous. The knowledge obtained from this analysis may help in warning the population more effectively against similar phenomena in the future.

REFERENCES

- Ashley W.S., Mote T.L., Bentley M.L., 2005, On the episodic nature of derecho-producing convective systems in the United States, International Journal of Climatology, 25 (14), 1915-1932, DOI: 10.1002/joc.1229.

- Atkins N.T., Laurent M.S., 2009, Bow echo mesovortices. Part II: Their genesis, Monthly Weather Review, 137, 1514-1532, DOI: 10.1175/2008MWR2650.1.

- Atkins N.T., Arnott J.M., Przybylinski R.W., Wolf R.A., Ketcham B.D., 2004, Vortex structure and evolution within bow echoes. Part I: Single-doppler and damage analysis of the 29 June 1998 derecho, Monthly Weather Review, 132, 2224-2242, DOI: 10.1175/1520-0493(2004)132<2224:VSAEWB>2.0.CO;2.

- Bentley M.L., Mote T.L., 1998, A climatology of derecho-producing mesoscale convective systems in Central and Eastern United States, 1986-95. Part I: Temporal and spatial distribution, Bulletin of the American Meteorological Society, 79 (11), 2527-2540, DOI: 10.1175/1520-0477(1998)079<2527:ACODPM>2.0.CO;2.

- Bentley M.L., Sparks J.A., 2003, A 15 yr climatology of derecho-producing mesoscale convective systems over the central and eastern United States, Climate Research, 24, 129-139, DOI: 10.3354/cr024129.

- Celiński-Mysław D., 2014, Derecho jako przykład silnych zjawisk anemonologicznych – dotychczasowy stan badań, Prace Geograficzne, 139, 21-32, DOI: 10.4467/20833113PG.14.022.3012.

- Celiński-Mysław D., Matuszko D., 2014, An analysis of the selected cases of derecho in Poland, Atmospheric Research, 149, 263-281, DOI: 10.1016/j.atmosres.2014.06.016.

- Coniglio M.C., Stensrud D.J., 2004, Interpreting the climatology of derechos, Weather and Forecasting, 19 (3), 595-605, DOI: 10.1175/1520-0434(2004)019<0595:ITCOD>2.0.CO;2.

- Coniglio M.C., Corfidi S.F., Kain J.S., 2011, Environment and early evolution of the 8 May 2009 derecho-producing convective system, Monthly Weather Review, 139 (4), 1083-1102, DOI: 10.1175/2010MWR3413.1.

- Davies C.A., Weisman M.L., 1994, Balanced dynamics of mesoscale vortices produced in simulated convective systems, Journal of the Atmospheric Sciences, 51, 2005-2030, DOI: 10.1175/1520-0469(1994)051<2005:BDOMVP>2.0.CO;2.

- Davies J.M., Johns R.H., 1993, Some wind and instability parameters associated with strong and violent tornadoes. Part 1. Wind shear and helicity, The Tornado: Its Structure, Dynamics, Prediction, and Hazards, Geophysical Monograph Series, 79, 573-582, DOI: 10.1029/GM079p0573.

- Duke J.W., Rogash J.A., 1992, Multiscale review of development and early evolution of the 9 April 1991 derecho, Weather and Forecasting, 7 (4), 623-635, DOI: 10.1175/1520-0434(1992)007<0623:MROTDA>2.0.CO;2.

- Evans J.S., Doswell III C.A., 2001, Examination of derecho environments proximity soundings, Weather and Forecasting, 16, 329-342.

- Fink A.H., Brücher T., Ermert V., Krüger A., Pinto J.G., 2009, The European storm Kurill in January 2007: synoptic evolution, meteorological impacts and some considerations with respect to climate change, Natural Hazards and Earth System Sciences, 9, 405-423, DOI: 10.5194/nhess-9-405-2009.

- Forbes G.S., Wakimoto R.M., 1983, A Concentrated outbreak of tornadoes, downbursts and microbursts, and implications regarding vortex classification, Monthly Weather Review, 111 (1), 220-236, DOI: 10.1175/1520-0493(1983)111<0220:ACOOTD>2.0.CO;2.

- Fujita T.T., 1978, Manual of downburst identification for project NIMROD, SMRP Research Paper 156, The University of Chicago, 104 pp.

- Fujita T.T., Wakimoto R.M., 1981, Five scale of airflow associated with a series of downbursts on 16 July 1980, Monthly Weather Review, 109 (7), 1438-1456., DOI: 10.1175/1520-0493(1981)109<1438:FSOAAW>2.0.CO;2.

- Funkt T.W., Darmofal K.E., Kirkpatrick J.D., DeWald Van L., Przybylinski R.W., Schmocker G.K., Lin Y., 1994, Storm reflectivity and mesocyclone evolution associated with the 15 April 1994 squall line over Kentucky and southern Indiana, Weather and Forecasting, 14 (6), 976-993.

- Gatzen C., 2004, A derecho in Europe: Berlin, 10 July 2002, Weather and Forecasting, 19 (3), 639-645, DOI: 10.1175/1520-0434(2004)019<0639:ADIEBJ>2.0.CO;2.

- Gatzen C., Pucik T., Ryva D., 2011, Two cold-season derechoes in Europe, Atmospheric Research, 100 (4), 740-748, DOI: 10.1016/j.atmosres.2010.11.015.

- Hamid K., 2012, Investigation of the passage of the derecho in Belgium, Atmospheric Research, 107, 86-105, DOI: 10.1016/j.atmosres.2011.12.013.

- Hinrichs G., 1888, Tornadoes and derecho, American Meteorological Journal, 5, 341-349.

- Johns R., Hirt W., 1987, Derechos: Widespread convectively induced windstorms, Weather and Forecasting, 2 (1), 32-49, DOI: 10.1175/1520-0434(1987)002<0032:DWCIW>2.0.CO;2.

- Jurczyk A., Szturc J., Ośródka K., 2020, Quality-based compositing of weather radar-derived precipitation, Meteorological Applications, 27 (1), DOI: 10.1002/met.1812.

- King A.D., Karoly D.J., Henley B.J., 2017, Australian climate extremes at 1.5°C and 2°C of global warming, Nature Climate Change, 7, 412-416, DOI: 10.1038/nclimate3296.

- Klemp J.B., Rotunno R., 1983, A study of the tornadic region within a supercell thunderstorm, Journal of Atmospheric Sciences, 40 (2), 359-377, DOI: 10.1175/1520-0469(1983)040<0359:ASOTTR>2.0.CO;2.

- Klimowski B.A., Hjelmfelt M.R., Bunkers M.J., 2004, Radar observations of the early evolution of bow echoes, Weather and Forecasting, 19 (4), 727-734, DOI: 10.1175/1520-0434(2004)019<0727:ROOTEE>2.0.CO;2.

- Klimowski B.A., Przybylinski R.W., Schmocker G., Hjelmfelt M.R., 2000, Observations of the formation and early evolution of bow echoes, [in:] 20th Conference on Severe Local Storms, American Meteorological Society, Orlando, 44-47.

- Lemon L.R., Doswell C.A., 1979, Severe thunderstorm evolution and mesocyclone structure as related to tornadogenesis, Monthly Weather Review, 107 (9), 1184-1197, DOI: 10.1175/1520-0493(1979)107<1184:STEAMS>2.0.CO;2.

- Lopez J.M., 2007, A Mediterranean derecho: Catalonia (Spain), 17th August 2003, Atmospheric Research, 83 (2-4), 272-283, DOI: 10.1016/j.atmosres.2005.08.008.

- Markowski P.M., 2002, Hook echoes and rear-flank downdrafts, Monthly Weather Review, 130 (4), 852-876, DOI: 10.1175/1520-0493(2002)130<0852:HEARFD>2.0.CO;2.

- Moller A.R., Doswell C.A., Przybylinski R.W., 1990, High-precipitation supercells: A conceptual model and documentation, 16th Conference on Severe Local Storms, October 22-26, Kananaskis Provincial Park, Bulletin of the American Meteorological Society, 71 (6), 884-900.

- Moller A.R., 2001, Severe local storms forecasting, [in:] Severe Convective Storms, C.A. Doswell (ed.), American Meteorological Society, Boston.

- Przybylinski R.W., 1995, The bow echo: observations, numerical simulations and severe weather detection methods, Weather and Forecasting, 10 (2), 203-218, DOI: 10.1175/1520-0434(1995)010<0203:TBEONS>2.0.CO;2.

- Pucik T., Francova M., Ryva D., Kolar M., Ronge L., 2011, Forecasting challenges during the severe weather outbreak in Central Europe on 25 June 2008, Atmospheric research, 100 (4), 680-704, DOI: 10.1016/j.atmosres.2010.11.014.

- Punkka A-J., Teittinen J., Johns R.H., 2006, Synoptic and mesoscale analysis of a high-latitude derecho-severe thunderstorm outbreak in Finland on 5 July 2002, Weather and Forecasting, 21 (5), 752-763, DOI: 10.1175/WAF953.1.

- Putsay M., Szenyan I., Simon A., 2009, Case study of mesoscale convective systems over Hungary on 29 June 2006 with satellite, radar and lighting data, Atmospheric Research, 98 (1-3), 82-92, DOI: 10.1016/j.atmosres.2008.10.026.

- Rasmussen E.N., Rutledge S.A., 1993, Evolution of quasi-two-dimensional squall lines. Part I: Kinematic and reflectivity structure, Journal of the Atmospheric Sciences, 50 (16), 2584-2606, DOI: 10.1175/1520-0469(1993)050<2584:EOQTDS>2.0.CO;2.

- Rasmussen E.N., Straka J.M., 1998, Variations in supercell morphology. Part I: Observations of the role of upper-level storm-relative flow, Monthly Weather Review, 126 (9), 2406-2421, DOI: 10.1175/1520-0493(1998)126<2406:VISMPI>2.0.CO;2.

- Rotunno R., Klemp J.B., Weisman M.L., 1988, A theory for strong, long-lived squall lines, Journal of the Atmospheric Sciences, 45 (3), 463-485, DOI: 10.1175/1520-0469(1988)045<0463:ATFSLL>2.0.CO;2.

- Schmid W., Schiesser H., Furger M., Jenni M., 2000, The origin of severe winds in a tornadic bow-echo storm over Northern Switzerland, Monthly Weather Review, 128 (1), 192-207, DOI: 10.1175/1520-0493(2000)128<0192:TOOSWI>2.0.CO;2.

- Sherburn K.D., Parker M.D., King J.R., Lackmann G.M., 2016, Composite environments of severe and nonsevere high-shear, low-CAPE convective events, Weather and Forecasting, 31 (6), 1899-1927, DOI: 10.1175/WAF-D-16-0086.1.

- Simon A., Kanak J., Sokol A., Putsay M., Uhrinova L., Csirmaz K., Okon L., Habrovsky R., 2011, Case study of a severe windstorm over Slovakia and Hungary on 25 June 2008, Atmospheric Research, 100 (4), 705-739, DOI: 10.1016/j.atmosres.2010.12.012.

- Surowiecki A., Taszarek M., 2020, A 10-year radar-based climatology of mesoscale convective system archetypes and derechos in Poland, Monthly Weather Review, 148 (8), 3471-3488, DOI: 10.1175/MWR-D-19-0412.1.

- Szturc J., 2010, Niepewność w radarowych pomiarach opadu z punktu widzenia hydrologii, IMGW, Warszawa, 148 pp.

- Taszarek M., Brooks H. E., Czarnecki B., 2017, Sounding-derived parameters associated with convective hazards in Europe, Monthly Weather Review, 145 (4), 1511-1528, DOI: 10.1175/MWR-D-16-0384.1.

- Taszarek M., Piguj N., Orlikowski J., Surowiecki A., Walczakiewicz S., Pilorz W., Piasecki K., Pajurek Ł., Półrolniczak M., 2019, Derecho evolving from a mesocyclone – a study of 11 August 2017 severe weather outbreak in Poland: event analysis and high-resolution simulation, Monthly Weather Review, 47 (6), 2283-2306, DOI: 10.1175/MWR-D-18-0330.1

- Trapp R.J., Tessendorf S.A., Godfrey E.S., Brooks H.E., 2005, Tornadoes from squall lines and bow echoes. Part I; Climatological distribution, Weather and Forecasting, 20 (1), 23-34, DOI: 10.1175/WAF-835.1.

- Tuszyńska I., 2011, Charakterystyka produktów radarowych, IMGW, Warszawa, 79 pp.

- Walczakiewicz S., Ostrowski K., 2010, Nawałnica z 4 VII 2002 r. jako przykład bow echo w Europie Środkowo-Wschodniej ze szczególnym uwzględnieniem burzy w Puszczy Piskiej, [in:] Materiały Geo-Sympozjum Młodych Badaczy Silesia 2010, Bytom (Polska), 213-230.

- Weisman M.L., 1992, The role of convectively generated rear-inflow jets in the evolution of long-lived mesoconvective systems, Journal of the Atmospheric Sciences, 49 (19), 1826-1847, DOI: 10.1175/1520-0469(1992)049<1826:TROCGR>2.0.CO;2.

- Weisman M.L., 1993, The genesis of severe, long-lived bow echoes, Journal of the Atmospheric Sciences, 50 (4), 645-670, DOI: 10.1175/1520-0469(1993)050<0645:TGOSLL>2.0.CO;2.

- Weisman M.L., 2001, Bow echoes: A tribute to T.T. Fujita, Bulletin of the American Meteorological Society, 82 (1), 97-116, DOI: 10.1175/1520-0477(2001)082<0097:BEATTT>2.3.CO;2.

- Wolf P.L., 1998, WSR-88D radar depiction of supercell–bow echo interaction: unexpected evolution of a large, tornadic, "Comma-Shaped" supercell over eastern Oklahoma, Weather and Forecasting, 13 (2), 492-504, DOI: 10.1175/1520-0434(1998)013<0492:WRDOSB>2.0.CO;2.

- Wrona B., Mańczak P., Wozniak A., Ogrodnik M., Folwarski M., 2022, Synoptic conditions of the derecho storm. Case study of the derecho event over Poland on August 11, 2017, Meteorology Hydrology and Water Management, DOI: 10.26491/mhwm/152798.

- Zipser E.J., 1982, Use of a conceptual model of the life cycle of mesoscale convective systems to improve very-short-range forecasts, [in:] Nowcasting, K. Browning (ed.), Academic Press, 191-204.

Monitoring the 11 August 2017 storm in central Poland with satellite data and products

Bożena Łapeta, Elżbieta Kuligowska, Paulina Murzyn, Piotr Struzik
Institute of Meteorology and Water Management – National Research Institute, Poland

38

ABSTRACT. This paper presents the evolution of the mesoscale convection system as seen on satellite images during all stages: pre-convection, initiation, and maturity. The evolution of any atmospheric phenomenon can be monitored effectively only when the data available have adequate temporal and spatial resolution. In case of convective storms the resolution should be minutes and kilometers. Therefore, data from the METEOSAT geostationary satellite, with 5-minute and 15-minute intervals were used operationally to monitor the storm of 11 August 2017; this was a most destructive storms, concentrated in several districts of the Pomeranian, Greater Poland, and Kuyavian-Pomeranian voivodeships. Analysis demonstrated that some alarming features, like cold rings or cold U/V shapes, can be visible on the single channel satellite images, without even referring to specific convective products. However, the nowcasting of the convective phenomena requires careful analysis of several dedicated products, including stability indices and water vapor content in the troposphere. It has been shown that with comprehensive analysis of the information provided by the different satellite images and satellite derived products, it is possible to draw conclusions about the severity of the observed storms as well as the probability of the occurrence of the extreme weather at the ground.

KEYWORDS: Satellite data, satellite products, convective storm monitoring.

1. INTRODUCTION

Progress in satellite data quality and speed of data acquisition over the past two decades, provides new insights for application to short-term weather forecasts, as well as so-called nowcasting weather forecasts. Nowcasting supplies a detailed description of current weather conditions obtained by extrapolation for a period of 0 to 6 hours ahead. Nowcasting is especially useful in the event of storms and downpours as well as flooding, because in its typical time range it is possible to forecast small features such as individual storms. Modern advances in satellite technology in terms of high resolution, multi-spectral coverage and sampling frequency (appearance of a given satellite over the same area of Earth) are improving satellite data to high accuracy, and thus of increasing importance in weather monitoring. Satellite data are also essential for the accurate numerical weather forecasts. These trends of increasing accuracy and temporal resolution of satellite retrievals, support improved models, and more accurate forecasts, even for the most violent storms.

The ability of satellite data to detect and monitor the Earth's atmosphere proved to be extremely useful during the one of the most destructive storms that was concentrated in several districts of the Pomeranian, Greater Poland, and Kuyavian-Pomeranian voivodeships on 11 August 2017. On that day, there was a humid and very hot mass of tropical air over Poland (Taszarek et al. 2019). The air temperature in the southern part of the country reached 35°C. Thermodynamic and kinematic conditions, including high wind shear, favored the development of severe storms and accompanying phenomena in the form of heavy rainfall and strong gusts of wind. In the afternoon, these storms appeared over southwest Poland, then quickly intensified and moved to the northeast in the form of a mesoscale convection system with an embedded squall line. The strongest phenomena occurred in the evening on the border of the Greater Poland, Pomeranian, and Kuyavian-Pomeranian voivodeships. The maximum wind gusts recorded that day are among the highest in the history of Polish measurements: 42 m/s in Elbląg, 36 m/s in Chrząstów, 35 m/s in Gniezno, and around 30 m/s at several other stations. The route of the most intensive wind gusts is shown on Figure 1.

In total, 5 people were killed in Poland (Dziennik Bałtycki 2018) and 39 were injured. In addition, 23 rescuers suffered minor injuries during the operation. In terms of the number of victims, the most tragic outcome was in Suszek (Pomeranian Voivodeship), where 5 people died. Storms this strong happen once every few years, but the mesoscale convection system (MCS) that occurred on 11 August, 2017 met the criteria for a derecho and was the one of the strongest storm incidents recorded recently in Poland (zmiana na (Wrona et al. 2022). The detailed synoptic analysis of this storm is presented in this issue of MHWM in the paper by Wrona et al. (2022).

This paper presents the evolution of the mesoscale convection system as seen on the satellite images during all the stages: pre-convection, initiation, and maturity. In Chapters 2 and 3 the satellite data and products used in the analysis are described. The evolution of the MCS on satellite images and products is shown in Chapter 4. The analysis presented in this chapter also includes satellite products that were not available at the time of the event but are now used operationally in forecasting offices, so that we could evaluate their suitability for detecting and monitoring severe convective systems.

2. SATELLITE IMAGES USEFUL FOR CONVECTION DETECTING AND MONITORING

Data from a geostationary satellite provide indirect information on the atmosphere with high temporal resolution for almost full coverage of one of the Earth's hemispheres. Depending on the spectral channel in which the satellite image is acquired, various types of weather phenomena and their characteristics can be detected. The analysis of all available spectral data enables the retrieval of meteorologically important information. Acquisition of satellite data in solar bands enables the estimation of optical thickness of the cloud and the water phase, but the monitoring is limited to the daytime only. Initiation and development of the severe weather phenomena regardless of the time of day can be tracked in the infrared channels that measure radiation emitted by the Earth and the atmosphere. These bands allow the estimation of cloud-top temperature, which is used as an indicator of the potential severity of thunderstorms (da Silva Neto et al. 2016). In the troposphere, the thicker and more developed the storm cloud is, the lower brightness temperature its top represents. Apart from IR single channel images, satellite derived products that either combine data from different channels or are obtained with dedicated software can be used for convection detection and monitoring. Both types of products are described below.

2.1. COLOR-ENHANCED IR BRIGHTNESS TEMPERATURE IMAGE

The METEOSAT SEVIRI instrument provides image data in eight IR channels, two of which (IR 10.8 μm and IR 12.0 μm) are known as IR window channels, because of relatively little absorption by the atmospheric gases in this spectral region. The two channels enable estimation of cloud top temperature, which provides crucial information for detection of highly developed clouds, including convective storms. For fast and easy recognition of the coldest parts of cloud tops, the IR 10.8 μm channel with color enhancement of cloud top temperature below −33°C is widely used. It provides information on the coldest parts of cloud tops that are often connected with deep convection occurring in the cloud (Setvak et al. 2010). The cold ring and cold U shape(s) on the convective cloud top (Fig. 2) are indicators of the possible severity of the convective cloud (Setvak et al. 2010), particularly if they are present during a longer time period.

2.2. SANDWICH

Another meteorological product providing information on convection initiation and storm tracking is METEOSAT SEVIRI "Sandwich" Product. It consists of two layers: a black and white visible channel image (in this case HRV 0.4-1.1 μm) and a color-enhanced IR Brightness Temperature image. With their high spatial resolution, the background images provide information on cloud top spatial structure, while the overlaid IR images are used to monitor cloud top temperature distribution. Therefore cloud top features indicating the cloud severity, such as cold rings, cold U, gravity waves, and above-anvil ice plumes can be much more easily detected. These features can be seen in Figure 3. The main limitation of the Sandwich product is its availability only during the daytime.

Both color enhanced IR and Sandwich images are useful in detecting and monitoring the cloud top features. Storms exhibiting cold rings belong to a category of storms whose tops exhibit some form of cold/warm couplets that are connected with overshooting tops. Under favorable conditions almost every major overshooting top generates a downwind counterpart, a warm spot of varying horizontal extent, with brightness temperature difference from the surrounding anvil, and duration (Setvak et al. 2010). The occurrence of warm spots downwind of the individual overshooting tops is supported by some specific air mass types and wind shear, therefore these features are not observed in every convective cloud (Setvak et al. 2010). In the works by Schlesinger (1984, 1988), Heymsfield and Blackmer (1988), and Heymsfield et al. (1991) the close link between storm severity and cold rings, or cold U/V-shapes with a duration of 40-45 minutes, was indicated.
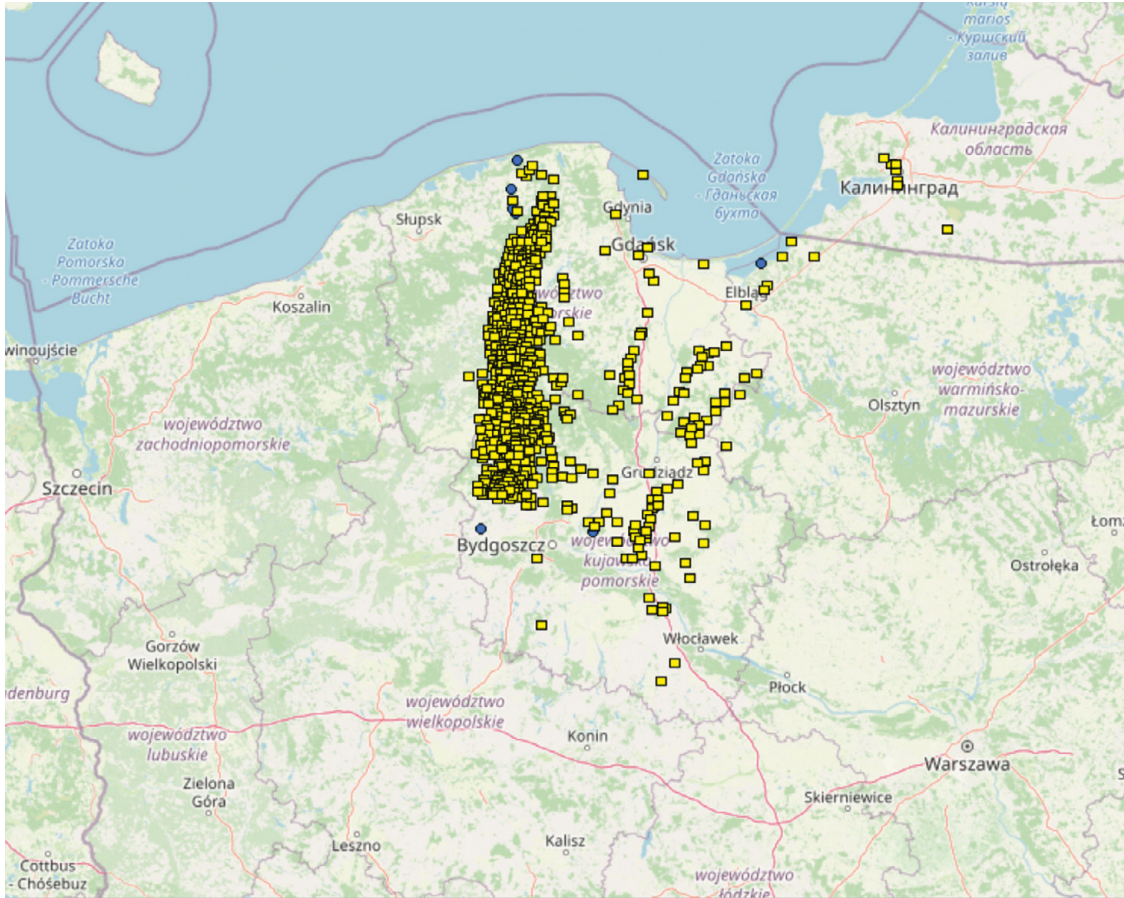
Fig. 1. Severe weather reports on 11 August 2017 in Poland (European Severe Weather Data Base).

2.3. THE WATER VAPOR (6.2 μM) CHANNEL IMAGE

The images in the 6.2 μm channel may indicate the development of convection over the area. The 6.2 μm images show the distribution of the water vapor concentration in the upper tropospheric column (in shades of grey) as well as clouds with high tops. Water vapor in the atmosphere plays a key role in storm formation. While the typical storm clouds are the real generators of static charge found in the atmosphere, their ability to hold massive amounts of electrical energy is related to the amount of water vapor present in the local area's air column (Schadowitz 1988).

Apart from detection of a pre-convectional environment, 6.2 μm images also can be used for monitoring highly-developed convection cells that are white on images in the grey scale.

2.4. THE BTD PRODUCT

As above, thunderstorms are clearly detectable on satellite maps showing the distribution of water vapor. The Brightness Temperature Difference (BDT) product, which shows differences in the brightness temperature between the 6.2 μm and 10.8 μm channels is dedicated to early recognition of rapidly developing storms.

In the case of vertically developed clouds, the radiation at the top of the atmosphere can be considered as the radiation at the cloud top, from the stratosphere. One of the main characteristics of the stratosphere is the increase of temperature with altitude. The increase is more pronounced in the absorption bands. The actual difference between the brightness temperatures depends on the actual height of the cloud top and on the amount of stratospheric water vapor (Schmetz et al. 1997). Difference values greater than 0 indicate areas in clouds where strong updrafts occur, leading to a strong uplift of the cloud

tops and the overshooting tops phenomenon (Setvak et al. 2007; Bedka et al. 2010; da Silva Neto et al. 2016). These tops can reach the tropopause and even extend into the stratosphere. Such areas are very often associated with violent phenomena such as heavy rainfall, wind gusts, hailstorms, or even tornados (Bedka et al. 2010; Setvak et al. 2010).

3. LEVEL 2 SATELLITE PRODUCTS

The level 2 products used in this analysis were derived using the NWC/GEO software package delivered by the EUMETSAT Satellite Application Facility in support of nowcasting and very short-range forecasting (NWC-SAF). Its main objective is to provide meteorological products which have application to nowcasting. It allows calculation of meteorological products related to clouds and their physical properties, precipitation, convection initiation, wind, clear air turbulence, and instability indices. Besides the satellite data, the NWC-SAF software uses numerical weather prediction (NWP) model fields. As the current operational version of the NWC/GEO software was created in 2018, i.e., after the 11 August 2017 storm, the products presented hereafter were obtained with an off-line run of the software with archived satellite and NWP model data.

3.1. LAYER PRECIPITABLE WATER PRODUCTS

Whereas the satellite data in the 6.2 μm channel provide information on the water vapor content in the upper troposphere, the Layer Precipitable Water product gives information about the amount of precipitable water in three discrete layers of the atmosphere: the boundary layer, from the surface to 850 hPa; the medium layer, from 850 hPa to 500 hPa; and the high layer: from 500 hPa to the top of the atmosphere. The moisture content
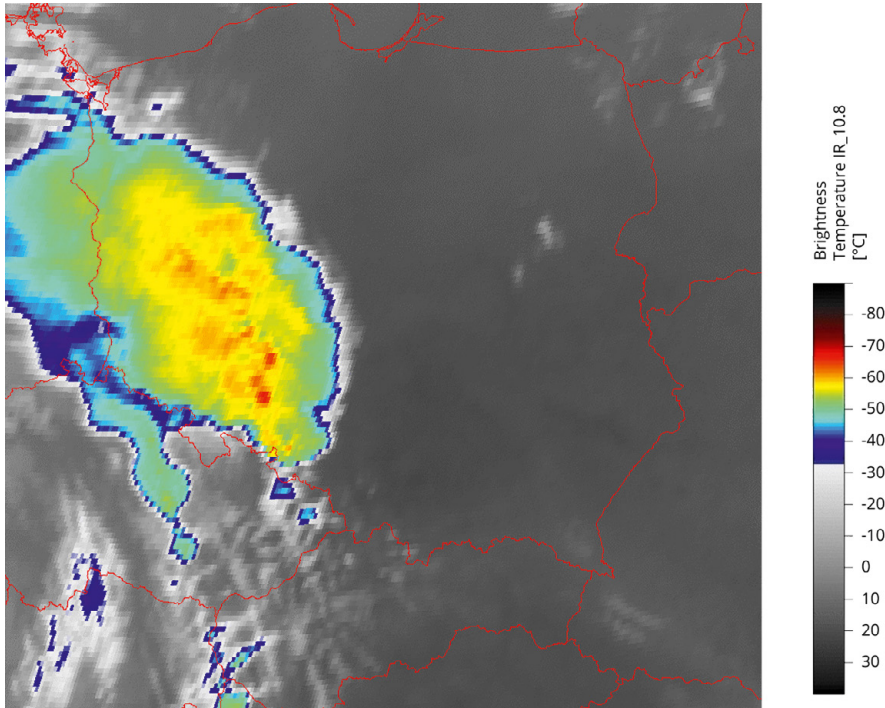
Fig. 2. METEOSAT SEVIRI color-enhanced IR brightness temperature image, 11 August 2017, 17:00 UTC (EUMETSAT 2017).
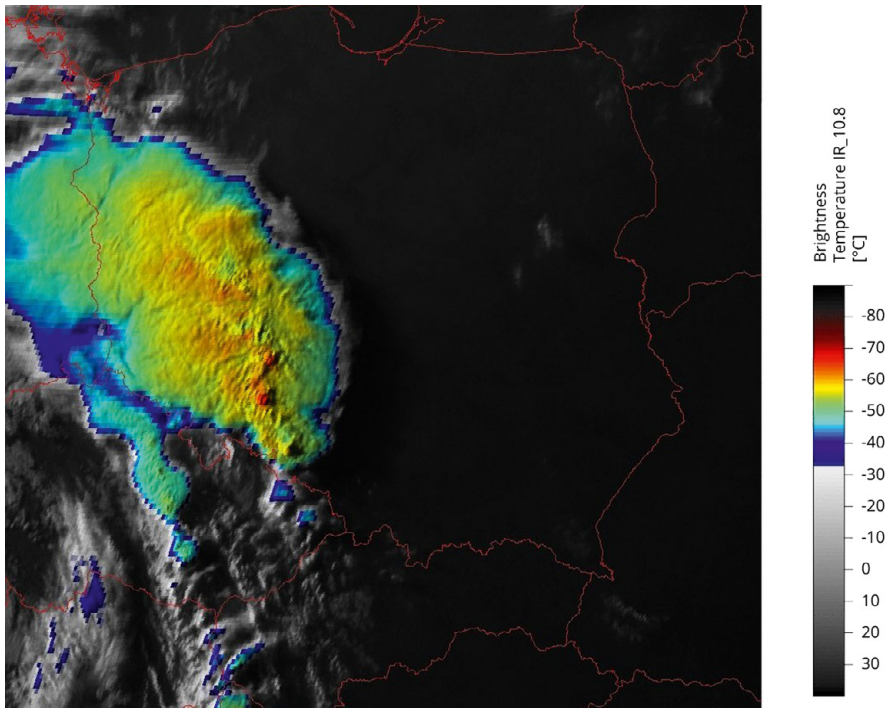
Fig. 3. METEOSAT SEVIRI Sandwich product, 11 August 2017, 17:00 UTC (EUMETSAT 2017).

in the lower and middle layers is an indicator of favorable conditions for convective activity (Murugavel et al. 2017). The parameters characterizing tropospheric moisture can be obtained with the NWC SAF Geo package for cloud free areas only.

3.2. STABILITY INDICES

Satellite data not only makes it possible to observe phenomena occurring in the atmosphere and on the land at any given moment. If used properly, they can also provide useful information for storm nowcasting.

A good example are the stability indices derived from METEOSAT satellite data for cloud free areas: K Index (KI), L Index (LI) and Showalter Index (SI).

The K Index (George's Index) is a measure of thunderstorm potential based on the vertical temperature lapse rate, and the amount and vertical extent of low-level moisture in the atmosphere. When less than 20°C, KI indicates no storm probability, if 20°C to 25°C – isolated storm cells only, 26°C to 30°C – widely scattered thunderstorms, 31°C to 35°C – scattered storms, and finally more than 35°C – numerous thunderstorms (George 1960). The K Index integrates measurements of vertical temperature

lapse rate, moisture content of the lower atmosphere, and vertical extent of the moist layer, and thus, may be useful for identifying convective and heavy-rain-producing environments. The K Index is a useful tool for diagnosing the potential for convection. However, it cannot be used to infer the severity of convection. Because it uses 850 hPa data, it is not applicable in mountainous regions, in which the surface pressure is less than 850 hPa.

The Lifted Index is another common measure of tropospheric instability. It is defined as the difference between the air temperature at a given level of the troposphere and the temperature of an air parcel raised from the Earth's surface (or the lower troposphere) up to the same level of the air mass. It is calculated using the following equation:

$$LI = T_{500} - T_{Ls} \tag{1}$$

Where T_{500} is the air temperature at 500 hPa and T_{Ls} is temperature of an air parcel lifted form the surface to the 500 hPa level. The LI presented in this paper was calculated assuming that the air parcel was lifted form the lowest layer of 100 hPa height. The more negative the LI values, the greater the possibility of strong convection. Thus, negative LI values indicate that the atmosphere is unstable, and convection may occur. The lower the LI values, the greater the chances of convection and the development of violent updrafts (Blanchard 1998).

The Showalter Index is another measure of thunderstorm potential and severity. It is given by:

$$SI = T_{500} - T_L \tag{2}$$

where T_L is the temperature (°C) of a parcel lifted from 850 to 500 hPa. As the SI decreases to zero and below, the likelihood of showers and thunderstorms is considered to increase (Showalter 1953). SI indicates mid-tropospheric instability, while LI usually indicates instability of the lower troposphere (depending on the level the virtual air parcel is lifted from). SI is especially useful when a shallow, cool layer of air below 850 hPa lies beneath air of greater convective potential (Showalter 1953). Threshold SI for thunderstorms vary, but showers and thunderstorms become more likely as the value of SI is less than −4°C (Huschke 1959). A Showalter Index greater than 0°C implies a generally stable atmosphere, with weak convection possible for SI equal to 1°-2°C, but only if strong air lifting is present. When SI is in the range of −3° to 0°C, the air is moderately unstable. If SI is between −4° and −6°C, the atmosphere is very unstable, and an SI less than −6°C means extreme instability, thus indicating a high probability of severe storms.

3.3. RAPIDLY DEVELOPING THUNDERSTORM – CONVECTION WARNING

The NWC SAF product developed for monitoring storms is Rapidly Developing Thunderstorm – Convection Warning (RDT-CW) (Moisselin, Autones 2020). RDT-CW is used for identification, monitoring, and tracking of intense convective clouds and detection of rapidly developing convective cells as well as forecasting (nowcasting) them. The object-oriented approach underlying the RDT-CW product allows one to add value to the satellite image by characterizing these convective entities through various parameters of interest to the forecaster such as motion vector, cooling and expansion rate, or cloud top height. These features make this particular product a valuable tool for both forecasters and research teams, or even aeronautical uses. RDT-CW was developed by Meteo-France in the framework of the EUMETSAT SAF in support of modern nowcasting, and uses mainly the geostationary satellite system.

4. THE STORM OF 11 AUGUST 2017 IN SATELLITE IMAGES AND PRODUCTS

Satellite data provide information about the state of the atmosphere and land over an area, limited only by orbit type and instrument technical design. The SEVIRI instrument aboard EUMETSAT METEOSAT satellite provides data from all of Europe with temporal resolution of 15 minutes for normal scanning mode and 5 minutes for rapid scan mode (RSS). These features make METEOSAT/SEVIRI data and products extremely useful either for detection of potentially dangerous meteorological phenomena before they reach the area of interest, or for defining the regions with conditions favorable for developing severe convective storms.

On 11 August 2017, rapid development of a convective system was observed. In the afternoon, the system started to grow in Czech territory and began to move over the southeastern part of Poland. A few hours later, the convective cells transformed into a mature system covering a vast area of the country. Late in the evening the convective system started to shift towards the north. All these phases were clearly seen on the satellite data and products. The lifecycle of this MCS is presented below using METEOSAT/SEVIRI satellite data and products.

In the morning hours of 11 August, 2017, stability indicators derived from satellite data over the cloud free area indicated the presence of a convection-favorable environment over Poland (Fig. 4). In each image, shades of brown mark the regions with stable atmosphere, while blue, green, and red indicate the presence of unstable conditions. One can easily notice the areas of unstable atmosphere over southeastern and eastern Poland at 09:00 UTC. The KI values in these regions were in the range of 28-34°C, while LI and SI were negative. Unstable conditions were also noted over central Poland, with KI and LI values of 28-34°C and <0°C, respectively (Fig. 4a). The western part of Poland is covered by clouds, so it is not possible to retrieve stability indices but adjacent to the cloud cover KI and LI indicated unstable air.

Moreover, high values of satellite-derived precipitable water content in the boundary and medium tropospheric layers were found over almost the entire cloud-free region of Poland (Fig. 5a-b). The highest values of the precipitable water content in the boundary layer were found over northern and northeastern Poland, (Fig. 5a), i.e. in the regions with unstable atmosphere (Fig. 4a-c), indicating convection-favorable conditions over these areas of Poland. Unfortunately, cloudiness precluded clear analysis in this region.

At same time, a few scattered clouds with reasonably cold tops (T_B around −50°C) were observed over Germany and western Poland (Fig. 6).

At 12:00 UTC, two convective systems can be seen on the Sandwich image (Fig. 7): the weaker one over western Poland and the more active one over the Czech Republic (Fig. 8).

At the same time, the growing instability was observed over cloud-free regions of Poland. The KI and LI values, respectively in the range of 28-40°C and −4 to −8°C , indicated unstable atmosphere over all of cloud-free Poland (Fig. 9a-b), while SI was negative over southern Poland, except for the eastern part of Podkarpackie voivodeship (Fig. 9c). It should be pointed out that the most unstable conditions were found over the southeastern part of cloud-free Poland with KI of 40°C, LI of −8°C and SI of −7°C (Fig. 9a-c). Such values of these indices, along with high values of total precipitable water content (around 40 mm, Fig. 8) indicated high probability of severe storms in these regions. As will be shown, no convective system developed there, demonstrating that satellite products can be used to recognize regions with the necessary conditions (precipitable water content, stability indices), which, however, may not be sufficient to induce convection.

A)

B)

43

C)
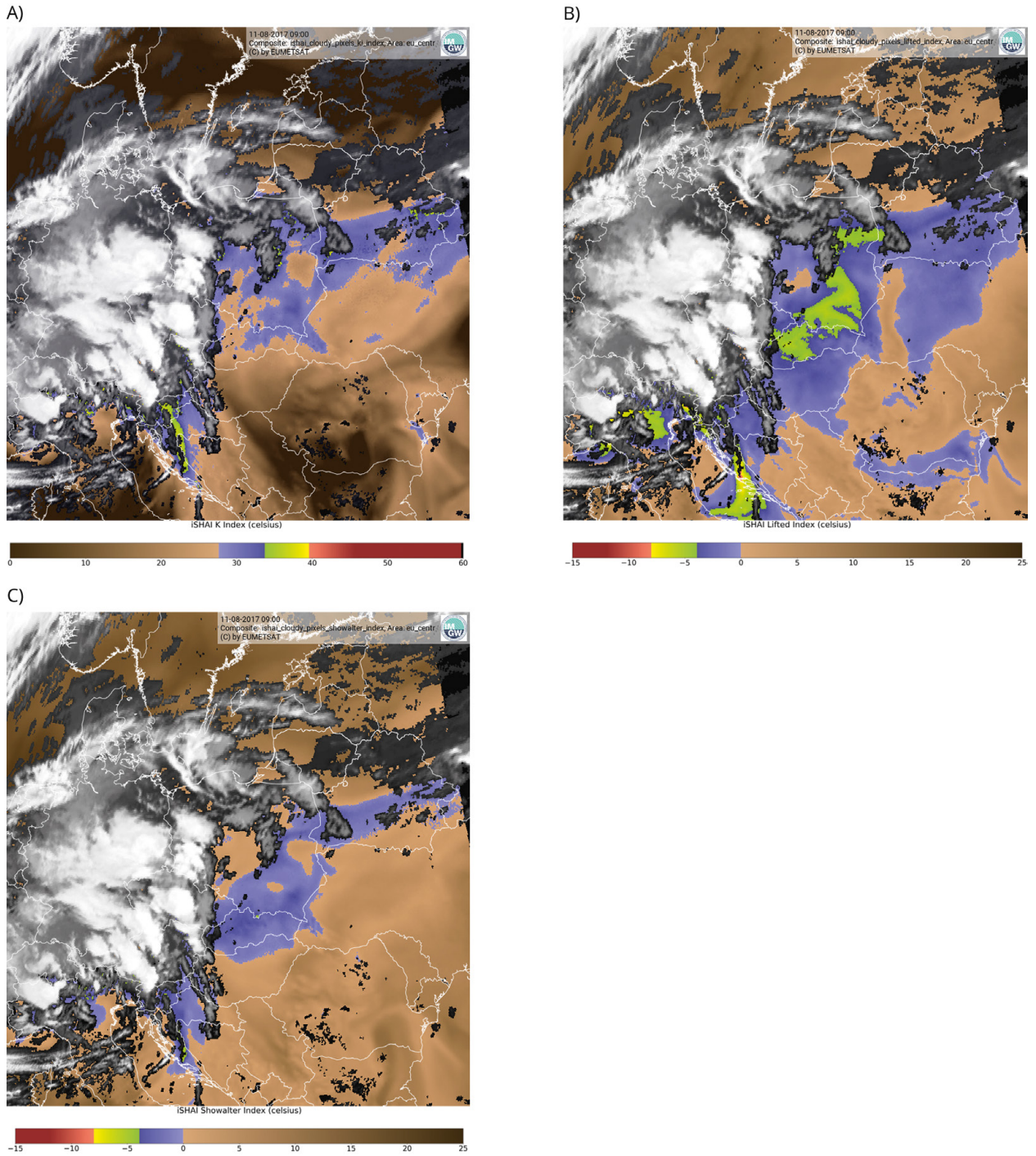
Fig. 4. Stability indices derived from METEOSAT/SEVIRI satellite data for cloud free areas with the EUMETSAT NWC SAF Geo package, 11 August 2017, 09:00 UTC: a) KI, b) LI and c) SI.

A)

B)
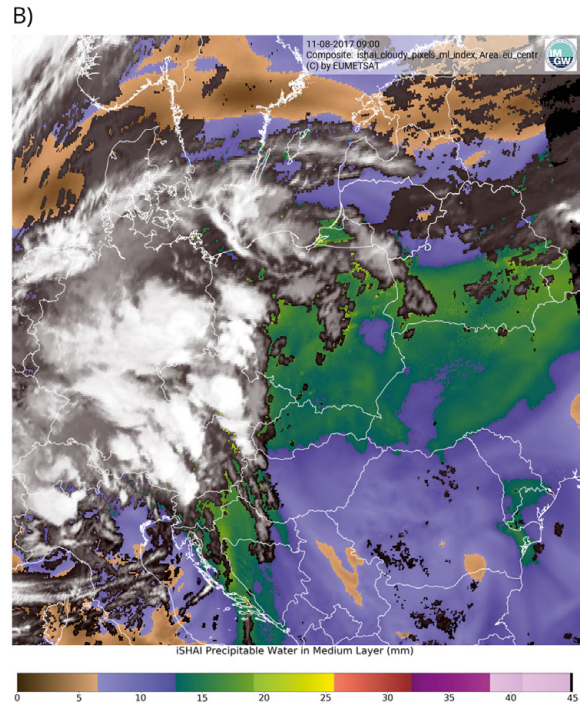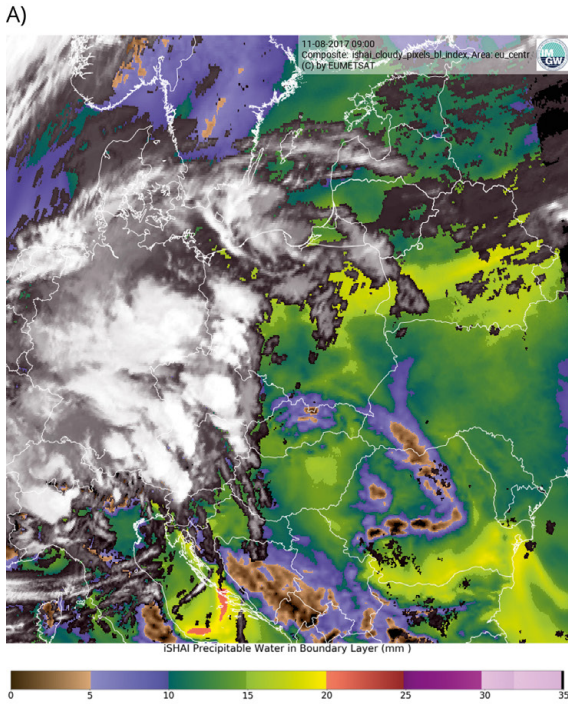
Fig. 5. Precipitable water content in a) the boundary and b) medium tropospheric layers derived from METEOSAT/SEVIRI satellite data for cloud free areas with the EUMETSAT NWC SAF Geo package, 11 August 2017, 09:00 UTC.
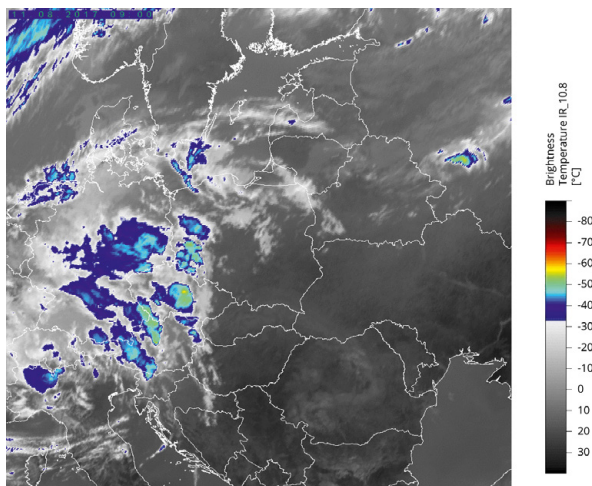
Fig. 6. METEOSAT/SEVIRI color-enhanced IR brightness temperature image, 11th of August 2017, 09:00 UTC.
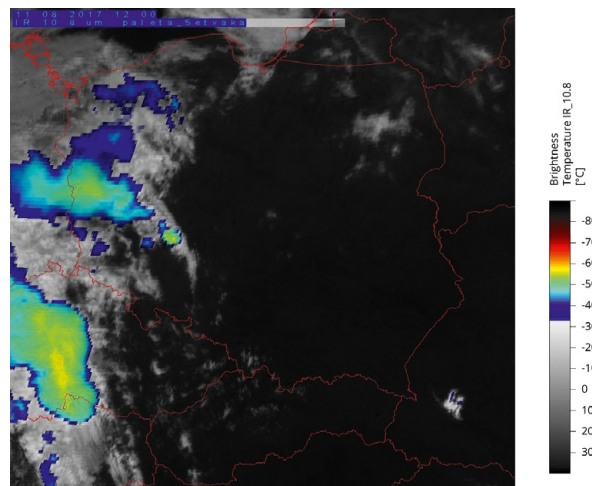
Fig. 7. METEOSAT/SEVIRI Sandwich image 11th of August 2017, 12:00 UTC.
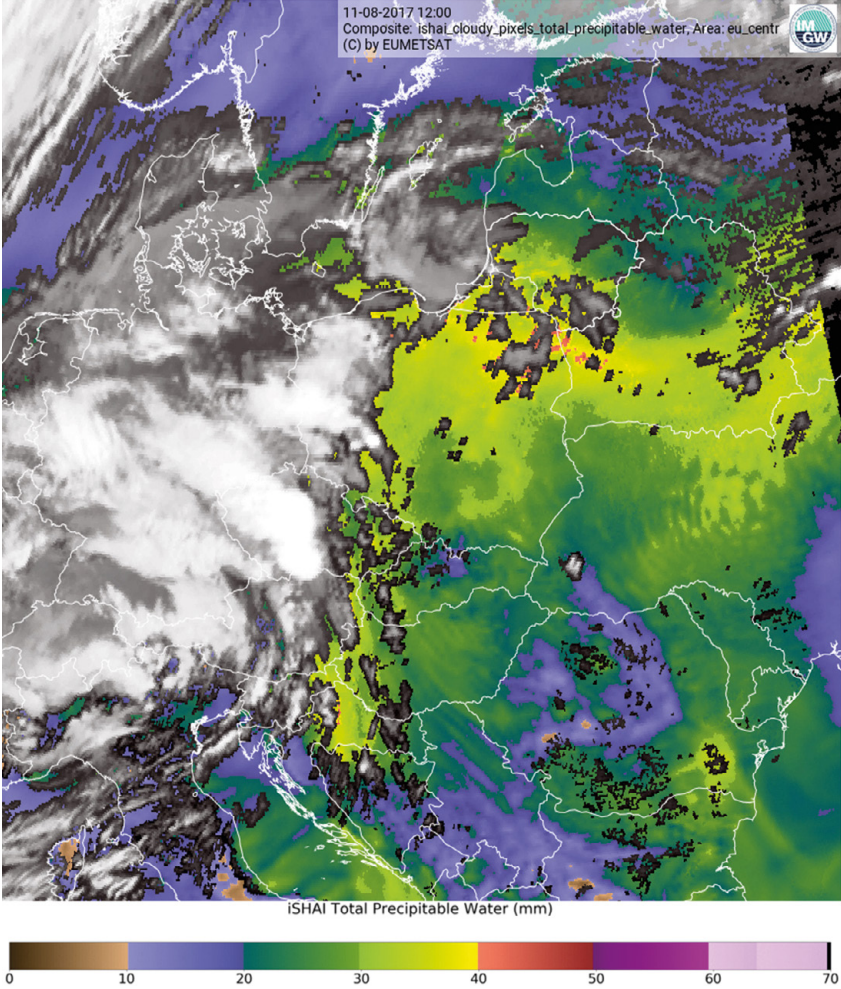
Fig. 8. Total precipitable water content derived from METEOSAT/SEVIRI satellite data with the EUMETSAT NWC SAF Geo package, 11 August 2017, 12:00 UTC.

45

A)

B)

46

C)
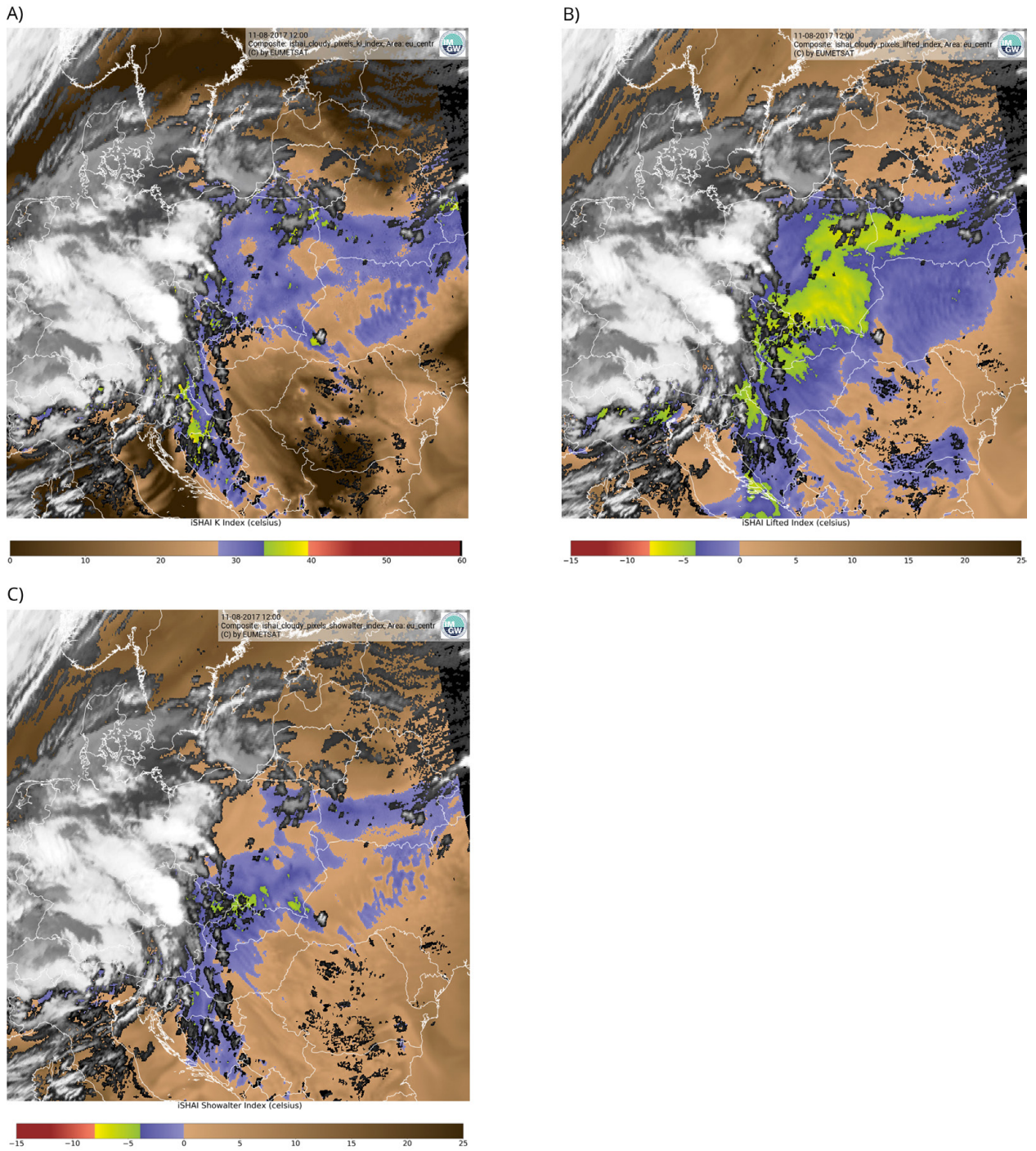
Fig. 9. Stability indices: a) KI, b) LI and c) SI derived from METEOSAT/SEVIRI satellite data with the EUMETSAT NWC SAF Geo package, 11 August 2017, 12:00 UTC.
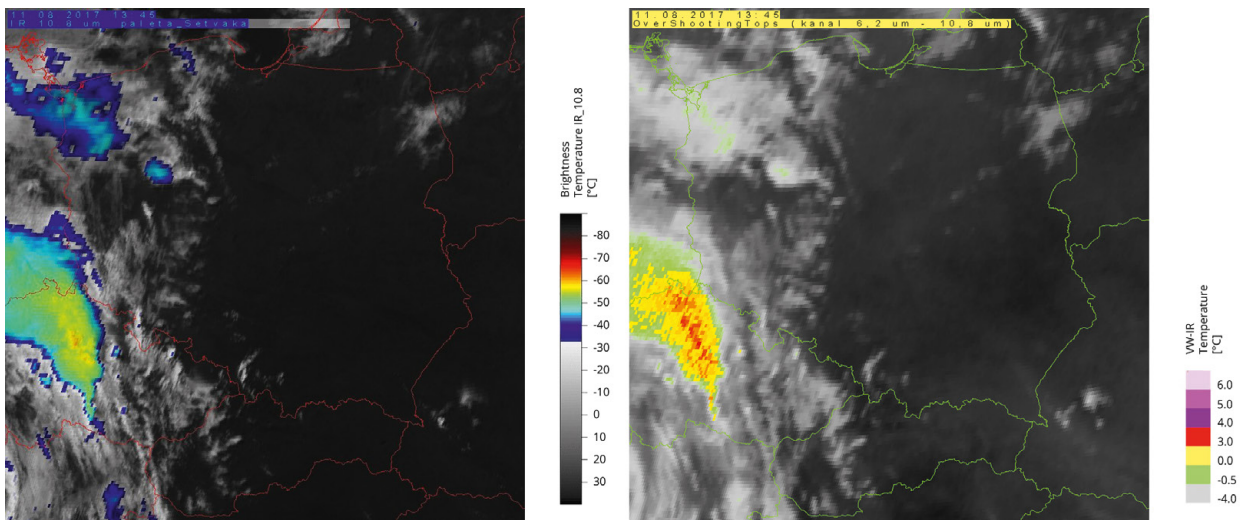
Fig. 10. METEOSAT/SEVIRI Sandwich image (a) and BTD image (b), 11 August 2017, 13:45 UTC.
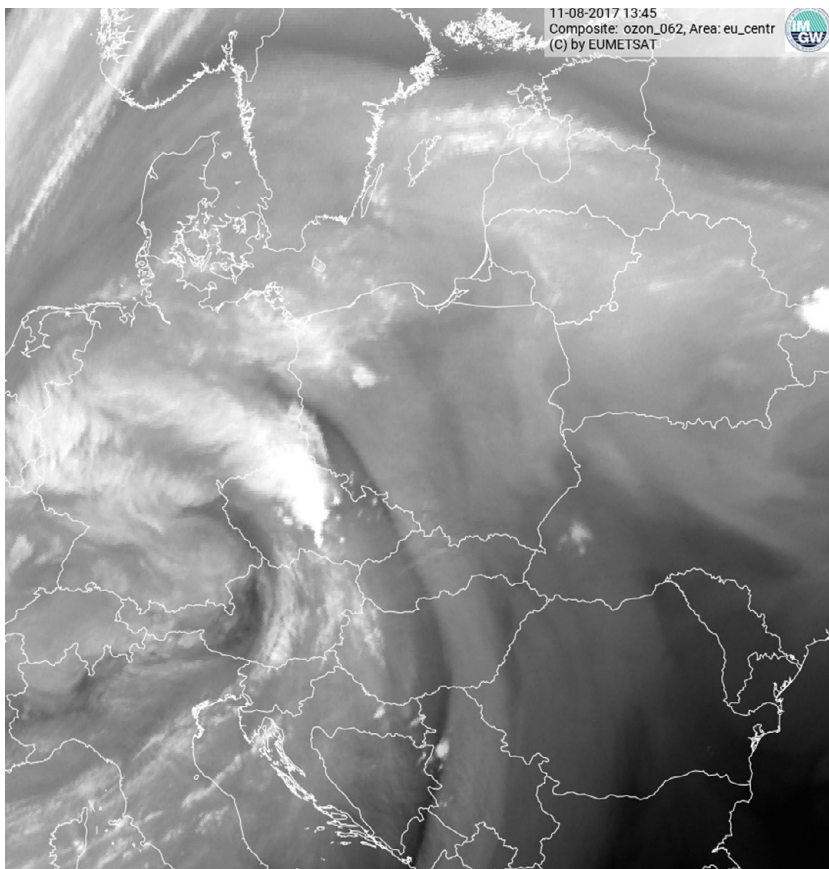
Fig. 11. METEOSAT/SEVIRI WV 6.2 µm channel image, 11 August 2017, 13:45 UTC. Moist air is indicated with light grey, and dry air with black. Highly developed cloudiness is white.

47
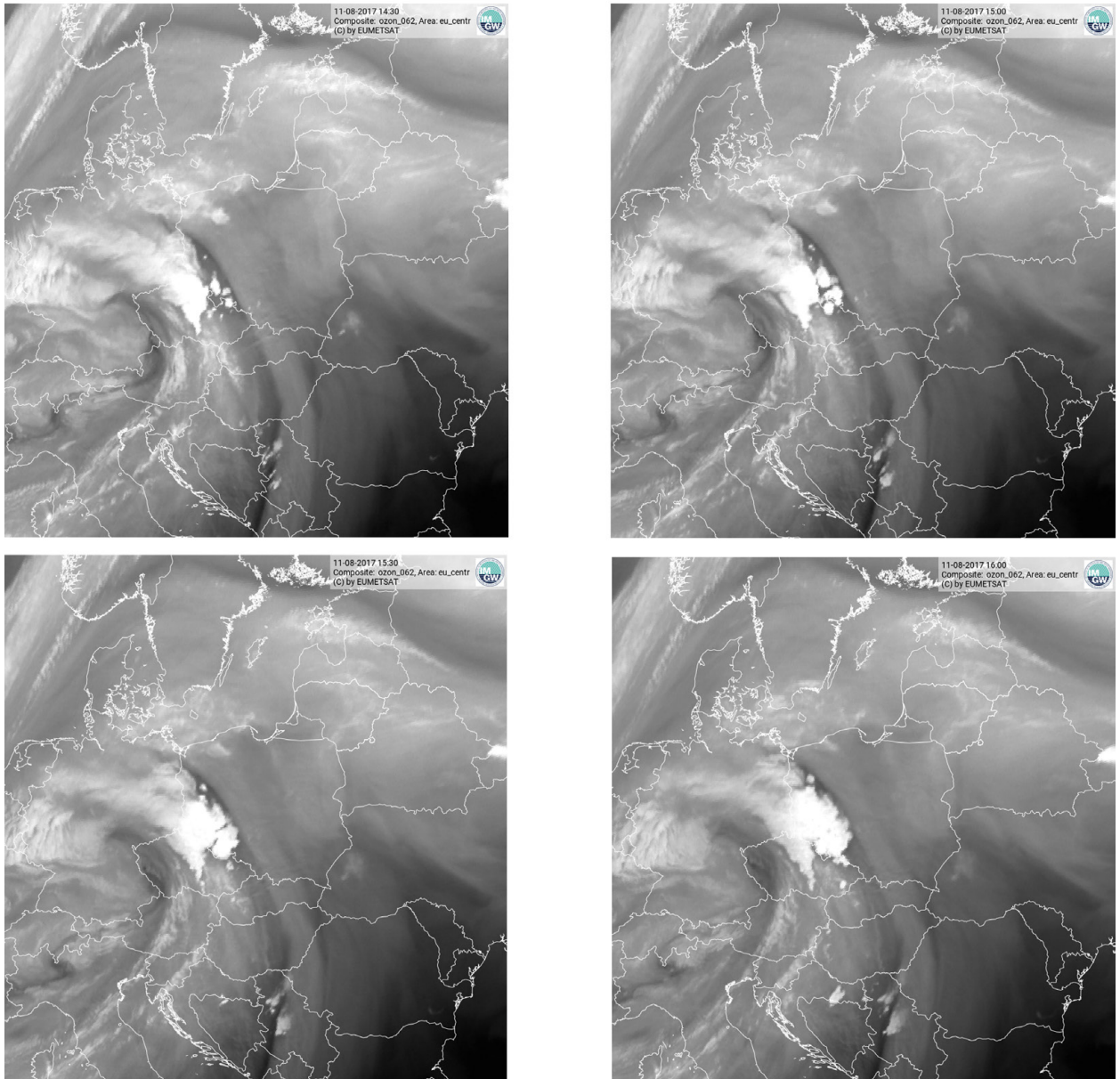
Fig. 12. METEOSAT/SEVIRI WV 6.2 μm channel images showing the convection intensification at 11 August 2017 early afternoon: 14:30 UTC (upper left) 15:00 UTC (upper right), 15:30 UTC (lower left) and 16:00 UTC (lower right).
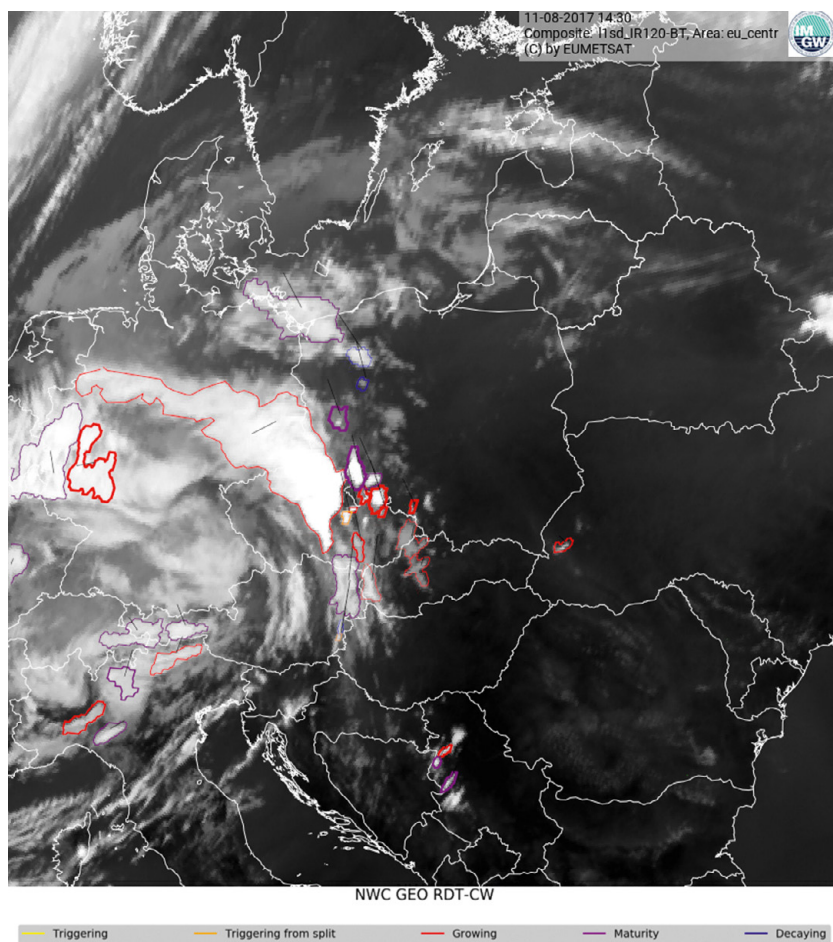
Fig. 13. RDT product derived from METEOSAT/SEVIRI satellite data with the EUMETSAT NWC SAF Geo package, 11 August 2017, 14:30 UTC. The color of the contour marks the convection phases: yellow = triggering, orange = triggering from split, red = growing, purple = maturity and blue = decaying.
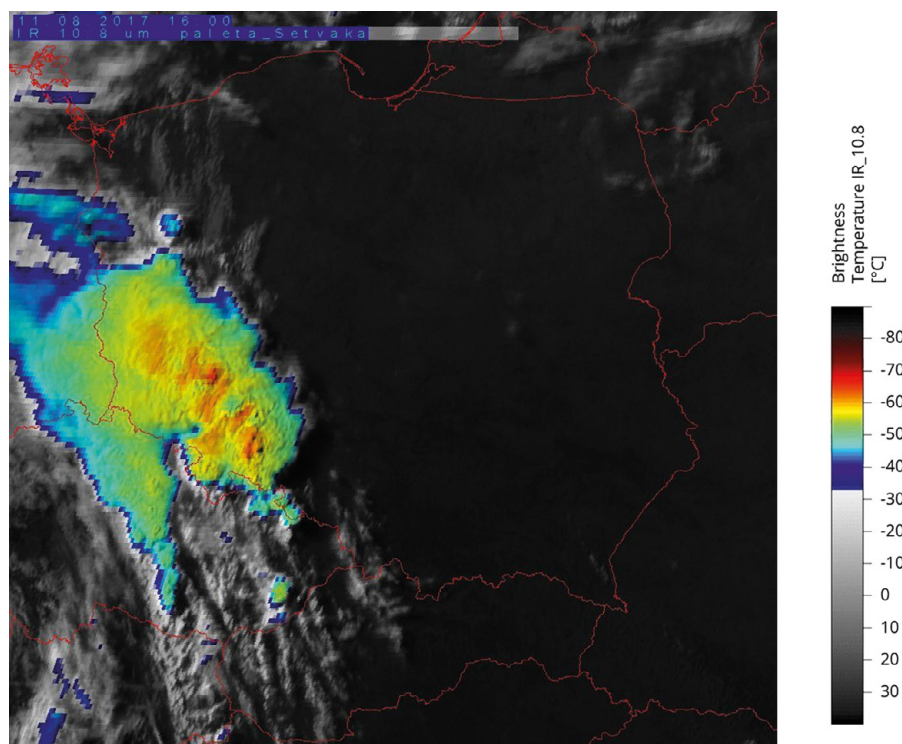
Fig. 14. METEOSAT/SEVIRI Sandwich image, 11 August 2017, 16:00 UTC.
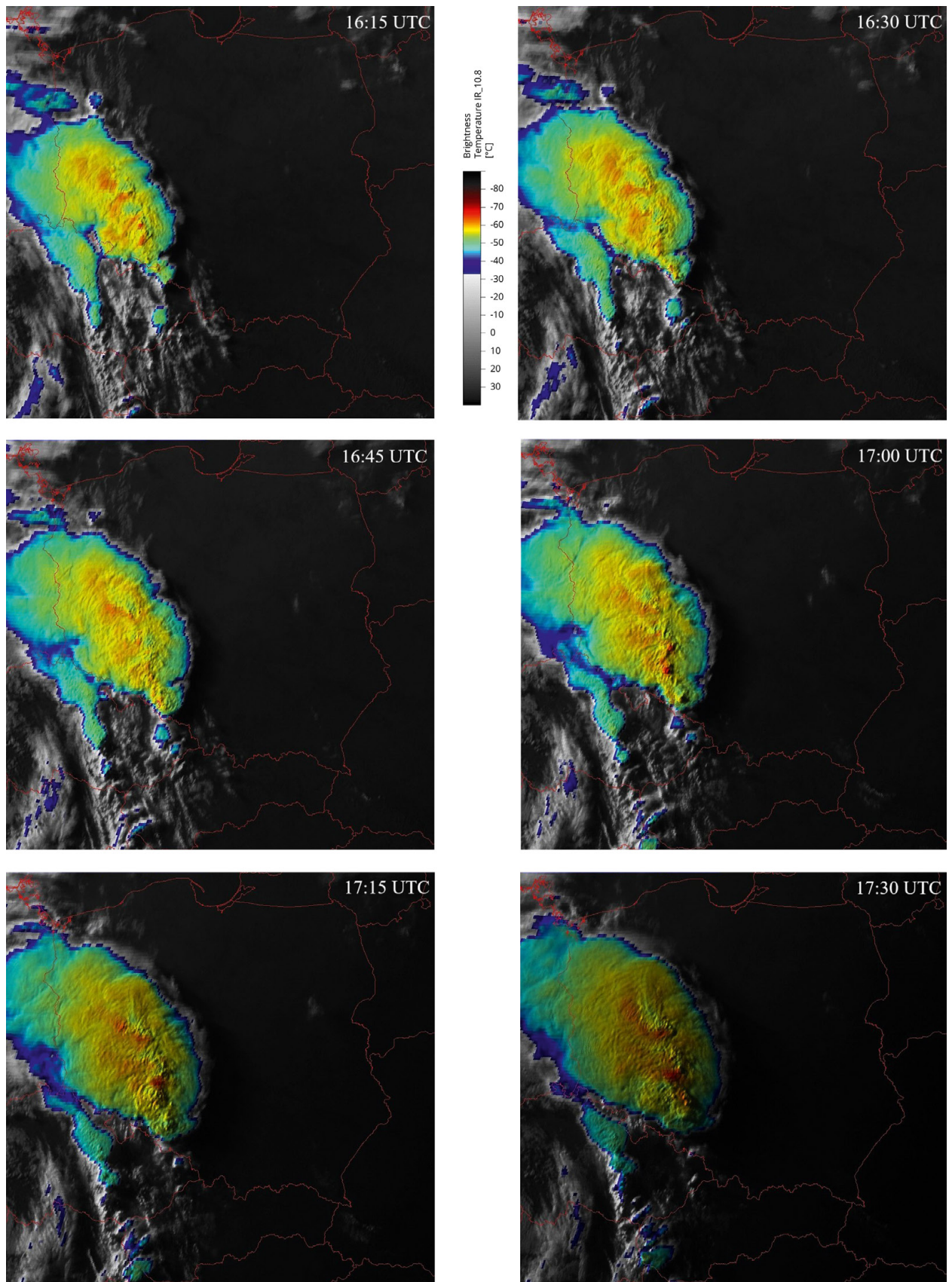
Fig. 15. Time series of METEOSAT/SEVIRI Sandwich images from 16:15 UTC to 17:30 UTC, 11 August 2017.
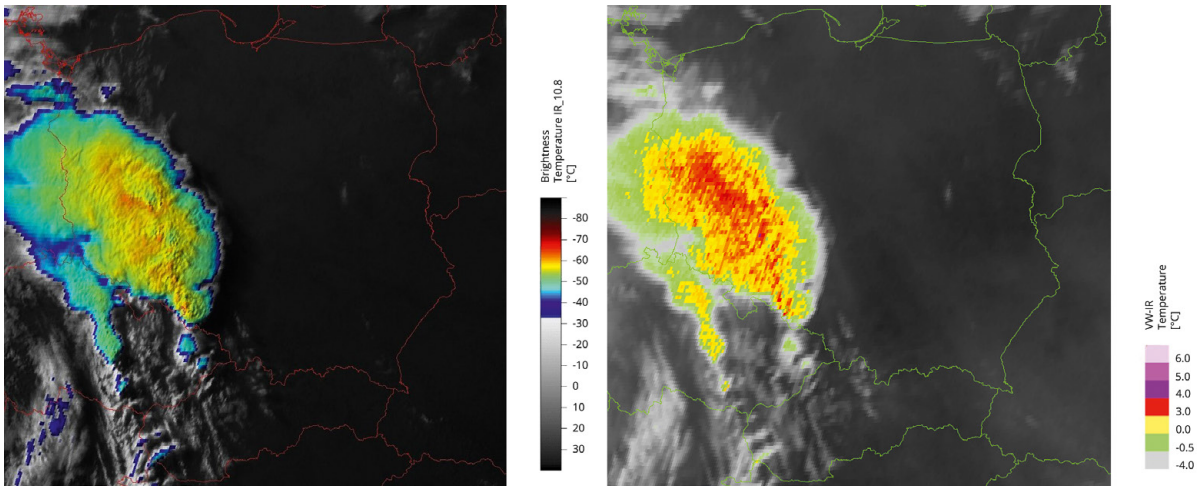
Fig. 16. METEOSAT/SEVIRI Sandwich product (a), and BTD product (b), 11 August 2017, 16:45 UTC.
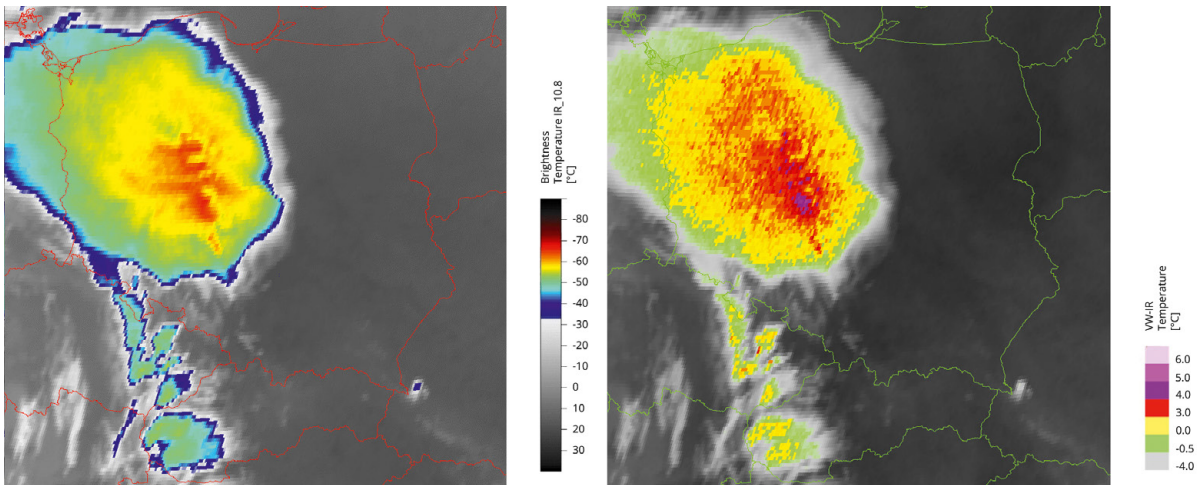
Fig. 17. METEOSAT/SEVIRI color-enhanced IR brightness temperature image (a) and BTD image (b), 11 August 2017, 18:45 UTC.

51
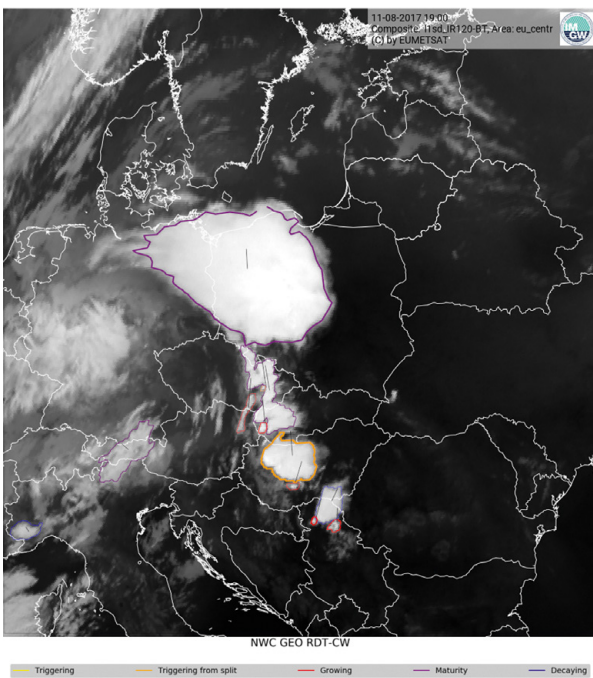
Fig. 18. RDT product derived from METEOSAT/SEVIRI satellite data with the EUMETSAT NWC SAF Geo package, 11 August 2017, 19:00. The color of the contour marks the convection phases: yellow = triggering, orange = triggering from split, red = growing, purple = maturity and blue = decaying.
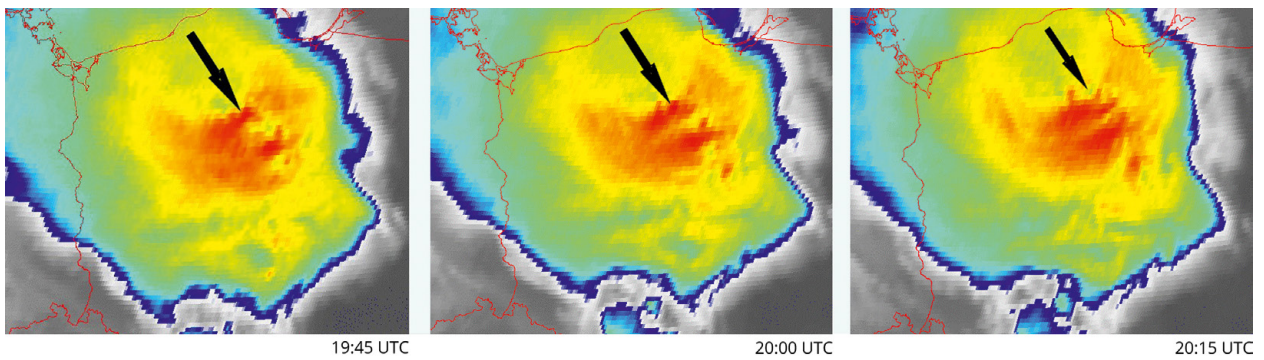
Fig. 19. METEOSAT/SEVIRI color-enhanced IR Brightness Temperature images, 11 August 2017.
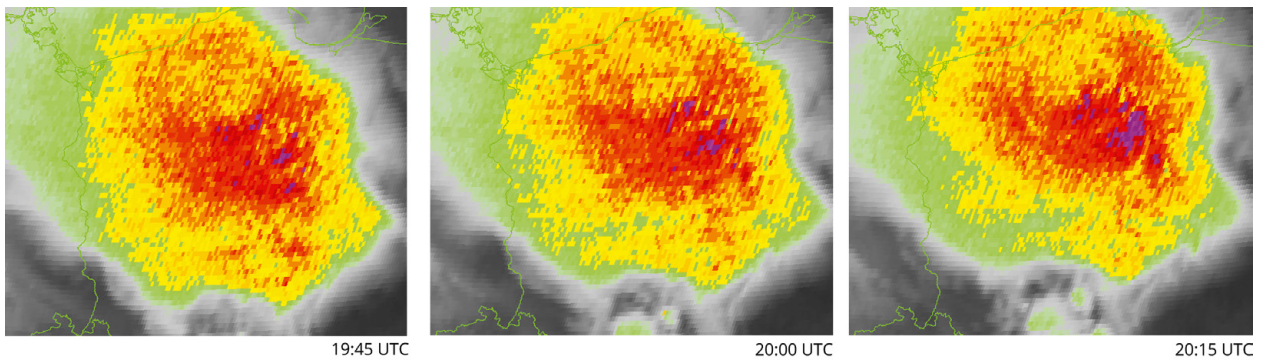
Fig. 20. METEOSAT/SEVIRI BDT images, 11 August 2017.
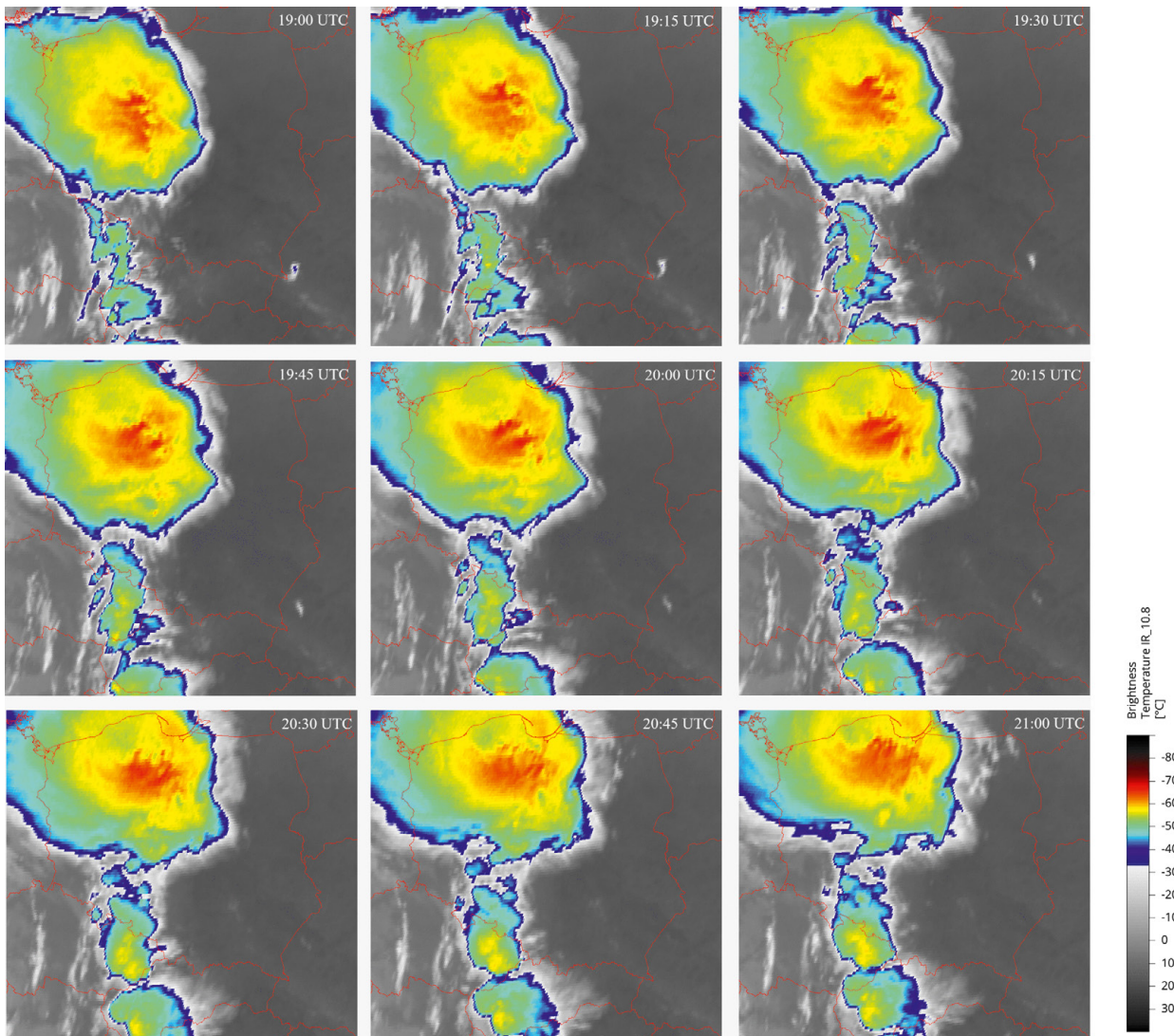
Fig. 21. Time series of METEOSAT/SEVIRI color-enhanced IR brightness temperature images from 19:00 UTC to 21:00 UTC, 11 August 2017.
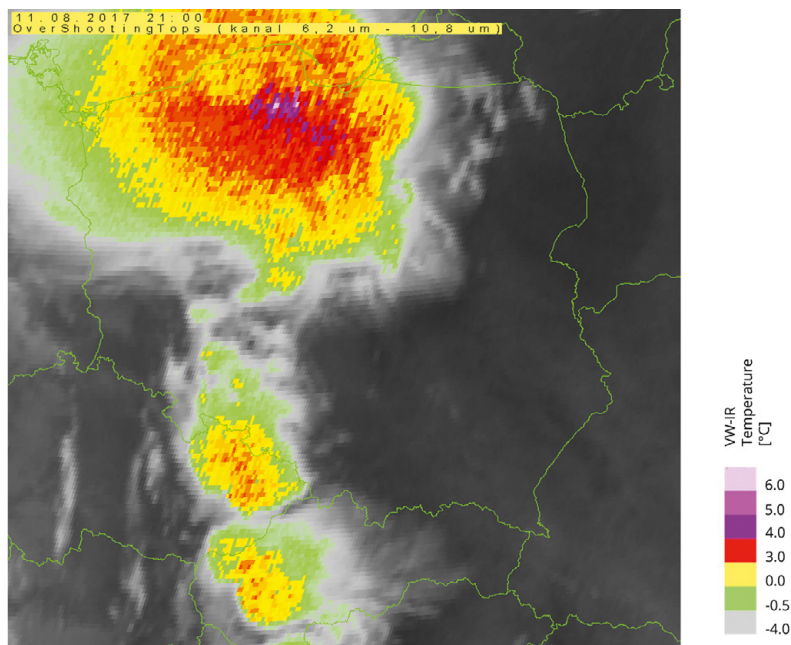
Fig. 22. METEOSAT/SEVIRI BTD image, 11 August 2017, 21:00 UTC.

53
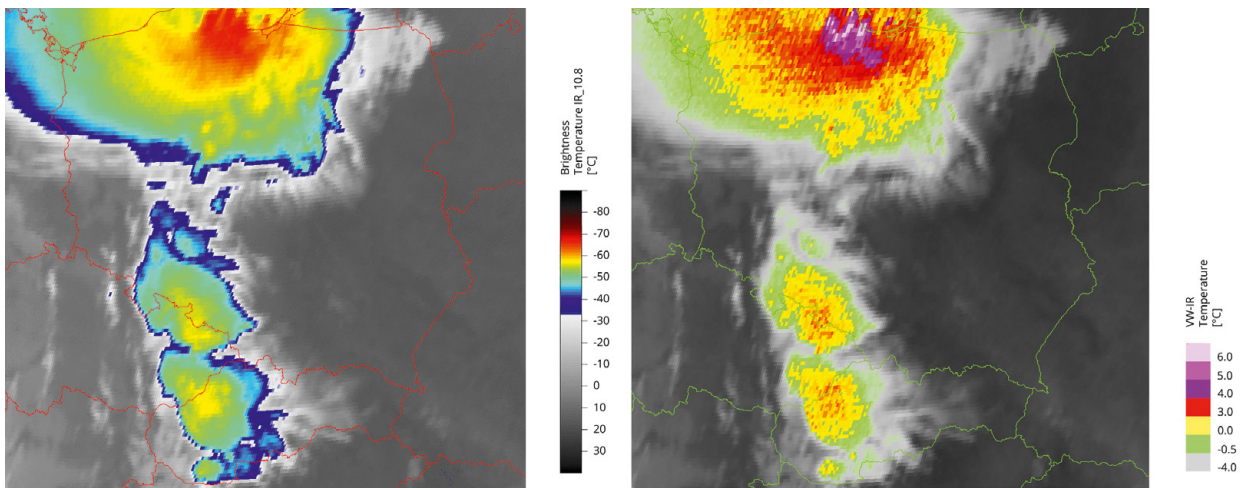
Fig. 23. METEOSAT/SEVIRI color-enhanced IR brightness temperature image (a) and BTD image (b), 11 August 2017, 21:30 UTC.
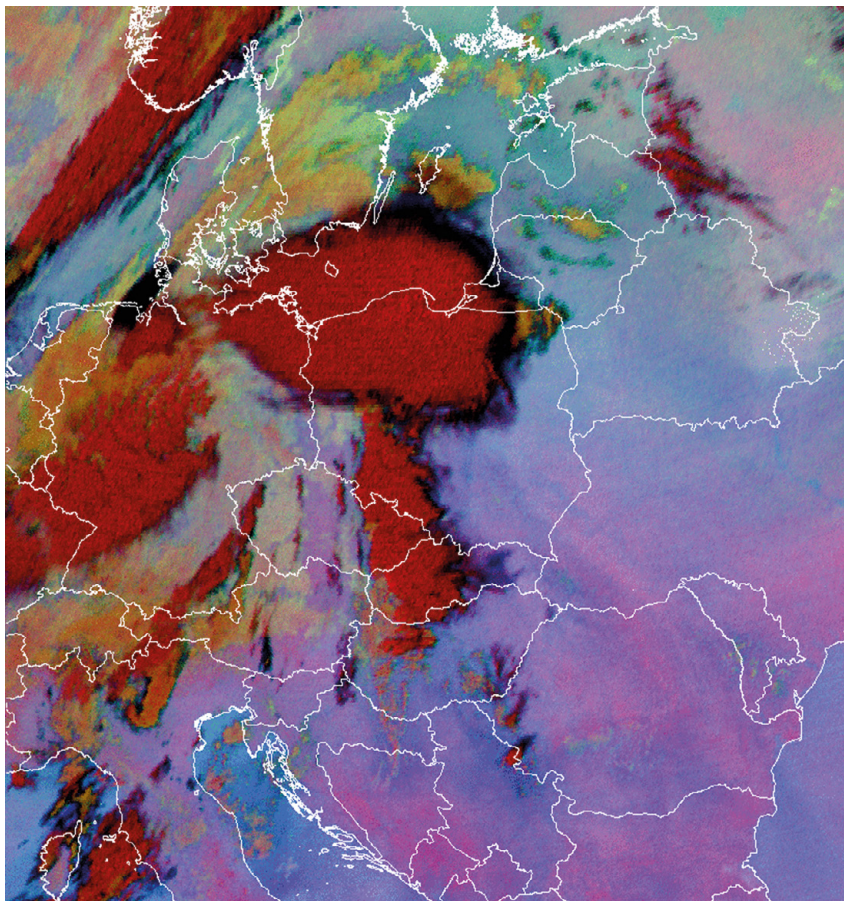
Fig. 24. METEOSAT/SEVIRI RGB Microphysics 24h image, 11 August 2017, 21:30 UTC.
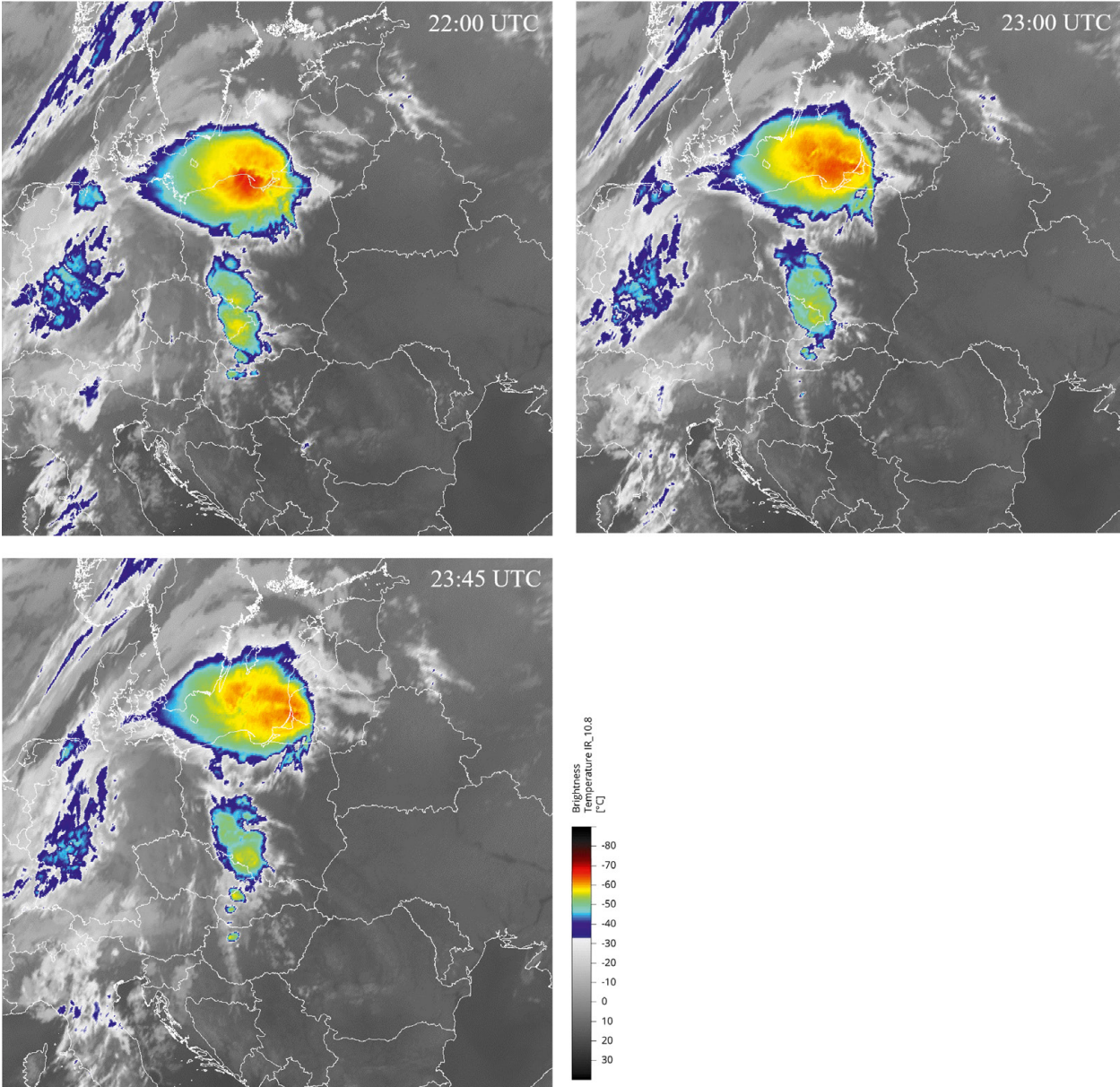
Fig. 25. METEOSAT/SEVIRI color-enhanced IR brightness temperature images at 22:00 UTC, 23:00 UTC and 23:45 UTC
on the 11 August 2017 (EUMETSAT 2017).
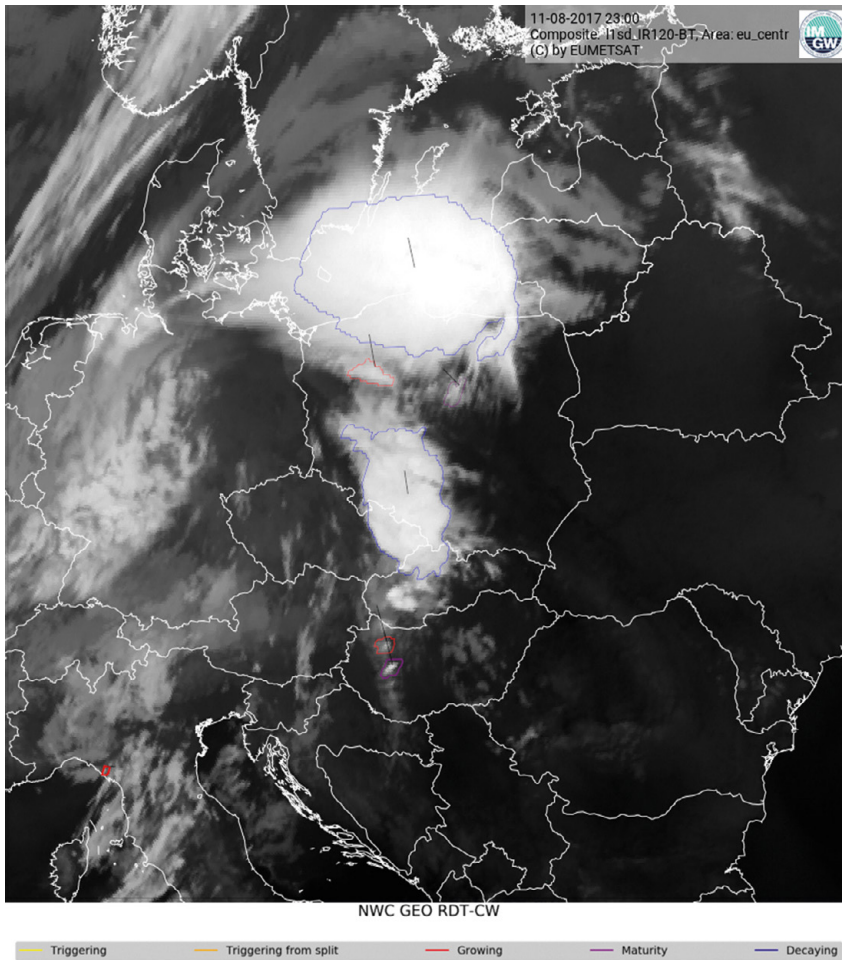
Fig. 26. RDT product derived from METEOSAT/SEVIRI satellite data with the EUMETSAT NWC SAF Geo package, 11 August 2017, 23:00 UTC. The color of the contour lines marks the convection phases The color of the contour marks the convection phases: yellow = triggering, orange = triggering from split, red = growing, purple = maturity and blue = decaying.

At 13:45 UTC, the convective system from the Czech Republic reached the southwest border of Poland. The convective system over Poland, seen in Figure 6, has moved north, and its intensity, as deduced from the Sandwich and BTD images that hour, weakened: the cloud top temperature warmed, and BDT values decreased. (Fig. 10a-b). However, the main, most powerful storm cell (from the Czech area) was yet to arrive over this area.

Useful information about the atmospheric state can be also brought by the water vapor images. As mentioned in Chapter 2, the 6.2 μm images represent the water vapor concentration in the upper tropospheric column. The more water vapor, the less radiation is measured by the satellite instrument so that the area with the moist air in the upper troposphere appears colder (marked with light shades of grey) on the 6.2 μm images than the area with dry air. These light areas on the images are associated with mid- to upper-tropospheric ascent, and dark areas with descent (Georgiev, Kozinarova 2009; Georgiev et al. 2016). Therefore, synoptic-scale boundaries between light and dark regions are related to significant upper-level flow features, one of which is the jet stream characterized by a strong dark/light gradient on the 6.2 μm image, with dry air on the polar side (Georgiev, Kozinarova 2009; Georgiev et al. 2016). At the 13:45 UTC, the 6.2 μm image showed several jet streams, among them the one running from southern Italy through Slovenia, Hungary, Slovakia, the Czech Republic, and ending in southwestern Poland (Fig. 11). The presence of convection in the left exit area of the jet stream (the area on the border of Poland, Czech Republic, and Germany) should be also pointed out here (Fig. 11).

At early afternoon (14:30 UTC), this jet stream was crossing the foot of the Sudety Mountains and new convection cells were formed over this area. In the following hours, these new convection cells continued to develop (Fig. 12). Moreover, the convection system from above the Czech Republic was recognized as developing convection, which can easily be seen on Figure 13, representing the Rapid Developing Thunderstorms product.

In the images from 15:30 UTC and 16:00 UTC (Fig. 11), the merging of the convective system with the newly developed convective cells into one larger entity can be observed over southwestern Poland.

From the images in Figure 15, it can be seen that the cold ring varied in shape and size during the time period but the fact that it was present all the time indicates that monitored convective system was very active. The central warm spots were created downwind from the overshooting, which can be evaluated by comparing the location of the warm spots in the Sandwich product (Fig. 16, 16:45 UTC). The largest values of the WV-IR brightness temperature difference (BTD) were on the order of 4. As indicated by Setvak et al. (2007) and da Silva Neto et al. (2016), values of this difference of the order of 4-6°C are extremely rare over central Europe and they are good indicators of overshooting above the coldest cloud tops.

The presence and especially the duration of a cold ring in the 11 August 2017 convective system indicated the possible severity of the system and hence the possibility of dangerous weather phenomena, such as heavy rainfall, gusts of wind, or hail.

At and after 18:45 UTC, satellite data indicated further development of the convective system, where BTD values of 4-5°C (Fig. 16b) might indicate the presence of strong updrafts. The presence of a cold ring should be pointed out as well (Fig. 17a).

According to the RDT product, the convective system reached maturity at 19:00 UTC (Fig. 18). It remained active, with the presence of a cold U shape (indicated by the blue arrow on Fig. 19) and smaller cold rings, resulting in overshooting tops during the next hour, which can be deduced from BDT images (Fig. 20).

The strongest wind gust occurred after 20:30 UTC over the area marked with the blue arrow on Figure 19. Of course, SEVIRI satellite data do not support wind gust recognition, but its presence is well documented in Wrona et al. (2022).

As most of the damages caused by the convective system occurred between 19:00 UTC and 21:00 UTC, the sequence of color-enhanced *IR* images is presented in Figure 21, showing the evolution of the system in its mature and most dangerous phase.

The cold ring is present in the images from 19:00 UTC and 19:15 UTC, after which it transformed into a cold-U shape with a large area of overshooting tops in its southern and southeastern parts. These features can be seen in the satellite images from 19:30 UTC to 20:00 UTC (Fig. 21). The transformation from cold-U shape into a cold ring structure again seemed to begin around 20:30 UTC, however, the temperature distribution along the ring was not homogenous and a distinctive minimum can be seen in its northwestern part. This complicated structure should be considered as the results of the interaction between single overshooting tops located close to each other. Actually, one could conclude that the ring is composed of two parts: the warmer one in the north and the colder one in the south, with small structures in the western part. These structures, marked with violet color, are also clearly seen on the BDT imagery from 21:00 UTC (Fig. 22). The mechanisms that caused the changes in the cold shapes at the convective system top cannot be recognized on the basis of the satellite images only, but require comprehensive analysis with other data, such as radar and NWP.

At 21:30 UTC, a strong updraft, manifested in low BT (Fig. 23a) and high positive BTD values (Fig. 23b) was still visible over a large area, as well as the two-part cold ring (Fig. 23a). As previously, the coldest parts of the ring match the highest BTD values. Unfortunately, the BTD product is generated for the Polish domain only, therefore, the BTD values were not available for the whole cold ring structure as the convective system moved towards Scandinavia.

The other product that can be used to monitor the storm is the RGB Microphysics 24H (24-hour). On this product, light blue and light purple areas indicate cloudless areas, while dark red colors correspond to optically thick clouds with ice crystals in their upper layer (so-called ice phase). They might be strongly developed anvils and/or storm pyrocumulonimbus. Black and navy-blue indicate thin cirrus, like the edge of an anvil. Such fragments of extensive storm clouds propagate mainly in front of the storm cell itself, thus giving us valuable information about its movement and area.

The RGB Microphysics 24 h at 21:30 UTS is shown in Figure 24. The convection system (dark red) covering the area of about 1/3 of Poland, with the anvil in black are easily seen. The black part (appearing as a contour), indicating thin cirrus clouds, extends for about 100 km north, east, and south. This indicates the presence of strong updraft in this mesoscale convection system.

During the next few hours, the mesoscale convection system headed to the northeast, leaving Poland about midnight (Fig. 25). The RDT product from 23:00 UTC (Fig. 26) shows the storm decay.

5. SUMMARY

This paper shows how satellite data and products can help in nowcasting by detecting and monitoring convective phenomena. Chapter 4 presents the series of satellite images and products showing the storm system developing beyond and over Poland. Taking into account the presently available satellite products allowed us to make this analysis useful for present satellite data users.

The satellite data and products were used to analyze the pre-convective environment in the cloud-free areas over Poland in the morning and noon

of 11 August 2017. Both the atmospheric stability indices and precipitable water contents indicated southeastern and northeastern Poland as the regions where convection could develop. However, the convective systems, including MCS, developed over western Poland. This region was covered by clouds in the morning that day so there were no stability nor humidity products derived from satellite data available for analysis. On the other hand, this example shows that satellite products describing a pre-convective environment can be used to recognize the regions with necessary conditions (precipitable water content, stability indices), which may not be sufficient to induce convection.

In the cloudy area of western Poland, the satellite images and products were used to detect and monitor the convective clouds in order to detect the rapidly developing storm. It has been shown that features indicating strong convective development, like cold rings or cold U/V shapes, can be visible on the single channel satellite images, only enhanced by a color palette, without referring to specific convective products. Moreover, satellite data can be used to detect and monitor potentially dangerous weather phenomena, like severe convective systems, before they cross the Polish borders – an added value of satellite data compared to other data sources like radars or ground stations.

A broader and simultaneous look at all the images and products mentioned in Chapter 4 can allow meteorologists to detect and monitor potentially dangerous convection clouds or a system forming over a given area. So, it is worth comparing or even superimposing multiple satellite maps (products) in real time to differentiate among them. In this case, the possible redundancy of the information is much less dangerous than the exclusion of given products from the overall analysis. On the other hand, parameters such as wind shear or wind gust cannot be retrieved from satellite data. Similarly, it is not possible to retrieve any information about the meteorological conditions under the clouds. So the satellite data should be analyzed together with data from other sources, such as radars, ground stations, and NWP. However, the satellite images and products can be used to detect the rapidly developing convective clouds that should be monitored for purposes of nowcasting and warning.

ACKNOWLEDGMENTS

REFERENCES

- Blanchard D.O., 1998, Assessing the vertical distribution of Convective Available Potential Energy, Weather and Forecasting, 13 (3), 870-877, DOI: 10.1175/1520-0434(1998)013<0870:AT-VDOC>2.0.CO;2.

- Bedka K.M., Brunner J., Dworak R., Feltz W., Otkin J., Greenwald T., 2010, Objective satellite-based overshooting top detection using infrared window channel brightness temperature gradients, Journal of Applied Meteorology and Climatology, 49 (2), 181-202, DOI: 10.1175/2009JAMC2286.1.

- da Silva Neto C.P., Barbosa H.A., Beneti C.A.A., 2016, A method for convective storm detection using satellite data, Atmosfera, 29 (4), 343-358, DOI: 10.20937/ATM.2016.29.04.05.

- Dziennik Bałtycki, 2018, Nawalnica 2017na Pomorzu. Pierwsza rocznica tragicznej nawalnicy na Pomorzu 11-12.08.2017. Zginęło pięć osób., available online https://dziennikbaltycki.pl/nawal-nica-2017-na-pomorzu-pierwsza-rocznica-tragicznej-nawalnicy-na-pomorzu-1112082017-zgi-nelo-piec-osob-wideozdjecia/ar/13385348 (data access 06.12.2021).

- George J.J., 1960, Weather Forecasting for Aeronautics, Academic Press, 673 pp.

- Georgiev C., Santurette P., Maynard K., 2016, Weather Analysis and Forecasting. Applying Satellite Water Vapour Imagery and Potential Vorticity Analysis, Academic Press, 360 pp.

- Georgiev C.G., Kozinarova G., 2009, Usefulness of satellite water vapour imagery in forecasting strong convection: A flash-flood case study, Atmospheric Research, 93 (1), 295-303, DOI: 10.1016/j.atmosres.2008.09.036.

- Heymsfield G.M., Blackmer Jr. R.H., 1988, Satellite-observed characteristics of Mid-west severe thunderstorm anvils, Monthly Weather Review, 116 (11), 2200-2224, DOI: 10.1175/1520-0493(1988)116<2200:SOCOMS>2.0.CO;2.

- Heymsfield G.M., Fulton R., Spinhirne J.D., 1991, Aircraft over flight measurements of Midwest severe storms: Implications on geosynchronous satellite interpretations, Monthly Weather Review, 119 (2), 436-456, DOI: 10.1175/1520-0493(1991)119<0436:AOMOMS>2.0.CO;2.

- Huschke R.E. (ed.), 1959, Glossary of Meteorology, American Meteorological Society, 638 pp.

- Moisselin J.-M., Autones F., 2020, RDT-CW: Toward a Multidimensional Description of Convection, Météo-France, DPREVI/PI, available online https://www.eumetsat.int/media/15711 (data access 06.12.2021).

- Murugavel P., Malap N., Balaji B., Mehajan R.K., Prabha T.V., 2017, Precipitable water as a predictor of LCL height, Theoretical and Applied Climatology, 130 (1-2), 467-476, DOI: 10.1007/s00704-016-1872-0.

- Schadowitz A., 1988, The Electromagnetic Field, Courier Corporation, 741 s.

- Schlesinger R.E., 1984, Mature thunderstorm cloud-top structure and dynamics: a three-dimensional numerical simulation study, Journal of Atmospheric Sciences, 41 99), 1551-1570, DOI: 10.1175/1520-0469(1984)041<1551:MTCTSA>2.0.CO;2.

- Schlesinger R.E., 1988, Effects of stratospheric lapse rate on thunderstorm cloud-top structure in a three-dimensional numerical simulation. Part I: some basic results of comparative experiments, Journal of Atmospheric Sciences, 45 (10), 1555-1570, DOI: 10.1175/1520-0469(1988)045<1555:EOSLRO>2.0.CO;2.

- Schmetz J., Tjemkes S.A., Gube M., van de Berg L., 1997, Monitoring deep convection and convective overshooting with METEOSAT, Advances in Space Research, 19 (3), 433-441, DOI: 10.1016/S0273-1177(97)00051-3.

- Setvak M., Lindsey D.T., Novak P., Wang P.K., Radova M., Kerkmann J., Grasso L., Su S-H., Rabin R.M., Stastka J., Charvat Z., 2010, Satellite-observed cold-ring-shaped features atop deep convective clouds, Atmospheric Research, 97 (1-2), 80-96, DOI: 10.1016/j.atmosres.2010.03.009.

- Setvak M., Rabin R.M., Wang P.K., 2007, Contribution of the MODIS instrument to observations of deep convective storms and stratospheric moisture detection in GOES and MSG imagery, Atmospheric Research, 83 (2-4), 505-518, DOI: 10.1016/j.atmosres.2005.09.015.

- Showalter A.K., 1953, A stability index for thunderstorm forecasting, Bulletin of the American Meteorological Society, 34 (6), 250-252, DOI: 10.1175/1520-0477-34.6.250.

- Taszarek M., Pilguj N., Orlikowski J., Surowiecki A., Walczakiewicz S., Pilorz W., Piasecki K., Pajurek Ł., Półrolniczak M., 2019, Derecho evolving from a mesocyclone – A study of 11 August 2017 severe weather outbreak in Poland: event analysis and high-resolution simulation, Monthly Weather Review, 147 (6), 2283-2306, DOI: 10.1175/MWR-D-18-0330.1.

- Wrona B., Mańczak P., Wozniak A., Ogrodnik M., Folwarski M., 2022, Synoptic conditions of the derecho storm. Case study of the derecho event over Poland on August 11, 2017, Meteorology Hydrology and Water Management, DOI: 10.26491/mhwm/152798.

The impact of initial and boundary conditions on severe weather event simulations using a high-resolution WRF model. Case study of the derecho event in Poland on 11 August 2017

Mariusz Figurski[1], Grzegorz Nykiel[1,2], Adam Jaczewski[1], Zofia Bałdysz[1], Marcin Wdowikowski[1]
[1] Institute of Meteorology and Water Management – National Research Institute, Poland
[2] Gdansk University of Technology, Faculty of Civil and Environmental Engineering, Poland

ABSTRACT. Precise simulations of severe weather events are a challenge in the era of changing climate. By performing simulations correctly and accurately, these phenomena can be studied and better understood. In this paper, we have verified how different initial and boundary conditions affect the quality of simulations performed using the Weather Research and Forecasting Model (WRF). For our analysis, we chose a derecho event that occurred in Poland on 11 August 2017, the most intense and devastating event in recent years. High-resolution simulations were conducted with initialization at 00 and 12 UTC (11 August 2017) using initial and boundary conditions derived from the four global models: Global Forecast System (GFS) from the National Centers for Environmental Prediction (NCEP), Integrated Forecast System (IFS) developed by the European Center for Medium-Range Weather Forecasts (ECMWF), Global Data Assimilation System (GDAS) and ERA5. For the last, we made separate calculations using data at the pressure and model levels. The results were evaluated against surface and radar data. We found that the simulations that used data from the GDAS and GFS models at 12 UTC were the more accurate, while ERA5 gave the worst predictions. However, all models were characterized by a low probability of detection and a high number of false alarms for simulations of extreme precipitation and wind gusts.

1. INTRODUCTION

In the era of an intensely changing climate, improving our understanding of weather phenomena, along with their reliable description using numerical models, is crucial. Numerical weather prediction (NWP) models are essential for supporting decision-making especially as global warming intensifies weather-derived natural hazards (Cornwall 2016; Herring 2018). Such extreme weather phenomena, including mesoscale convective systems (MCS), which can be organized into bow echo structures with mesoscale vortices, pose a particular risk of life-threatening and economic losses (EEA 2020). Emergency management and mitigation efforts related to such phenomena strongly rely on weather forecasts, which have seen intense progress in accuracy during the last 40 years (Bauer et al. 2015).

Among many factors, initial conditions were recognized to have tremendous implications on weather prediction accuracy, since even small initial differences between two NWP solutions will grow significantly over time (Lorenz 1963; Krishnamurthy 2019). Consequently, assessing the impact of initial conditions on forecast skill has become an important task in developing reliable weather predictions. Reichler and Roads (2003) pointed out that initial conditions have a significant impact on short-term forecasts, which are dominant in extreme weather predictions, when the model error itself is less powerful. Sutton et al. (2006) used the Weather Research and Forecasting (WRF) model and verified that in the case of a high-resolution grid (5 km), the initial conditions (related to soil moisture) were comparable to the differences resulting from adopting various convective parameterizations to the lower resolution grid (20 km). From the point of view of extreme weather event predictions, Jankov et al. (2007) conducted a detailed study on the influence of various physical schemes on the mesoscale convective system for rainfall forecasting. They found that WRF rainfall forecasts modelled with various treatments of convection, microphysical schemes, and planetary boundary layers are sensitive to the datasets used for model initialization. The impact of the initial conditions on the predictability of heavy rainfall was also investigated by Bei and Zhang (2007), who pointed out that the error related to small disturbances in initial conditions leads to significant uncertainties in a mesoscale forecast. Since global models are recognized as the best source of a real-time atmospheric state that can be used as initial conditions for short-term mesoscale forecasts, their uncertainties may also degrade the final NWP accuracy (Wei et al. 2010). As a consequence, the impact of these models on the mesoscale model forecasts was investigated by, among others, Kumar et al. (2015). Using the WRF model and four different global models, namely, the Integrated Forecast System (IFS), developed by the European Center for Medium-Range Weather Forecasts (ECMWF), the National Centers for Environmental Prediction (NCEP) Global Data Assimilation System (GDAS), the NCEP Global Forecasting System (GFS), and the National Center for Medium-Range Weather Forecasting (NCMRWF), they found that forecasts initialized using ECMWF/IFS produced the best solution for the Indian region. Some advantages from using IFS for the initialization of the WRF model were also found by Taszarek et al. (2019). Based on a derecho event, they found that, in contrast to the GFS, all IFS-based simulations correctly pointed out the possibility of extreme winds, although GFS-based simulations with a shorter lead time performed better for both the location and timing of extreme strong wind gusts (over 40 m·s⁻¹).

In this study, we present the effects of using varied initial conditions on simulations of severe weather events. Our analysis focused on a derecho event that occurred in Poland on 11 August 2017, one of the most intense and devastating events in recent years (Widawski, Pilorz 2018). We were
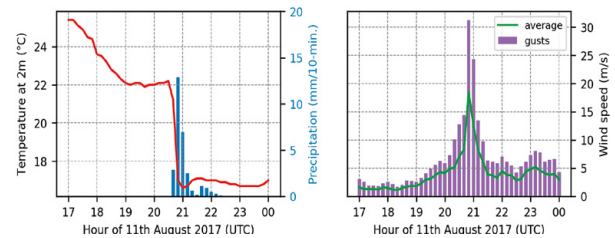

Fig. 1. Series of meteorological parameters observed at the Chojnice meteorological station. Air temperature (left, red line), precipitation (left, blue bars), wind speed (right, green line), and wind gusts (right, purple bars) are presented.

looking for answers as to which initial conditions would predict this phenomenon as accurately as possible. First, we provide information about the event. Second, we introduce the data and methodology, including a description of the WRF model domains and parameterization, information on all initial conditions tested, and the meteorological data used for quality evaluation. Next, we present results of the simulated meteorological parameters and validation using in situ ground measurements. Finally, we provide some conclusions and a discussion of the analysis.

2. DERECHO IN POLAND, 11 AUGUST 2017

Although the derecho analyzed in this study occurred on 11 August 2017, the weather conditions that contributed to its creation started to develop a few days earlier. They were mainly related to the formulation and movements of two pressure systems, namely a long-wave trough over western Europe and a wide ridge that was situated over central and eastern Europe. The hot and dry subtropical air masses associated with the ridge were separated from the much more humid, westerly located polar air masses by a wavy cold front that stretched along the western border of Poland. On 10 August, a slight change in the orientation of the low-pressure system enhanced the meridian-directed flow of tropical air from the Mediterranean Basin over central Europe. This dynamic triggered a mesoscale convective system over the Czech territory, which during the night passed over the territory of Poland. The storms associated with the system contributed to increased cloudiness, which effectively reduced the insolation over southwestern Poland until afternoon. At the same time, the air masses over the eastern part of Poland were constantly heating under cloudless conditions, contributing to the creation of a strong thermal gradient. The convergence line between these two pressure systems was moving northward, under the influence of the mid-level jet stream, which led to the formulation of a distinct vertical wind shear. At about 1800 UTC the convective cells embedded in the northerly propagating bow echo that was constantly growing and finally evolved into a mesoscale convective vortex (MCV). The development and transformation of convective cells into MCV, and as a consequence into a derecho, was supported by the appearance of a rear inflow jet (Sulik, Kejna 2020). The thunderstorm reached its strongest form between 20:00 and 2100 UTC, when the echo structure was about 150 km long. At that time, at the Chojnice synoptic station, precipitation exceeded 13 mm·10 min⁻¹ and was accompanied by a sharp drop in temperature (from 22.2 to 16.5°C) (Fig. 1, left). At the same time, the average wind speed exceeded 18.4 m·s⁻¹ with a wind gust of up to 31.2 m·s⁻¹ (Fig. 1, right). Very high wind gusts were also recorded at synoptic stations in Elblag (42 m·s⁻¹), Chrzastowo (36 m·s⁻¹), and Gniezno (35 m·s⁻¹). At 2230 UTC, the convective system reached the coast of the Baltic Sea and began to weaken visibly. The synoptic situation was described in detail by Wrona et al. (2022).

3. DATA AND METHODOLOGY

Here, we provide information on the WRF model used for simulations, together with domain characteristics, settings, and parameterization of physical processes. We also briefly introduce the initial conditions with some notes on their implementation in the WRF model. Lastly, we show meteorological data used for simulation verification: reflectivity and basic parameters from telemetry meteorological stations.

3.1. WRF MODEL

We used the WRF model version 4.2.1 in nonhydrostatic mode, which has wide applications in atmospheric research and operational weather forecasting (Skamarock et al. 2019). Our version of the model was adapted to work on a high-powered Tryton computer at the Academic Computer Centre in Gdansk. For the simulation, 568 cores of the supercomputer were used, with 552 cores for the WRF model and 16 for I/O operations. This approach minimized the time it took to write the results by a factor of 10 compared to a standard run without I/O enabled.

The derecho event was simulated using various initial and boundary conditions derived from the four global models: NCEP/GFS, ECMWF/IFS, GDAS, and ERA5. All models were provided with a time resolution of 3 hours. The spatial resolution of the GFS, GDAS, and ERA5 models is 0.25°. Therefore, in our simulations, we designed three nested domains in one direction with a nesting ratio of 5. Horizontal resolutions of domains, in Lambert conformal projection, were 12.5, 2.5, and 0.5 km. The time steps were 60, 12, and 3 seconds, respectively, for each domain. The time resolution was 1 hour for the outermost domain and 10 minutes for the other two. Because the spatial resolution of the IFS model is 0.125°, the first domain in our simulations was 7.5 km. The areas covered by these three domains were the same for all models. The first domain (domain 1) covers most of Europe, the second one (domain 2), the area of Poland, while the third one (domain 3 – with the highest resolution) covers the area where the bow echo and the greatest damage occurred. In Figure 2, the coverages of domains 2 and 3 are presented in detail. Vertically, simulations were done for 50 levels up to 50 hPa. Since the ERA5 model levels are provided on the model levels (137) and pressure levels (38), we performed calculations using both of them, called ERA5M and ERA5P, respectively.

For all simulations, the same parameterization of physics and model dynamics was used. We applied a single-moment microphysics scheme with six hydrometeor classes (WSM6) (Zaidi, Gisen 2018), which is the most suitable for high-resolution simulations (see, e.g., Hong et al. 2010; Parodi et al. 2019). For domain 1, parameterization of convective processes was performed using the Grell-Freitas method (Grell, Freitas 2014), while for domains 2 and 3, explicit wet process physics was used. Moreover, we applied short-wave and long-wave radiation parameterizations according to the RRTMG radiation propagation scheme, which is a new version of the RRTM (Iacono et al. 2008). The Mellor Yamada Nakanishi Niino (MYNN) turbulence scheme with closure 2.5 was used to model boundary layer processes (Nakanishi, Niino 2009). The near-surface layer was parameterized according to the MYNN scheme (Nakanishi, Niino 2006). To remove numerical noise at the start of the simulations, digital filter initialization (DFI) was used (Peckham et al. 2016). The land topography, land use, and soil type datasets were included in the model at the WRF preprocessing stage. For domains 1 and 2, the standard data contained in the WRF model geographic database (LULC) of IGBP MODIS and USGS GMTED2010 (30 arc seconds) were used. However, these data are insufficient for high-resolution simulations, as indicated by other studies (De Meij, Vinuesa 2014; Jiménez-Esteve et al. 2018; Siewert, Kroszczynki, 2020). Therefore, for domain 3 with a 0.5 km spatial step, we prepared new geographic data based on CORINE Land Cover (CLC) 2018 with 100 m and terrain topography from the Shuttle Radar Topography Mission (SRTM) with 30 m resolution. Siewert and Kroszczynski (2020) showed
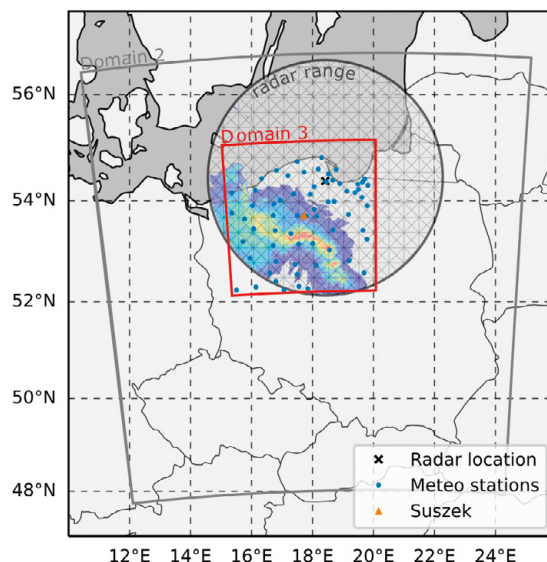

Fig. 2. WRF domain used in the study. The red rectangle represents a 500 m domain analyzed in this paper. The black cross shows the location of the meteorological radar in Gdansk (Poland) with a range equal to 250 km. The blue dots show the meteorological stations used for the validation of the results. The orange triangle identifies the location of Suszek, a village where the greatest damage was observed. In the background, the reflectivity derived from the meteorological radar in Gdansk is shown at 2000 UTC on 11 August 2017.

that CLC and SRTM data for microscale halves yield more accurate values for temperature and humidity at 2 m and wind at 10 m (speed and direction) compared to using default data from the WRF database.

In our analyses, we focused on the results derived from the innermost domain, which were stored with a 10-minute interval. Furthermore, we took into account initialized simulations at 0000 and 1200 UTC on 11 August 2017 to assess how the results depend on the starting time of the simulations.

3.2. REFLECTIVITY DATA

In this study, the WRF reflectivity data were compared with data from the Meteor 1500C Doppler meteorological radar in Gdansk (Fig. 2, the black cross) included in the POLRAD network. This radar provides reflecitivity scans in the range of 250 km, with 10-min interval. Also, Doppler velocity scans are available in the range of 125 km, at a 6 min interval. Each scan contains 9 slices for different elevation angles: 0.5°, 1.4°, 2.4°, 3.4°, 5.3°, 7.7°, 10.6°, 14.1°, 18.5°, 23.8°. In the analysis, we used only reflectivity data after quality improvement using the RADVOL-QC system (Ośródka et al. 2014). In Figure 2 the radar range together with example maximum reflectivity extracted at 2000 UTC are presented.

3.3. METEOROLOGICAL OBSERVATIONS

We used meteorological data from the basic measurement and observation network owned by the Institute of Meteorology and Water Management, National Research Institute. The meteorological situation on 11 August 2017 was represented based on data from 66 ground automated weather stations (AWS), located in the 52-55°N and 16-20°E domain, as shown in Figure 2 (blue dots). Data at 10-minute intervals of the following meteorological elements were analyzed: precipitation, air temperature, and wind speed, including wind gusts. Measurement data were subjected to the completeness verification procedure (looking for missing data caused by technical reasons) and data correctness

(analysis of differences in time series for stations that had more than one data source). The most frequent sources of data gaps from AWS are data transfer, sensor malfunctioning, exceptional equipment maintenance, and unreasonable recorded data (Storch et al. 1999; Lompar et al. 2019).

For synoptic stations with series of hourly data made by meteorological observers, the data gaps from AWS were supplemented with data from an observer. In the case of missing data, which could not be filled with the simple interpolation between adjacent time series records (up to 30 minutes), the analyzed time series data were supplemented with data from at least three neighboring stations using triangulation or inverse distance weighting methods, commonly used in climatic research (Storch et al. 1999; Daly et al. 2000; Claridge, Chen 2006; Henn et al. 2013). When verifying the completeness and correctness of the measurement data, it was found that data deficiencies were less than 1% of all analyzed cases.

3.4. SIMULATION VERIFICATION

To evaluate the quality of the simulated temperature and wind speed, we calculate the following statistical parameters:

• Bias or mean error (ME):

$$ME = \frac{\sum_{i=1}^{n}(F_i - O_i)}{n} \qquad (1)$$

• Root mean square error ($RMSE$):

$$RMSE = \sqrt{\frac{\sum_{i=1}^{n}(F_i - O_i)^2}{n}} \qquad (2)$$

• Unbiased $RMSE$ ($uRMSE$):

$$uRMSE = \sqrt{\frac{\sum_{i=1}^{n}\left((F_i - \bar{F}) - (O_i - \bar{O})\right)^2}{n}} \qquad (3)$$

• Pearson correlation (R):

$$R = \frac{\sum_{i=1}^{n}\left((F_i - \bar{F})(O_i - \bar{O})\right)}{\sigma_F \sigma_O} \qquad (4)$$

Where F_i, O_i are the forecast and observed values, respectively, indexed with ; means the total number of observations and σ denotes the standard deviation. ME is the mean difference between the forecasted and observed values, and therefore a valuable metric to present the tendency of the model to being over- or underestimated. On the other hand, averaging of positive and negative ME values may result in misinterpretation. $RMSE$ or $uRMSE$ is the square root of the squared forecast deviations and is used to mark better or worse simulations. We provide ME and R calculated for all time steps between 1700 and 0000 UTC and present them as time series. These measures are also calculated for individual stations and presented on the map as scatter plots for hourly time steps. We utilize Taylor (Taylor 2001) and target (Jolliff et al. 2009) diagrams to show the relationship between statistical parameters and summarize model performance. The former is a polar coordinate diagram that assigns radial coordinates to the standard deviation and azimuth to the inverse cosine of the correlation coefficient (Eq. 4). The reference point (observation) is indicated for the polar coordinates (σ_O, 0). The model-to-observation distance is proportional to $uRMSE$ (Eq. 3) and provides a measure of the model uncertainty. In the target diagram, $uRMSE$ is assigned to the X-axis, and ME (Eq. 1) is assigned to the Y-axis. The distance between origin and the model versus observation statistics is equal to $RMSE$ (Eq. 2). As $uRMSE$ is always pos-

itive, Jolliff et al. (2009) proposed to utilize the positive region of the X-axis and multiply $uRMSE$ by the sign of the standard deviation difference:

$$\sigma_d = sign(\sigma_F - \sigma_O) \qquad (5)$$

Table 1. The 2×2 contingency table.

Forecast \ Observation	Yes	No
Yes	A	B
No	C	D

Verification of forecasts for precipitation and wind gusts is based on the contingency table (Table 1). For dichotomous forecast verification, the following quality measures were calculated:

• Probability of detection (POD):

$$POD = \frac{A}{A+C} \qquad (6)$$

• False alarm ratio (FAR):

$$FAR = \frac{B}{A+B} \qquad (7)$$

• $bias$:

$$bias = \frac{A+B}{A+C} \qquad (8)$$

• Critical success index (CIS):

$$CSI = \frac{A}{A+B+C} \qquad (9)$$

The POD, CSI (also known as threat score) is represented by the so-called success ratio (SR) which ranges from 0 (worst) to 1 (best). For FAR, $SR = 1 - FAR$. A bias score equal to 1 indicates an unbiased model. Higher or lower values indicate that the forecast is overestimated or underestimated, respectively. Analyzes were performed for selected levels. Values of 0.5 and 1.0 mm of accumulated precipitation were chosen over 10 minutes. For wind gusts, the values of 5 and 10 m·s⁻¹ were chosen. The CSI are presented in the same manner as for temperature and wind speed. The performance of individual models is summarized by means of a diagram introduced by Roebber (2009).

The Roebber performance diagram is utilized to summarize the dichotomous verification of precipitation and wind gust. With simple algebraic manipulations, one can relate CSI and $bias$ to SR and POD :

$$bias = \frac{POD}{SR} \qquad (10)$$

$$CSI = \frac{1}{\frac{1}{SR} + \frac{1}{POD} - 1} \qquad (11)$$

If SR and POD are assigned to the X- and Y-axes, respectively, then isolines of $bias$ and CSI can be drawn on a figure. A perfect forecast should be located on the upper right of the diagram.

63
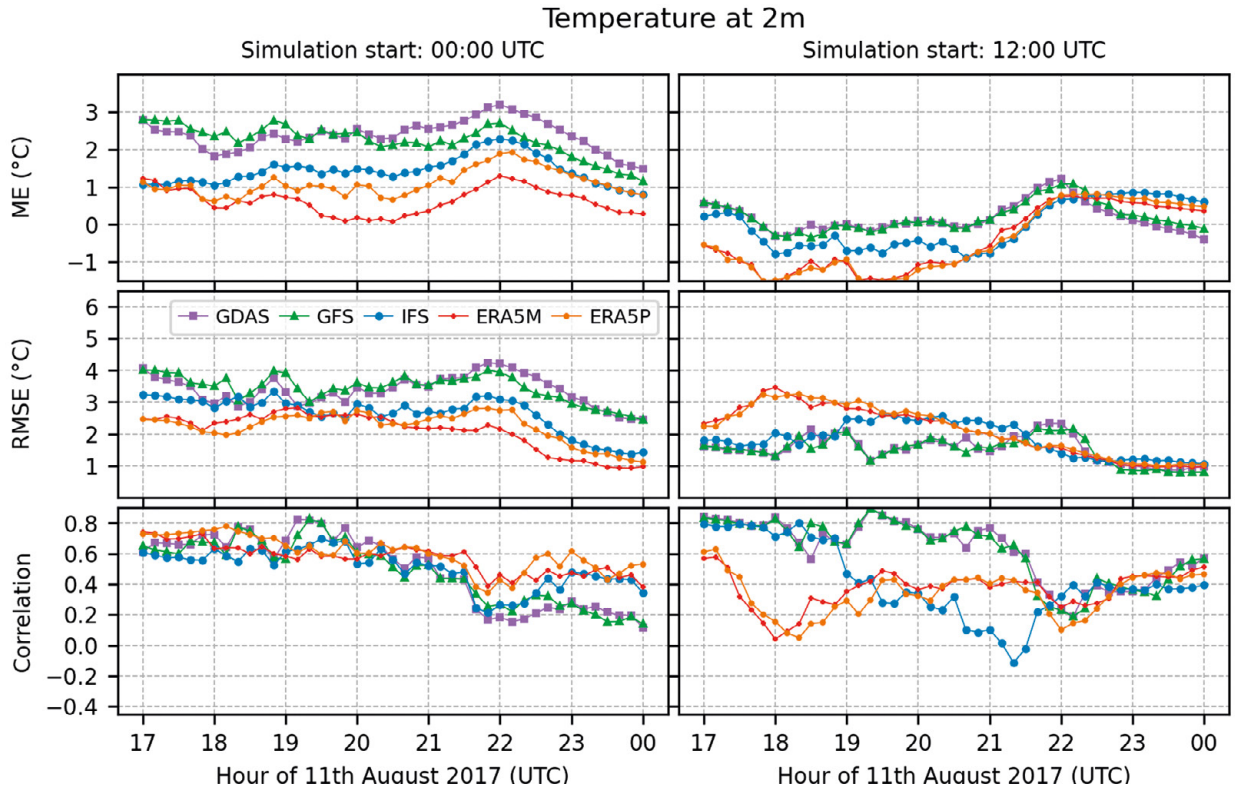
Temperature at 2m

Fig. 3. Statistical parameters of the comparison temperature at 2 m derived from WRF simulations and in situ observations at meteorological stations. From the top: mean error (*ME*), root mean square error (*RMSE*), correlation coefficient.

Reflectivity was verified using maximum reflectivity fields derived from meteorological radar. To access which model gives more reliable results, we used the index of agreement proposed by Willmott and Wicks (1980) and Willmott (1981). This index is a dimensionless measurement of the accuracy of the model and is used in several meteorological and hydrological studies. We used a modified version of this index (d_{mod}) proposed by Willmott (1984), which may be regarded as a more rigorous method than the original version (Pereira et al. 2018). As shown by Willmott et al. (2012), d_{mod} reaches its maximum value more slowly as the predicted values approach the observed values. The modified Willmott index is described by the following formula:

$$d_{mod} = 1 - \frac{\sum_{i=1}^{n}|F_i - O_i|}{\sum_{i=1}^{n}(|F_i - \bar{O}| + |O_i - \bar{O}|)} \qquad (12)$$

d_{mod} is bounded by 0 and 1: no agreement and a perfect fit, respectively.

4. RESULTS

This section describes the results of the simulations, as well as their verification based on in situ measurements. We divided this section into subsections by meteorological parameters: temperature, wind speed, precipitation, wind gusts, and reflectivity. Some visualizations of the results are included in the Appendix. The analysis of temperature and wind speed is divided into two stages. In the first, model errors are analyzed in subsequent time steps, and in the second, at the location of each station. Results are presented separately for simulations initialized at 0000 and 1200 UTC. Evaluation of precipitation and wind gusts is based on dichotomous verification for two exceedance levels. The range and spatial distribution of *CSI* are presented. For reflectivity, the range of the Willmott index is shown.

4.1. TEMPERATURE

In general, the predicted temperatures for 0000 UTC were noticeably higher than those obtained from the simulation at 1200 UTC. It is clearly seen in Figure 3 where *ME*, *RMSE* and the correlation of the temperature at 2 m between all simulations and in situ measurements are shown. For all calculations initialized at 0000 UTC, the temperature is overestimated. The largest *ME* are observed for GDAS-driven simulations with a maximum of 3°C at 2200 UTC. *ME* for runs initialized at 1200 UTC, in turn, are in the range of –1.5 to 1.5, except for ERA5-driven simulations that exceed –1°C. The most accurate results were obtained for simulations driven by GDAS and GFS. *ME* are slightly fluctuating for all runs until 2100 UTC, then the errors approach maximum values and decrease after 2200 UTC. The *RMSE* series for 1200 UTC runs follows the *ME* behavior. The highest values were found for GDAS and GFS with a maximum >4°C at about 2200 UTC. Following the coldest bias, ERA5-driven simulations initialized at 1200 UTC show the highest *RMSE* values with a peak at 1800 UTC. After 2200 UTC, the *RMSE* is visibly decreasing for all results. Correlation values calculated for every time step can be interpreted as quasi-spatial correlation of observation and model fields, except that the data are non-uniformly gridded. The correlation values for the 0000 UTC models are very close and quite high (0.5-0.8) until 2000 UTC when the *R* values decrease and clearly differ between models; the highest are for the ERA5 models (0.5-0.6) and the lowest for GDAS and GFS (0.2). For models initialized at 1200 UTC, the correlations are quite high for GDAS and GFS until 2100 and for IFS until 1900 UTC. Then, the *R* values decrease rapidly for the latter model. The correlations for the ERA5 models are the smallest, except for the period between 1900 and 2200 UTC where the IFS is the least correlated. The *R* values of all calculations initial-
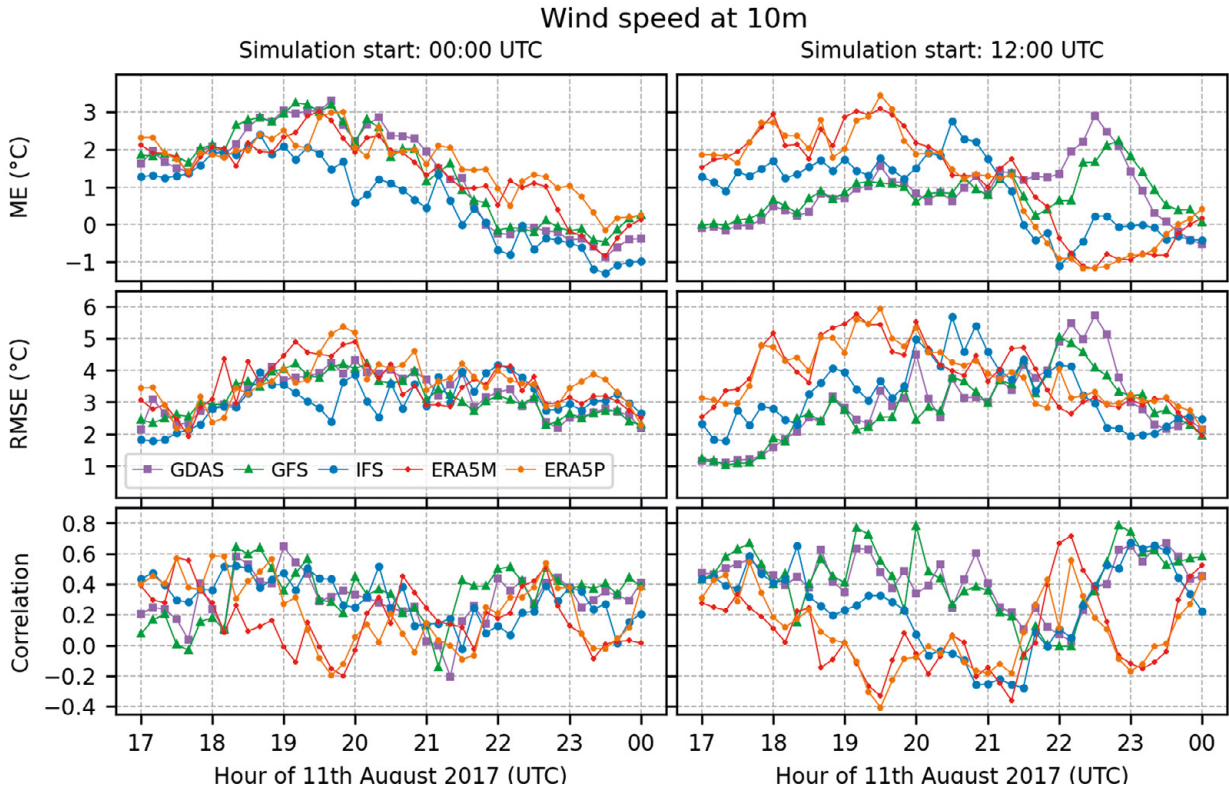
Fig. 4. Statistical parameters comparing wind speed at 10 m derived from the WRF model and in situ observations at meteorological stations.
From the top: mean error (*ME*), root mean square error (*RMSE*), correlation.

ized at 1200 UTC behave similarly and increase slightly from 0.1-0.4 at 22 UTC to 0.4-0.6 at the end of the simulations.

More details about simulation differences are given in Figures A1 and A2 (Appendix), where selected temperature distribution maps between 0000 and 1200 UTC are shown. Among all results, those based on the ERA5 model stand out, mainly due to the differences in temperature between the 0000 and 1200 UTC simulations. Also, *ME* values for 0000 UTC GDAS- and GFS-driven WRF simulations are the highest for most of the stations (Fig. A3). The lowest values are found in the western part of the domain. The *ME* values for the IFS model are highest in the southern part and lowest in the northern part. The mean errors for the ERA5-driven simulations are the highest in the eastern part and the lowest in the western part of the domain. The *ME* values for the 1200 UTC models are quite similar in all domains except for the simulations driven by IFS and ERA5, which exhibit negative values in the eastern region. The *RMSE* (Fig. A4) are the largest for GDAS- and GFS- driven WRF calculations initialized at 0000 UTC, with maximum values in the eastern region, much like ERA5 driven runs initialized at 1200 UTC. The lowest *RMSE* are seen for GDAS and GFS from 1200 UTC. The correlation (Fig. A5) is >0.5 in all domains for all results, with the lowest value for the station located on the Baltic coast.

4.2. WIND SPEED AT 10 M

As in the case of temperature, the difference in wind speed was obtained for various initial conditions and the initialization of the simulation time. The mean error of the wind speed (Fig. 4) predicted from 0000 UTC increases to a maximum value of 2-3 m·s⁻¹ at 1920 UTC and then decreases to negative values for all models except ERA5P. The lowest *ME* values are found until 2100 UTC for the GDAS and GFS predictions initialized at noon.

The values increase slightly from 0 to 1 m·s⁻¹ at 2100 UTC. After this time, the *ME* for GDAS and GFS is rapidly increasing to 3 m·s⁻¹ and 2 m·s⁻¹, respectively, and decreasing to the (−1, 0) range for other models. Maximum *RMSE* values are found at 2000 UTC, the largest for ERA5 driven simulations. The discrepancy for predictions initialized at 1200 UTC is much greater. The *RMSE* for ERA5 driven calculations exceeds 3 m·s⁻¹. Spatial correlations do not exceed 0.6 and decrease to −0.2. Positive correlation for the entire series is only found for IFS initialized at 0000 UTC and GDAS and GFS started at 1200 UTC. The results for the subsequent initialization time are more variable.

Detailed differences in the spatial distribution of the winds and their speed, obtained by adopting various initial conditions, can be observed in Figures A6 and A7, where wind gusts at 10 m between 1800 and 2200 UTC are presented. The spatial distribution of *ME* (Fig. A8) and *RMSE* (Fig. A9) is very variable and does not reveal any special pattern, unlike in the case of correlation (Fig. A10). Stations with high temporal correlations are found in the western and southern part of the GDAS and GFS WRF predictions initialized at 0000 UTC. The simulations of these models also have high *R* values for most locations except the southern region.

4.3. PRECIPITATION

CSI values for events with precipitation sum >0.5 mm·10 min⁻¹ (Fig. 5) are lower than 0.4 except for 2 cases for GDAS-driven simulations initialized at 0000 UTC. The cases are related to isolated precipitation events that appear from the southwestern direction (Fig. A11). Similar events are seen for the initialized predictions for IFS and ERA5P at 1200 UTC (Fig. A12). The *CSI* for runs initialized at 1200 UTC has larger values than those initialized at midnight (Fig. 6). Precipitation events of 1 mm·10 min⁻¹ and greater have slightly lower predictability.

Precipitation > 0.5 mm
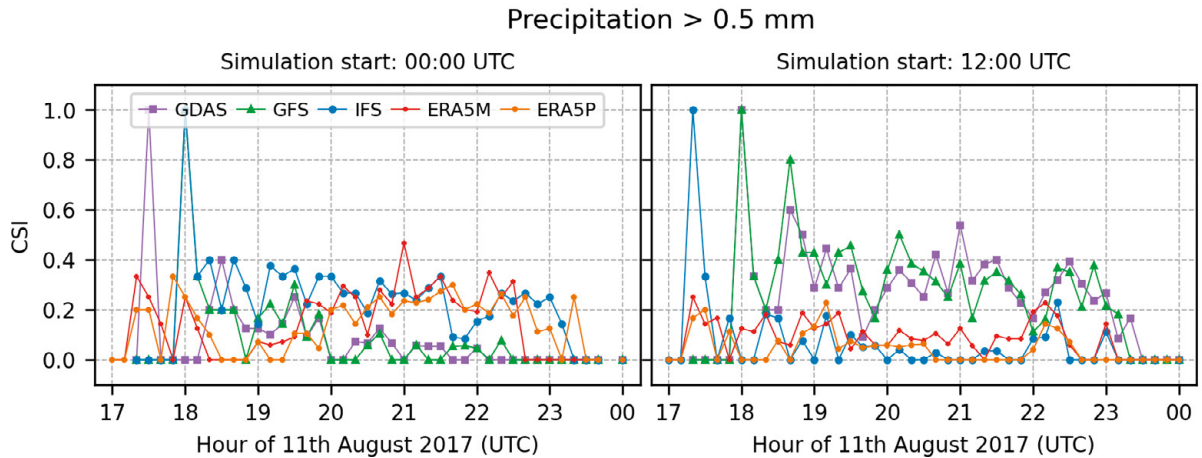
Fig. 5. Critical success index (*CSI*) of precipitation >0.5 mm·10 min⁻¹.

Precipitation > 1.0 mm
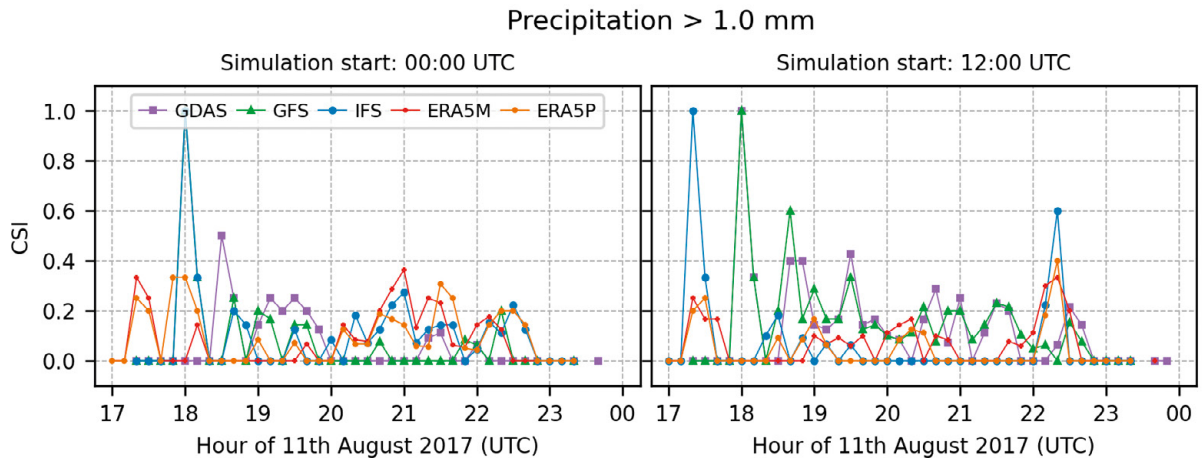
Fig. 6. Critical success index (*CSI*) of precipitation >1.0 mm·10 min⁻¹.

The spatial distributions of the *CSI* values for precipitation events >0.5 and 1 mm·min⁻¹ are presented in Figures A13 and A14, respectively. The former events are slightly more predictable for IFS- and ERA5-driven simulations initialized at 0000 UTC. On the other hand, GDAS and GFS play the primary role among other models initialized at 1200 UTC. Events >1 mm·10 min⁻¹ have worse predictability at particular locations.

4.4. WIND GUSTS

During the subject derecho event, wind gusts were the most dangerous and caused numerous property losses. In this study, the simulated values differ significantly between each case. The largest damages were reported in the vicinity of the synoptic station in Chojnice. The maximum observed wind velocity from meteorological sensors at this station was 31.2 m·s⁻¹ at 2050 UTC. In general, all simulations significantly underestimated the maximum wind gust. The calculation based on the ERA5M and ERA5P model initialized at 0000 UTC was close to the actual value amounting to approximately 19.5 m·s⁻¹. However, the simulated time of the maximum gusts was earlier than the actual time, 1830 and 1930 UTC, respectively. Simulations based on IFS (at 0000 UTC) and GDAS (at 0000 and 1200 UTC) were nearest in time to the occurrence of the phenomenon, taking place at 2040, 2020, and 2040 UTC, respectively. However, the predicted values were also underestimated: 15.6, 15.5, and 18.1 m·s⁻¹, respectively.

In Figure 7, the *CSI* series for wind gusts >5 m·s⁻¹ are presented for models initialized at 0000 UTC. It is seen that the obtained values differ

between the models. Only the GDAS model has slightly better performance between 1900 and 2100 UTC for that exceedance level. Predictions initialized at 1200 UTC have lower predictability (Fig. 8), slightly more than 0.6, but touching the lowest possible level in some periods (GDA, GFS, and ERA5M). The *CSI* values vary much more than for predictions initialized at 0000 UTC. *CSI* for wind gusts >10 m·s⁻¹ is much smaller and varies greatly over time.

The high predictability of wind gust events >5 m·s⁻¹ (Fig. A15) is found for about half of the stations and simulations initialized at 0000 UTC. This is also the case for predictions driven by GDAS, GFS, and IFS initialized at 1200 UTC. Single locations are found to be more predictable in the southern part of the domain for the ERA5-driven computation of the 1200 UTC initialization time. For the 10 m·s⁻¹ exceedance level, higher *CSI* values (Fig. A16) are found for only a few stations and mainly for predictions driven by GDAS and GFS for both initialization times. Some single stations with higher *CSI* are also found for the IFS prediction initialized at 0000 UTC.

4.5. REFLECTIVITY

The temporal evolution of the maximum reflectivity field for values higher than 45 dBZ with 30-min steps is presented in Figure 9 against measured values. The simulation of maximum reflectivity is presented with 1-h steps in Figures A17 and A18 for initialized runs of 0000 UTC and 1200 UTC,
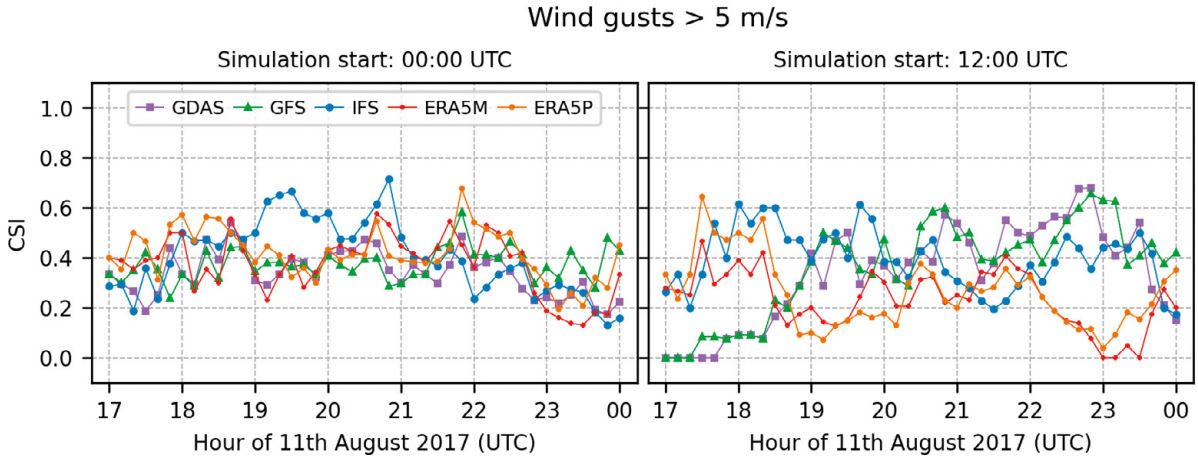
Fig. 7. Critical success index (*CSI*) of wind gusts >5 m·s⁻¹.
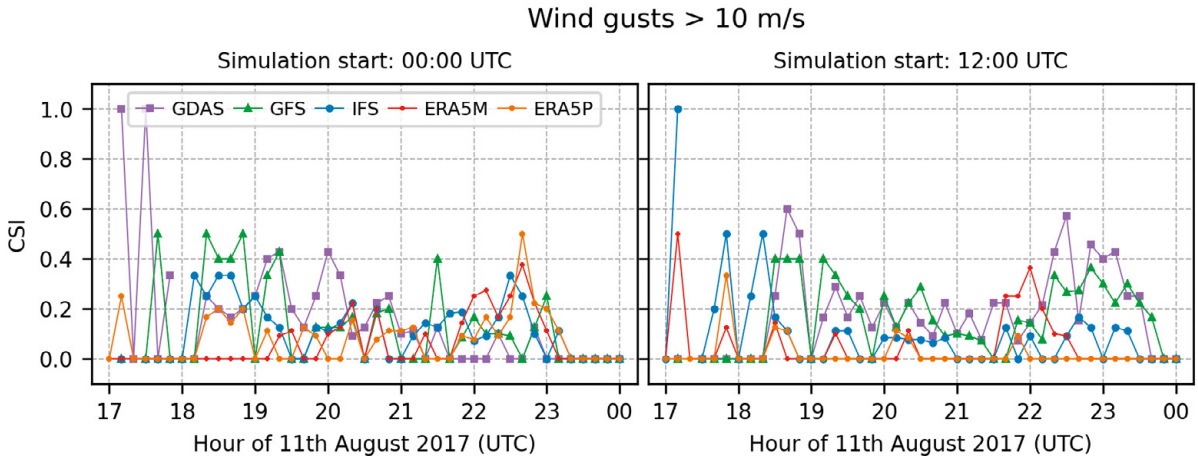
Fig. 8. Critical success index (*CSI*) of wind gusts > 10 m·s⁻¹.

respectively. It is clear (Fig. 9) that the modelled track of the convective line match was observed one only for GDAS and GFS predictions initialized at 1200 UTC. On the other hand, the shape and location of the thunderstorm are different from the observed one. Also, the modelled structure is not as sharp as detected by the radar. It has also been found that, in general, maximum reflectivity fields were simulated more westward for models initialized at 0000 UTC than at 1200 UTC. This is in line with the results shown by Taszarek et al. (2019). This visual inspection is reflected in the Willmott index (Fig. 10). All models, except GDAS and GFS started at 0000 UTC, and IFS started at 1200 UTC are in advance of event. Afterward, the index is slightly increasing to about 0.4 at 2000 UTC. Thereafter, the values reduce to about 0.2 at about 2130 UTC and increase to about 0.5 afterward, mostly for GDAS and GFS runs initialized at 1200 UTC.

4.6. SUMMARY OF THE EVALUATION OF STATISTICAL MODELS

The Taylor diagram for temperature (Fig. 11, left panel) shows that simulations of GDAS and GFS initialized at 1200 UTC performed best. The correlations are the highest, close to 0.9, and *uRMSE* is the lowest and closest to the observed value. It is also found that predictions initialized at 0000 UTC (indicated by blue markers) have larger deviations and those initialized at 1200 UTC (red marker) had smaller deviations or were nearly equal to the observed values. This pattern also can be

seen in the target diagram (Fig. 11, right panel), where blue markers are placed in the positive region of the X axis, and red markers (except for GDAS with slightly larger σ_F than σ_O) are placed in the negative region. The mean errors are the lowest for 1200 UTC initialized runs and the largest for 0000 UTC runs that are warm-biased. According to the above diagrams, the ERA5 computations started at 0000 UTC seem to be the second best performing predictions.

The Taylor diagram for wind speed at 10 m (Fig. 12, left panel) shows the best performance of the GDAS and GFS simulations for both initialization times and the IFS initialized at 0000 UTC, but the skill is very low. *uRMSE* is about 3 m·s⁻¹. The performance is the lowest for ERA5 predictions initialized at 1200 UTC with a correlation close to zero. All models are positively biased (Fig. 12, right panel) and the lowest mean errors are found for GDAS, GFS and GFS runs initialized at 1200 UTC and IFS initialized at 0000 UTC. The *ME* values differ slightly between models.

$$bias = \frac{POD}{SR} \quad CSI = \frac{1}{\frac{1}{SR} + \frac{1}{POD} - 1} \qquad (13)$$

In Figure 13, Roebber's performance diagram is presented for precipitation events >0.5 mm (left panel) and 1 mm (right panel) per 10-minutes. According to this figure, the best skill was found for the GDAS and GFS models initialized at 1200 UTC, but the *POD* and *SR* values

Maximum reflectivity comparison
Simulation start: 00:00 UTC, 11th August 2017

WRF+GDAS   WRF+GFS   WRF+IFS   WRF+ERA5M   WRF+ERA5P

Simulation start: 12:00 UTC, 11th August 2017

46 48 50 52 54 56 58 60 62 64 [dBz]
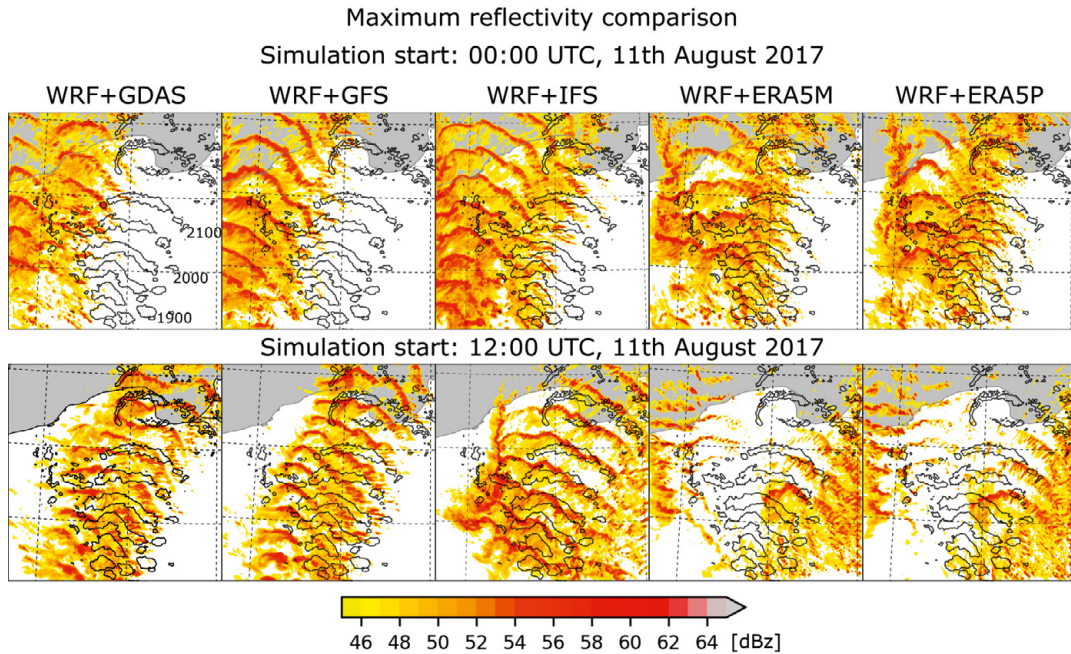
Fig. 9. Maximum reflectivity derived from the WRF model with various initial conditions and from meteorological radar. Data presented for hours between 1830 and 2300 UTC in 30-minute intervals. The black outlines represent the measured values. Reflectivity was plotted only for values higher than 45 dBz.
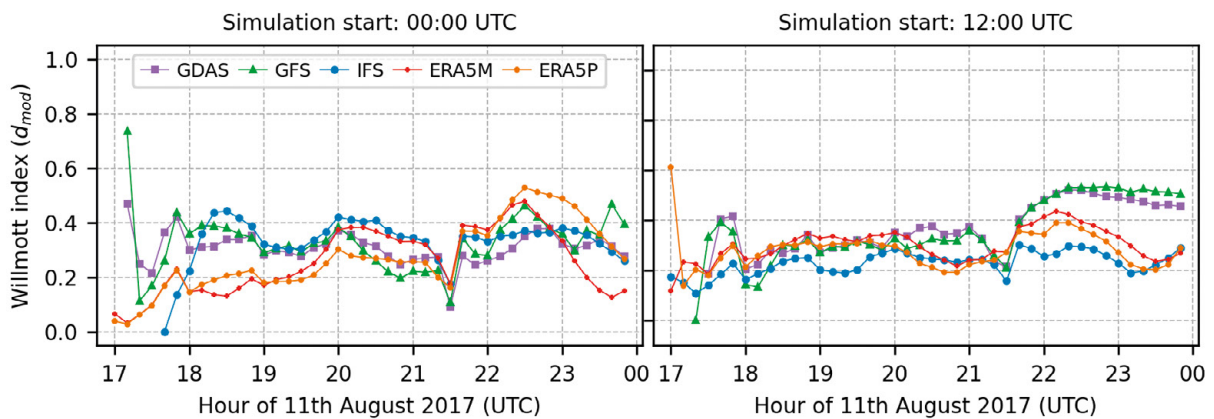
Fig. 10. Comparison of the Willmott index between WRF models with various initial and boundary conditions. The index was calculated on the basis of maximum reflectivity fields derived from the WRF model and meteorological radar.

do not exceed 0.5 and 0.3 for events >0.5 and 1 mm·10 min⁻¹ respectively. Unlike these models, which are initialized at 0000 UTC, they suffer from very low prediction skills. The same applies to IFS and ERA5 runs initialized at 1200 UTC.

The performance diagrams for wind gust events are presented in Figure 14. All models, except ERA5 initialized at 1200 UTC, are located near $CSI = 0.4$ isoline for weaker wind gust events, but GDAS and GFS have the lowest false alarm ratio. Stronger wind gust event predictions are worse, with the highest skill provided by the GDAS and GFS simulations initialized at 1200 UTC. The least skill is found for ERA5 predictions initialized at 1200 UTC and for both events.

5. CONCLUSIONS AND DISCUSSION

In this paper, we present a detailed verification of various WRF simulations that differ in initial and boundary conditions. As a case study, we chose the derecho event of 11 August 2017 that, was one of the most in-

tense and devastating hazardous phenomena in recent years in Poland. We performed high-temporal (10 minute) and spatial resolution (0.5 km for the third domain) simulations with initialization at 0000 and 1200 UTC. As boundary and initial conditions, we used a suite of global models. The bow echo feature was clearly seen in GFS- and IFS-based simulations initialized at both times, and GDAS initialized at 1200 UTC. Simulations performed using ERA5 data produce maximum reflectivity fields that are very different from those observed. The characteristic bow echo structure was visible in ERA5 simulations started at 0000 UTC, but the MCS was evolving too fast and only in the western part of the domain. The observed event was also reconstructed by other simulations initialized at that time. Simulations based on ERA5 at 1200 UTC show the field scattered throughout the domain. The closest to observed evolution of the bow echo structure was obtained from the results of GFS- and GDAS-based simulations started at a later initialization time. The results of all simulations were evaluated against surface observational and radar data. The best
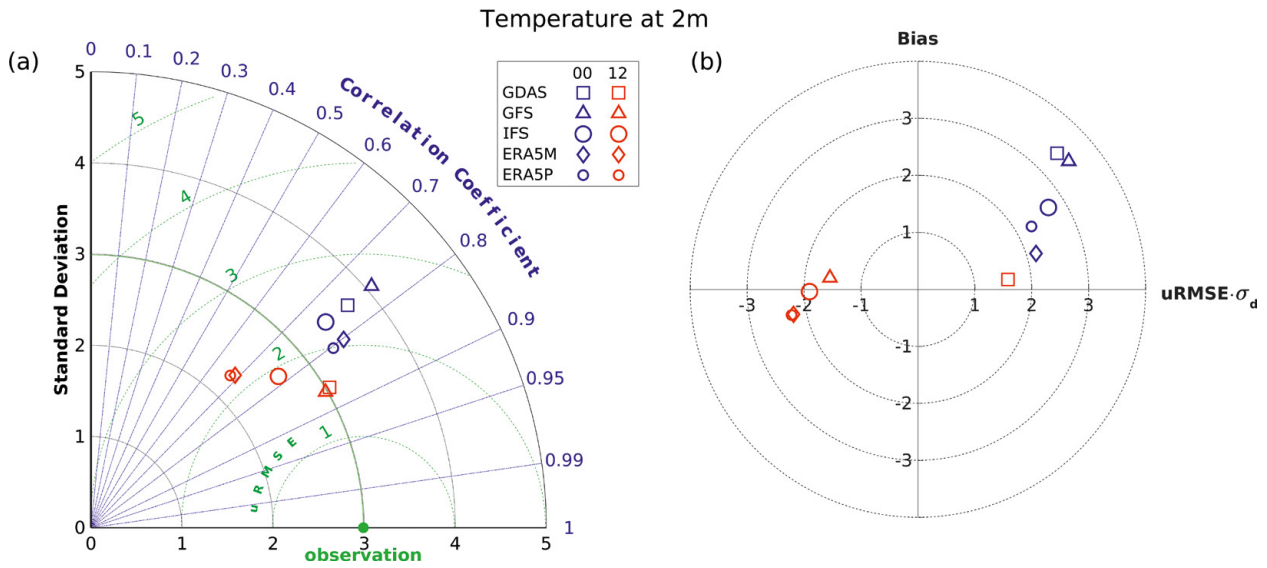
Temperature at 2m

Fig. 11. Taylor (left) and target (right) diagrams showing model-to-observation statistics for temperature at 2 m.
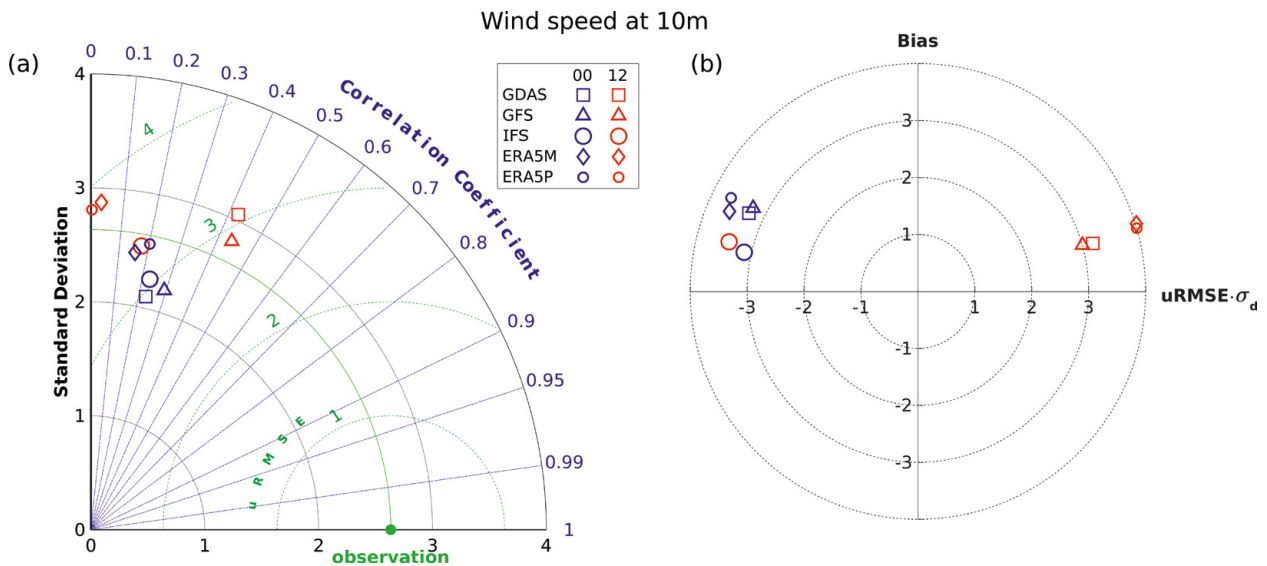
Wind speed at 10m

Fig. 12. Taylor (left) and target (right) diagrams showing model-to-observation statistics for wind speed at 10 m.

skill was found for GFS- and GDAS-driven simulations and shorter lead times. For the same time, ERA5-based results were characterized by the worst predictions. Middle-ranking IFS-driven runs show a similar dependence on lead time. This finding can be confirmed by the daily cycle for the *RMSE* signal found by Ylinen et al. (2020) for the temperature forecasts of the IFS ensemble prediction system for Europe. Goutham et al. (2021) found a similar correlation for the surface wind but a smaller *RMSE* for the IFS model. For the 0000 UTC initialization, all models predicted a more westward phenomenon than the actual case. The 1200 UTC simulations look better in this respect, which was also found by Taszarek et al. (2019). Although the GDAS and GFS models were the best predictors of the location of the derecho, all models were characterized by a low probability of detection and a high number of false alarms forecasting extreme precipitation and wind gusts. The study by Gevorgyan (2018) also shows that exact prediction of extreme convective events is a hard challenge and WRF simulations are very sensitive to chosen microphysics and forcing data.

DATA AVAILABILITY

Data from all simulations, in NetCDF format, are available on The Bridge of Knowledge platform of Gdansk University of Technology under the CC BY-NC-SA license (Figurski, Nykiel 2020a, b, c, d, e).

Wind gust at 10 m
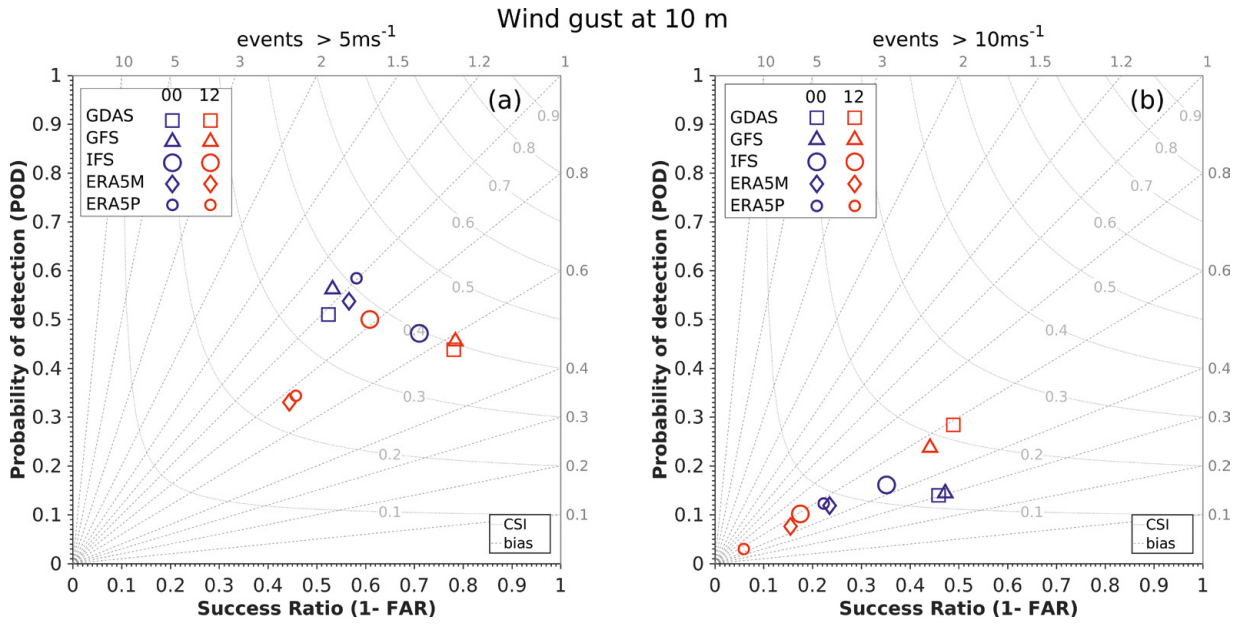
Fig. 13. Roebber performance diagram presenting results of dichotomous verification of precipitation events with a sum of 10 min >0.5 mm (left panel) and >1 mm (right panel).

Wind gust at 10 m
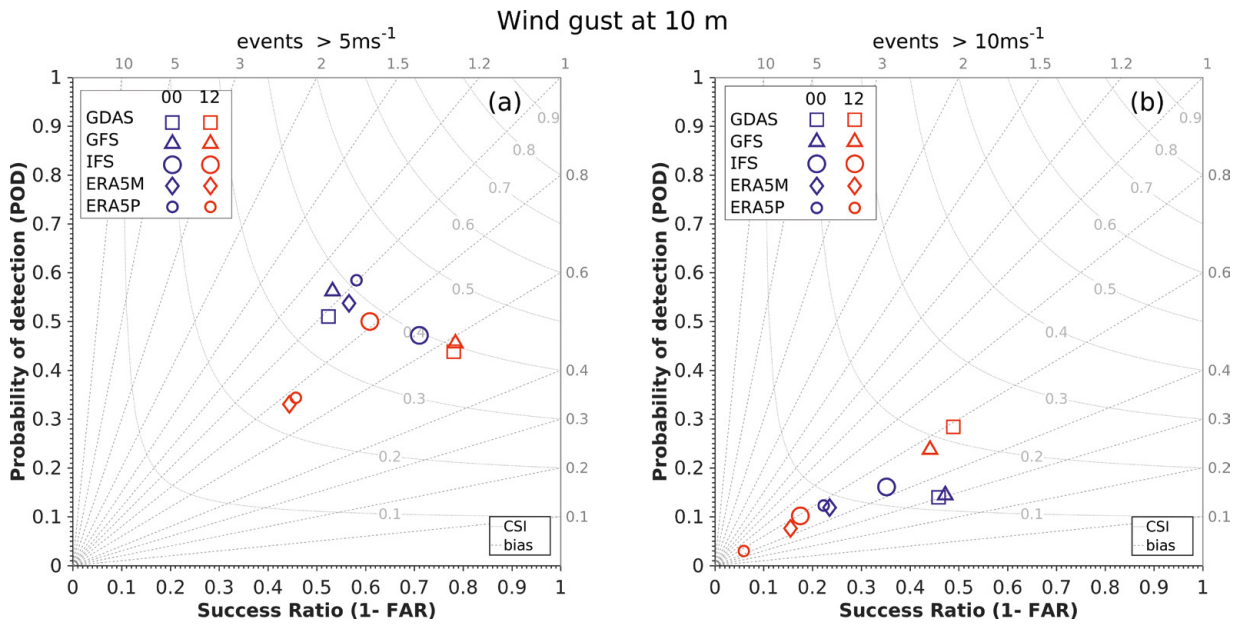
Fig. 14. Roebber's performance diagram presenting results of dichotomous verification of wind gust events with speeds >5 m·s^{-1} (left panel) and >10 m·s^{-1} (right panel).

REFERENCES

- Bauer P., Thorpe A., Brunet G., 2015, The quiet revolution of numerical weather prediction, Nature, 525, 47-55, DOI: 10.1038/nature14956.

- Bei N., Zhang F., 2007, Impacts of initial condition errors on mesoscale predictability of heavy precipitation along the Mei-Yu front of China, Quarterly Journal of Royal Meteorological Society, 133 (622), 83-99, DOI: 10.1002/qj.20.

- Claridge D.E., Chen H., 2006, Missing data estimation for 1-6 h gaps in energy use and weather data using different statistical methods, International Journal of Energy Research, 30 (13), 1075-1091, DOI: 10.1002/er.1207.

- Cornwall W., 2016, Efforts to link climate change to severe weather gain ground, Science, 351 (6279), 1249-1250, DOI: 10.1126/science.351.6279.1249.

- Daly S.F., Davis R., Ochs E., Pangburn T., 2000, An approach to spatially distributed snow modelling of the Sacramento and San Joaquin basins, California, Hydrological Processes, 14 (18), 3257-3271, DOI: 10.1002/1099-1085(20001230)14:18<3257::aid-hyp199>3.0.co;2-z.

- De Meij A., Vinuesa J.F., 2014, Impact of SRTM and Corine Land Cover data on meteorological parameters using WRF, Atmosphere Research, 143, 351-370, DOI: 10.1016/j.atmosres.2014.03.004.

- EEA, 2020, Economic losses from climate-related extremes in Europe, CSI 042 , CLIM 039, available online at https://www.eea.europa.eu/ds_resolveuid/cf171dde4a5846f99ac-722b92807e9f1 (data access 11.11.2021).

- Figurski M., Nykiel G., 2020a, Simulation of the derecho event in Poland of 11th August 2017 using the WRF model and ECMWF data as initial conditions [Data set], Gdańsk University of Technology, DOI: https://doi.org/10.34808/kxnc-rc32.

- Figurski M., Nykiel G., 2020b, Simulation of the derecho event in Poland of 11th August 2017 using the WRF model and ERA5 data on pressure levels as initial conditions [Data set], Gdańsk University of Technology, DOI: https://doi.org/10.34808/ava3-yd08.

- Figurski M., Nykiel G., 2020c, Simulation of the derecho event in Poland of 11th August 2017 using the WRF model and ERA5 data on model levels as initial conditions [Data set], Gdańsk University of Technology, DOI: https://doi.org/10.34808/fkmj-dh09.

- Figurski M., Nykiel G., 2020d, Simulation of the derecho event in Poland of 11th August 2017 using the WRF model and GFS data as initial conditions [Data set], Gdańsk University of Technology, DOI: https://doi.org/10.34808/3s00-kn10.

- Figurski M., Nykiel G., 2020e, Simulation of the derecho event in Poland of 11th August 2017 using the WRF model and GDAS data as initial conditions [Data set], Gdańsk University of Technology, DOI: https://doi.org/10.34808/ceh3-7z70.

- Gevorgyan A., 2018, Convection-permitting simulation of a heavy rainfall event in Armenia using the WRF model, Journal of Geophysical Research. Atmospheres, 123 (19), DOI: 10.1029/2017jd028247.

- Goutham N., Alonzo B., Dupré A., Plougonven R., Doctors R., Liao L., Mougeot M., Fischer A., Drobinski P., 2021, Using machine-learning methods to improve surface wind speed from the outputs of a numerical weather prediction model, Boundary-Layer Meteorology, 179, 133-161, DOI: 10.1007/s10546-020-00586-x.

- Grell G.A., Freitas S.R., 2014, A scale and aerosol aware stochastic convective parameterization for weather and air quality modeling, Atmospheric Chemistry and Physics, 14 (10), 5233-5250, DOI: 10.5194/acp-14-5233-2014.

- Henn B., Raleigh M.S., Fisher A., Lundquist J.D., 2013, A comparison of methods for filling gaps in hourly near-surface air temperature data, Journal of Hydrometeorology, 14 (3), 929-945, DOI: 10.1175/JHM-D-12-027.1.

- Herring S.C., Christidis N., Hoell A., Kossin J.P., Schreck C.J., Stott P.A., 2018, Explaining extreme events of 2016 from a climate perspective, Bulletin of the American Meteorological Society, 99 (1), S1-S157. DOI: 10.1175/BAMS-ExplainingExtremeEvents2016.1.

- Hong S.-Y., Limn J.-O.J., 2006, The WRF single–moment 6–class microphysics scheme (WSM6), Journal of Korean Meteorological Society, 42 (2), 129-151.

- Hong S.Y., Lim K.S.S., Lee Y.-H., Ha J.C., Kim H.W., Ham S.J., Dudhia J., 2010, Evaluation of the WRF Double-Moment 6-Class microphysics scheme for precipitating convection, Advances in Meteorology, 10, DOI: 10.1155/2010/707253.

- Iacono M.J., Delamere J.S., Mlawer E.J., Shephard M.W., Clough S.A., Collins W.D., 2008, Radiative forcing by long–lived greenhouse gases: Calculations with the AER radiative transfer models, Journal of Geophysical Research. Atmospheres, 113 (D13), DOI: 10.1029/2008JD009944.

- Jankov I., Gallus Jr. W.A, Segal M., Koch S.E., 2007, Influence of initial conditions on the WRF–ARW model QPF response to physical parameterization changes, Weather and Forecasting, 22 (3), 501-519, DOI: 10.1175/WAF998.1.

- Jiménez-Esteve E.B., Udina M., Soler M.R., Pepin N., Miró J.R., 2018, Land use and topography influence in complex terrain area: A high resolution mesoscale modeling study over the Eastern Pyrenees using the WRF model, Atmospheric Research, 202, 49-62, DOI: 10.1016/j.atmosres.2017.11.012.

- Jolliff J.K., Kindle J.C., Shulman I., Penta B., Friedrichs M.A.M., Helber R., Arnone R.A., 2009, Summary diagrams for coupled hydrodynamic-ecosystem model skill assessment, Journal of Marine Systems, 76 (1), 64-82. DOI: 10.1016/j.jmarsys.2008.05.014.

- Krishnamurthy V., 2019, Predictability of weather and climate, Earth and Space Science, 6 (7), 1043-1056, DOI: 10.1029/2019EA000586.

- Kumar P., Kishtawal C.M., Pal P.K., 2017, Impact of ECMWF, NCEP, and NCMRWF global model analysis on the WRF model forecast over Indian Region, Theoretical and Applied Climatology, 127, 143-151, DOI: 10.1007/s00704-015-1629-1.

- Lompar M., Lalić B., Dekić L., Petrić M., 2019, Filling gaps in hourly air temperature data using debiased ERA5 data, Atmosphere, 10 (1), 13, DOI: 10.3390/atmos10010013.

- Lorenz E.N., 1963, The predictability of hydrodynamic flow, Transactions of the New York Academy of Sciences, 25 (4), 409-432, DOI: 10.1111/j.2164-0947.1963.tb01464.x.

- Los F.J., Blaas M., 2010, Complexity, accuracy and practical applicability of different biogeochemical model versions. Journal of Marine Systems, 81 (1), 44-74, DOI: 10.1016/j.jmarsys2009.12.011.

- Nakanishi M., Niino H., 2006, An improved Mellor–Yamada level-3 model: its numerical stability and application to a regional prediction of advection fog, Boundary-Layer Meteorology, 119, 397-407, DOI: 10.1007/s10546-005-9030-8.

- Nakanishi M., Niino, H., 2009, Development of an improved turbulence closure model for the atmospheric boundary layer, Journal of the Meteorological Society of Japan. Serie II, 87 (5), 895-912, DOI: 10.2151/jmsj.87.895.

- Ośródka K., Szturc J., Jurczyk A., 2014, Chain of data quality algorithms for 3-D single-polarization radar reflectivity (RADVOL-QC system), Meteorological Applications, 21 (2), 256-270, DOI: 10.1002/met.1323.

- Parodi A., Lagasio M., Maugeri M., Turato B., Gallus W, 2019, Observational and modelling study of a major downburst event in Liguria: The 14 October 2016 case, Atmosphere, 10 (12), 788, DOI: 10.3390/atmos10120788.

- Peckham S.E., Smirnova T.G., Benjamin S.G., Brown J.M., Kenyon J.S., 2016, Implementation of a Digital Filter Initialization in the WRF model and its application in the rapid refresh, Monthly Weather Review, 144 (1), 99-106, DOI: 10.1175/MWR-D-15-0219.1.

- Pereira H.R., Meschiatti M.C., Pires R.C. de M., Blain G.C., 2018, On the performance of three indices of agreement: an easy-to-use r-code for calculating the Willmott indices, Bragantia, 77, 394-403, DOI: 10.1590/1678-4499.2017054.

- Reichler T.J., Roads J.O., 2003, The role of boundary and initial conditions for dynamical seasonal predictability, Nonlinear Processes in Geophysics, 10 (3), 211-232, DOI: 10.5194/npg-10-211-2003.

- Roebber P.J., 2009, Visualizing multiple measures of forecast quality, Weather and Forecasting, 24 (2), 601-608, DOI: 10.1175/2008WAF2222159.1.

- Siewert J., Kroszczynski K., 2020, GIS Data as a valuable source of information for increasing resolution of the WRF model for Warsaw, Remote Sensing, 12 (11), 1881, DOI: 10.3390/rs12111881.

- Skamarock C., Klemp B., Dudhia J., Gill O., Liu Z., Berner J., Wang W., Powers G., Duda G., Barker D., Huang X., 2019, A description of the advanced research WRF model version 4, DOI: 10.5065/1dfh-6p97.

- Sulik S., Kejna M., 2020, The origin and course of severe thunderstorm outbreaks in Poland on 10 and 11 August, 2017, Bulletin of Geography, Physical Geography Series, 18 (1), 25-39, DOI: 10.2478/bgeo-2020-0003.

71

- Sutton C., Hamill T.M., Warner T.T., 2006, Will perturbing soil moisture improve warm-season ensemble forecasts? A proof of concept, Monthly Weather Review, 134 (11), 3174-3189, DOI: 10.1175/MWR3248.1.

- Storch H., Zwiers F., 1999, Statistical analysis in climate research, Cambridge University Press, DOI: 10.1017/CBO9780511612336.

- Taszarek M., Pilguj N., Orlikowski J., Surowiecki A., Walczakiewicz S., Pilorz W., Piasecki K., Pajurek Ł., Półrolniczak M., 2019, Derecho evolving from a mesocyclone – a study of 11 August 2017 severe weather outbreak in Poland: Event analysis and high-resolution simulation, Monthly Weather Review, 147 (6), 2283-2306, DOI: 10.1175/MWR-D-18-0330.1.

- Taylor K.E., 2001, Summarizing multiple aspects of model performance in a single diagram, Journal of Geophysical Research. Atmospheres, 106 (D7), 7183-7192, DOI: 200110.1029/2000JD900719.

- Wei M., Toth Z., Zhu Y., 2010, Analysis differences and error variance estimates from multi-centre analysis data, Australian Meteorological and Oceanographic Journal, 59, 25-34, DOI: 10.22499/2.5901.005.

- Widawski A., Pilorz W., 2018, The mesoscale convective systems with bow echo radar signatures as an example of extremely severe and widespread geohazard in Poland, Environmental and Socio-Economic Studies, 6 (1), 10-16, DOI: 10.2478/environ-2018-0002.

- Willmott C.J., Wicks D.E., 1980, An Empirical method for the spatial interpolation of monthly precipitation within California, Physical Geography, 1 (1), 59-73, DOI: 10.1080/02723646.1980.10642189.

- Willmott C.J., 1981, On the validation of models, Physical Geography, 2 (2), 184-194, DOI: 10.1080/02723646.1981.10642213.

- Willmott C.J., 1984, On the evaluation of model performance in physical geography, [in:] Spatial statistics and models, G.L. Gaile, C.J. Willmott (eds.), Springer, Dordrecht, 443-460, DOI: 10.1007/978-94-017-3048-8_23.

- Willmott C.J., Robeson S.M., Matsuura K., 2012, A refined index of model performance, International Journal of Climatology, 32 (13), 2088-2094, DOI: 10.1002/joc.2419.

- Wrona B., Mańczak P., Wozniak A., Ogrodnik M., Folwarski M., 2022, Synoptic conditions of the derecho storm. Case study of the derecho event over Poland on August 11, 2017, Meteorology Hydrology and Water Management, DOI: 10.26491/mhwm/152798.

- Ylinen K., Räty O., Laine M., 2020, Operational statistical postprocessing of temperature ensemble forecasts with station-specific predictors, Meteorological Applications, 27 (6), e1971, DOI: 10.1002/met.1971.

- Zaidi S.M., Gisen J.I.A., 2018, Evaluation of Weather Research and Forecasting (WRF) microphysics single moment class-3 and class-6 in precipitation forecast, [in:] MATEC Web of Conferences, 03007, DOI: 10.1051/matecconf/201815003007.

APPENDIX
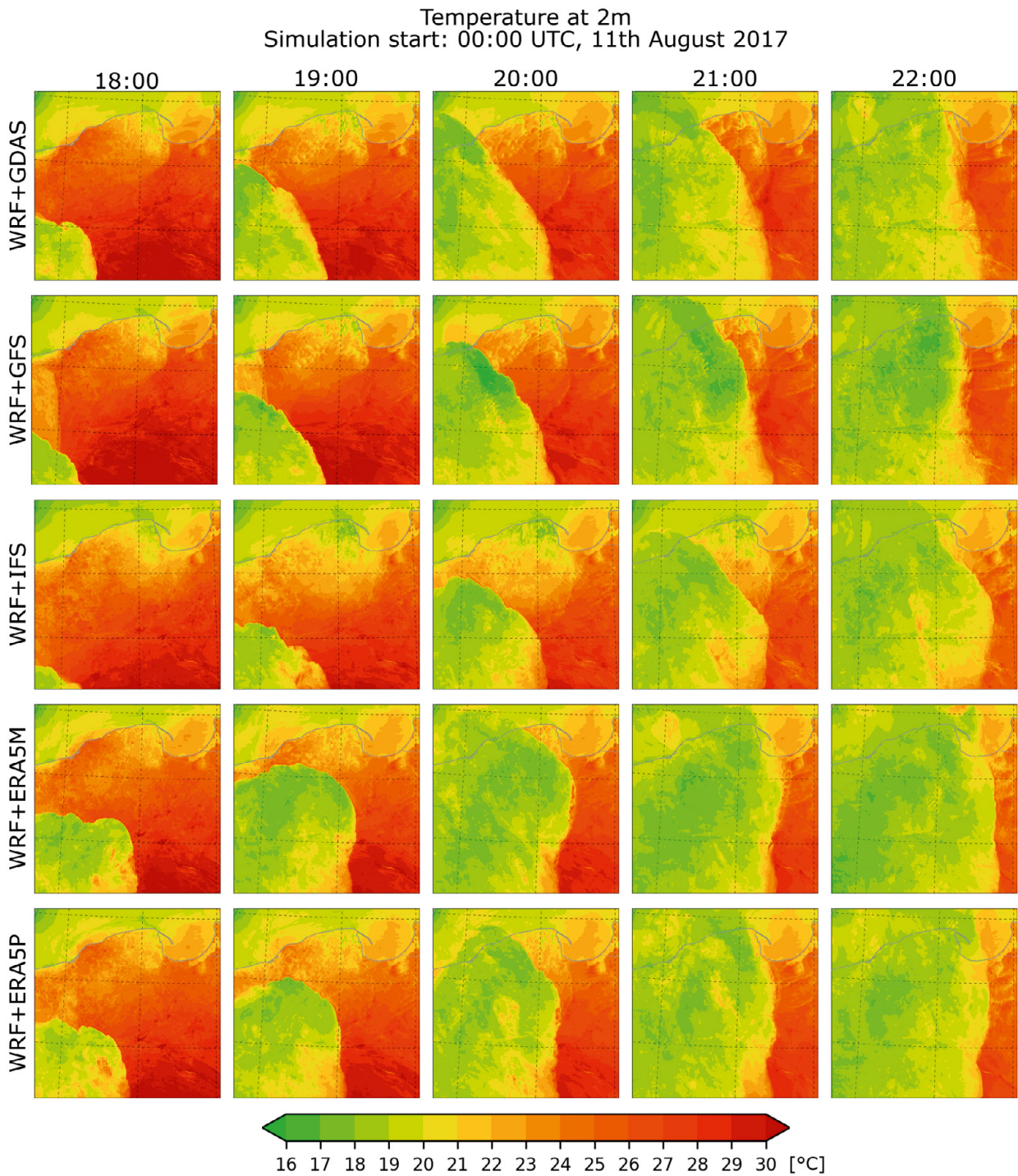
Fig. A1. Temperature at 2 m derived from the WRF between 1800 and 2200 UTC with various initial conditions: GDAS, GFS, IFS, ERA5M (model levels), ERA5P (pressure levels). Forecast start: 0000 UTC, 11th August 2017.
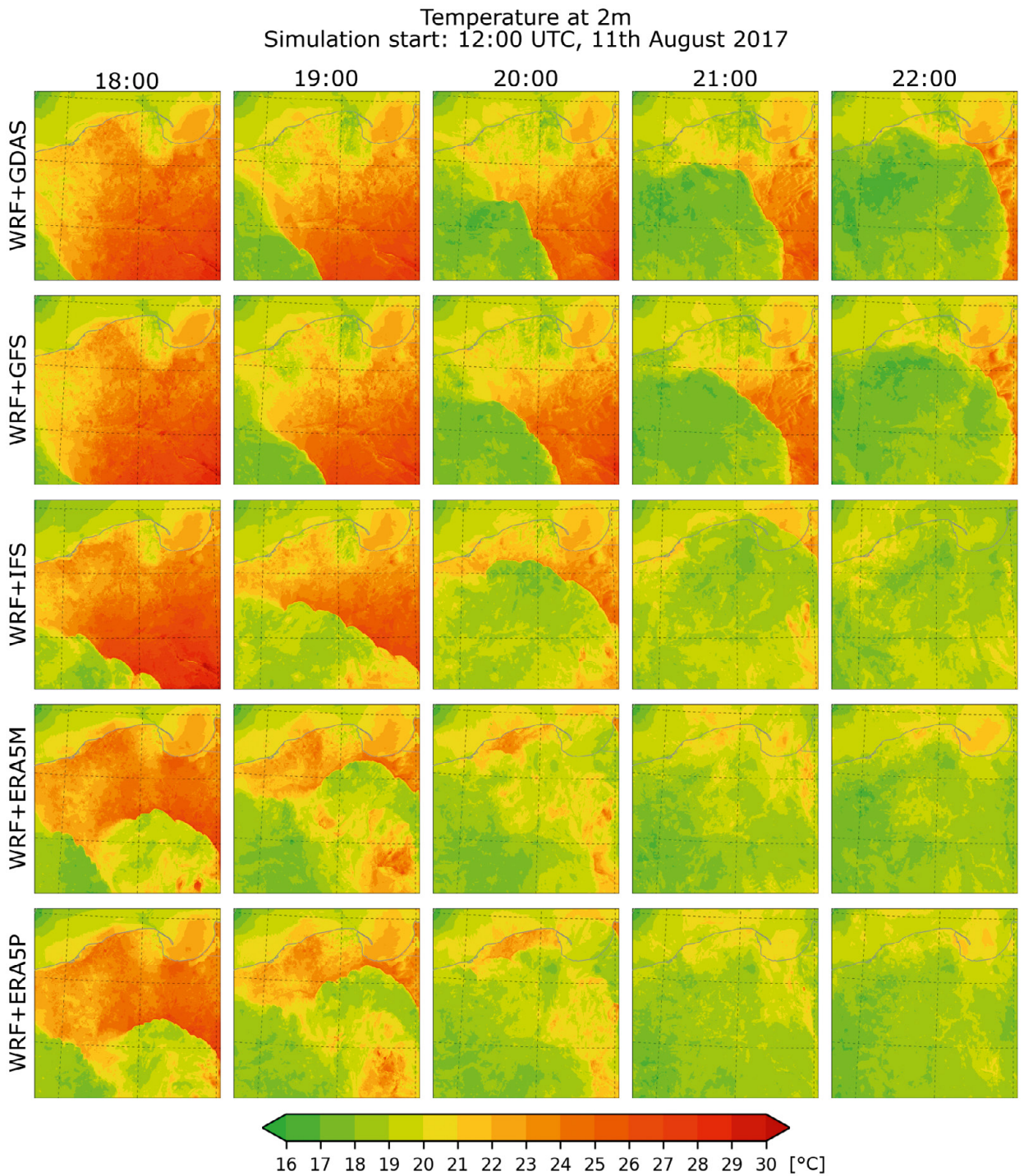
Fig. A2. Temperature at 2 m derived from the WRF between 1800 and 2200 UTC with various initial conditions: GDAS, GFS, IFS, ERA5M (model levels), ERA5P (pressure levels). Forecast start: 1200 UTC, 11th August 2017.
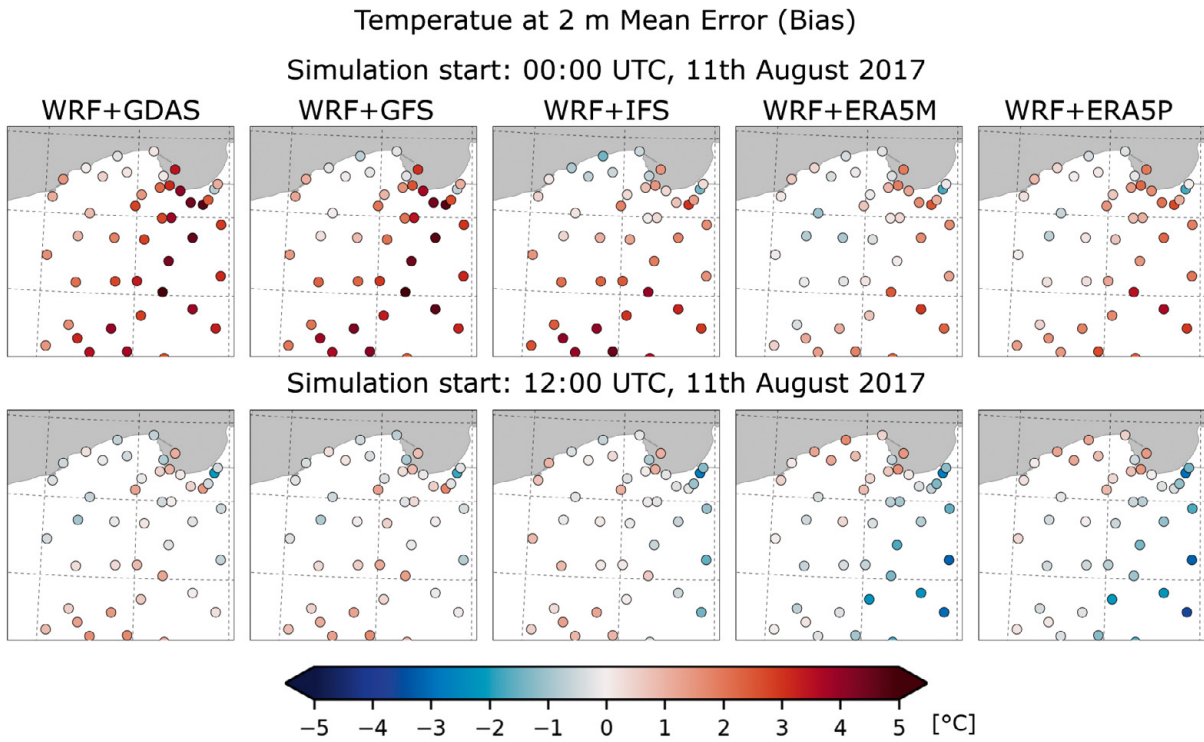
Fig. A3. Mean error (bias) of air temperature (at 2 m) derived from the WRF model and from in situ observations at meteorological stations. Only data between 1700 and 2400 UTC were analyzed.
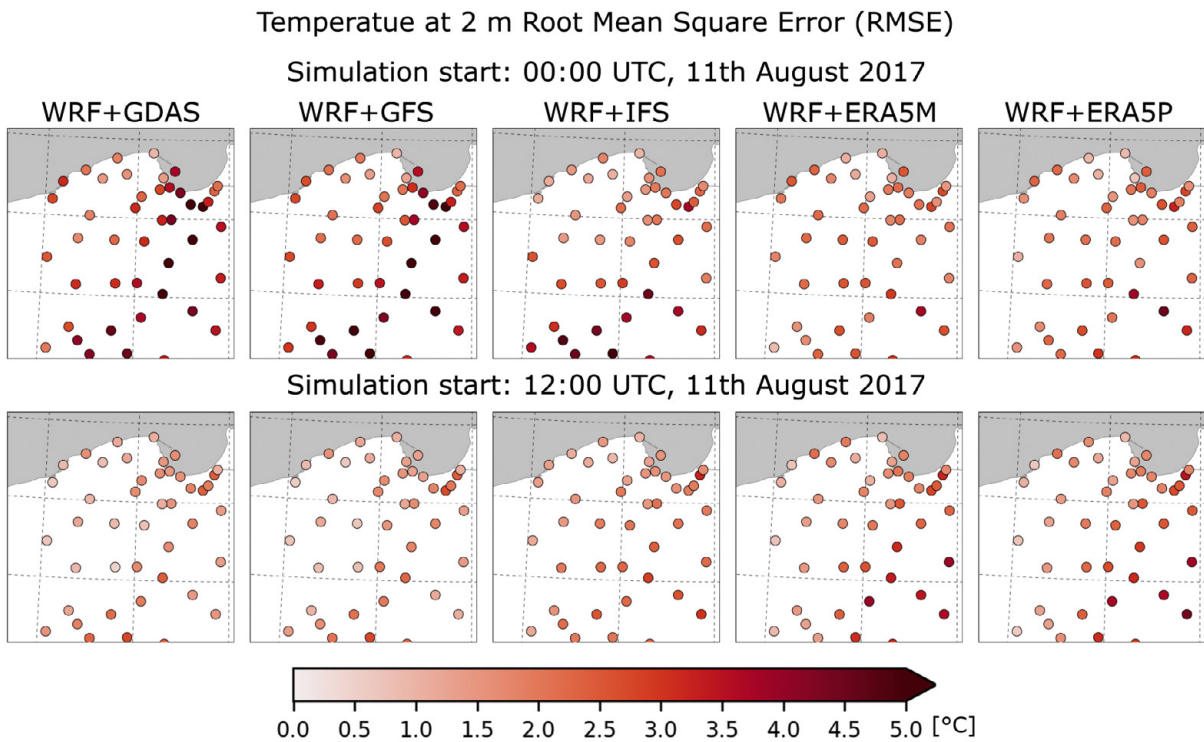
Fig. A4. Root mean square error (RMSE) of air temperature (at 2 m) derived from the WRF model and from in situ observations at meteorological stations. Only data between 1700 and 2400 UTC were analyzed.

Temperatue at 2 m Correlation (R)

Simulation start: 00:00 UTC, 11th August 2017

WRF+GDAS   WRF+GFS   WRF+IFS   WRF+ERA5M   WRF+ERA5P

Simulation start: 12:00 UTC, 11th August 2017

0.5   0.6   0.7   0.8   0.9   1.0
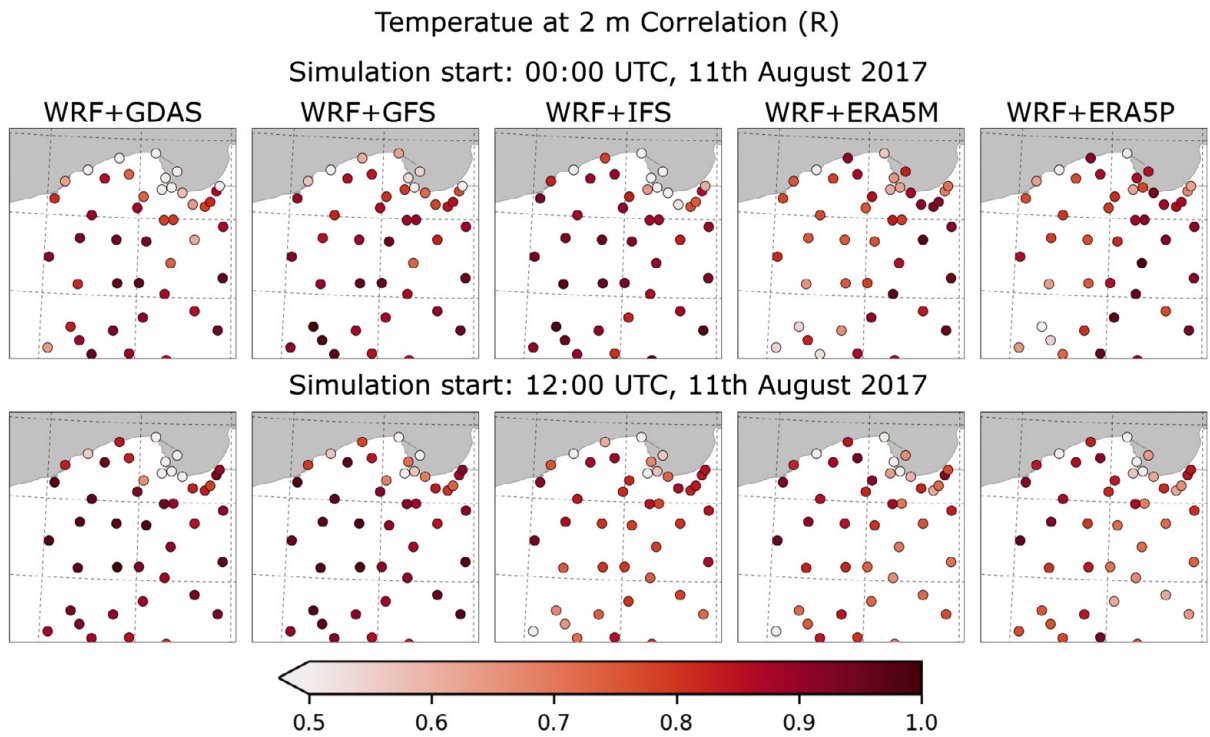
Fig. A5. Correlation of air temperature (at 2 m) derived from the WRF model and from in situ observations at meteorological stations. Only data between 1700 and 2400 UTC were analyzed.
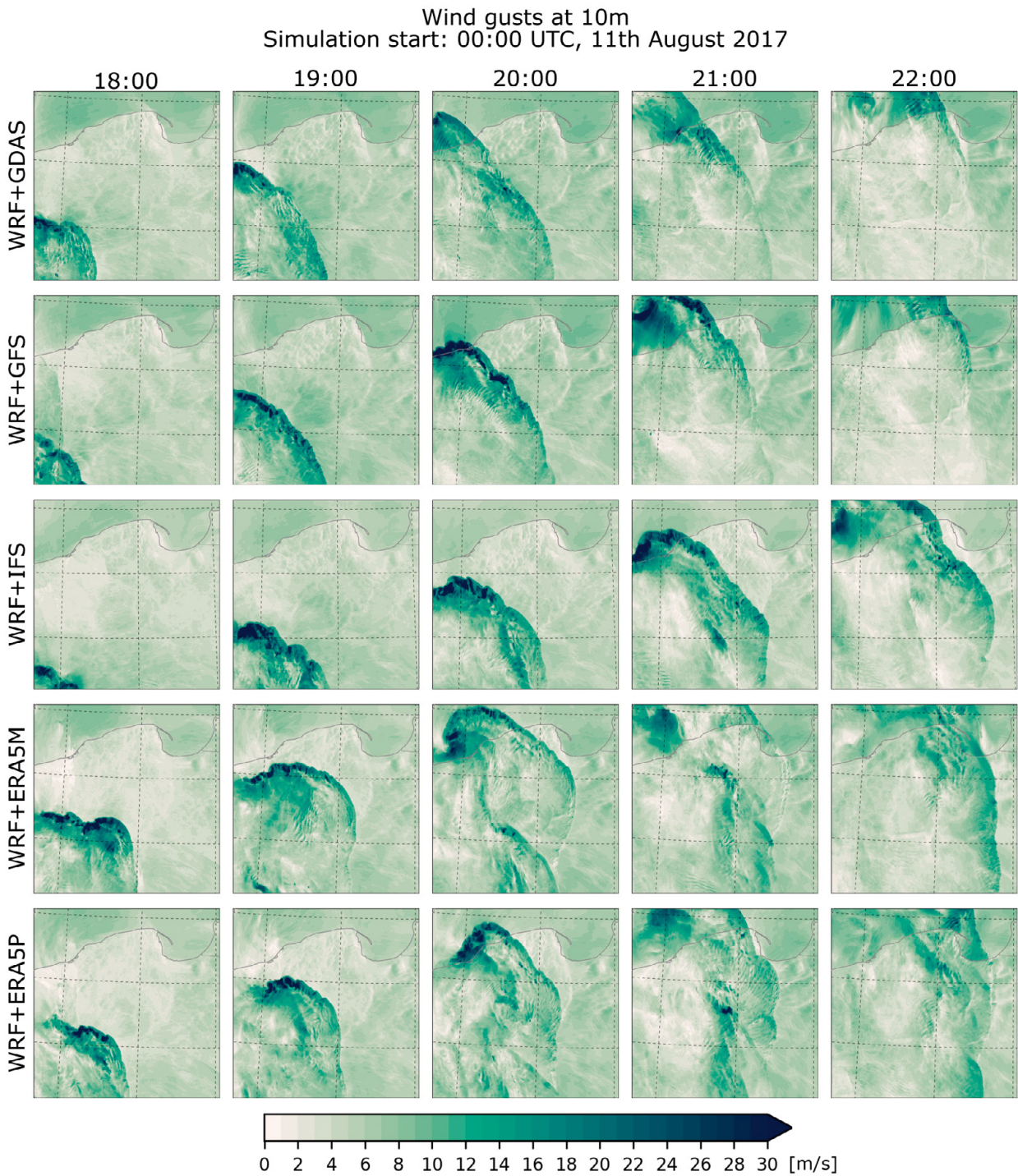
Fig. A6. Wind gusts at 10 m derived from the WRF between 1800 and 2200 UTC with various initial conditions: GDAS, GFS, IFS, ERA5M (model levels), ERA5P (pressure levels). Forecast start: 0000 UTC, 11th August 2017.

Fig. A7. Wind gusts at 10 m derived from the WRF between 1800 and 2200 UTC with various initial conditions: GDAS, GFS, IFS, ERA5M (model levels), ERA5P (pressure levels). Forecast start: 1200 UTC, 11th August 2017.

Wind speed at 10 m Mean Error (bias)

Simulation start: 00:00 UTC, 11th August 2017

WRF+GDAS　　WRF+GFS　　WRF+IFS　　WRF+ERA5M　　WRF+ERA5P
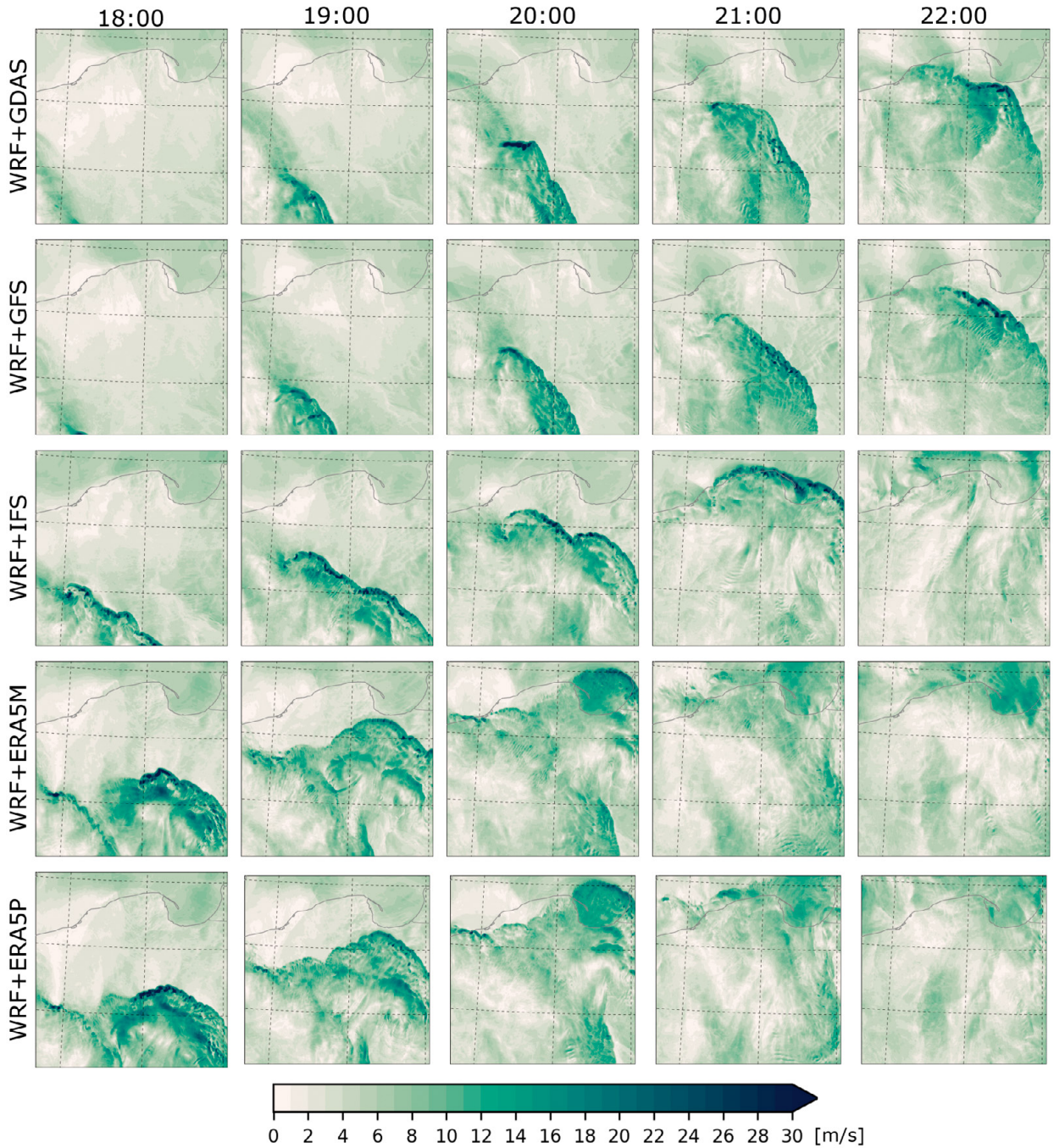
Simulation start: 12:00 UTC, 11th August 2017
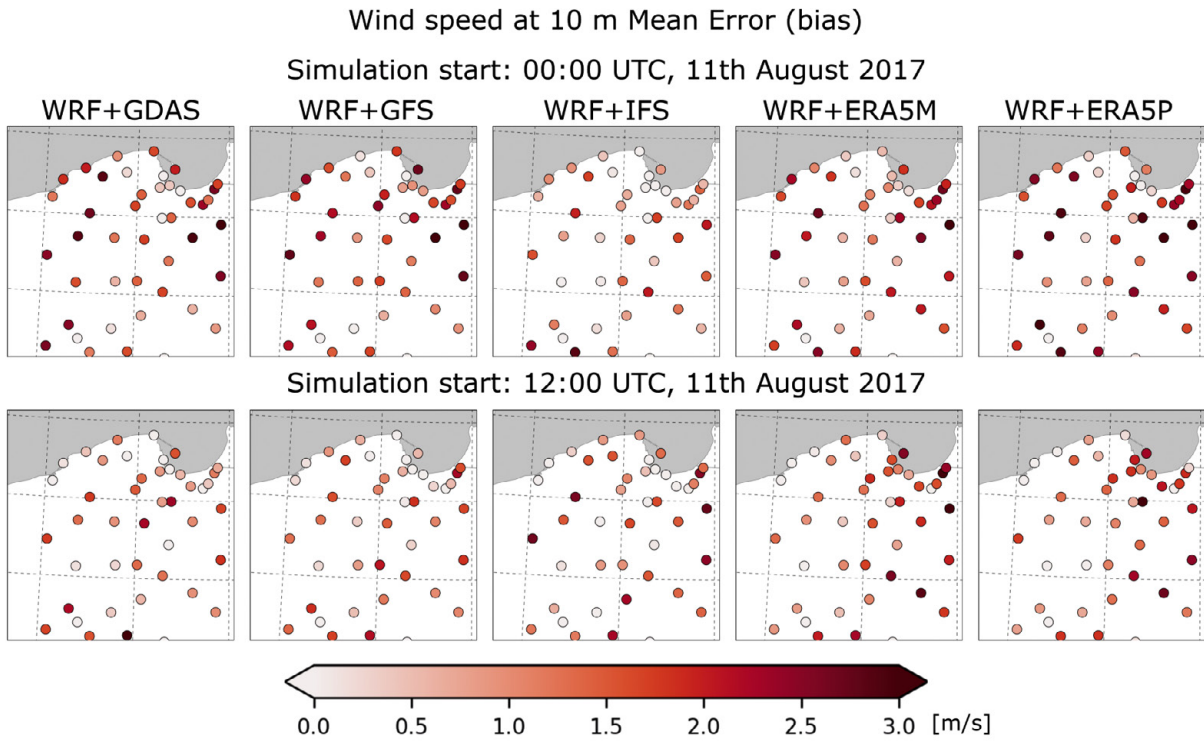
Fig. A8. Mean error (bias) of wind speed (at 10 m) derived from the WRF model and from in situ observations at meteorological stations.
Only data between 1700 and 2400 UTC were analyzed.

Wind speed at 10 m Root Mean Square Error (RMSE)

Simulation start: 00:00 UTC, 11th August 2017

WRF+GDAS　　WRF+GFS　　WRF+IFS　　WRF+ERA5M　　WRF+ERA5P

Simulation start: 12:00 UTC, 11th August 2017
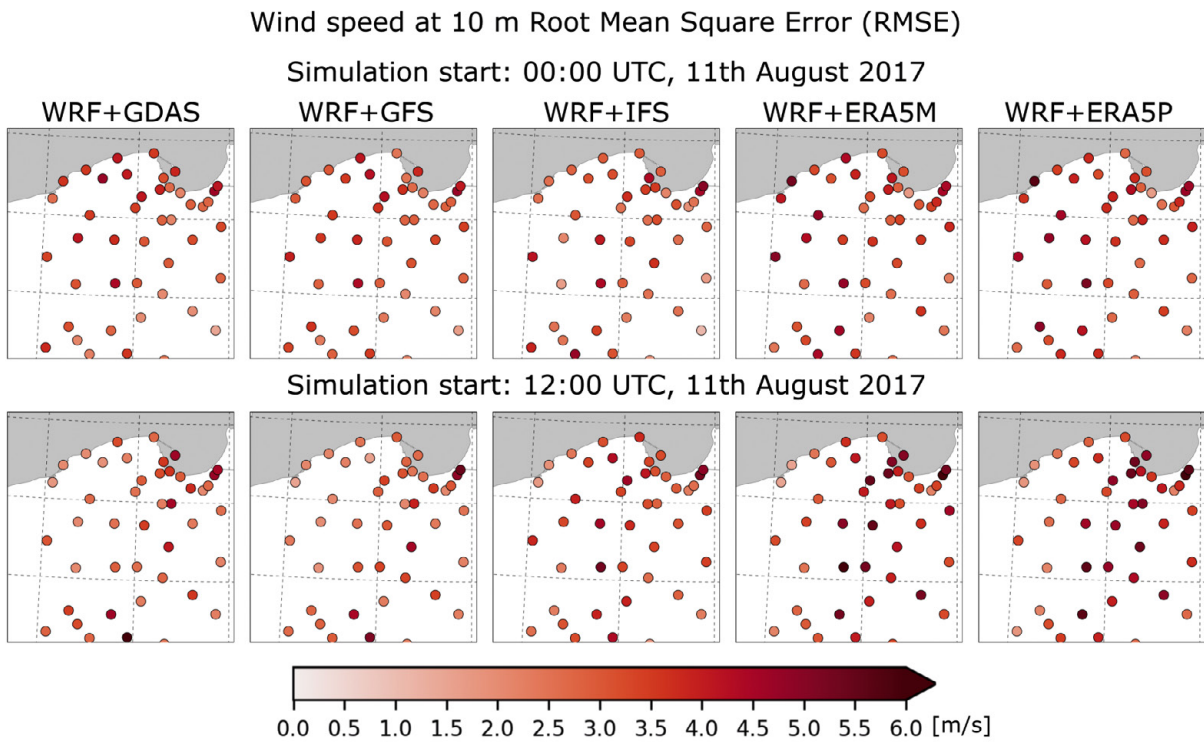
Fig. A9. Root mean square error (RMSE) of wind speed (at 10 m) derived from the WRF model and from in situ observations at meteorological stations.
Only data between 1700 and 2400 UTC were analyzed.

Wind speed at 10 m Correlation (R)

Simulation start: 00:00 UTC, 11th August 2017

WRF+GDAS	WRF+GFS	WRF+IFS	WRF+ERA5M	WRF+ERA5P

Simulation start: 12:00 UTC, 11th August 2017
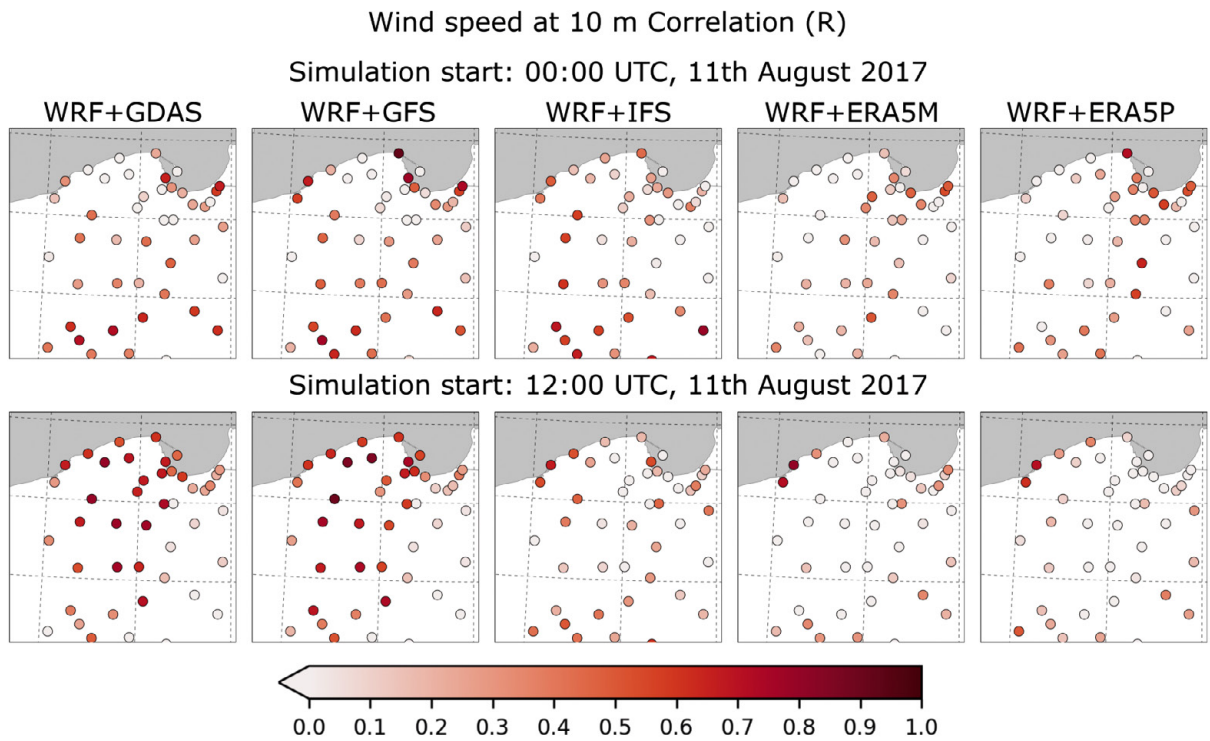
Fig. A10. Correlation of wind speed (at 10 m) derived from the WRF model and from in situ observations at meteorological stations. Only data between 1700 and 2400 UTC were analyzed.

Accumulated precipitation
Simulation start: 00:00 UTC, 11th August 2017
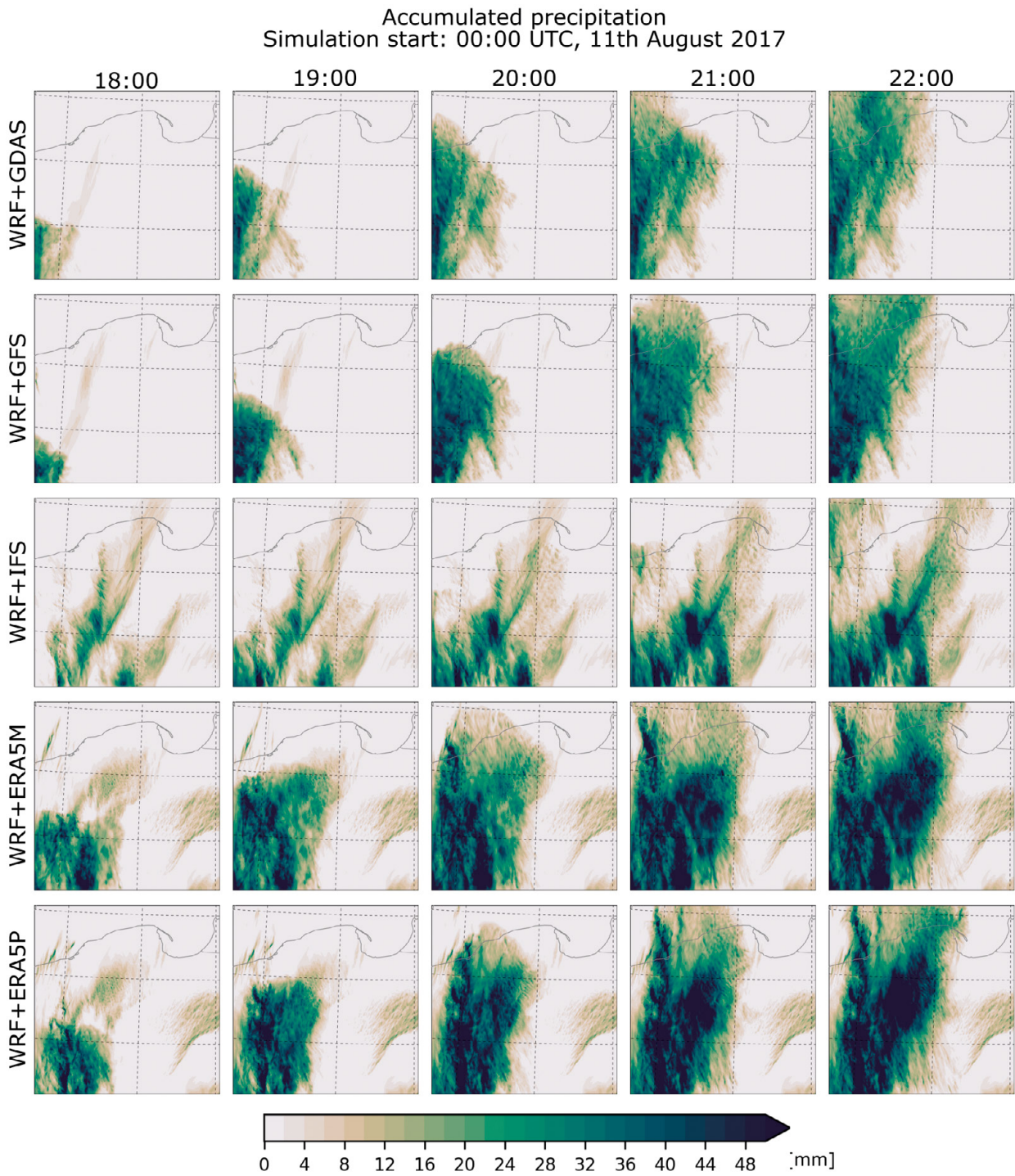
Fig. A11. Accumulated precipitation derived from the WRF between 1800 and 2200 UTC with various initial conditions: GDAS, GFS, IFS, ERA5M (model levels), ERA5P (pressure levels). Forecast start: 0000 UTC, 11th August 2017.
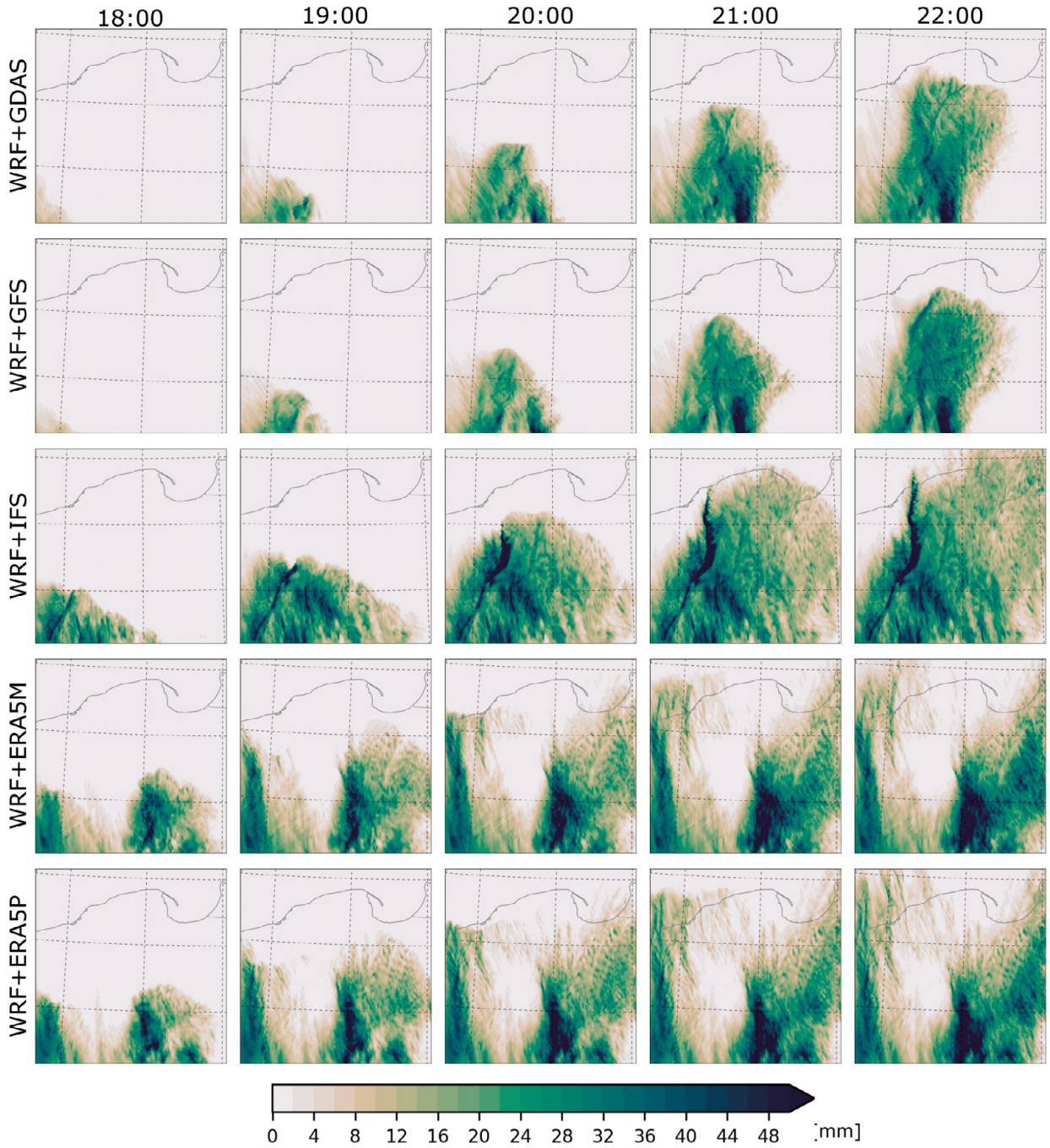
Fig. A12. Accumulated precipitation derived from the WRF between 1800 and 2200 UTC with various initial conditions: GDAS, GFS, IFS, ERA5M (model levels), ERA5P (pressure levels). Forecast start: 1200 UTC, 11th August 2017.

Precipitation > 0.5 mm critical success index (CSI)

Simulation start: 00:00 UTC, 11th August 2017

WRF+GDAS   WRF+GFS   WRF+IFS   WRF+ERA5M   WRF+ERA5P

Simulation start: 12:00 UTC, 11th August 2017
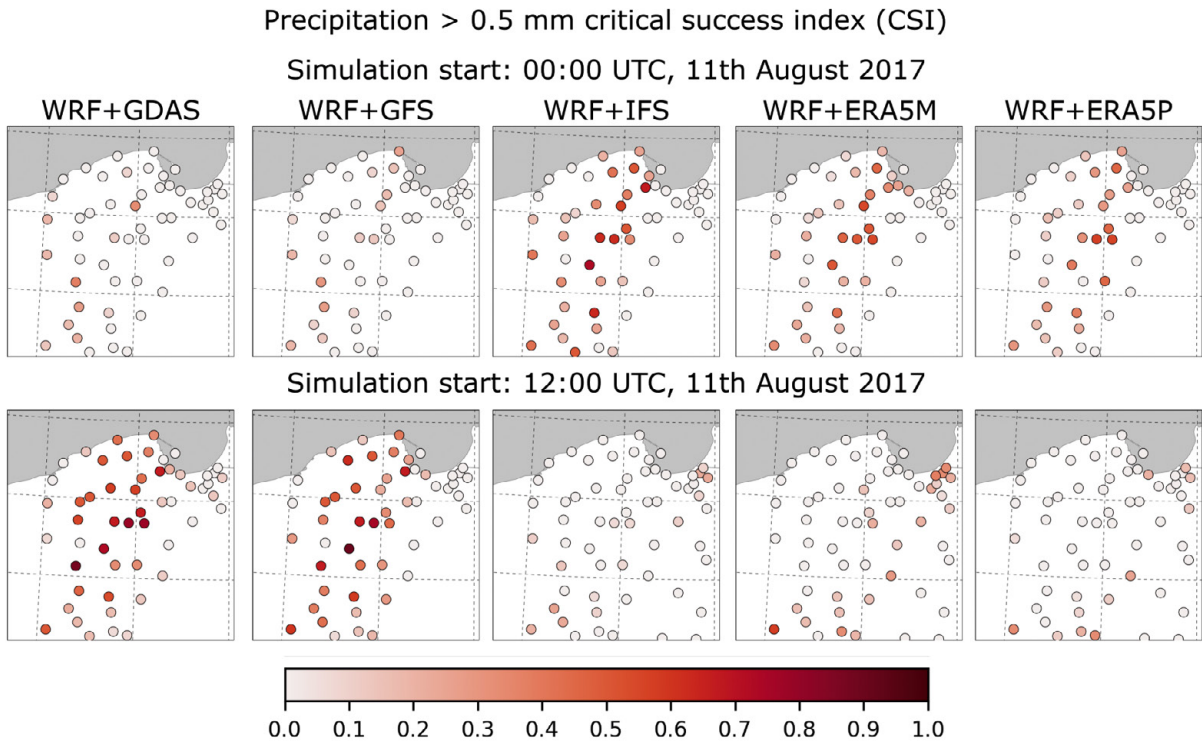
Fig. A13. Critical success index (CSI) of precipitation events > 0.5 mm·10min-1 derived from the WRF model and from in situ observations at meteorological stations. Only data between 1700 and 2400 UTC were analyzed.

Precipitation > 1.0 mm critical success index (CSI)

Simulation start: 00:00 UTC, 11th August 2017

WRF+GDAS   WRF+GFS   WRF+IFS   WRF+ERA5M   WRF+ERA5P

Simulation start: 12:00 UTC, 11th August 2017
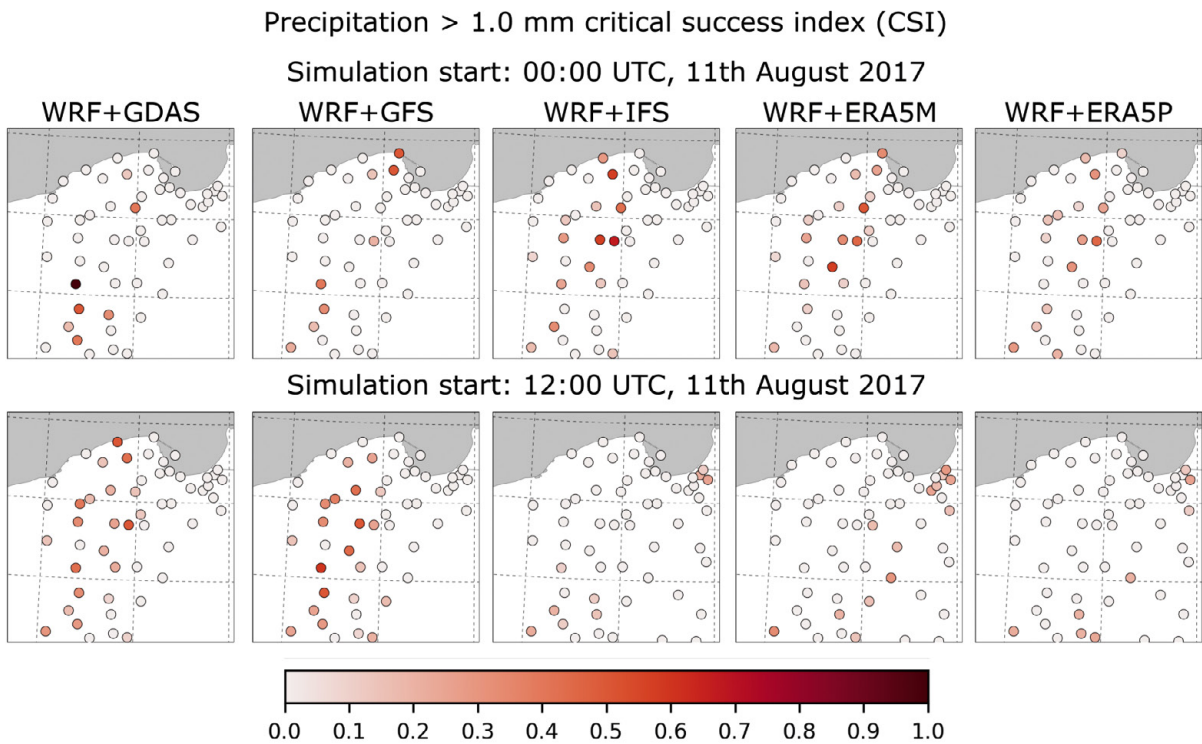
Fig. A14. Critical success index (CSI) of precipitation events > 1 mm·10 min-1 derived from the WRF model and from in situ observations at meteorological stations. Only data between 1700 and 2400 UTC were analyzed.

Wind gusts > 5 m/s critical success index (CSI)

Simulation start: 00:00 UTC, 11th August 2017

WRF+GDAS   WRF+GFS   WRF+IFS   WRF+ERA5M   WRF+ERA5P

Simulation start: 12:00 UTC, 11th August 2017

0.0 0.1 0.2 0.3 0.4 0.5 0.6 0.7 0.8 0.9 1.0
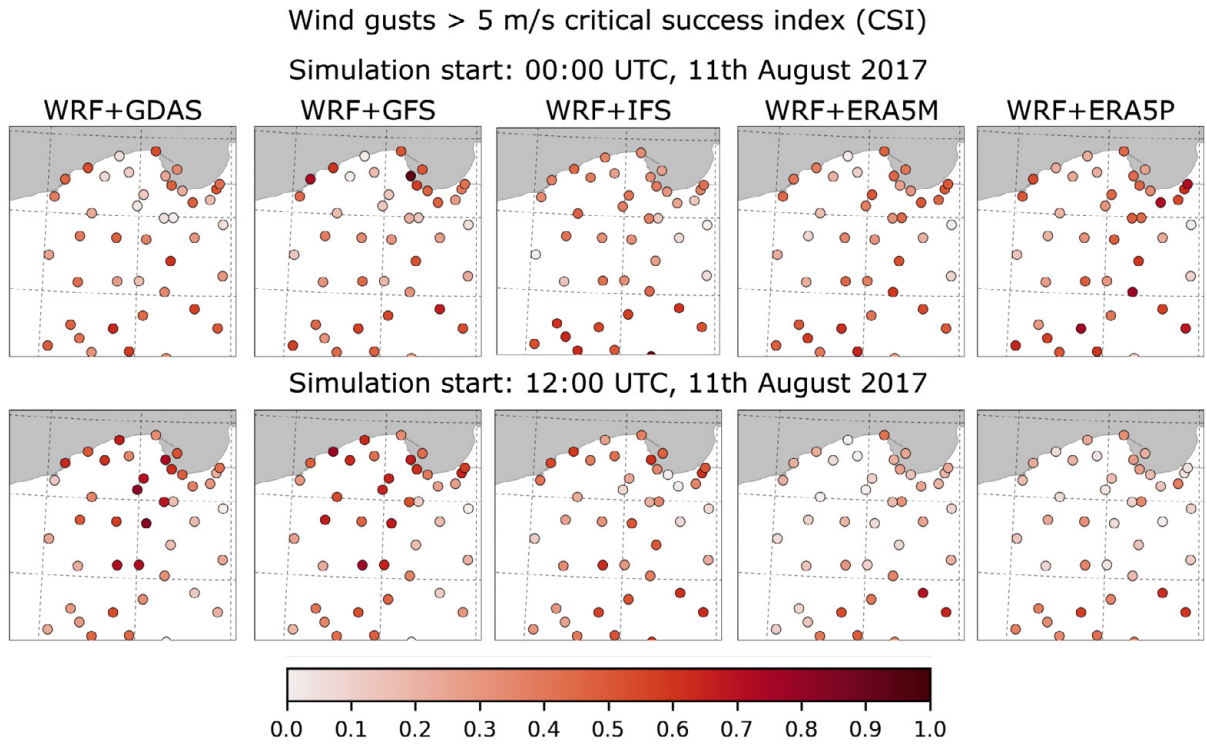
Fig. A15. Critical success index (CSI) of wind gust events > 5 m·s-1 derived from the WRF model and from in situ observations at meteorological stations. Only data between 1700 and 2400 UTC were analyzed.

Wind gusts > 10 m/s critical success index (CSI)

Simulation start: 00:00 UTC, 11th August 2017

WRF+GDAS   WRF+GFS   WRF+IFS   WRF+ERA5M   WRF+ERA5P

Simulation start: 12:00 UTC, 11th August 2017

0.0 0.1 0.2 0.3 0.4 0.5 0.6 0.7 0.8 0.9 1.0
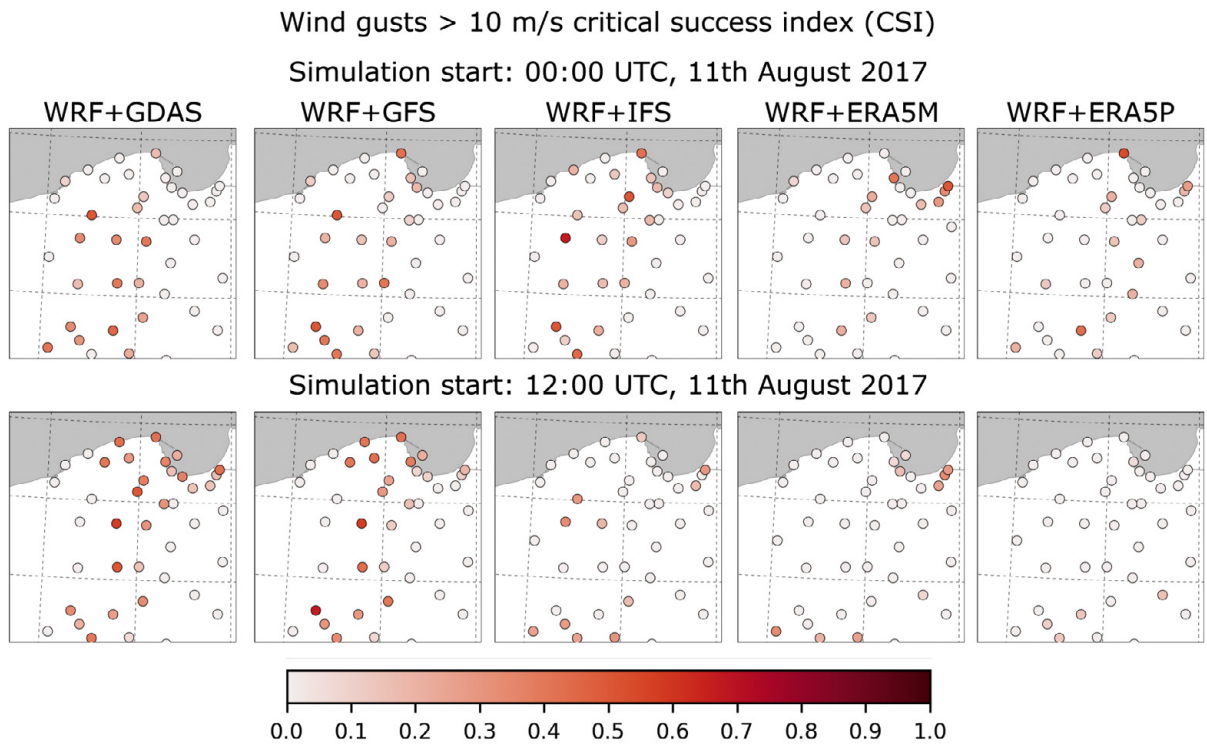
Fig. A16. Critical success index (CSI) of wind gust events > 10 m·s-1 derived from the WRF model and from in situ observations at meteorological stations. Only data between 1700 and 2400 UTC were analyzed.
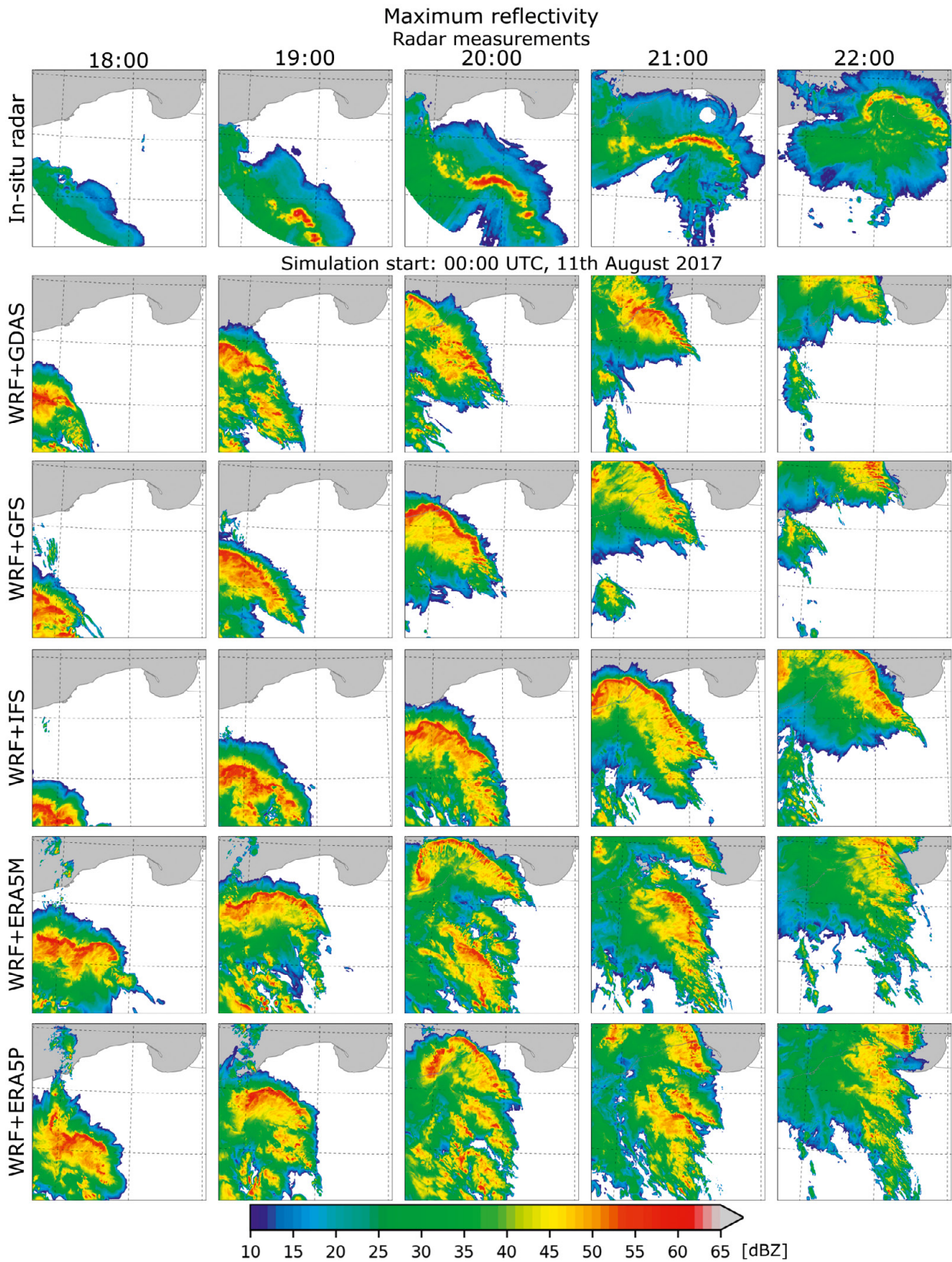
Fig. A17. Maximum reflectivity derived from the WRF between 1800 and 2200 UTC with various initial conditions: GDAS, GFS, IFS, ERA5M (model levels), ERA5P (pressure levels). Forecast start: 0000 UTC, 11th August 2017. For comparison, data from meteorological radar are presented at the top.

Maximum reflectivity
Radar measurements
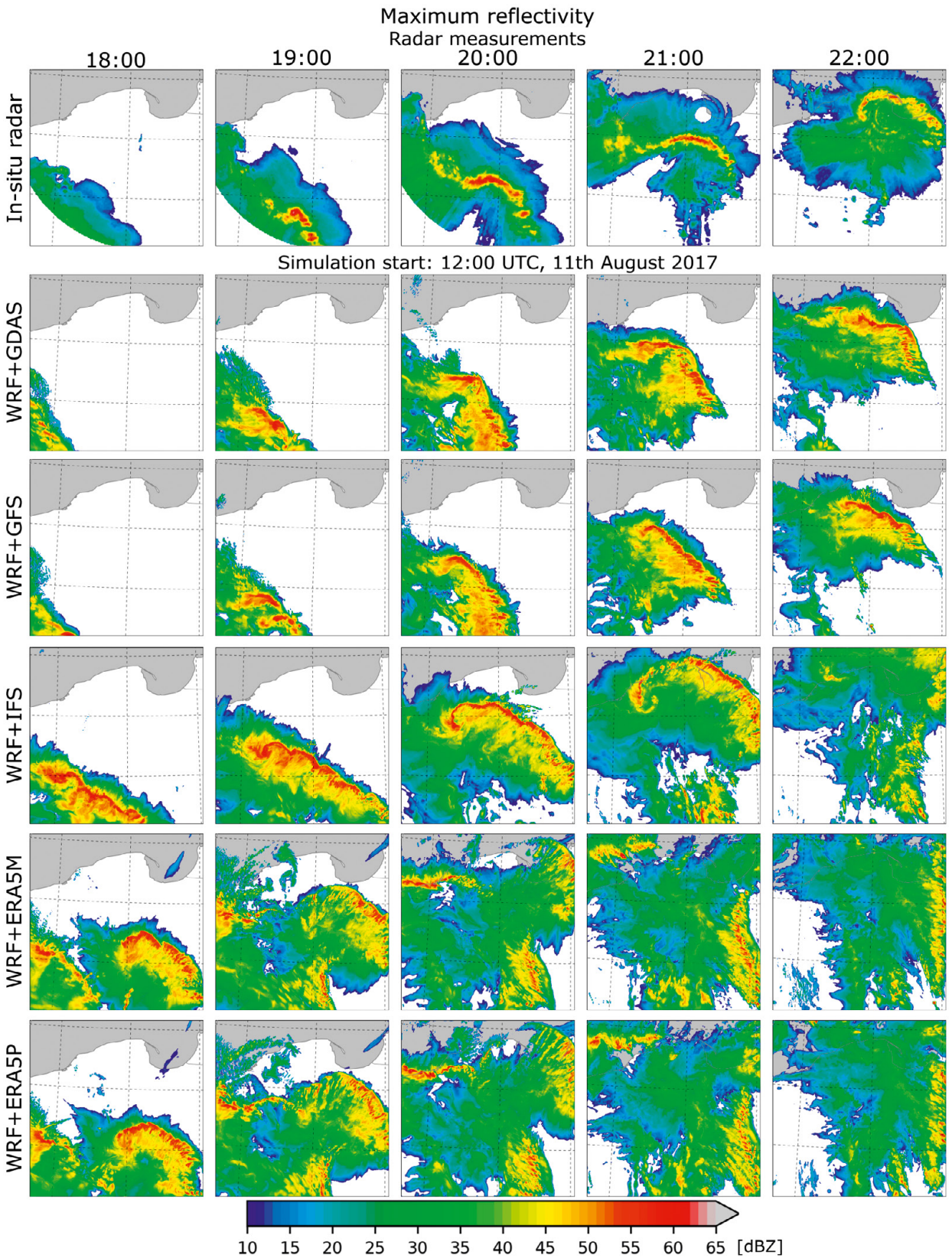
Fig. A18. Maximum reflectivity derived from the WRF between 1800 and 2200 UTC with various initial conditions: GDAS, GFS, IFS, ERA5M (model levels), ERA5P (pressure levels). Forecast start: 1200 UTC, 11th August 2017. For comparison, data from meteorological radar are presented at the top.

Using ALARO and AROME numerical weather prediction models for the derecho case on 11 August 2017

Marcin Kolonko, Małgorzata Szczęch-Gajewska, Bogdan Bochenek, Gabriel Stachura, Piotr Sekuła
Institute of Meteorology and Water Management – National Research Institute

ABSTRACT. On average, a derecho occurs once a year in Poland while bow echoes happen several times per year. On 11 August 2017, severe meteorological phenomena were observed in Poland, including extremely strong wind gusts. We focused especially on the convective windstorm of a derecho type which occurred on that date in northern and north-western Poland. A rapidly moving mesoscale convective system (MCS) resulted in a bow echo, a mesoscale convective vortex (MCV), and finally fulfilled the criteria for a derecho. To establish whether our operational models in the Institute of Meteorology and Water Management, National Research Institute (IMGW-PIB) could reproduce a derecho of such intensity as that of 11 August 2017, the results from two mesoscale numerical weather prediction models were analyzed. The Application of Research to Operation at Mesoscale (AROME) and the ALADIN & AROME (ALARO) models were applied in the non-hydrostatic regime. We also examine how models differ with respect to mesoscale convective system drivers (such as vertical wind shear and convective available potential energy) and representation of deep convection (e.g., vertical velocities, cold pool generation). Forecasts are compared with observations of wind gusts and radar data. Severe weather phenomena, such as rear inflow jet and cold pool, were predicted by both models, visible on the maps of the wind velocity at 850 and 925 hPa pressure levels and on the map of air temperature at 2 m above the ground level, respectively. Relative vorticity maps of the middle and lower troposphere were analyzed for understanding the evolution of MCV.

KEYWORDS: Derecho, mesocyclone convective system, mesoscale convective vortex, numerical weather prediction model, ALARO model, AROME model.

1. INTRODUCTION

Early forecasting and warning about the possibility of severe convective phenomena, such as mesoscale convective system (MCS), mesoscale convective vortex (MCV), rear inflow jet (RIJ), can be supported by mesoscale numerical weather models with kilometer-scale resolution (Baldauf et al. 2011; Seity et al. 2011; Powers et al. 2017). Compared to global models, limited-area models have the advantage of providing more realistic representation of small-scale phenomena. However, in some convective situations they are still subject to imperfections (Bouttier, Marchal 2020; Schumacher, Rasmussen 2020).

Severe thunderstorms accompanied by strong wind gusts, intense precipitation, hail, and even tornadoes occur every summer in central Europe. In Poland, such phenomena are most frequent in July, between 14 and 16 UTC and over the southeastern parts of the country (Poręba et al. 2022). Well-organized storm complexes, which create their own internal circulation and require stronger environmental wind shear, are called mesoscale convective systems (MCS). One of the first attempts to investigate morphological and precipitation archetypes of MCSs over Poland was presented by Surowiecki and Taszarek (2020). They studied which fraction of active MCS are Quasi-Linear Convective Systems (QLCS), and how often in QLCS the bow echo emerges. The conclusion is that bow echoes appear in 72% of QLCS, and QLCS in 17% of MCS. On the other hand, only 3.5% of MCS were associated with MCV. The squall bow (radar signature of bow echo) happens a few times a year in Poland, whereas its more dangerous version, derecho, happens once per year on average (Celiński-Mysław, Matuszko 2014; Celiński-Mysław et al. 2019). In the paper of Gatzen et al. (2020), the average frequency of derechos in Germany was estimated to be about 2 each year. Studies of convective windstorms in Europe, based on climatological data and reports from the European Severe Weather Database (ESWD) indicates that only 10% of convective windstorms were associated with bow echoes (Pacey et al. 2021).

The evolving convective system observed on 11 August 2017 fulfilled criteria for a derecho, with observed maximal wind gusts exceeding 42 m·s^{-1} (150 km·h^{-1}; Taszarek et al. 2019) and was accompanied by a Mesoscale Convective Vortex (MCV). In northwestern Poland huge material damages were reported, including almost 80,000 ha of devastated forest and 6 fatalities (Chmielewski et al. 2020).

Detailed analysis of radar data from 11 August 2017 (using composite maximum reflectivity and radial velocities) confirmed the presence of MCV within the mature stage of MCS (Taszarek et al. 2019; Figurski et al. 2021; Łuszczewski, Tuszyńska 2022). The MCV occurs within surface frontal zones with large temperature and moisture gradients across the environmental vertical shear vector (Davis, Trier 2007). Raymond and Jiang (Walter 2016) idealized MCVs as balanced mid-tropospheric potential vorticity anomalies and postulated that the lifting associated with potential vorticity anomalies in vertical shear may explain some cases of MCS longevity. Placement and evolution of the MCV is presented on relative vorticity maps (Fig. 8).

Typical for MCS is also a presence of a cold pool which emerges under strong convection zone and closely behind it, in an area of higher pressure (Fujita 1960). The cold pool is an area of cold air near the ground created by a downdraft and a loss of heat due to evaporation of rain (Charba 1974). It contributes to creation of new convective cells and supports a squall line (Goff 1976; Droegemeier, Wilhelmson 1985). At the back of the MCS, a current called Rear Inflow Jet (RIJ) can emerge, blowing perpendicularly to a squall line, in agreement with the direction of MCS movement (Houze 2004). It helps to deliver cool and dry air from middle layers of the troposphere (around 500-700 hPa) to the ground (Glickman 2000).

During the past few decades numerous developments in physical parameterizations and data assimilations have been applied to more precise model predictions of mesoscale convective windstorms (e.g. Brousseau et al. 2016; Tao et al. 2016; Wimmer et al. 2021). In a crucial study, Weisman et al. (2013) described a derecho in the United States using the Advanced Research core of the Weather Research and Forecasting model (WRF-ARW)) with spatial resolution of 3 km × 3 km and the explicit convection-permitting algorithm. Dixon (2016) tested capabilities of data assimilation for improving model forecasts at horizontal grid sizes of 10 km × 10 km and 4 km × 4 km when predicting the derecho situation of 29 June 2012 in Utah. Because the event of 11 August 2017 in Poland caused huge material damage, it has been the subject of studies by many research groups. Taszarek et al. (2019) is one of the most significant review papers related to the 11 August 2017 derecho, in which the NWP, synoptic, and radar contexts are thoroughly described. Tropospheric parameters during that day were also analyzed with global navigation satellite systems (GNSS) to estimate precipitable water vapor (PWV) (Nykiel et al. 2019). The study has proven it possible to monitor the derecho event with GNSS. Another study (Figurski et al. 2021) aimed to assess the impact of initial and boundary conditions on severe weather simulations using a high-resolution WRF model with four global model predictions. The study indicated that the best forecast was obtained using initial/boundary conditions from the National Centers for Environmental Prediction (NCEP) Global Data Assimilation System (GDAS) and Global Forecasting System (GFS) models at 12 UTC, while using the ERA5 (Hersbach et al. 2020) data gave the predictions least consistent with the observations of the maximum reflectivity fields (Figurski et al. 2021).

The research reported here was undertaken to assess quantitatively different configurations of ALARO and AROME models for the derecho of 11 August 2017. We have verified how different initial and boundary conditions affect the quality of simulations by using two non-hydrostatic models, ALARO and AROME. Studies were also designed to estimate which meteorological fields (e.g., wind gusts, CAPE, 0-3 km wind shear) would be appropriate for prediction of such phenomena.

All the analyses of the forecasts of severe weather phenomena (related to wind gusts) by ALARO and AROME refer to the forecasts for 11 August 2017. Both models were computed for 3 sets of different initial conditions: 00 UTC (from now on, r00 run), 06 UTC (r06 run) and 12 UTC (r12). In Section 2, the synoptic context of the 11 August 2017 derecho is described; data and methods are presented in Section 3. The results (mainly forecast maps and their description) can be found in Section 4. Section 5 is their discussion and Chapter 6 presents general conclusions. The last Section 7 contains summary and outlook.

2. SYNOPTIC SITUATION

The synoptic situation which led to the storm on 11 August 2017 is described in the paper of Wrona et al. 2022 (see also Figurski et al. 2021). From 9 August 2017, warm and moist tropical air was advected over central and eastern Poland and persisted for several days. In the meantime, cold, polar-maritime air lingered above Germany. At the level of 850 hPa the temperature difference between the air masses reached 10 C. The temperature gradient was visible also on the prognostic maps of the ALARO model (Fig. 1). This gradient was gradually increasing due to frontogenesis over the western border of Poland.

Developing storms in a warm air mass before a waving front (Fig. 2) transformed from single cells and disorganized multi-cell systems into supercells and coalesced into the large MCS (Taszarek et al. 2019; Łuszczewski, Tuszyńska 2022). Then a quasi-linear-convective-system (QLCS) developed and finally turned into a strong bow echo and MCV. The radar signature
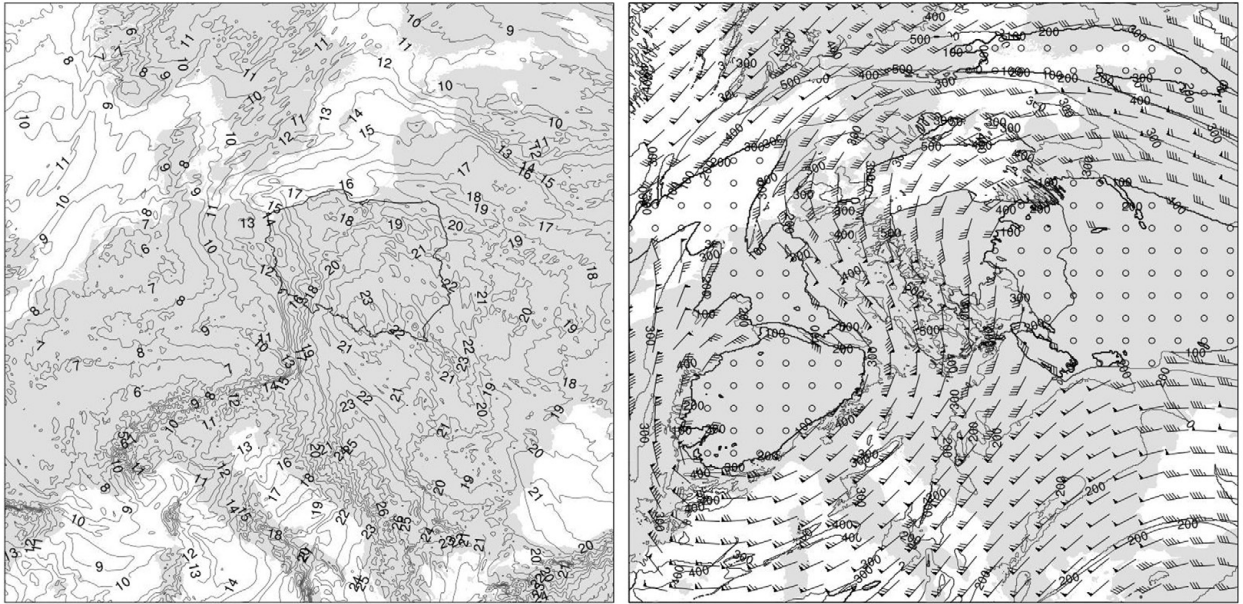
Fig. 1. The ALARO NH forecast for r00 run at 15 UTC on 11 August 2017. On the left panel, the temperature at the 850 hPa pressure level; on the right panel, jet stream and pressure at the height of 11 km (ICAO tropopause).
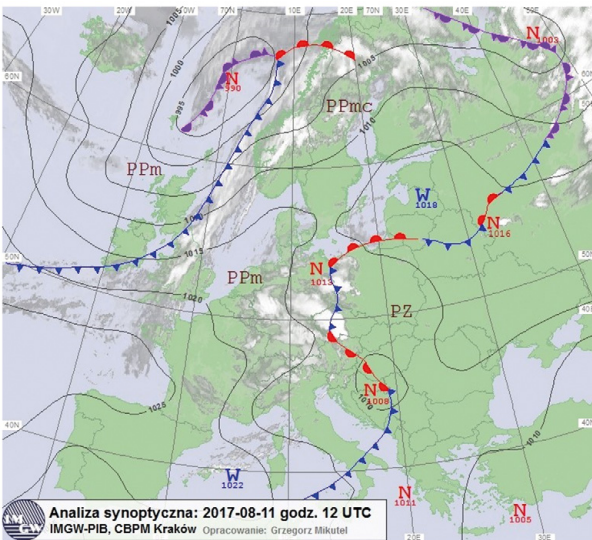
Fig. 2. The synoptic situation on 11 August 2017, 12 UTC. Credit: IMWM-NRI, Central Office for Meteorological Forecasts, Krakow.
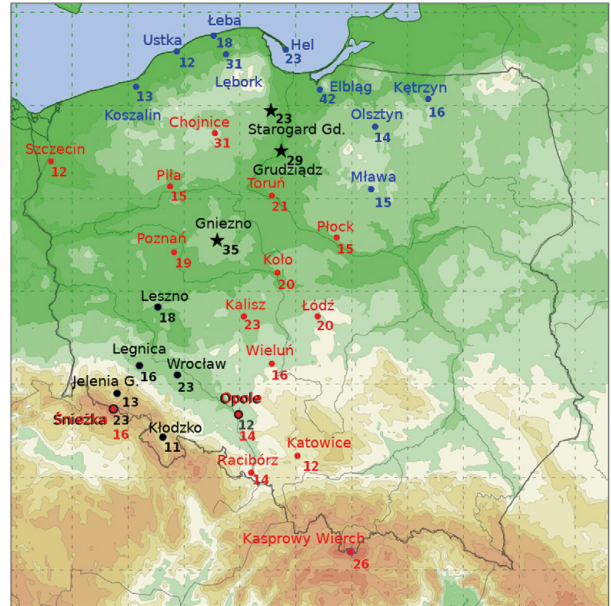
Fig. 3. Synoptic stations on which wind gusts exceeded 10 m·s-1 on 11 of August 2017. Colors refer to the following time spans: 15:00-18:00 UTC (black), 18:00-21:00 UTC (red) and 21:00-24:00 UTC (blue). Stations marked with stars are later used for quantitative evaluation of forecasted wind gusts.

of the bow echo indicates the possibility of strong wind gusts in that area. We checked that it corresponds with the maps of CMAX simulated by NWP models (Fig. 7). Additionally, on the basis of vertical wind profiles from Prag, Prostejov, and Wroclaw we reasoned the existence of a strong jet stream.

The velocities of wind gusts that exceeded 10 m·s^{-1} on 11 of August 2017, as well as station names, are plotted on Figure 3. (The forecasted velocities are plotted on the map in Figure 4b.) Colors refer to the following time spans: 15:00-18:00 UTC (black), 18:00-21:00 UTC (red) and 21:00-24:00 UTC (blue), while velocities are expressed in m·s^{-1}. Stations marked with stars are later used for quantitative evaluation of forecasted wind gusts.

The wind gusts approached from the southwest. Initially, high values were recorded before 15 UTC on synoptic stations at Śnieżka and Kasprowy Wierch (not marked on the map). Then the zone of extreme wind values moved to central Poland and then northwards. The top wind gust speed, 42 m·s^{-1},was recorded in Elbląg.

3. DATA AND METHODS

In the Center for Meteorological Modelling of the Institute of Meteorology and Water Management – National Research Institute (IMGW-PIB), two models of Aire Limitée Adaptation Dynamique Development International (ALADIN) have been used operationally for nearly 3 years for numerical weather prediction (NWP): Application of Research to Operation at Mesoscale (AROME) and ALARO (ALADIN-AROME) in version cy43t2. Both ALARO and AROME are the part of the Aladin System developed by the international consortium ACCORD (ALADIN until November 2020) and successors of the former ALADIN model (also used by the ALADIN
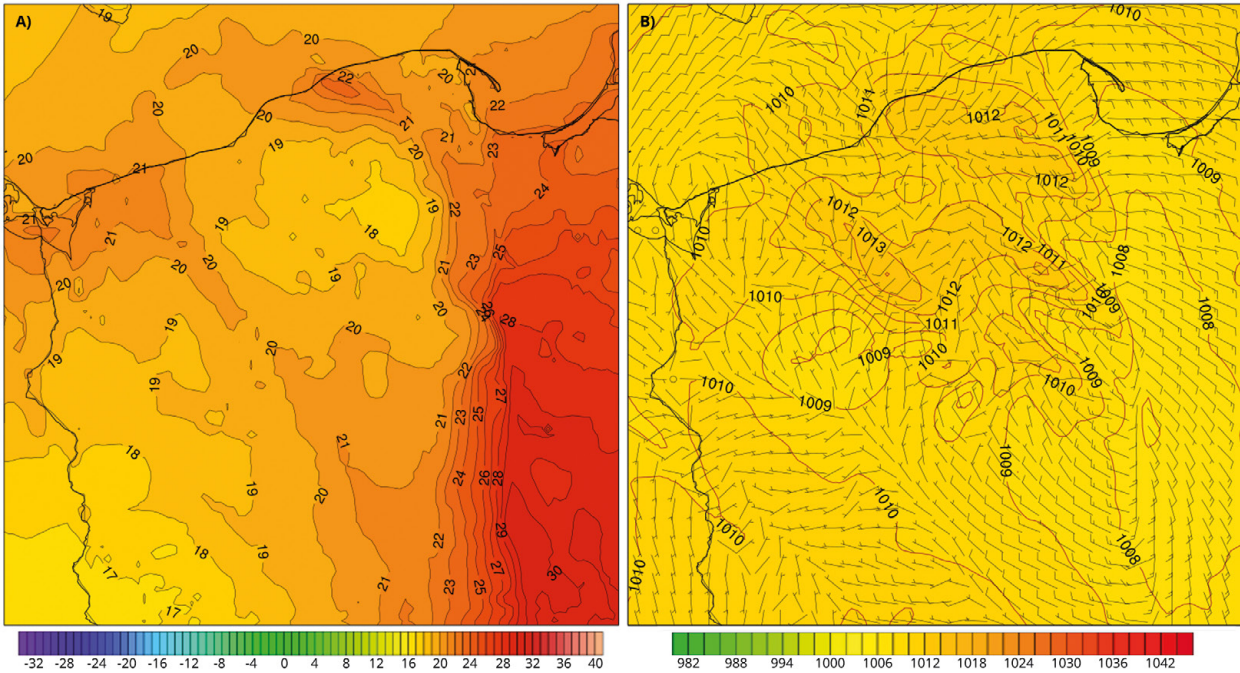
Fig. 4. Cold pool from ALARO: a) temperature at 2 m AGL; b) atmospheric pressure and surface wind. The forecast for 21 UTC 11 August 2017, r00.

Poland team). Both models in their earlier versions were used previously for prediction of severe storms (Seity et al. 2011; De Meutter et al. 2015).

The ALARO is non-hydrostatic (contrary to its predecessor, ALADIN), includes vertical accelerations in the equations of motion and has a shorter time step than ALADIN. The current version of the model uses a 4 km × 4 km horizontal grid, 60 hybrid vertical sigma-levels (following the orography) and has a forecast range of 72 h. Horizontally, the computing grid had 789 × 789 points and the domain was 3156 km × 3156 km. The initial and boundary conditions come from the global model ARPEGE in its cy42 version. The dynamical core of ALARO is based on fully compressible Euler equations. The surface processes' parameterization is based on the Interaction Soil-Biosphere-Atmosphere (ISBA) module. The microphysics scheme covers 6 types of hydrometeors: dry air, water vapor, suspended water, cloud ice crystals, rain, and snow (Lopez 2002). Shallow convection is computed according to the TOUCANS scheme, and deep convection by Modular and Mesoscale Microphysics and Transport (3MT, described by Gerard et al. 2009). For parameterization of clouds, the Cloud System Resolving Model (CSRM) and deep convection model were used (Termonia et al. 2018).

The AROME model was implemented with a horizontal grid size of 2 km × 2 km and 60 hybrid vertical levels (following the orography); it is non-hydrostatic and assumed to represent convection explicitly. It employs 799×799 grid points and the domain size is 1630 km × 1630 km. The forecast range equals 30 hours and one time step of integration is less than 1 minute. The initial and boundary conditions are taken from ALARO, which means that AROME is integrated after the end of ALARO forecast computation. Coupling of AROME version cy43t2 with ALARO occurs once every hour. The shallow convection scheme is described by Pergaud at al. (2009). Microphysics is parameterized by the three-phase ICE3 scheme, and the surface by the SURFEX module (Masson et al. 2013). The parameterization of clouds is done statistically, and there is no parameterization of deep convection (Seity et al. 2013). Both of these configurations were used in this study but were not available in 2017.

The fields used for the analysis of the situation include mesoscale drivers of convective system (such as Convective Available Potential Energy;

CAPE, and vertical wind shear), deep convection related parameters (e.g., vertical velocities and cold pools), as well as wind gusts, relative vorticity, reflectivity CMAX, wind, and 2 m temperature. CAPE as used in this study is the Most Unstable Convective Available Potential Energy (MU-CAPE), which computation starts from the parcel at the most unstable model level defined by the largest theta-e value. Derechos are frequently associated with MU-CAPE values in excess of 3000 J·kg^{-1} in the source region (Evans, Doswell 2001). Coniglio and Stensrud (2001) have shown that mid-level shear (0-3 km) helps to maintain deep convective systems and that shear exceeding 15 m·s^{-1} connected with sufficient instability may lead to very severe storms with damaging wind gusts (Weisman at el. 2013; Celiński-Mysław et al. 2019).

For quantitative evaluation of forecast wind gusts, data from three automatic weather stations were used: Gniezno, Grudziądz, and Starogard Gdański. These stations were situated on the track of the MCS. Since model data were available hourly and data from stations were recorded every 10 minutes, for comparison we use maximum wind gust values from every hour. We also computed root mean square errors (RMSE) and bias for ALARO and AROME models for all synoptic stations in Poland (Table 1).

4. RESULTS
4.1. ALARO FORECAST OF CONVECTIVE PHENOMENA

The possibility of large MCS with strong updrafts together with extreme wind gusts (using ALARO forecast on 11 August 2017, at 18, 21, 22 and 23 UTC the same day and r00, r06 and r12 model runs) was analyzed.

Analysis of vertical velocity maps from ALARO (Fig. 5) prove that the convective phenomena were far more extended for r06 and r12 runs. Vertical velocities of convective upward motions cover a wider area, and the maps show that strong, dominating upward motions (red) neighbor on downward motions (blue) in many places. These dynamics reflect a highly unstable atmosphere, with convective potential energy strengthened by a warm tropical air mass which occupied eastern Poland. Strong upward motions were visible up to the 300 hPa pressure level and persisted through

91
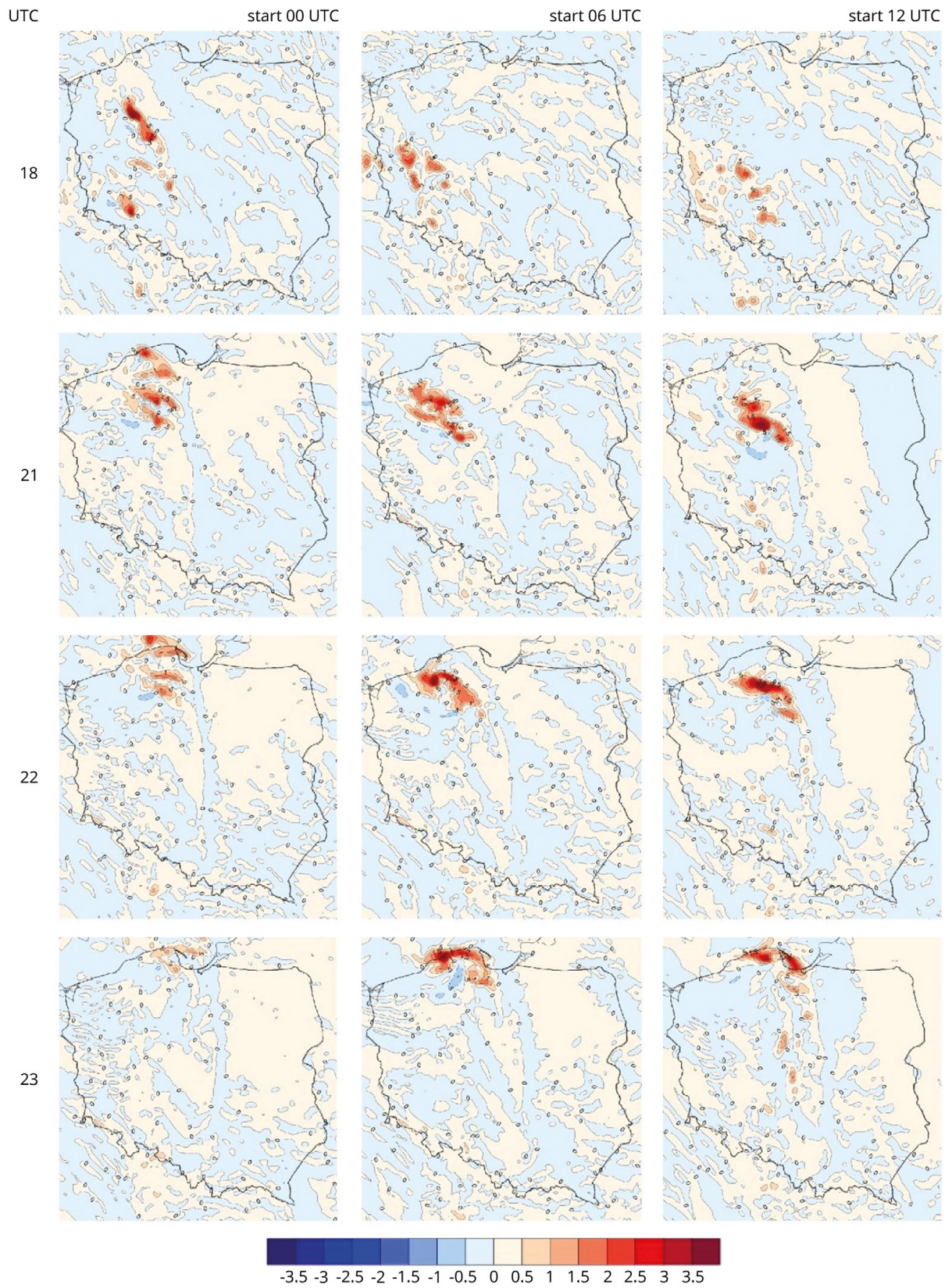
Fig. 5. The forecast of vertical velocities [m·s⁻¹] at 925 hPa level for various runs (r00, r06 and r12) of ALARO on 11 August 2017.
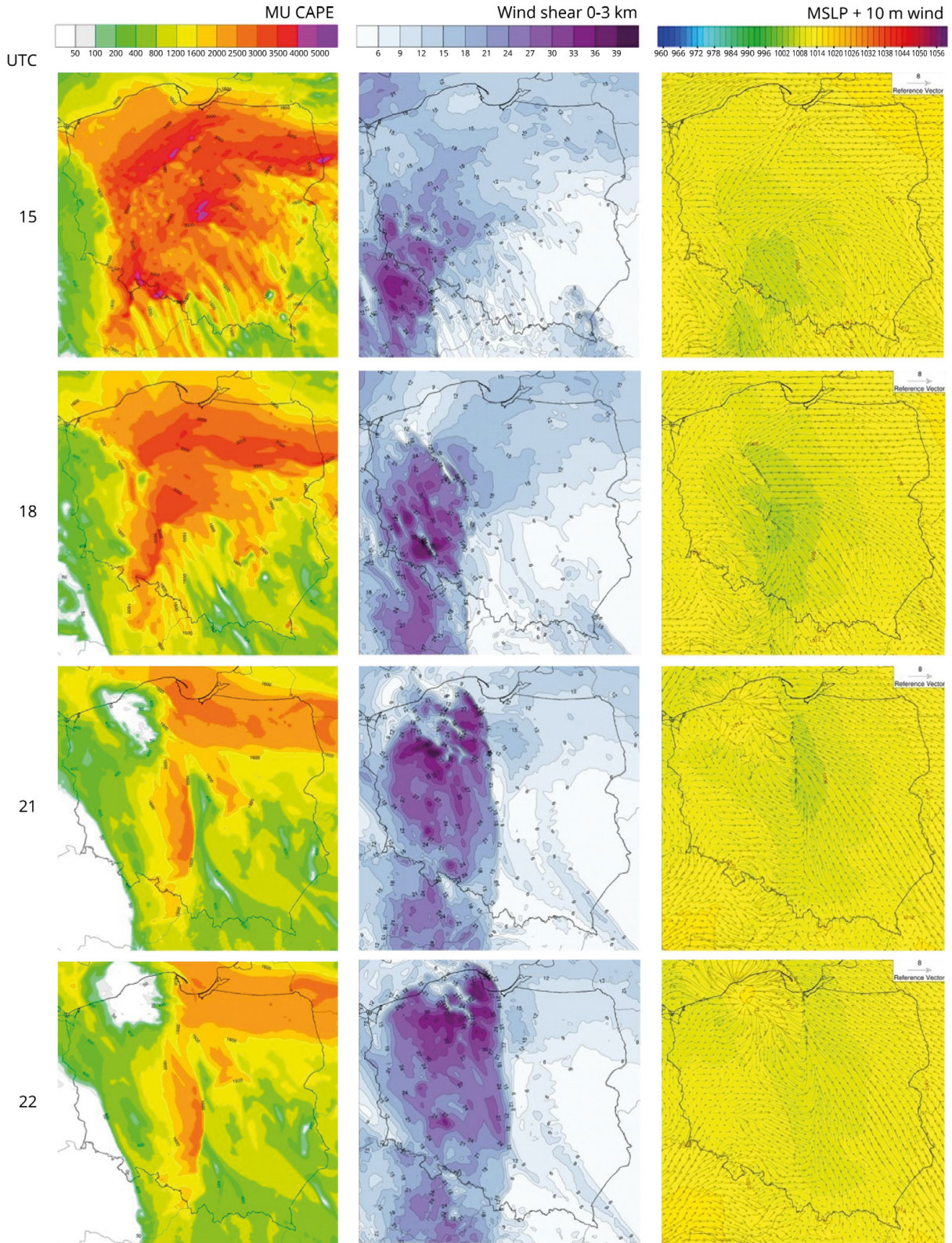
Fig. 6. MU CAPE [J·kg⁻¹], 0-3 km wind shear [m·s⁻¹] and pressure [hPa] + wind [m·s⁻¹] for NH version of ALARO, the forecast of 11 August 2017, r00.
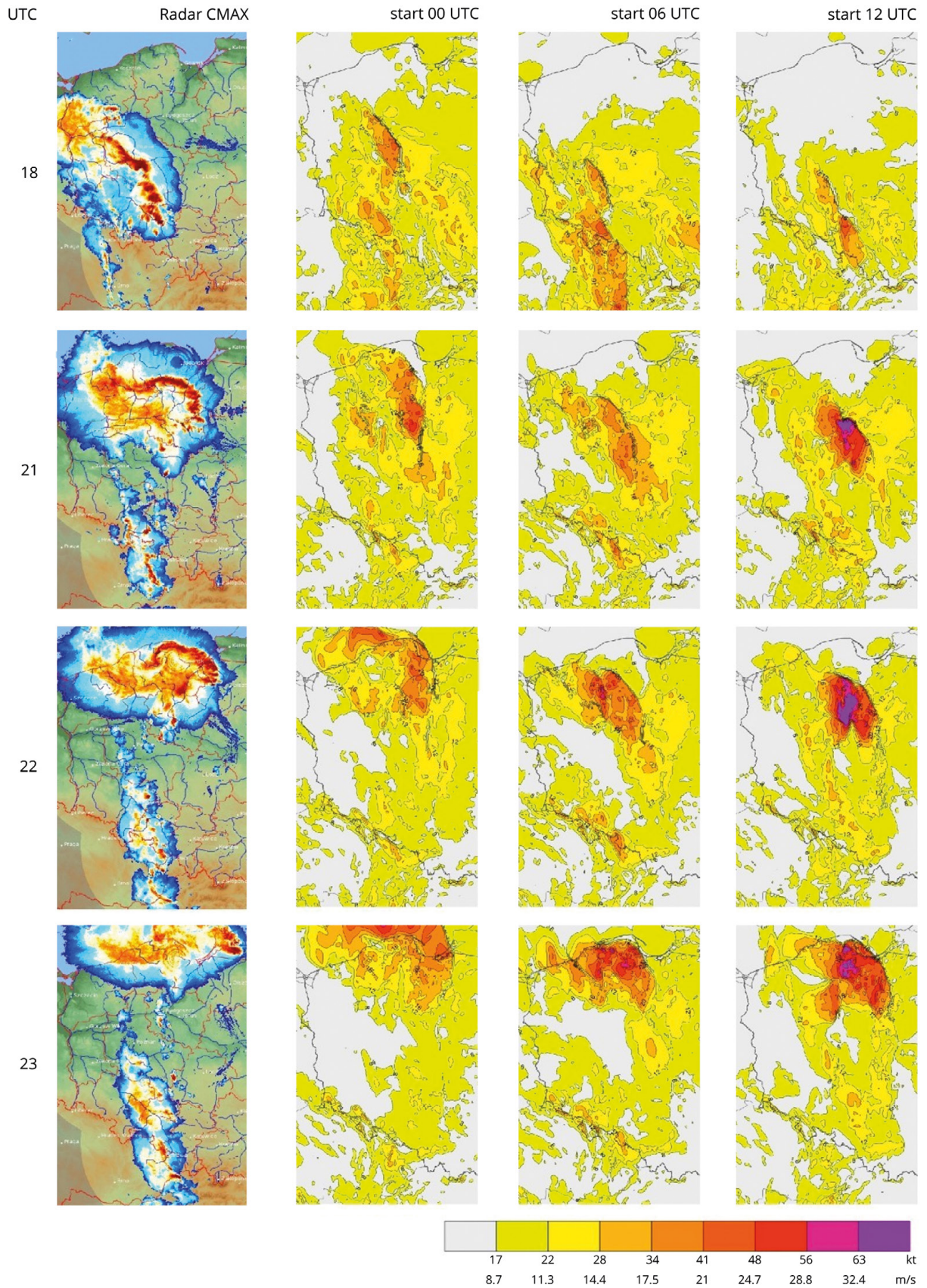
Fig. 7. Forecasts of wind gusts of ALARO cy43t2 NH model from 11 August 2017, for various base runs (r00, r06 and r12). The first column is radar reflectivity, CMAX, observed for 8 radar stations.
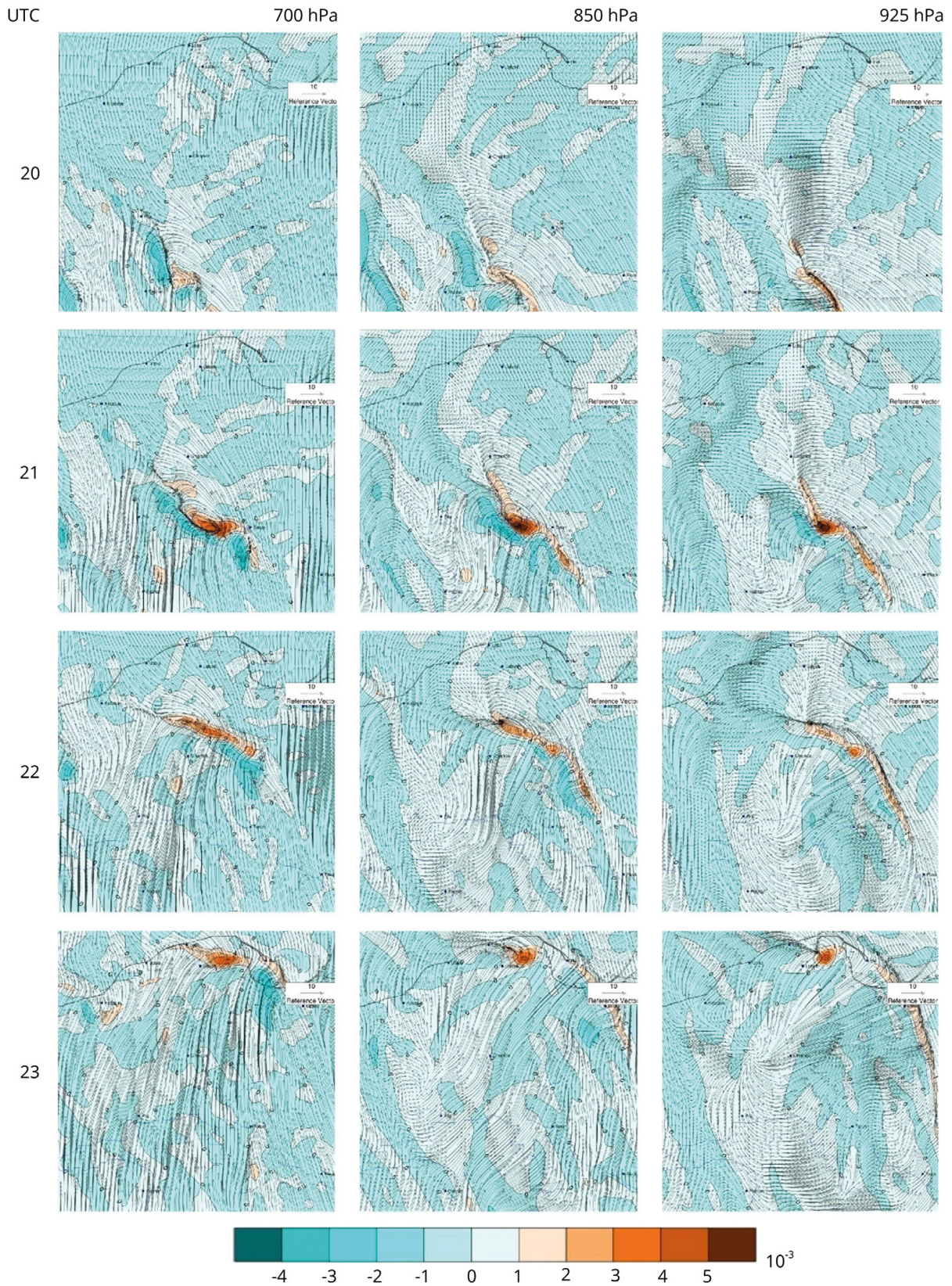
Fig. 8. The forecast of MCV and RIJ. Wind (m·s^{-1}, vectors) and relative vorticity (s^{-1}, color) at the levels of 700, 850, and 925 hPa between 20 and 23 UTC. ALARO r12 on 11 August 2017.
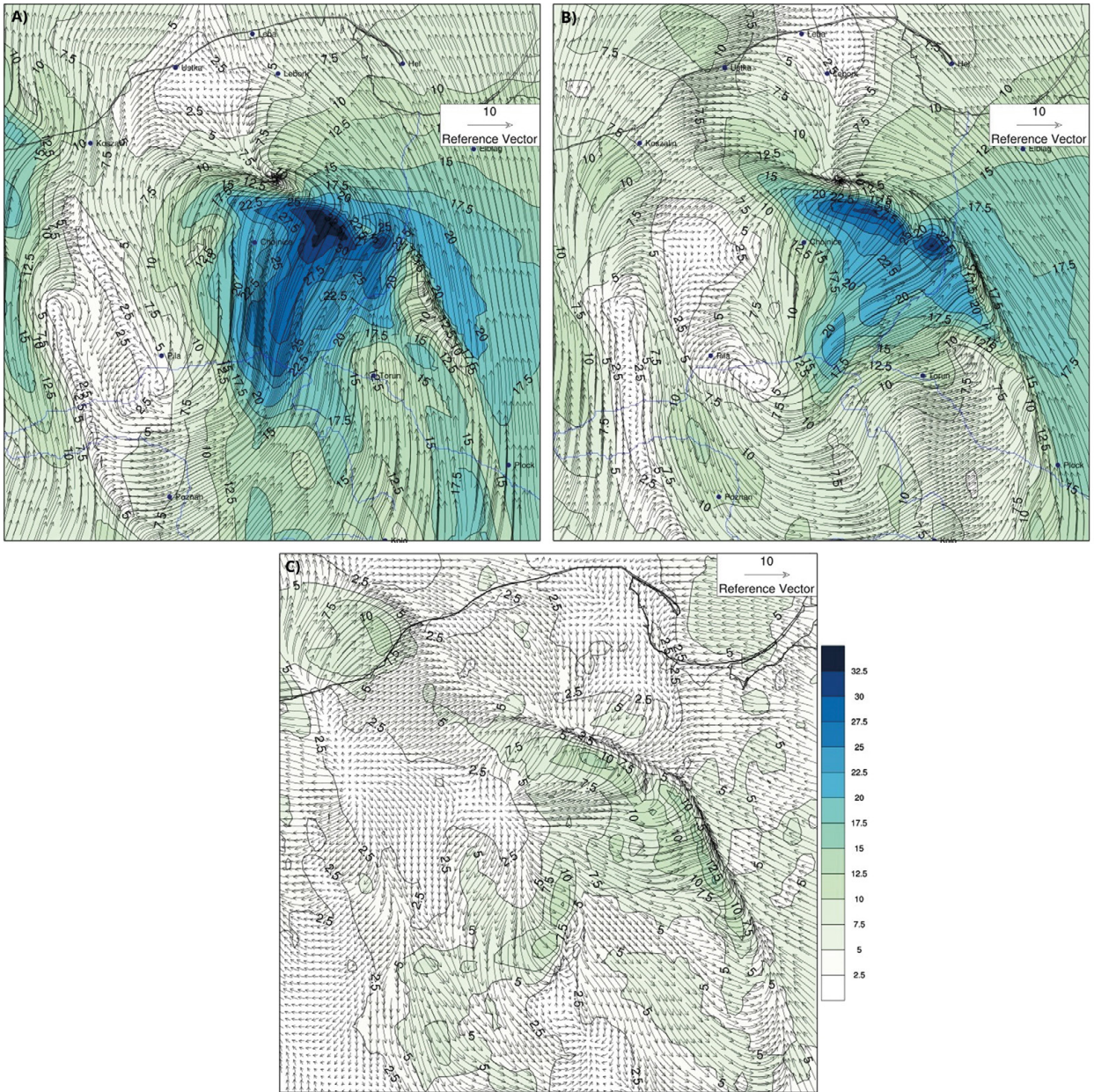
Fig. 9. Wind and the module of velocity (color) at pressure levels of 850 (a) and 925 hPa (b); wind and the module of velocity (color) at 10 m AGL (c). ALARO r12 forecast for 22 UTC, 11 August 2017.

the whole duration of MCS over Poland. The greatest forecasted velocities of upward motions were for r12 run: 4.1 m·s^{-1} (21 UTC), 3.8 m·s^{-1} (22 UTC) and 3.2 m·s^{-1} (23 UTC). The highest predicted downward motion was equal to −1.0 m·s^{-1} at 21 UTC, also for r12 run.

The three columns of Figure 6 are maps of MU CAPE (left), 0-3 wind shear (middle) and MSLP + 10 m wind (right) for ALARO r00 run; rows represent hours: 15 UTC (top), 18 and 21 UTC (middle), and 22 UTC (bottom). We note that the MU CAPE values at an early hour (15 UTC) are higher than at 21 and 22 UTC, the physical consequence of passage of the MCS. The values of wind shear remain high for all hours, but the position changes towards the northeast later (21-22 UTC). MSLP and 10m wind from 18 UTC to 22 UTC change in a very dynamic way as they reflect the cold pool evolution (Fig. 7). In Figure 7, the observed radar column maximum reflectivity, CMAX, is compared with the forecasted position of wind gusts of dif-

ferent model runs. All the model forecasts produce close positions of the severe weather phenomena.

The ALARO r00 forecast underestimates the strength of wind gusts but reflects well the position of the moving MCS (Fig. 7). The ALARO r06 and r12 forecasts are late in comparison with observations, but still the MCS track is well-predicted. As the MCS moved northwards, the intensity of wind and convection increased, with culmination after 18UTC and persistence until the late evening hours on 11 August 2017. In each of the forecasts (Fig. 7) wind gusts velocity exceed 63 knots (32.4 m·s^{-1}), with maximum local values of 55.49 m·s^{-1} (21 UTC), 69.3 m·s^{-1} (22 UTC) and 43.78 m·s^{-1} (23 UTC) for run r12. The shift in time of forecasted track position in comparison with observations may be explained by the fact that for r06 and r12 there was too little time to develop a derecho fully from the forecast initiation. Such an effect (stronger for more complex phenomena) is met

in the forecast of cloudiness, deep convection, or storms and is called spin-up. This means that a model needs some time to develop a full range of weather phenomena from initial and boundary conditions. Such time is dependent on the construction of a given NWP model.

During the analyzed period the MCV was accompanying the MCS. The most developed MCV was forecasted by ALARO r12. Figure 8 presents ALARO r12 wind and relative vorticity forecast at 700, 850, and 925hPa pressure levels. The Figure shows the evolution of the mesocyclone (an area with higher vorticity, with colors) movement and intensity between 18 and 23UTC.

In the case of r00, the less consistent structure of the convective system has a form of two smaller vortices, whereas r06 predicts weaker intensity of a single MCV (not shown here). According to ALARO r12, the vorticity of the MCV appears at 925 hPa level and then propagates upwards, reaching 700 hPa level at 20 UTC (Fig. 8). In its culmination (21 UTC) it stretches from 500hPa downwards, reaching top values from $3.7 \cdot 10^{-3} s^{-1}$ (500 hPa) to $6.6 \cdot 10^{-3} s^{-1}$ (for 925 hPa). At that time, in the high troposphere (at the 300 hPa level), directly above the MCV, there is an increase of the geopotential, and rise of air pressure. After 21 UTC the vortex in the middle troposphere weakens, lasting longest at 850 and 925 hPa levels.

Other phenomena accompanying MCS are RIJ and cold pool. All three ALARO model runs predict RIJ, but its smallest intensity is predicted by the forecast run from r00. The reason is that the MCS for that run was less compact, with several smaller squall lines. R06 and r12 runs forecasted the consistent structure, at the back of which we found strong current in the direction of MCS motion (Fig. 8 for r12) which can be seen also for 20 UTC at pressure levels 700, 850, and 925 hPa. As it is a gradually descending current, its length was greater at higher levels, and the shortest was near the surface. This structure is well represented in the forecasts for 22 UTC (Fig. 9 for r12).

For ALARO, the cold pool forecast is most distinct for the r00 run. We noticed it between 19 and 20 UTC on the map of temperature at 2 m AGL, and we saw it at 21 UTC in the form of closed isotherms of colder air (Fig. 4a). Despite the modest temperature contrast (2-4°C), the cold pool is clearly imposed over the area of higher pressure near the ground (Fig. 4b) closely behind the squall line, in the northwestern direction from the low-pressure region, which overlaps the area of relatively high surface temperatures. The area of lower temperature was also visible on the maps of temperature at altitudes of 850 and 925 hPa (not presented).

4.2. AROME FORECAST OF CONVECTIVE PHENOMENA

The AROME was created as non-hydrostatic, high-resolution (convective scale) model for prediction of storms and torrential rain. It appeared to precisely describe a wider family of severe weather phenomena including bow echoes, derechos, and tornadoes, as well as strong wind gusts connected to these events (Seity et al. 2011).

The simulated maximum reflectivity CMAX predicted by AROME (and presented in Fig. 10) is higher than measured by radars, suggesting a larger quantity of hydrometeors than in actuality. The bow echo (visible on radar maps) is well reconstructed in the AROME forecasts. Also, the area of lower reflectivity (appearing usually behind a squall bow) is visible, as well as the eddy on the northern west end of the squall bow. For the r12 run, the maps of simulated radar maximum reflectivity were in best agreement with observed maximal reflectivity in terms of position and signal intensity in dBZ. For the r00 run on 11 August 2017, the AROME model forecasted strong wind gusts farther north than the CMAX measurements (reflectiv-

ity; Fig. 10). For the evening hours of this forecast run, the model predicted maximum wind gusts over the Baltic Sea, which was not in agreement with CMAX positions measured by the radar. The AROME r12 forecast underestimated wind gusts but reflected well the position of the moving MCS (Fig. 10). The predicted wind gust velocity exceeded 63 knots (32.4 m·s^{-1}), with maximum local values of 49 m·s^{-1} (20 UTC), 43 m·s^{-1} (21 UTC), and 47 m·s^{-1} (22 UTC) for r12 (Fig. 10).

Figures 11 and 12 present the maps of severe weather indices, relative vorticity, and wind for the AROME model.

Another severe weather phenomenon forecasted by AROME was a cold pool. Despite a small temperature contrast, it is clearly visible on the maps of 2 m temperature for the 21 UTC r12 run (Fig. 13a) and overlaps the area of increased pressure (Fig. 13b) right behind the squall line. At the levels of 925 and 850 hPa (not shown), one can notice a decrease of air temperature in that area. For the AROME r06 run a cold pool was not easy to notice. In the middle and lower troposphere, at the back of the system, a strong influx of air towards the squall line can be found (Fig. 12 for 700, 850 and 925 hPa, for r12). This RIJ was traced more clearly by the AROME r12 run than at r00 and r06. For r12, RIJ was most visible on the 21 UTC map (Fig. 14) in the area stretching close to the ground from the squall line up to about 100 km southwest from it, parallel to MCS movement. At the levels of 850 and 925 hPa (Fig. 14b), the zone of high wind speeds (exceeding 63.5 m·s^{-1}) is more extended than for ALARO (Fig. 9).

Considering MCV, from 19 UTC at 850 hPa one can see a cyclonic curl of wind, faintly visible also at 700 hPa (Fig. 12 for r12). It is accompanied by a local minimum of relative vorticity. For 20 UTC, the mesocyclone is visible also at 925 hPa (Fig. 14a). About 21 UTC the relative vorticity reaches its peak of $1.6 \cdot 10^{-3} s^{-1}$ (850 hPa) and an expansion of the high vorticity region follows (Fig. 12). After 22 UTC, according to the AROME forecast, the MCS reaches Gdansk Bay and MCV vanishes because the Baltic Sea is colder than Pomerania and the coast.

4.3. FORECAST EVALUATION

In order to better visualize the capability for forecasting wind gusts by ALARO and AROME models, a quantitative verification is presented in Figure 15. Three stations that recorded high values of wind gusts were selected (stations are ordered from southernmost to northernmost): Gniezno, Grudziądz and Starogard Gdański. For both models and runs from 00, 06 and 12 UTC, wind gust forecasts are presented along with recorded values. All runs and both models are characterized precisely by the timing of the greatest wind gusts. For Gniezno station (Fig. 15 top row), the AROME model (green line) performs better both in terms of timing and magnitude, but the maximum wind gusts are underestimated by almost 10 m·s^{-1}. The best forecasts for Grudziadz (Fig. 15 middle row) are obtained from 12 UTC runs (Fig. 15 right column) with almost perfect timing and values for observed peak wind gusts (blue line), especially for AROME forecasts, whereas the ALARO model (red line) predicted the maximum value better, but one hour later than observations. For the Starogard Gdański station (Fig. 15 bottom row) the forecasts from 12 UTC turned out to be the worst for both models, with overestimation of wind gusts and forecasting them one (AROME) or two hours (ALARO) late.

ALARO and AROME wind gust forecasts starting from 00, 06, and 12 UTC were also compared with measurements from all synoptic stations in Poland. Table 1 presents RMSE and bias scores for both models. The AROME model starting at 00 UTC outperforms other forecasts both in terms of RMSE and bias. The biggest errors were noted for both models for 12 UTC runs.

97
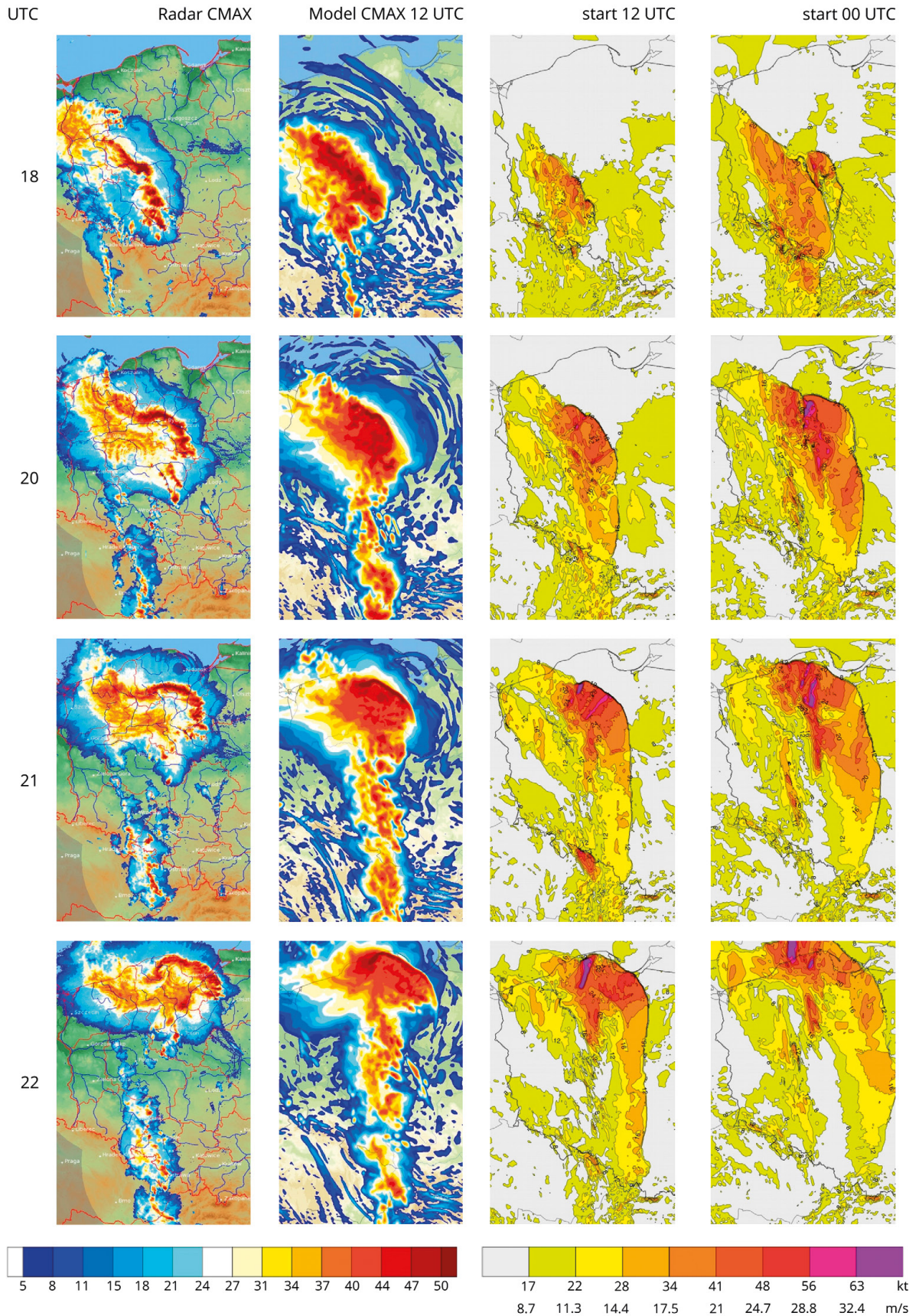
Fig. 10. The CMAX and wind gusts forecasts from AROME cy43t2 on 11 August 2017, for different forecast bases (runs). The first column is CMAX from the radar, based on observations from several radar stations. Color scale is valid for both radar and model CMAX maps.
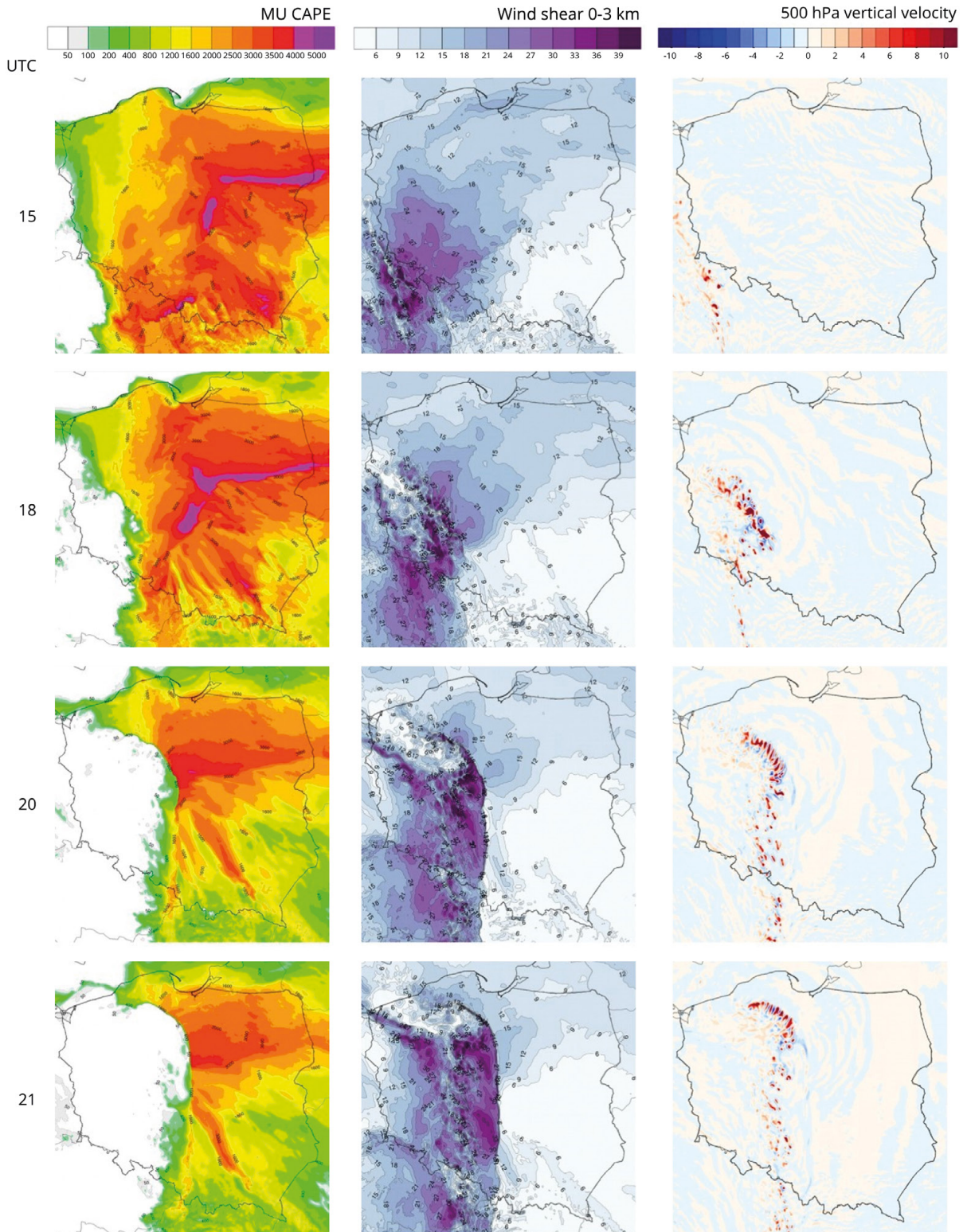
Fig. 11. MU CAPE [J·kg⁻¹], 0-3km wind shear [m·s⁻¹] and 500 hPa vertical velocity [m·s⁻¹] for AROME cy43t2 r12 forecast on 11 August 2017.

700 hPa

850 hPa

925 hPa

19

20

100

21

22
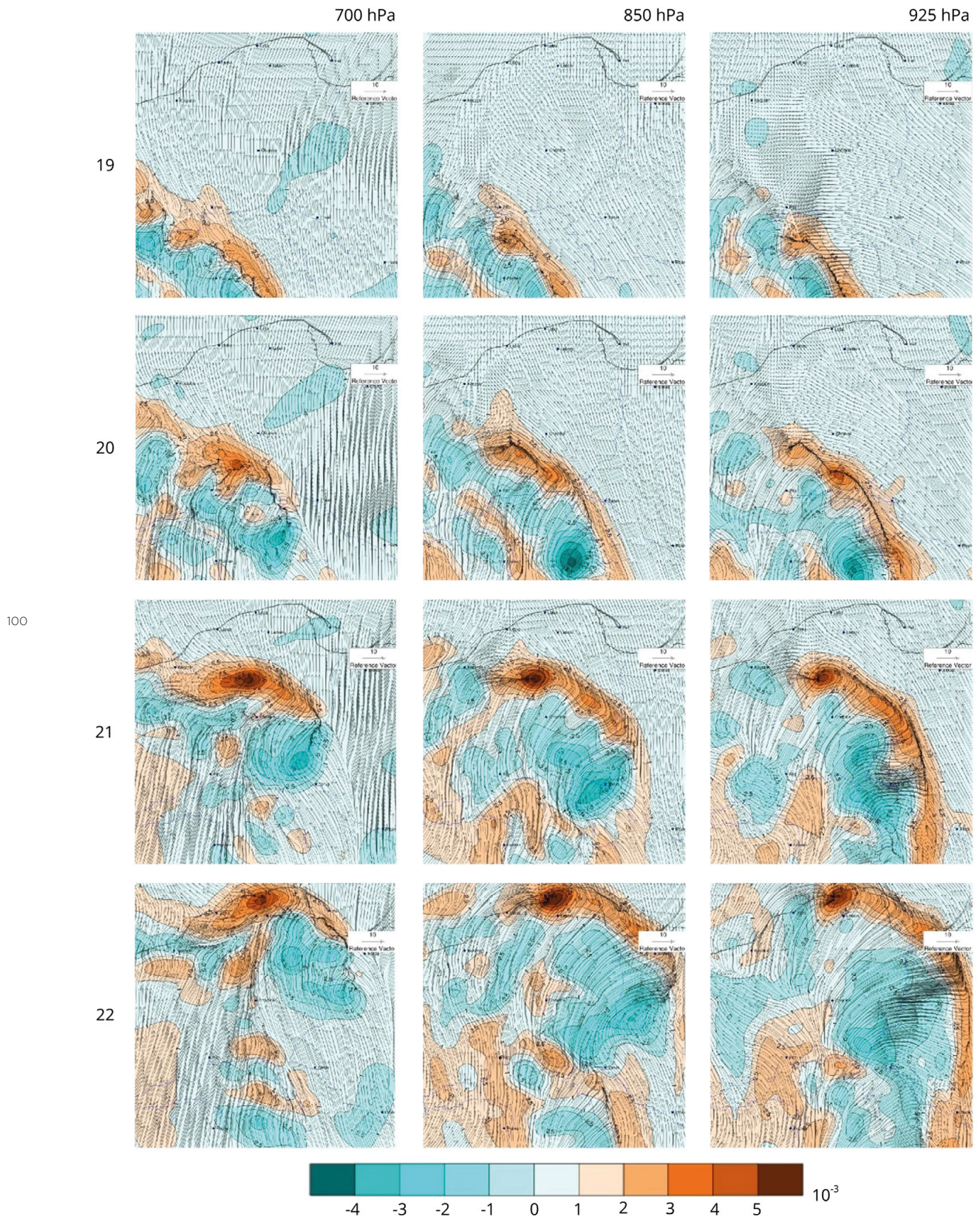
Fig. 12. MCV forecast. The wind and relative vorticity (color) at the 700, 850 and 925 hPa levels for AROME cy43t2 r12 forecast on 11 August 2017.
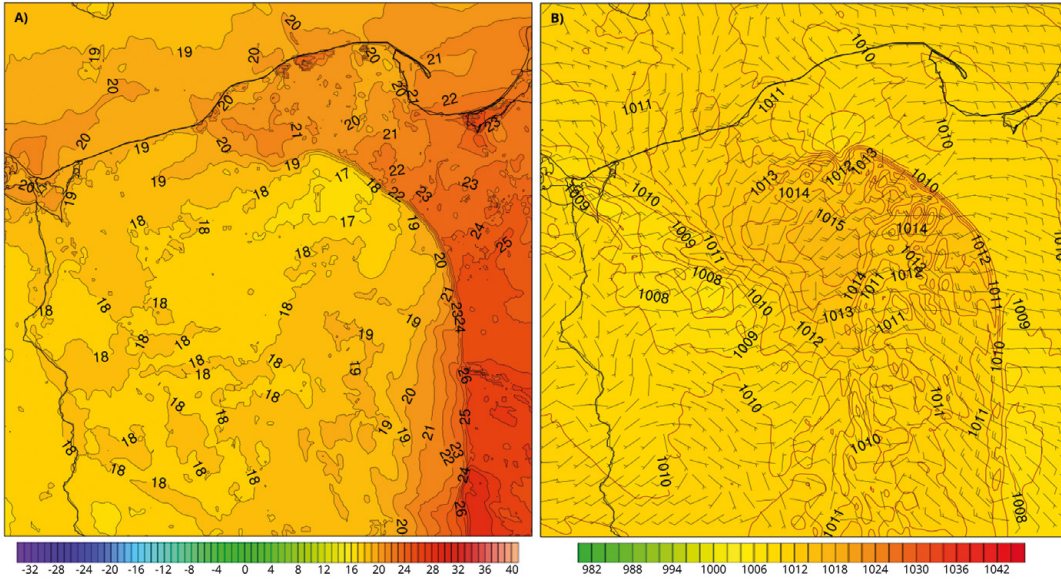
Fig. 13. Cold pool, AROME forecast: (a) 2 m temperature, (b) atmospheric pressure on the ground. The forecast for 21UTC 11 August 2017, r12.
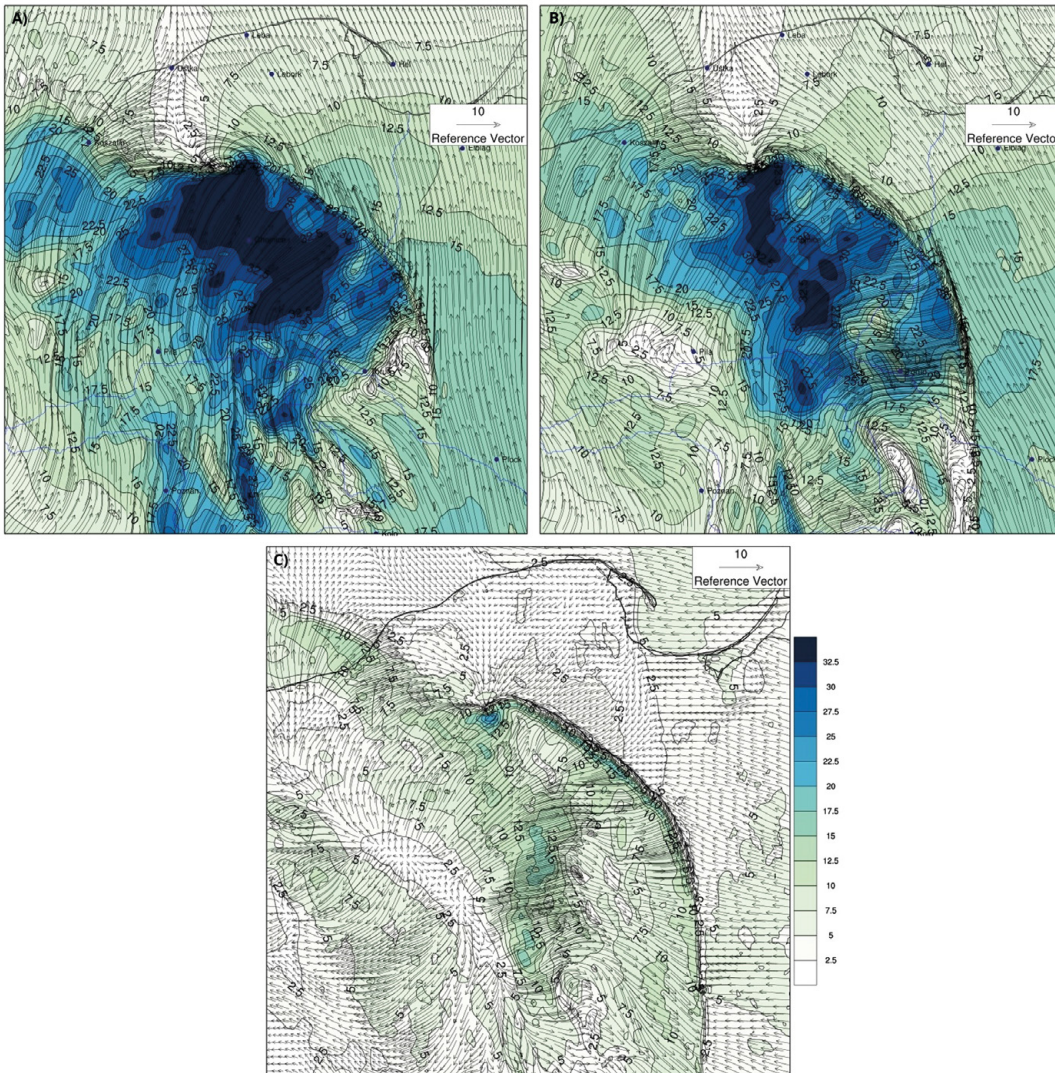
Fig. 14. Wind and the module of wind speed (color) on the map of 850 and 925hPa pressure levels (a and b); c) wind and the module of the wind speed (color) at 10m AGL AROME forecast for 21UTC, 11 August 2017, r12.
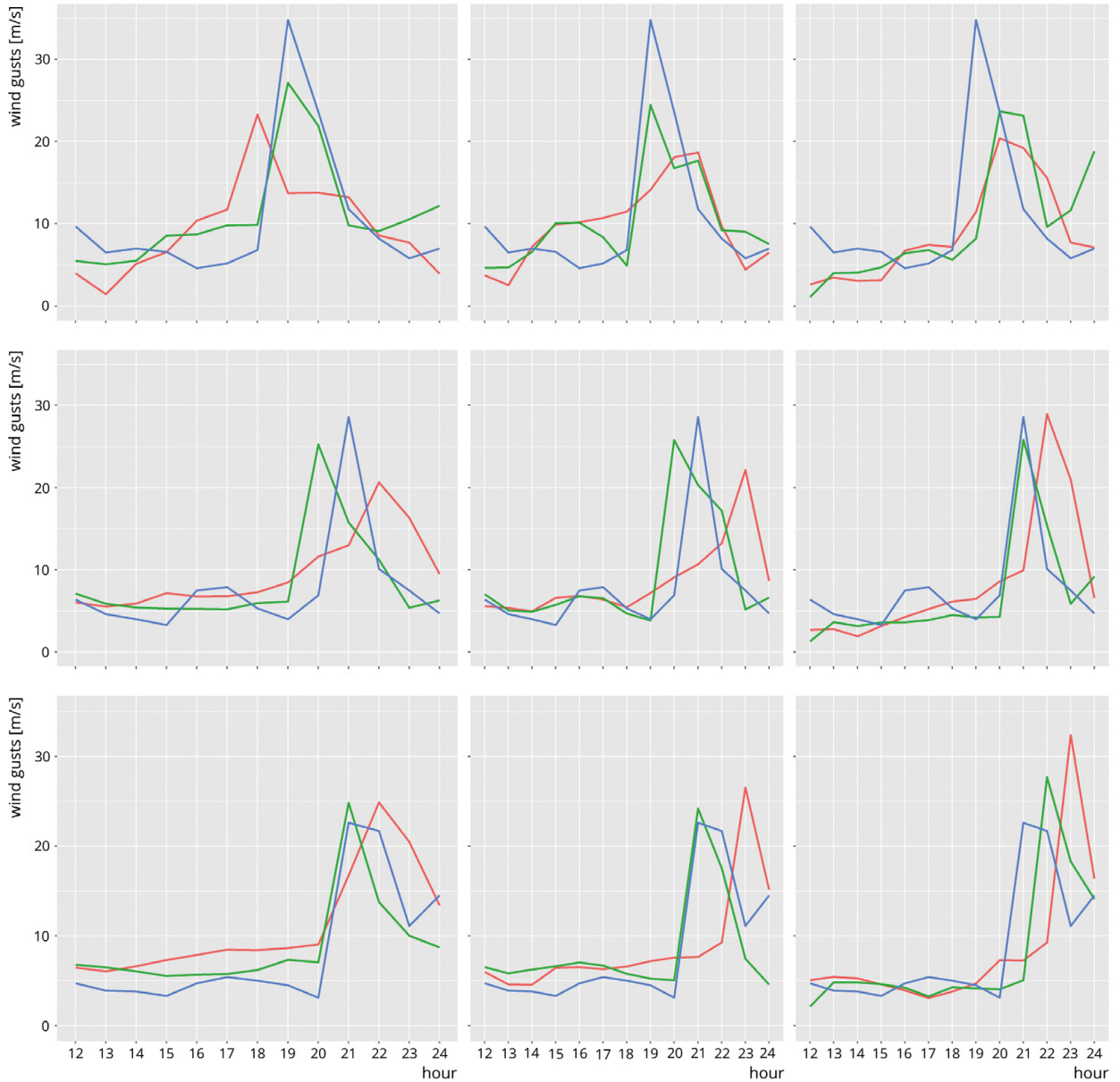
Fig. 15. Wind gust measurements (blue lines) and forecasts from ALARO (red lines) and AROME (green lines) models starting from 00 UTC (left), 06 UTC (middle) and 12 UTC (right) for stations Gniezno (top row), Grudziądz (middle row) and Starogard Gdański (bottom row) for 11 August 2017 from 12 UTC to 24 UTC.

Table 1. Evaluation of wind gust forecasts for all synoptic stations in Poland.

	ALARO			AROME		
	00	06	12	00	06	12
RMSE [m·s⁻¹]	5.56	5.37	7.41	5.19	6.21	7.88
BIAS [m·s⁻¹]	1.81	2.9	3.71	0.42	2.26	4.03

It is not straightforward to evaluate models based on observational data in the case of such an intensive phenomenon, and using forecasts up to 24 hours instead of reanalysis. Models can predict the behavior of an event accurately, but with a small number of synoptic stations or coarse resolution of gridded data, standard scores can be misleading. Therefore we decided to evaluate the possibility of predicting the intensity of the derecho by analyzing the distribution of wind gusts in Poland (grid points from ALARO and AROME models within the Polish border and over the Baltic Sea up to 55.5 N) from various models and runs. Figure 16 presents the distribu-

tion of forecasts of wind gusts from 12 UTC to 24 UTC on 11 August 2017, with the AROME model on the top row and ALARO on the bottom row. Runs for 00 UTC are displayed on the left column, 06 UTC runs on the middle column, and 12 UTC runs on the right column. All runs for both models predict very strong wind gusts, but the ALARO model for 12 UTC predicts values exceeding 60 m·s⁻¹ at 22 UTC; ALARO from 06 UTC predicts values slightly less than 60 m·s⁻¹ at 24 UTC, while AROME runs from 00 and 12 UTC predicted maximum wind gusts close to 50 m·s⁻¹.

5. DISCUSSION

Severe weather phenomena such as MCV, RIJ, and a cold pool were optimally mapped by r12 of AROME. For the earlier runs (r00 and r06) the model forecasted the squall line slightly too far northeast (Fig. 10) and strong wind gusts over a wider area than the AROME r12 forecast. Moreover, maximum wind gusts (for the maps of Fig. 10) were shifted northwards, over the Baltic Sea.
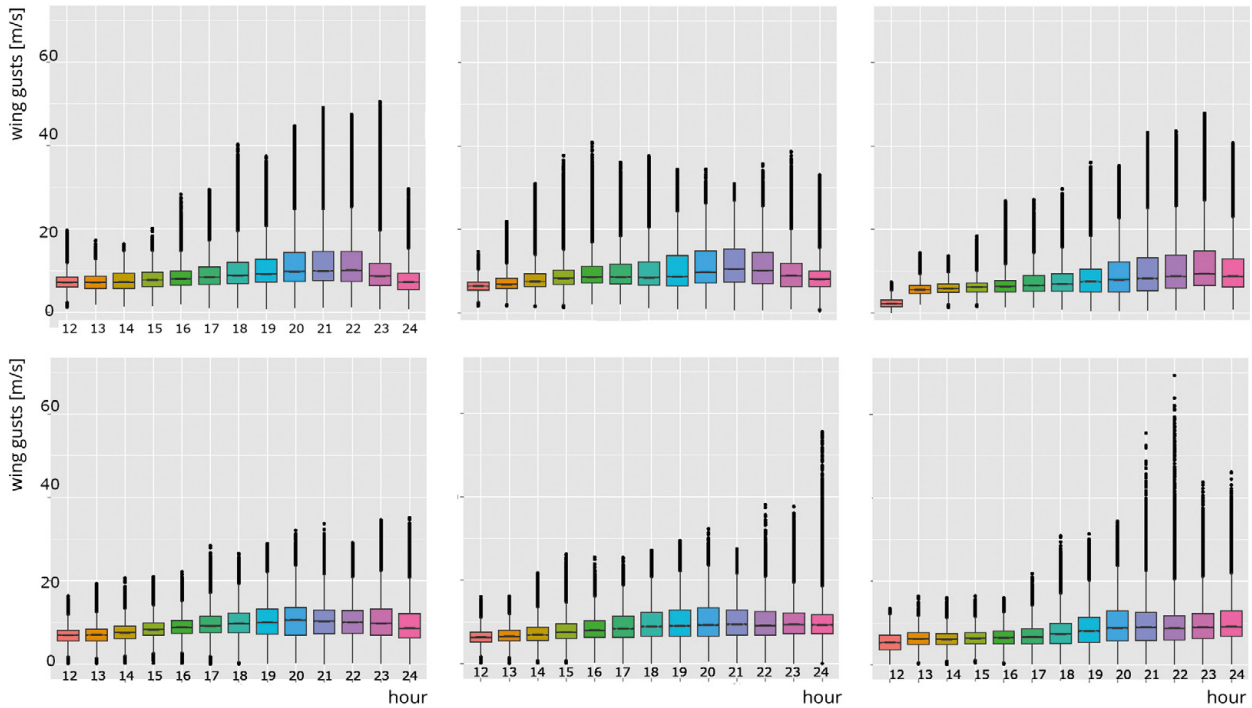
Fig. 16. Distribution of wind gust values in Poland for 11 August 2017 from 12 UTC to 24 UTC. AROME top row, ALARO bottom row, 00 UTC runs left column, 06 UTC runs middle column, 12 UTC runs right column.

For the r00 forecast of ALARO, the location of the leading edge of the strong wind gusts area was shifted by tens of kilometers to the north-east, compared to the position of higher radar reflectivity (Fig. 10). The discrepancy is probably influenced by initial and boundary conditions for earlier runs of ALARO

Mis-positioning of the event for the r00 and r06 runs occurs also in simulations from the WRF model done by Taszarek et al. (2019), however the reported shift was towards the west. Additionally, one of their simulations, which was based on initial conditions from GFS, suffers from an underestimation of wind gusts, which is consistent with our results from ALARO. Similar issues were confirmed for all considered sources of initial conditions for the WRF model by Figurski et al. (2021). Both research teams found the latest forecasts (r12) to be the most precise regarding the position and the strength of the event. Taszarek et al. (2019) suggested that this result might be an effect of a proper simulation of mid-tropospheric cloud cover in a pre-convective environment, contrary to our findings regarding ALARO.

The AROME forecast values of CAPE and 3-0 km wind shear (Fig. 11) were higher compared to those predicted by ALARO (Fig. 6). At 15 UTC the maximum value for MU CAPE from the AROME forecast reached 5956 J·kg⁻¹, while for ALARO it was 4669 J·kg⁻¹. Until 21 UTC for both models maximum CAPE values were decreasing, but still were over 4000 J·kg⁻¹. Wind shear in the 0-3 km layer from 15 to 21 UTC has constantly high values (>35 m·s⁻¹ for ALARO and >45 m·s⁻¹ for AROME). The models predicted the greatest wind shear at 20 UTC: ALARO 40.8 m·s⁻¹ and AROME 48.3 m·s⁻¹. The values of vertical velocity at 500 hPa (Fig. 11, right column) were significantly higher for the model using full deep convection equations, reaching 20 m·s⁻¹ (18 and 20UTC) and 26 m·s⁻¹ (19 UTC). For AROME, the strongest convection regions at 925 hPa were very narrow and overlapped the convergence lines of wind (not shown).

The evolution of the MCV is not predicted identically by both models.

6. CONCLUSIONS

Both ALARO and AROME models forecasted a mesoscale convective system (MCS), a bow echo structure as well as MCV – a mesoscale convective vortex. The fields, such as: pressure and wind, geopotential and wind, temperature, as well as vertical velocity maps, CAPE and wind shear were valuable for the analysis of the atmospheric state. The maps of simulated reflectivity (CMAX from ALARO, Fig. 7) visualize the path of the phenomenon for evening hours on 11 August 2017, thus both the evolution of a structure and a position of MCS. AROME model forecast from 12 UTC predicted properly MCV, however the prediction of position of convective phenomena like MCV (for AROME r00 and r06) was more misleading than for ALARO.

One should be aware of necessity for forecasters to use better resolution maps which can be obtained by downscaling the most complex areas. That seems to be the future but would be crucial in the process of immediate diagnosis of the meteorological situation by the team of forecasters.

7. SUMMARY AND OUTLOOK

On 11 August 2017, the system of strong winds caused serious damage and fatalities while passing through north-western Poland. The post-factum weather forecast by the means of the presently available model, a non-hydrostatic one with 4 km × 4 km horizontal resolution (unavailable in 2017), predicted wind gusts of velocity exceeding 150 km·h⁻¹. In the past, there were several papers confirming that enhancing accuracy of forecast can be obtained by better model resolution (Bryan et al. 2003; Lean et al. 2008; Brousseau et al. 2016; Squitieri, Gallus 2020). It would be valuable to explore the weather system by AROME model with different initial and boundary conditions or run models with higher horizontal and vertical resolution. Such models could be a test version of AROME with horizontal resolution 1 km × 1 km and over 100 vertical levels, or ALARO with horizontal resolution of 2 km × 2 km. Operational run of higher resolution models may help forecasters to predict future severe convective events more efficiently.

REFERENCES

- Baldauf M., Seiferd A., Foerstner J., Majewski D., Raschendorfer M., Reinhardt T., 2011, Operational convective-scale numerical weather prediction with the COSMO model: description and sensitivities, Monthly Weather Review, 139 (12), 3887-3905, DOI: 10.1175/MWR-D-10-05013.1.

- Bouttier F., Marchal H., 2020, Probabilistic thunderstorm forecasting by blending multiple ensembles, Tellus A: Dynamic Meteorology and Oceanography 72 (1), DOI: 10.1080/16000870.2019.1696142.

- Brousseau P., Seity Y., Ricard D., Léger J., 2016, Improvement of the forecast of convective activity from the AROME-France system, Quarterly Journal of the Royal Meteorological Society, 142 (699), 2231-2243, DOI: 10.1002/qj.2822.

- Bryan G.H., Wyngaard J.C., Fritsch J.M., 2003, Resolution requirements for the simulation of deep moist convection, Monthly Weather Review, 131 (10), 2394-2416, DOI: 10.1175/1520-0493(2003)131<2394:RRFTSO>2.0.CO;2.

- Celiński-Mysław D., Matuszko D., 2014, An analysis of selected cases of derecho in Poland, Atmospheric Research, 149, 263-281, DOI: 10.1016/j.atmosres.2014.06.016.

- Celiński-Mysław D., Palarz A., Łoboda Ł., 2019, Kinematic and thermodynamic conditions related to convective systems with a bow echo in Poland, Theoretical and Applied Climatology, 137, 2109-2123, DOI: 10.1007/s00704-018-2728-6.

- Charba J., 1974, Application of gravity current model to analysis of squall-line gust front, Monthly Weather Review, 102 (2), 140-156, DOI: 10.1175/1520-0493(1974)102<0140:AOGCMT>2.0.CO;2.

- Chmielewski T., Szer J., Bobra P., 2020, Derecho wind storm in Poland on 11-12 August 2017: results of the post-disaster investigation, Environmental Hazards, 19 (5), 508-528, DOI: 10.1080/17477891.2020.1730154.

- Coniglio M.C., Stensrud D.J., 2001, Simulation of a progressive derecho using composite initial conditions, Monthly Weather Review, 129 (7), 1593-1616, DOI: 10.1175/1520-0493(2001)129<1593:SOAPDU>2.0.CO;2.

- Davis C.A., Trier S.B., 2007, Mesoscale convective vortices observed during BAMEX. Part I: Kinematic and thermodynamic structure, Monthly Weather Review, 135 (6), 2029-2049, DOI: 10.1175/MWR3398.1.

- De Meutter P., Gerard L., Smet G., Hamid K., Hamdi R., Degrauwe D., Termonia P., 2015, Predicting small-scale, short-lived downbursts: case study with the NWP limited-area ALARO Model for the Pukkelpop thunderstorm, Monthly Weather Review, 143 (3), 742-756, DOI: 10.1175/MWR-D-14-00290.1.

- Dixon K., Mass C.F., Hakim G.J., Holzworth R.H., 2016, The impact of lightning data assimilation on deterministic and ensemble forecasts of convective events, Journal of Atmospheric and Oceanic Technology, 33 (9), 1801-1823, DOI: 10.1175/JTECH-D-15-0188.1.

- Droegemeier K.K., Wilhelmson R.B., 1985, Three-dimensional numerical modeling of convection produced by interacting thunderstorm outflows. Part II: Variations in vertical wind shear, Journal of the Atmospheric Sciences 42 (22), 2404-2414, DOI: 10.1175/1520-0469(1985)042<2404:TDNMOC>2.0.CO;2.

- Evans J.S., Doswell C.A., 2001, Examination of derecho environments using proximity soundings, Weather and Forecasting, 16 (3), 329-342, DOI: 10.1175/1520-0434(2001)016<0329:EODEUP>2.0.CO;2.

- Figurski M., Nykiel G., Jaczewski A., Baldysz Z., Wdowikowski M., 2021, The impact of initial and boundary conditions on severe weather event simulations using a high-resolution WRF model. Case study of the derecho event in Poland on 11 August 2017, Meteorolology Hydrology and Water Management, DOI: 10.26491/mhwm/143877.

- Fujita T., 1960, Structure of connective storms, [in:] Physics of Precipitation: Proceedings of the Cloud Physics Conference, Woods Hole, Massachusetts, June 3-5, 1959, American Geophysical Union (AGU), 61-66, DOI: 10.1029/GM005p0061.

- Gatzen C.P., Fink A.H., Schultz D.M., Pinto J.G., 2020, An 18-year climatology of derechos in Germany, Natural Hazards and Earth System Sciences, 20 (5), 1335-1351, DOI: 10.5194/nhess-20-1335-2020.

- Gerard L., Piriou J.-M., Brožková R., Geleyn J.-F., Banciu D., 2009, Cloud and precipitation parameterization in a meso-gamma-scale operational weather prediction model, Monthly Weather Review, 137 (11), 3960-3977, DOI: 10.1175/2009MWR2750.1.

- Glickman T.S., 2000, Glossary of Meteorology, American Meteorological Society, available online at https://glossary.ametsoc.org/wiki/Welcome (data access 31.01.2023).

- Goff R.C., 1976, Vertical structure of thunderstorm outflows, Monthly Weather Review, 104 (11), 1429-1440, DOI: 10.1175/1520-0493(1976)104<1429:VSOTO>2.0.CO;2.

- Hamid K., 2012, Investigation of the passage of a derecho in Belgium, Atmospheric Research, 107, 86-105, DOI: 10.1016/j.atmosres.2011.12.013.

- Hersbach H., Bell B., Berrisford P., Hirahara S., Horányi A., Muñoz-Sabater J., Nicolas J., Peubey C., Radu R., Schepers D., Simmons A., Soci C., Abdalla S., Abellan X., Balsamo G., Bechtold P., Biavati G., Bidlot J., Bonavita M., De Chiara G., Dahlgren P., Dee D., Diamantakis M., Dragani R., Flemming J., Forbes R., Fuentes M., Geer A., Haimberger L., Healy S., Hogan R.J., Hólm E., Janisková M., Keeley S., Laloyaux P., Lopez P., Lupu C., Radnoti G., de Rosnay P., Rozum I., Vamborg F., Villaume S., Thépaut J.-N., 2020, The ERA5 global reanalysis, Quarterly Journal of the Royal Meteorological Society, 146 (730), 1999-2049, DOI: 10.1002/qj.3803

- Houze R.A., 2004, Mesoscale convective systems, Reviews of Geophysics, 42 (4), DOI: 10.1029/2004RG000150.

- Jirak I.L., Cotton W.R., 2007, Observational analysis of the predictability of mesoscale convective systems, Weather and Forecasting, 22 (4), 813-838, DOI: 10.1175/WAF1012.1.

- Łapeta B., Kuligowska E., Murzyn P., Struzik P., 2021, Monitoring the 11 August 2017 storm in central Poland with satellite data and products, Meteorology, Hydrology and Water Management, DOI: 10.26491/mhwm/144590.

- Lean H.W., Clark P.A., Dixon M., Roberts N.M., Fitch A., Forbes R., Halliwell C., 2008, Characteristics of high-resolution versions of the Met Office Unified Model for forecasting convection over the United Kingdom, Monthly Weather Review, 136 (9), 3408-3424, DOI: 10.1175/2008MWR2332.1.

- Lelątko I., Ziemiański M., 2004, Skrócony przewodnik po wybranych wskaźnikach konwekcji, internal publication of forecasters office IMWM-NRI, Gdynia.

- Lopez P., 2002, Implementation and validation of a new prognostic large-scale cloud and precipitation scheme for climate and data-assimilation purposes, Quarterly Journal of the Royal Meteorological Society, 128 (579), 229-257, DOI: 10.1256/00359000260498879.

- Łuszczewski H., Tuszyńska I., 2022, Derecho analysis of August 11, 2017, Meteorology, Hydrology and Water Management, DOI: 10.26491/mhwm/152504.

- Marquet P., Santurette P., 2009, Convective parameters computed ALADIN and AROME models for the Hautmont (F4) tornado, 5th European Conference on Severe Storms, Landshut, Germany, available online at https://www.essl.org/ECSS/2009/preprints/O05-07-marquet.pdf (data access 31.01.2023).

- Masson V., Le Moigne P., Martin E., Faroux S., Alias A., Alkama R., Belamari S., Barbu A., Boone A., Bouyssel F., Brousseau P., Brun E., Calvet J.-C., Carrer D., Decharme B., Delire C., Donier S., Essaouini K., Gibelin A.-L., Giordani H., Habets F., Jidane M., Kerdraon G., Kourzeneva E., Lafaysse M., Lafont S., Lebeaupin Brossier C., Lemonsu A., Mahfouf J.-F., Marguinaud P., Mokhtari M., Morin S., Pigeon G., Salgado R., Seity Y., Taillefer F., Tanguy G., Tulet P., Vincendon B., Vionnet V., Voldoire A., 2013, The SURFEXv7.2 land and ocean surface platform for coupled or offline simulation of earth surface variables and fluxes, Geoscientific Model Development, 6 (4), 929-960, DOI: 10.5194/gmd-6-929-2013.

- Nykiel G., Figurski M., Baldysz Z., 2019, Analysis of GNSS sensed precipitable water vapour and tropospheric gradients during the derecho event in Poland of 11th August 2017, Journal of Atmospheric and Solar-Terrestrial Physics, 193, DOI: 10.1016/j.jastp.2019.105082.

- Pacey G.P., Schultz D.M., Garcia-Carreras L., 2021, Severe convective windstorms in Europe: climatology, preconvective environments, and convective mode, Weather and Forecasting 36 (1), 237-252, DOI: 10.1175/WAF-D-20-0075.1.

- Pergaud J., Masson V., Malardel S., Couvreux F., 2009, A parameterization of dry thermals and shallow cumuli for mesoscale numerical weather prediction, Boundary-Layer Meteorology, 132, 83-106, DOI: 10.1007/s10546-009-9388-0.

- Poręba S., Taszarek M., Ustrnul Z., 2022, Diurnal and seasonal variability of ERA5 convective parameters in relation to lightning flash rates in Poland, Weather and Forecasting, 37 (8), 1447-1470, DOI: 10.1175/WAF-D-21-0099.1.

- Poręba S., Ustrnul Z., 2020, Forecasting experiences associated with supercells over South-Western Poland on July 7, 2017, Atmospheric Research, 232, DOI: 10.1016/j.atmosres.2019.104681.

- Powers J.G., Klemp J.B., Skamarock W.C., Davis C.A., Dudhia J., Gill D.O., Coen J.L., Gochis D.J., Ahmadov R., Peckham S.E., Grell G.A., Michalakes J., Trahan S., Benjamin S.G., Alexander C.R., Dimego G.J., Wang W., Schwartz C.S., Romine G.S., Liu Z., Snyder C., Chen F., Barlage M.J., Yu W., Duda M.G., 2017, The Weather Research and Forecasting model: overview, system efforts, and future directions, Bulletin of the American Meteorological Society, 98 (8), 1717-1737, DOI: 10.1175/BAMS-D-15-00308.1.

- Schumacher R.S., Rasmussen K.L., 2020, The formation, character and changing nature of mesoscale convective systems, Nature Reviews Earth and Environment, 1, 300-314, DOI: 10.1038/s43017-020-0057-7.

- Seity Y., Brousseau P., Malardel S., Hello G., Bénard P., Bouttier F., Lac C., Masson V., 2011, The AROME-France Convective-Scale Operational Model, Monthly Weather Review, 139 (3), 976-991, DOI: 10.1175/2010MWR3425.1.

- Seity Y., Lac C., Bouyssel F., Riette S., Bouteloup Y., 2013, Cloud and microphysical schemes in ARPEGE and AROME models, conference paper, Workshop on Parametrization of Clouds and Precipitation, available online at https://www.ecmwf.int/en/elibrary/76343-cloud-and-microphysical-schemes-arpege-and-arome-models (data access 31.01.2023).

- Squitieri B.J., Gallus W.A., 2020, On the forecast sensitivity of MCS cold pools and related features to horizontal grid spacing in convection-allowing WRF simulations, Weather Forecasting, 35 (2), 325-346, DOI: 10.1175/WAF-D-19-0016.1.

- Stensrud D.J., Fritsch J.M., 1994, Mesoscale convective systems in weakly forced large-scale environments. Part II: Generation of a mesoscale initial condition, Monthly Weather Review, 122 (9), 2068-2083, DOI: 10.1175/1520-0493(1994)122<2068:MCSIWF>2.0.CO;2.

- Surowiecki A., Taszarek M., 2020, A 10-year radar-based climatology of mesoscale convective system archetypes and derechos in Poland, Monthly Weather Review, 148 (8), 3471-3488, DOI: 10.1175/MWR-D-19-0412.1.

- Tao W.-K., Wu D., Lang S., Chern J.-D., Peters-Lidard C., Fridlind A., Matsui T., 2016, High-resolution NU-WRF simulations of a deep convective-precipitation system during MC3E: Further improvements and comparisons between Goddard microphysics schemes and observations, Journal of Geophysical Research: Atmospheres, 121 (3), 1278-1305, DOI: 10.1002/2015JD023986.

- Taszarek M., Allen J.T., Púčik T., Hoogewind K.A., Brooks H.E., 2020, Severe convective storms across Europe and the United States. Part II: ERA5 environments associated with lightning, large hail, severe wind, and tornadoes, Journal of Climate, 33 (23), 10263-10286, DOI: 10.1175/JCLI-D-20-0346.1.

- Taszarek M., Pilguj N., Orlikowski J., Surowiecki A., Walczakiewicz S., Pilorz W., Piasecki K., Pajurek Ł., Półrolniczak M., 2019, Derecho evolving from a mesocyclone – a study of 11 August 2017 severe weather outbreak in Poland: event analysis and high-resolution simulation, Monthly Weather Review, 147 (6), 2283-2306, DOI: 10.1175/MWR-D-18-0330.1.

- Termonia P., Fischer C., Bazile E., Bouyssel F., Brožková R., Bénard P., Bochenek B., Degrauwe D., Derková M., El Khatib R., Hamdi R., Mašek J., Pottier P., Pristov N., Seity Y., Smolíková P., Španiel O., Tudor M., Wang Y., Wittmann C., Joly A., 2018, The ALADIN system and its canonical model configurations AROME CY41T1 and ALARO CY40T1, Geoscientific Model Development, 11 (1), 257-281, DOI: 10.5194/gmd-11-257-2018.

- Walter H., 2016, Raymond and Jiang (1990): Long-lived mesoscale convective systems, available online at http://hannahlab.org/raymond-and-jiang-1990-long-lived-mesoscale-convective-systems/ (data access 31.01.2023).

- Weisman M.L., Evans C., Bosart L., 2013, The 8 May 2009 superderecho: analysis of a real-time explicit convective forecast, Weather and Forecasting, 28 (3), 863-892, DOI: 10.1175/WAF-D-12-00023.1.

- Whitney L.F., 1977, Relationship of the subtropical jet stream to severe local storms, Monthly Weather Review, 105 (4), 398-412, DOI: 10.1175/1520-0493(1977)105<0398:ROTSJS>2.0.CO;2.

- Wimmer M., Raynaud L., Descamps L., Berre L., Seity Y., 2021, Sensitivity analysis of the convective-scale AROME model to physical and dynamical parameters, Quarterly Journal of the Royal Meteorological Society, 148 (743), 920-942, DOI: 10.1002/qj.4239.

- Wrona B., Mańczak P., Woźniak A., Ogrodnik M., Folwarski M., 2022, Synoptic conditions of the derecho storm. Case study of the derecho event over Poland on August 11, 2017, Meteorology, Hydrology and Water Management, DOI: 10.26491/mhwm/152798

- Zurbenko I.G., Sun M., 2016, Jet stream as a major factor of tornados in USA, Atmospheric and Climate Sciences, 6 (2), 236-253, DOI: 10.4236/acs.2016.62020.

105

Influence of computational grid resolution on the quality of forecasts of dangerous convection phenomena: a case study of August 11, 2017

Andrzej Mazur, Grzegorz Duniec
Institute of Meteorology and Water Management – National Research Institute

ABSTRACT. On August 11, 2017, a violent convection phenomenon took place in northwestern Poland, i.e., a storm combined with intense rainfall and hurricane winds. This paper presents an attempt to analyze this case by using the results of a numerical weather model, at grid spacings of 7 km, 2.8 km, and 0.7 km. Various convective indicators were analyzed to assess the nature of the event. The key question the authors try to answer is: "To what extent, if any, did a tenfold increase in resolution improve the quality of the numerical forecasts?" This question, however, has not been conclusively resolved. The most likely cause of this event was a supercell rapidly moving from south to northeast. This supercell's path has been mapped (qualitatively at least) by the Supercell Detection Index at all resolutions used. As the resolution increased, the forecasted maximum gusts also increased from 25 m/s in the domain with a resolution of 7 km to 35 m/s at a resolution of 2.8 km and up to about 50 m/s at the highest resolution of 0.7 km. A key conclusion is that the results of the model at a resolution of 2.8 km are much closer to reality than at 7 km. This effect did not pertain to differences between the 2.8 km and 0.7 km models. The latter increase in resolution did not significantly improve the quality of the forecast.

KEYWORDS: Meteorological model, supercell, high-resolution approach, convection-permitting scale.

1. INTRODUCTION

On August 11, 2017, roughly at 20:30 UTC, a very strong storm passed over the Polish voivodeships of Kujawsko-Pomorskie and Pomorskie, the effects of which are still being analyzed. Six people died, and two were residing at the scout camp in Suszek. Many people were also injured as a result of being hit by broken trees. More detailed information about the consequences of this event may be found in Chmielewski et al. (2020).

As reported from synoptic weather forecasts and synoptic surface maps published by the Polish Institute of Meteorology and Water Management, National Research Institute (IMGW-PIB), on August 11 at 00:00 UTC, northwestern and western Poland were under the influence of a warm, wavy-shaped atmospheric front (Sulik, Kejna 2020). During the day it changed its location slightly and moved to the northern part of the country. The rest of Poland was under the influence of the low-pressure system. The situation remained roughly unchanged throughout the day. The western part of the country was within the range of the cold atmospheric front. The center of the shallow low-pressure system was in western Germany. In the evening, the western provinces were under the influence of an occluded front. The southern regions were within reach of the cold front, and the eastern ones were under the influence of the warm front.

On that day, as measured at synoptic stations in northern Poland, the temperature first increased to >20°C (Toruń 26.7, Szczecinek 23.2, Elbląg 23.9, Chojnice 23.6) at 18:00 UTC. Then, after the passage of the storm, the temperature dropped sharply to 17-18°C (respectively, Toruń 18.6, Szczecinek 17.8, Elbląg 17.4, Chojnice 16.5) at 22:00 UTC, and remained practically unchanged for the rest of the day. A maximum wind gust of 42 m/s was recorded at the synoptic station in Elbląg (about 115 km northeast of Suszek).
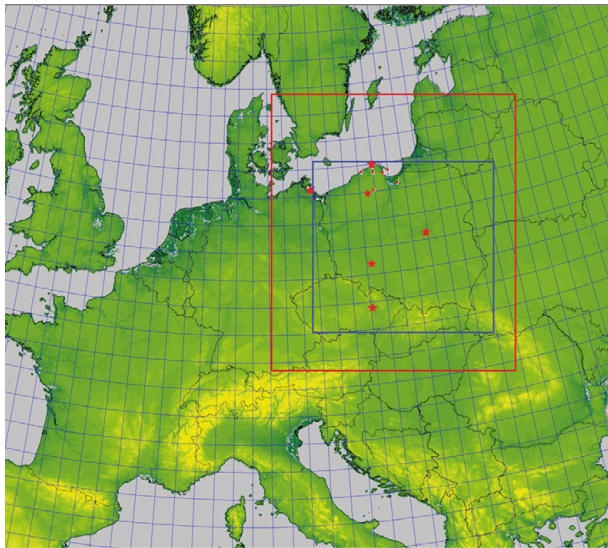

Fig. 1. Basic computational domain of the COSMO model with a resolution of 7 km × 7 km, 385×321 grid points (red square indicates the nested domain 2.8 km × 2.8 km, 380×405 grid points, blue = nested domain 0.7 km × 0.7 km, 1140×1020 grid points). The big red diamond indicates the location of Suszek (53.72N, 17.76E), small red squares are locations of SYNOP stations as listed in Table 1; red stars are upper air sounding stations as listed in Table 1.

The probability of occurrence of the unstable (convective) situation was confirmed by the radio-sounding analysis, in particular, the atmospheric sounding diagrams at 12:00 UTC from Legionowo, Wrocław, Łeba, Greifswald, and Prostejov sounding stations (Table 1, Figure 1). All the data from sounding stations were collected in the archives of the University of Wyoming[1].

For example, the difference between Lifting Condensation Level (LCL) and the Level of Free Convection (LFC) levels from the sounding in Legionowo was rather small, less than 100 hPa, which may have favored the development of convective phenomena.

Table 1. Locations of SYNOP (black) and upper air (red) stations, common for domains in all model resolutions.

Station	Longitude(degrees)	Latitude (degrees)	WMO Code
Gdańsk	18.933	54.333	12155
Łeba	17.533	54.750	12120
Elbląg	19.433	54.167	12160
Chojnice	17.533	53.717	12235
Ustka	16.867	54.583	12115
Lębork	17.750	54.550	12125
Hel	18.817	54.600	12135
Greifswald	13.400	54.100	10184
Legionowo	20.970	52.400	12374
Łeba	17.533	54.750	12120
Wrocław	16.980	51.130	12425
Prostejov	17.130	49.450	11475

Other soundings from Łeba, Wrocław, and Greifswald also indicated the occurrence of strong wind shear in the lower troposphere and high wind velocities. In Łeba and Wrocław, there were rapid changes in wind speed and direction in the lower troposphere. In Greifswald, the wind direction in the lower troposphere changed from 60 degrees at 12 m altitude to 200 degrees at an altitude of approximately 3 km asl. The difference between LCL and LFC (969 hPa and 955 hPa, respectively) was quite small, indicating the possibility of intensive convective phenomena, which favor the formation and development of storms. Moreover, most of the values of basic convective indices like the Lifted Index, Total Totals Index, or Showalter Index from the soundings suggested a very unstable atmosphere with the possibility of the occurrence of dangerous phenomena such as storms, supercells, and, eventually, tornadoes (University of Wyoming Webpage, see also Sulik, Kejna 2020). An overlap of strong vertical wind shear and these kinds of instabilities can support organized convective modes such as supercells and squall lines (Thompson et al. 2012). A detailed description of the genesis of this particular event was presented by Taszarek et al. (2019).

This paper presents an analysis aimed at answering the question of how the COSMO[2] numerical model running at different resolutions predicted the occurrence and features of the mesoscale convective system of August 11, 2017. Another equally important issue to analyze was to what extent increasing the resolution and, consequently, the ex-

[1] http://weather.uwyo.edu/upperair/sounding.html
[2] http://cosmo-model.org/content/model/documentation/core

tension of the computation time, improved numerical forecasts, especially the forecasts of intense convective phenomena.

Previous studies on the effect of resolution enhancement on convection parameterization found that the sensitivity of parameterized convection and large-scale precipitation to resolution results from an increase in the value of vertical velocities (Herrington, Reed 2017, 2020). However, the improvement of forecasts, especially forecasts considering strong convective phenomena with the increase in resolution, was not so obvious. It has been found (Potvin, Flora 2015; Sun et al. 2021) that increasing the horizontal resolution does not necessarily improve the description of convection, and for operational purposes related to storm forecasts and warnings, the 2-3 km grid spacing seemed to be sufficient.

We do not attempt to explain the causes of intense convective phenomena at kilometer and sub-kilometer scales. The aim of this research is to determine to what extent models with finer resolution can be used in synoptic practice. An additional question was whether it is worth using such models to support decisions on warnings, even at the cost of a significant increase in calculation time.

The genesis, course, and effects of such events showed that the development of appropriate tools to predict and estimate the intensity of such phenomena could be very important.

2. METHODOLOGY

In this work, the authors used numerical forecasts in nested domains with the COSMO model working successively at grid spacings of 7 km, 2.8 km, and 0.7 km. The nested domains in the cascade are shown in Figure 1, along with the marked location of Suszek, SYNOP stations, and sounding stations. The input data and initial/boundary conditions (IC/BC) for the model with horizontal grid spacing equal to 7 km were obtained using the results of the global ICOsahedral Non-hydrostatic model (ICON; Zängl et al. 2015). ICON's native grid resolution is 13 km. In the vertical, the model defines 90 atmospheric levels up to the maximum altitude of 75 km. In the sequence of calculations, the results of the COSMO model in 7 km resolution were used as IC/BC for calculations in 2.8 km resolution, which in turn were the source of IC/BC for calculations at 700 m resolution. In addition, an important difference in the description of convection processes at different resolutions was the use of the deep convection scheme at a resolution of 7 km and the shallow convection scheme (2.8 km, 0.7 km), both based on Tiedtke's scheme (Tiedtke 1989). All the parameterizations included in the COSMO model were described in its documentation (see COSMO webpage in references, model version 2018). Brief information on model settings is as follows (see also Duniec et al. 2017 for operational setup):

- model version 5.05, February 2018;
- non-hydrostatic core;
- 40 vertical levels (in all resolutions);
- model maximum altitude 22 km;
- time horizon of forecast 24 hours;
- time steps 40, 15, and 5 seconds for 7, 2.8, and 0.7 km, respectively;

At each resolution, forecasts of the fields of the following meteorological elements and indicators were calculated:
- Supercell Detection Index (SDI1/SDI2; Baldauf, Seifert 2008);
- Maximum windspeed at 10 m above ground level (VMAX at 10 m agl., COSMO webpage);

- Radar reflectivity (see below);
- Storm Relative Helicity 0-3 km (SRH; Markowski et al. 1998);
- Vertical component of vorticity (Dahl et al. 2014).

Of the above quantities, VMAX, and reflectivity (un-attenuated, in Rayleigh approximation) values were obtained as Direct Model Output (DMO, COSMO webpage for documentation), while the others were derived as a result of post-processing of standard model results (wind speed and direction, atmospheric pressure, temperature, etc.). In turn, reflectivity observation data were available as HDF5 files in spatial resolution of 1 km, i.e., approximately 0.008 degrees (latitude) × 0.01 degrees (longitude at 50°N). The observed reflectivity values have been transferred to a common grid. Namely, for comparison and verification, the observational reflectivity data have been transferred to the 7 km grid (considered the basic one) along with the corresponding data from the forecasts in resolutions of 2.8 and 0.7 km (and, of course, at 7 km).

Due to the large volume of the material, other convection-related quantities and parameters, although computed, were not included in this work.

At each specified resolution, numerical forecasts for a specific date could be obtained by selecting the starting moment and a sufficiently long forecast time horizon. Thus, if one set the starting point of the forecast, for example, on August 10, 2017, at 00:00 UTC, the time horizon should not be shorter than 48 hours (until 00:00 UTC, August 12, 2017). By shifting the starting point forward with a time step of six hours, it would be possible to shorten the length of the forecast by an appropriate period. The "latest" runs might start at 18:00 UTC on August 11, 2017, with a corresponding forecast horizon of six hours. This procedure resulted in a set of eight increasingly shorter forecasts, each of which could provide information on the state of the atmosphere during the period of interest, i.e., between 20:00 and 21:00 UTC on August 11, 2017. However, the results of these subsequent forecasts were inconsistent in the sense that they changed along with the change in the starting point of the model. For this reason, the authors limited the entire analysis to three 24-hour runs of the model at all resolutions, starting at 00:00 and ending at 12:00 UTC.

The calculation results (forecasts) changed as the result of two factors. First, there were successive changes to the initial conditions (the closer to the date in question, the newer initial data could be used, from which a supposedly more accurate forecast could be generated). Second, there was a shorter time interval between the spin-up of the model (see e.g. Bonekamp et al. 2018) and the occurrence of the phenomenon under consideration. Therefore, a balance had to be established between the influence of these two elements to assess which of the two factors influenced the results more significantly and positively.

3. RESULTS AND DISCUSSION

It should be emphasized that in addition to the studies presented below, concerning issues and quantities related to convection, the authors also assessed the quality of forecasts of the atmosphere's state in terms of basic parameters, such as temperature at 2 m agl or wind speed at 10 m agl, as measured at synoptic stations.

The latter quantities may be the subject of separate work, but in this study, they only provide arguments about the quality of the model results at the specified resolutions, because they do not
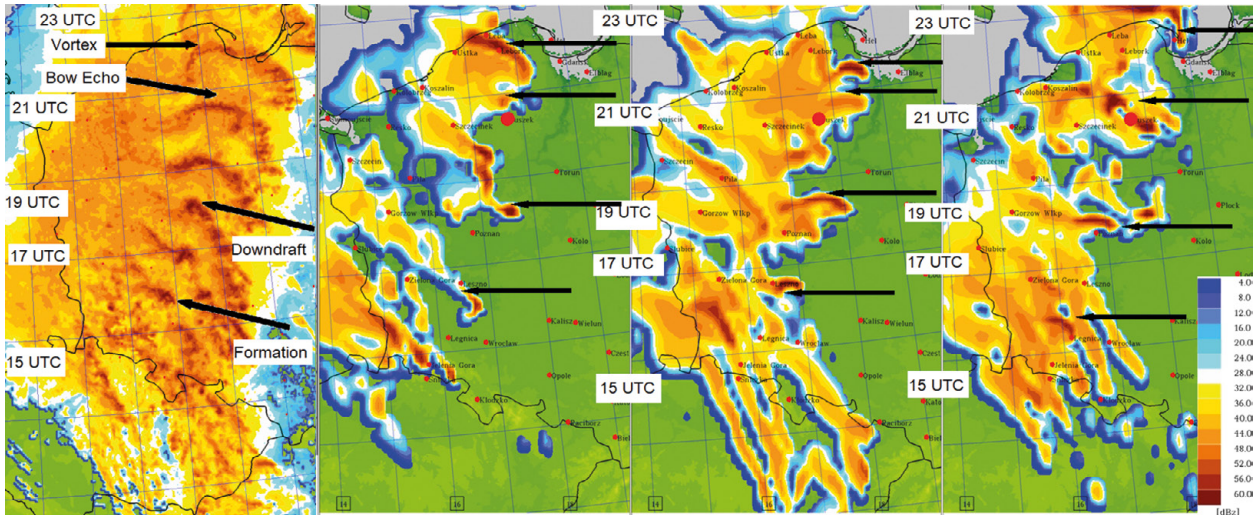
Fig. 2a. Reflectivity, maximum hourly values. Left to right: the actual reflectivity image (POLRAD network); reflectivity forecasts at 7 km resolution, model runs starting at 00:00, 06:00, and 12:00 UTC, August 11, 2017. Time markers added for the forecast started at 06:00 (see explanations in text).
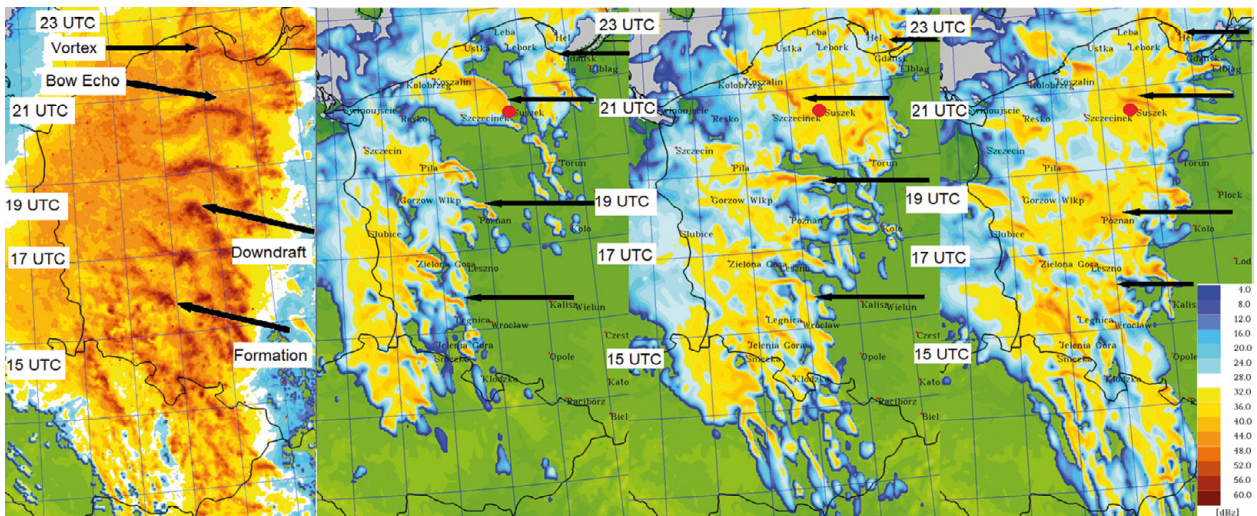

Fig. 2b. Reflectivity, maximum hourly values. Left to right: the actual reflectivity image (POLRAD network); reflectivity forecasts at 2.8 km resolution, model runs starting at 00:00, 06:00, and 12:00 UTC, August 11, 2017.
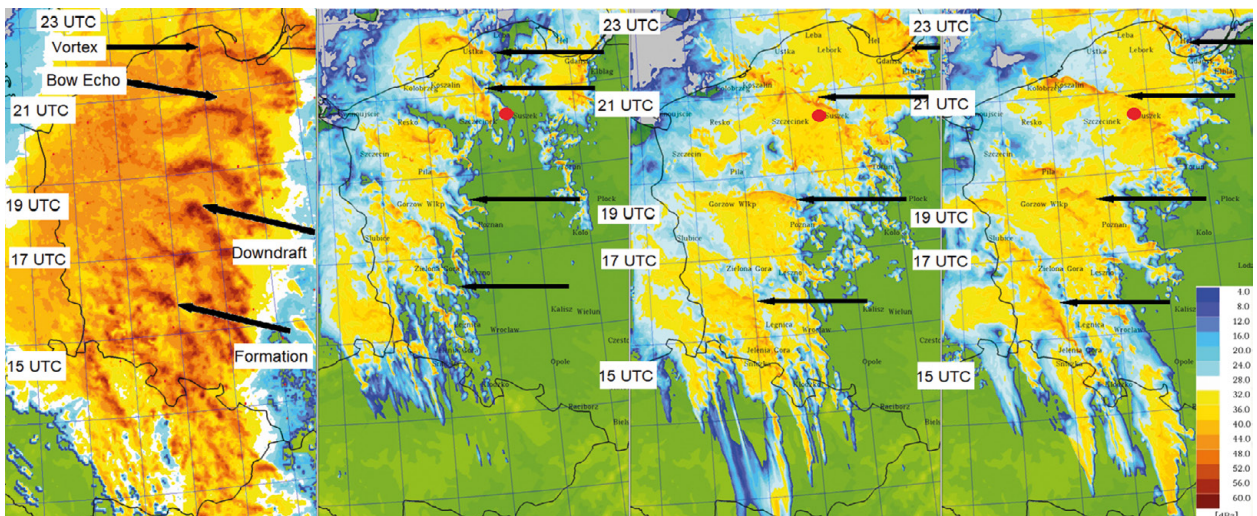

Fig. 2c. Reflectivity, maximum hourly values. Left to right: the actual reflectivity image (POLRAD network); reflectivity forecasts at 0.7 km resolution, model runs starting at 00:00, 06:00, and 12:00 UTC, August 11, 2017.
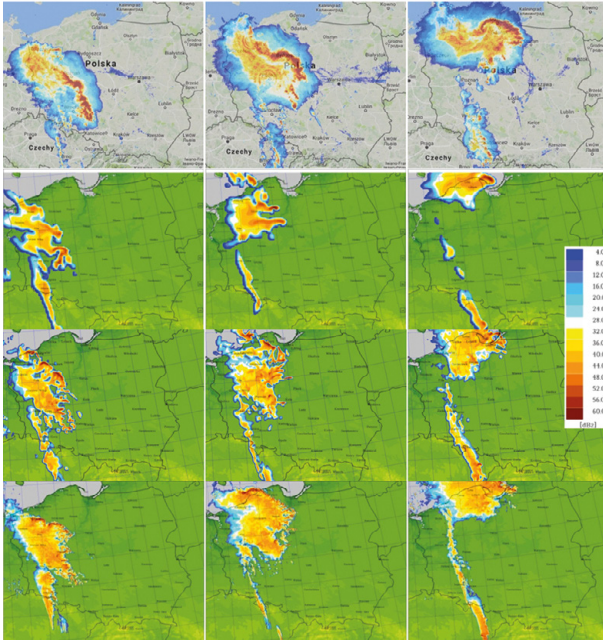
Fig. 3. Reflectivity (radar image, source: IMWM-PIB; top panel) and the forecast of the radar image based on the model results in resolutions (top to bottom) 7.0 km, 2.8 km, 0.7 km, from 18:00, 20:00 and 22:00 UTC (left to right). Model run start 00:00 UTC. See explanations in the text.

define either the nature or the intensity of convective phenomena, the main subjects of this study. In general, every model run that extended from 00:00 UTC to 12:00 UTC gave a similar quality forecast and did not differ significantly at practically all resolutions, except maybe for the 0.7 km resolution run at 12:00 UTC.

The key issue here is, however, that the comparison of forecasts and actual images of radar reflectivity (resolution of 1km, POLRAD network; Łuszczewski, Tuszyńska 2022) showed that the earlier runs, from 00:00 UTC until 06:00 UTC on August 11, predicted the beginning and development of the phenomenon too west, compared to observations (Figures 2a-c). This conclusion agrees with other studies (Taszarek et al. 2019). One exception is the forecasts with a resolution of 2.8 km at 06:00 UTC. In this situation, according to forecasts, the phenomenon started too far west, but the speed of the system's movement was so great (in fact, greater than reality and much greater than, for example, the launch of the model at 12:00 UTC) that it reached the Bay of Gdańsk sooner than in the actual situation. This example is presented in Figure 2b, with the time stamps added to observations and this particular forecast.

In Figure(s) 2 (left panes, the actual radar images) it can be seen that the bow echo (for detailed information about structures of this kind see Celiński-Mysław et al. 2020 or Surowiecki, Taszarek 2020) formation started at around 17:00 UTC, which is shown with the southernmost arrow (labeled as "Formation"). This and subsequent (from the bottom to the top of the Figure) arrows in charts of reflectivity forecasts correspond to the areas and structures identified in the study of Taszarek et al. (2019), and labeled as "Downdraft", "Bow Echo" and "Vortex". However, this recognition and comparison were made only qualitatively (through the visual similarity of the images of subsequent structures) rather than quantitatively, via direct reflectivity values. A similar procedure, i.e., qualitative recognition of structures identified in the actual radar area, was used for Figure 5.
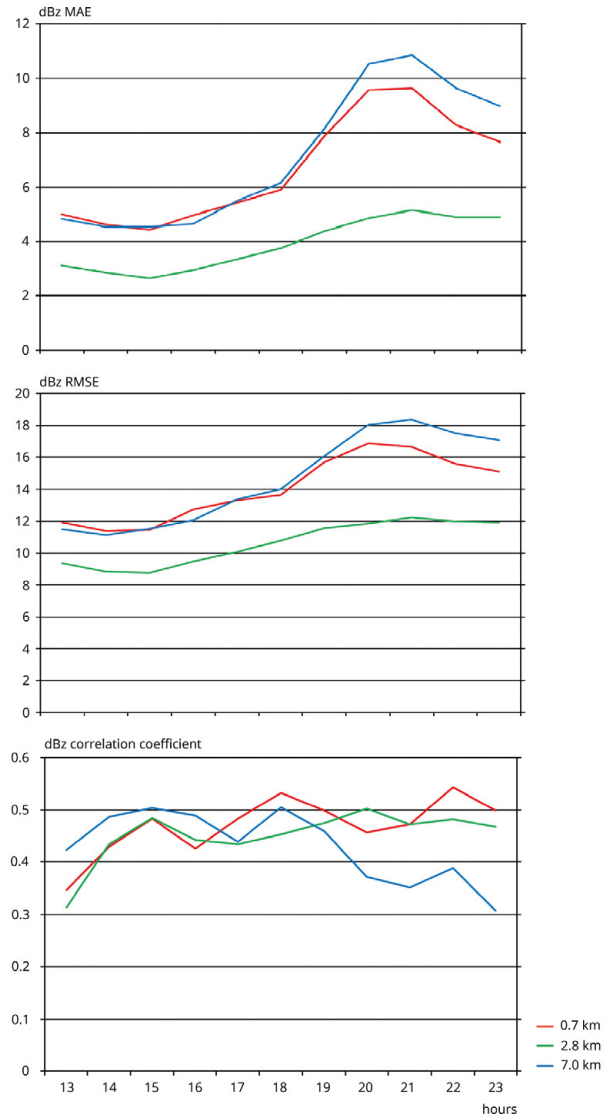
Fig. 4. Reflectivity, observations vs. forecasts. Top to bottom: Mean Absolute Error, Root Mean Square Error, Pearson's correlation coefficient for resolution 0.7 (red line), 2.8 (green line), and 7.0 km (blue line). The results of the forecast run started at 12:00 UTC.

Figure 3 shows a comparison of the radar reflectivity (from 18:00 to 22:00 UTC in 2-hour intervals) with the forecasts of the radar image at three model resolutions. The comparisons are rendered strict and quantitative by assessing compliance with the observations (POLRAD network) of the model results using MAE, RMSE, and Pearson correlation coefficients calculated for the common area of all three model domains, i.e., the entire model domain with a resolution of 0.7 km (see Figure 1).

The values of the model forecasts for maximum reflectivity, based on the forecasts that started at 6:00 and 12:00 UTC with a resolution of 7 km, agree well with the actual values (see e.g., Figure 2a). The areas of maximum reflectivity occur at a certain distance from the location of the scout camp in Suszek. The maximum reflectivity is best represented by the forecast starting at 12:00 UTC, but also in this case the maximum values are shifted to the southeast and northwest of Suszek. In the model started at 00:00 UTC, the predicted peak reflectivity is shifted to the north. Similar maximum reflectivity
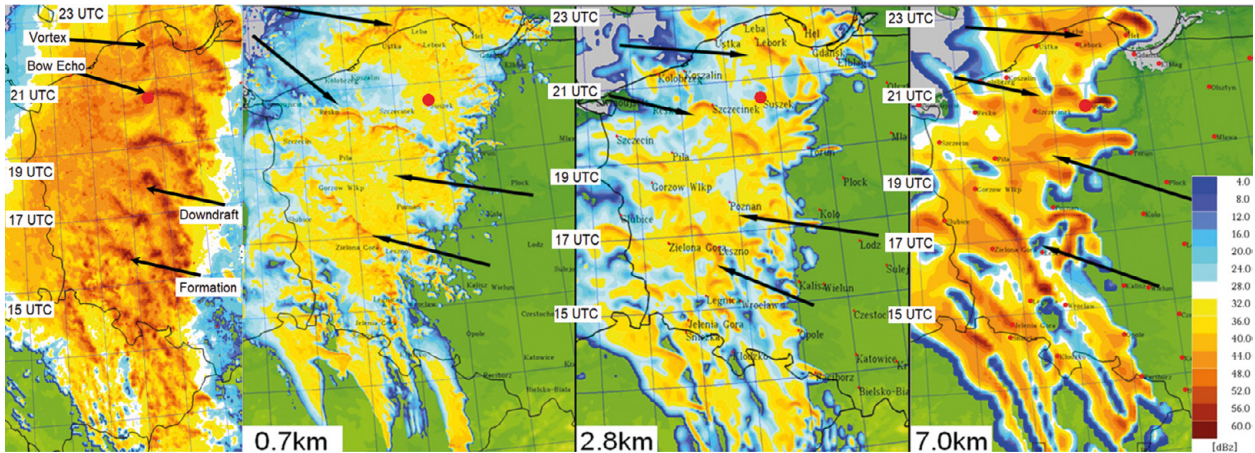
Fig. 5. Maximum reflectivity with 1 h step. Left to right: image from the POLRAD network; forecasts based on the model results at resolution 0.7km, 2.8 km, and 7.0 km from 12:00 to 22:00 UTC. The arrows indicate the structures identified in the actual radar image and the corresponding areas obtained from the reflectivity forecasts. Formation = suggested location of formation of supercell; Downdraft = rear flank downdraft, strong outflow; Bow Echo= structure of bow echo accompanied with rear inflow; Vortex = convective vortex.

forecasts were obtained from the model with a resolution of 2.8 km (Figure 2b), the most accurate of all the model runs initiated at 06:00 and 12:00 UTC. The forecast obtained from the model started at 12:00 UTC shows a characteristic bow with increased reflectivity north of Suszek. In contrast, in the forecast starting at 00:00 UTC, the predicted reflectivity is shifted to the west, and no significant vorticity was found in this area of interest (Figures 9 and 10). Analogous conclusions can be drawn from the analysis of the maximum reflectivity forecast obtained with a resolution of 0.7 km as shown in Figure 2c. The forecasts of maximum reflectivity values are closest to reality for model runs starting at 06:00 and 12:00 UTC. Similarly to the model forecast with a resolution of 2.8 km, obtained from the run from 00:00 UTC, the area of the maximum reflectivity value did not include the Suszek region. In forecasts for runs starting at 06:00 and 12:00 UTC, the area of maximum reflectivity covers the area where dangerous phenomena occurred. Figure 2c shows the characteristic high reflectivity (bow-shaped echo) that has passed through this region. Comparing the reflectivity predictions obtained from the model with resolutions of 0.7, 2.8, and 7 km with the reflectivity values obtained from the radar showed that the reflectivity values were best predicted by the model with resolutions of 2.8 and 0.7 km (Figures 4 and 5). The analysis of the maximum reflectivity in one-hour steps showed that the characteristic bow echo structures are best represented with the forecast from the model with a resolution of 0.7 km.

All these differences and all the arguments listed above allow for an informed decision that the forecasts starting at 12:00 UTC on August 11, 2017 would be used for further research as the closest to the actual development of the situation. Hence, unless specifically stated, results, description(s), and discussion will pertain to the forecast starting at this hour.

The results presented in Figure 4 allowed for the following conclusion: increasing the resolution from 7 km to 2.8 km significantly improves the results. Comparing the results of the model at a resolution of 7 km and 0.7 km also shows an improvement (as compared to observation), but not necessarily to the extent that one might expect. This result is especially visible when MAE and RMSE are smaller for 2.8 km than for 0.7 km, although both resolutions gave significantly better results than the model at 7 km resolution.
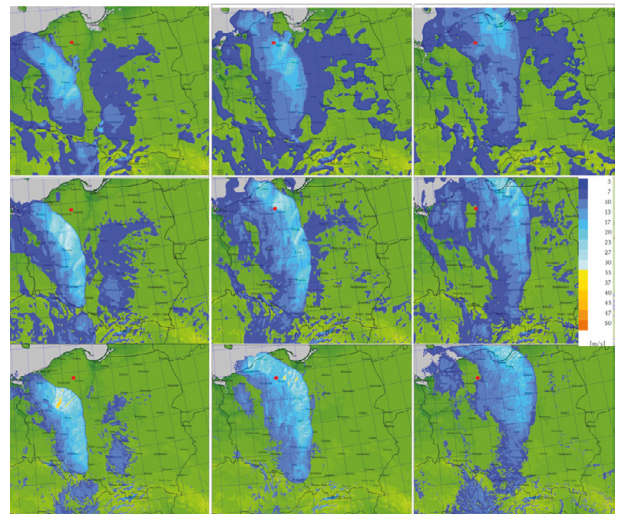

Fig. 6. Maximum values of wind speed at 10 m agl: forecast based on the model results in resolutions (top to bottom) 7.0 km, 2.8 km, 0.7 km from 18:00, 20:00, and 22:00 UTC (left to right).

It should be mentioned that there is quite an important conclusion, worth repeating. Increasing the resolution to 0.7 km, at the cost of significantly extending the computation time compared to the model with a resolution of 2.8 km, did not significantly improve the results, at least in terms of reflectivity values.

Figure 5 shows the development of structures identified (cf. Taszarek et al. 2019) in the real radar image and all resolutions of reflectivity forecasts. Even a rough analysis of the actual radar images and the corresponding reflectivity forecasts indicated that an active storm system with the bow echo structure has migrated over Poland for more than four hundred kilometers. The end of the path was positioned, according to the reflectivity forecasts, in the area of the Gdańsk Bay around 23:00 UTC. This pattern is, in general, similar for all resolutions. The following conclusion can be drawn from the qualitative comparison of the position of the maxima and the location of the areas of increased reflectivity on radar images and the model results in all resolutions. It can be concluded that this structure was best captured (at least qualitatively, but not necessarily quantitatively)

111

Wind gusts - observation vs. forecasts
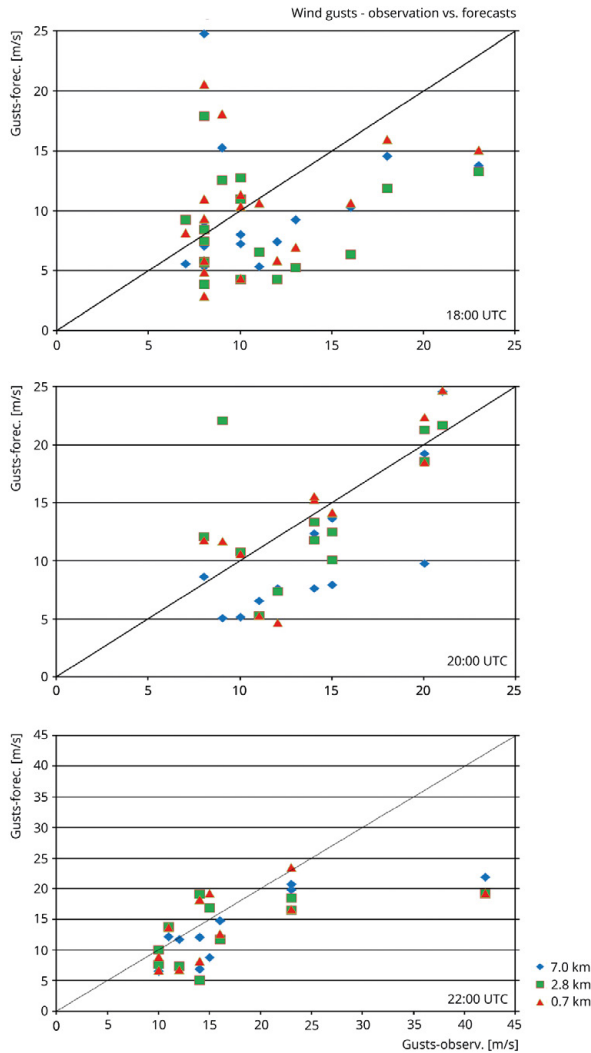
Fig. 7. Maximum values of wind speed at 10 m agl. Observations at Polish SYNOP stations vs. forecasts, top to bottom, 18:00, 20:00, and 22:00 UTC. Blue diamonds are model results for resolution of 7 km: green squares for 2.8 km, and red triangles for 0.7 km.

as a result of calculations using a meteorological model with a resolution of 0.7 km, considering the location(s) related to the time(s) of occurrence of the maximum reflectivity values. This thesis was confirmed by the following figures presenting forecasts (in the same period) of VMAX and SDI1.

Considering the forecast maximum wind speed (Figure 6) and measurements at the SYNOP stations in the study area (Suszek-Chojnice) it should be stressed that while the highest wind speed occurred near Suszek around 20:30-21:00 UTC, Figure 6 shows that the simulations predict an equally strong wind throughout the entire period shown. This qualitative compliance is also valid for data from the Elbląg station (WMO Code 12160), where wind gusts of up to 42 m/s were recorded around 22:00 UTC, that is, after the incident in Suszek. Model simulations showed the maximum VMAX wind speed for Elbląg ranged from 25 m/s for calculations at a resolution of 7 km, to >35 m/s for a resolution of 2.8 km, to >50 m/s at a resolution of 0.7 km. However (see Figure 7), models in all resolutions, compared to measurements at SYNOP

stations, rather tended to underestimate the values. This effect occurs for all stations considered, as listed in Table 1, except WMO 12155 in Gdańsk (located over Gdańsk Bay), for which the VMAX values are overestimated. Perhaps this is because the intensity of the phenomenon decreased after reaching the coast, which was not reflected in the model results. High wind speed values are best represented in the 2.8 km model runs for 20:00-21:00 UTC. With the 2.8 km resolution model, the predicted wind speed values were lower than for the 0.7 km version (see Figure 6).

The distribution of the SDI1 values was the most consistent with the actual distribution of dangerous convective phenomena, shown by radar images, based on which it was possible to estimate the potential trajectory of these phenomena with resolutions of 2.8 km and 0.7 km. In the 7 km model, high SDI values were forecast east of Suszek, which suggested a movement of dangerous phenomena in this direction. Although as the resolution increases from 7 to 2.8 km the SDI1 extreme structures (positive and negative) have a more linear than two-dimensional structure, for each resolution a repeating pattern is visible: a maximum followed by a minimum. Could this fact conclusively indicate the presence of a supercell associated with a low-pressure cyclonic circulation system (based on SDI2; Baldauf, Seifert 2008)? It is difficult to answer this question because such structures (clearly marked) cannot be seen at a resolution of 0.7 km. At the same time, it can be observed, especially based on simulations for a resolution of 7 km, that the center(s) of the storm has been moving at an average speed >50 km/h. The maximum speed of the potential supercell was about 100 km/h, and the whole system ended as it reached the Baltic Sea. In addition, it could be seen that between 19:00 and 20:00 UTC the supercell split into two systems (for orientation, in the center of the domain with a resolution of 0.7km, near Toruń and Bydgoszcz). In Figure 8 the red lines, connecting local maxima (with the closest values) of SDI at specific hours, showed the route of the supercell (maximum SDI1 values) with a split into two supercells between 19:00 and 20:00 UTC. This effect was not visible when forecasting the SDI1 index at a resolution of 7 km; also, at a resolution of 0.7 km, this split effect is very weak.

Finally, Figures 9 and 10 show the vorticity and storm-relative helicity at each resolution. Analysis of the results of numerical forecasts obtained from the model at a resolution of 7, 2.8, and 0.7 km suggested a vorticity significantly different from zero, indicating the possibility of intense convective phenomena (e.g., Weijenborg et al. 2017; Figure 9) in the Suszek region forecasts at resolutions of 2.8 and 0.7 km. These values were about $0.005 \cdot s^{-1}$ and more. On the other hand, the forecast obtained at resolution 7 km for this hour(s) did not suggest a significant vorticity (>0.0005 s^{-1}) in the Suszek region. In turn, values of SRH greater than 250 m^2/s^2 may suggest an increased threat of high-impact convective structures (see NOAA webpage for detailed explanation[3]), but high values of this index do not necessarily suggest that the environment supports supercell formation (Figure 10). Larger values are generally more indicative, but there is, basically, no clear distinction between supercell and non-supercell signatures (NOAA's NWP SPC web page; Markowski et al. 1998). The analysis of the forecast of SRH values at 20:00 and 22:00 UTC from the model at all resolutions did not show that there were any (very) dangerous supercells (Rasmussen, Blanchard 1998) in the Suszek area. Positive values of SRH (warm

---

[3] https://www.spc.noaa.gov/exper/mesoanalysis, also sub-page https://www.spc.noaa.gov/exper/mesoanalysis/help/begin.html
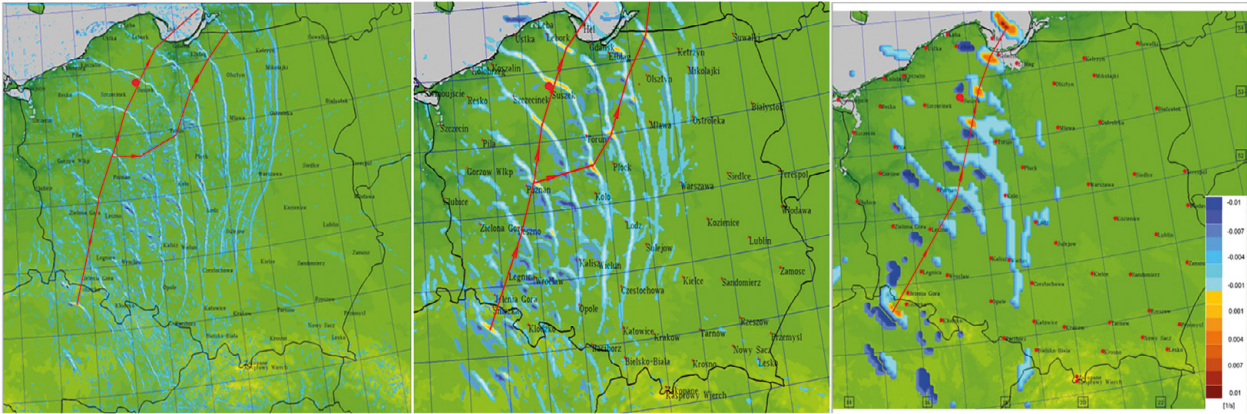
Fig. 8. Supercell Detection Index 1 values. Forecast based on the model results in resolutions (left to right) 0.7 km, 2.8 km, and 7.0 km from 12:00 to 22:00 UTC. Positive SDI1 values (warm colors) correspond to the updraft, negative (cold colors), and downdraft (Wicker et al. 2005). The red lines connect local maxima of SDI at specific hours (see further explanations in text).
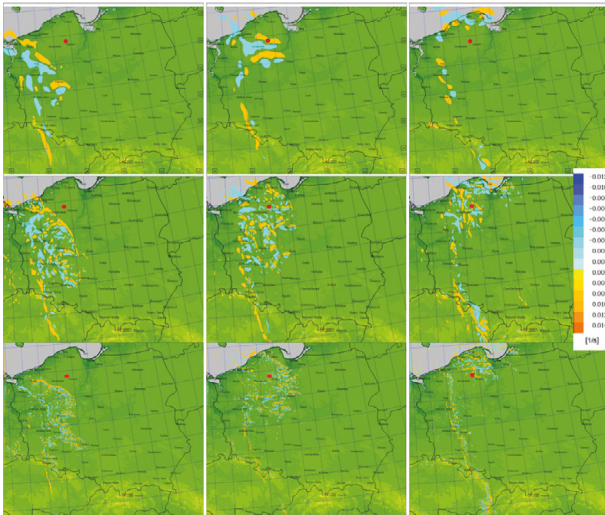

Fig. 9. Vorticity (vertical component, calculated as average values from 1000 m to 3000 m); forecast based on the model results in resolutions (top to bottom) 7.0 km, 2.8 km, 0.7 km from 18:00, 20:00, and 22:00 UTC (left to right). Warm colors correspond to positive values, cold colors to negative ones.
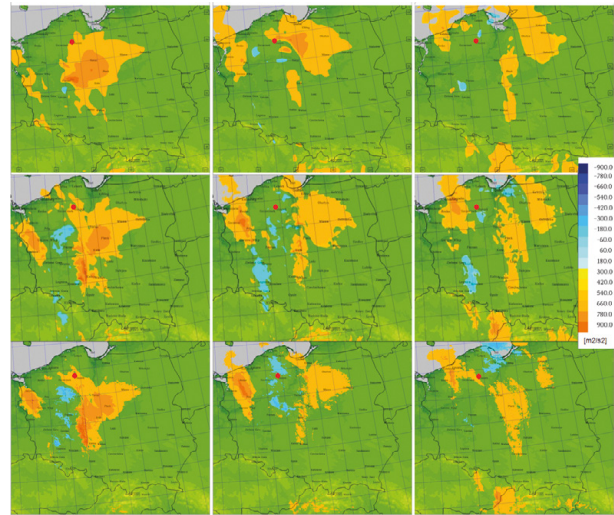

Fig. 10. Values of storm-relative helicity 0-3 km; forecast based on the model results in resolutions (top to bottom) 7.0 km, 2.8 km, 0.7 km from 18:00, 20:00, and 22:00 UTC (left to right). Warm colors correspond to positive values, cold colors to negative ones.

113

color on the map) were forecast at all resolutions in the Zachodnio-pomorskie, Warminsko-Mazurskie, northern Lubuskie, Wielkopol-skie, Mazowieckie, Kujawsko-Pomorskie, and Pomorskie voivode-ships. In the indicated regions, the projected minimum and maximum SRH values were <-700 and >700 m²/s², respectively. Negative values of the SRH indicator (anti-cyclonic, i.e., anticlockwise movements; cold color on the map) were forecast in the Pomorskie and Ku-jawsko-Pomorskie regions with a resolution of 0.7 km, and for Ku-jawsko-Pomorskie and Dolnośląskie voivodeships with a resolution of 2.8 km. Negative forecast values of SRH from the model at a resolu-tion of 7 km are for very small areas in Pomorskie, Kujawsko-Pomor-skie, and Wielkopolskie. Only the forecast from the model at a resolu-tion of 2.8 km for 18:00 UTC in the Suszek area predicted SRH values of about 500 m²/s², which could suggest the occurrence of dangerous meteorological phenomena, especially supercells. In terms of high-im-pact weather analysis, it is important to note that sufficiently large val-ues were found around Suszek.

4. SUMMARY

The analysis shows that increasing the model resolution from 7 to 2.8 km better reflects the values of meteorological fields and im-proves the spatial forecast. It should be noted that the forecasts in high-er resolution are burdened with greater errors of MAE and RMSE of surface parameters (results not included in this study in detail), but not necessarily of convective quantities (e.g., radar reflectivities). Increasing the resolution also resulted in a more accurate forecast of the trajectory of a dangerous weather phenomenon.

Increasing the resolution to 0.7 km did not improve the predictions of any variables considered, except for wind gusts. The simulations showed a strong enhancement in maximum wind speed with increased resolution.

To conclude, it should be remembered that the models with reso-lution greater than 2.8 km were not (and still are not) being launched in the operational mode. In other words, the results of the 0.7 km mod-el were not available at the time of the incident.

REFERENCES

- Baldauf M., Seifert A., 2008, COSMO-DE Ausgabe: erweitert durch SDI (Supercell Detection Index) und Ceiling, available online at https://www.dwd.de/DE/fachnutzer/ forschung_lehre/numerische_wettervorhersage/nwv_aenderungen/_functions/DownloadBox_modellaenderungen/cosmo_de/pdf_2006_2008/pdf_lmk_16_01_2008.html (data access 16.01.2023).

- Bonekamp P.N.J., Collier E.C., Immerzeel W.W., 2018, The impact of spatial resolution, land use, and spinup time on resolving spatial precipitation patterns in the Himalayas, Journal of Hydrometeorology, 19(10), 1565-1581, DOI: 10.1175/JHM-D-17-0212.s1.

- Celiński-Mysław D., Matuszko M., Taszarek M., 2020, Climatology and atmospheric conditions associated with cool season bow echo storms in Poland, Atmospheric Research, 240, 104944, DOI: 10.1016/j.atmosres.2020.104944.

- Chmielewski T., Szer J., Bobra P., 2020, Derecho wind storm in Poland on 11112 August 2017: results of the post-disaster investigation, Environmental Hazards, 19 (5), 508-528, DOI: 10.1080/17477891.2020.1730154.

- Dahl J.M., Parker M.D., Wicker L.J., 2014, Imported and storm-generated near-ground vertical vorticity in a simulated supercell, Journal of Atmospheric Sciences, 71 (8), 3027-3051, DOI: 10.1175/JAS-D-13-0123.1.

- Duniec G., Interewicz W., Mazur A., Wyszogrodzki A., 2017, Operational setup of the COSMO-based, time-lagged Ensemble Prediction System at the Institute of Meteorology and Water Management – National Research Institute, Meteorology, Hydrology and Water Management, 5 (2), 43-51, DOI: 10.26491/mhwm/71048.

- Herrington A.R., Reed K.A., 2017, An explanation for the sensitivity of the mean state of the community atmosphere model to horizontal resolution on aquaplanets, Journal of Climate, 30 (13), 4781-4797, DOI: 10.1175/JCLI-D-16-0069.1.

- Herrington A.R., Reed K.A., 2020, On resolution sensitivity in the community atmosphere model, Quarterly Journal of the Royal Meteorological Society, 146 (733), 3789-3807, DOI: 10.1002/qj.3873.

- Łuszczewski H., Tuszyńska I., 2022, Derecho radar analysis of August 11, 2017, Meteorology, Hydrology and Water Management, DOI: 10.26491/mhwm/152504.

- Markowski P.M., Straka J.M., Rasmussen E.N., Blanchard D.O., 1998, Variability of Storm-Relative Helicity during VORTEX, Monthly Weather Review, 126 (11), 2959-2971, DOI: 10.1175/1520-0493(1998)126<2959:VOSRHD>2.0.CO;2.

- Potvin C.K., Flora M.L., 2015, Sensitivity of idealized supercell simulations to horizontal grid spacing: Implications for Warn-on-Forecast, Monthly Weather Review, 143 (8), 2998-3024, DOI: 10.1175/MWR-D-14-00416.1

- Rasmussen E.N., Blanchard D.O., 1998, A baseline climatology of sounding-derived supercell and tornado forecast parameters, Weather and Forecasting, 13 (4), 1148-1164, DOI: 10.1175/1520-0434(1998)013<1148:ABCOSD>2.0.CO;2.

- Sulik S., Kejna M., 2020, The origin and course of severe thunderstorm outbreaks in Poland on 10 and 11 August, 2017, Bulletin of Geography. Physical Geography Series, 18, 25-39, DOI: 10.2478/bgeo-2020-0003.

- Sun S., Zhou B., Xue M., Zhu K., 2021, Scale-similarity subgrid-scale turbulence closure for supercell simulations at kilometer-scale resolutions: comparison against a large-eddy simulation, Journal of Atmospheric Sciences, 78 (2), 417-437, DOI: 10.1175/ JAS-D-20-0187.1

- Surowiecki A., Taszarek M., 2020, A 10-year radar-based climatology of mesoscale convective system archetypes and derechos in Poland, Monthly Weather Review, 148 (8), 3471-3488, DOI: 10.1175/MWR-D-19-0412.1.

- Taszarek M., Pilguj N., Orlikowski J., Surowiecki A., Walczakiewicz S., Pilorz, W., Piasecki, K., Pajurek, Ł., Półrolniczak M., 2019, Derecho evolving from a mesocyclone – a study of 11 August 2017 severe weather outbreak in Poland: event analysis and high-resolution simulation, Monthly Weather Review, 147 (6), 2283-2306, DOI: 10.1175/ MWR-D-18-0330.1.

- Thompson R.L., Smith B.T., Grams J.S., Dean A.R., Broyles C., 2012, Convective modes for significant severe thunderstorms in the contiguous United States. Part II: Supercell and QLCS tornado environments, Weather and Forecasting, 27 (5), 1136-1154, DOI: 10.1175/WAF-D-11-00116.1.

- Tiedtke M., 1989, A comprehensive mass flux scheme for cumulus parameterization in large-scale models, Monthly Weather Review, 117 (8), 1779-1799, DOI: 10.1175/1520-0493(1989)117<1779:ACMFSF>2.0.CO;2.

- Weijenborg C., Chagnon J.M., Friederichs P., Gray S.L., Hense A., 2017, Coherent evolution of potential vorticity anomalies associated with deep moist convection, Quarterly Journal of the Royal Meteorological Society, 143 (704), 1254-1267, DOI: 10.1002/ qj.3000.

- Wicker L.J., Kain J., Weiss S., Bright D., 2005, A brief description of the supercell detection index, Technical Report, NOAA/SPC, 10 pp.

- Zängl G., Reinert, D., Ripodas P., Baldauf M., 2015, The ICON (ICOsahedral Non-hydrostatic) modelling framework of DWD and MPI-M: Description of the non-hydrostatic dynamical core, Quarterly Journal of the Royal Meteorological Society, 141 (687), 563-579, DOI: 10.1002/qj.2378.

**Reviewers Cooperating with Editorial Board
of Meteorology Hydrology and Water Management
magazine in 2022**

Alexander Chernokulsky
Bartosz Czernecki
Stavros Dafis
Christopher Gatzen
Paweł Gilewski
Younes Hamed
Krzysztof Kochanek
Leszek Kolendowicz
Andrzej Kotarba
Maciej Kryza
Zoya Mateeva
Ionut Minea
Natalia Pilguj
Wojciech Pilorz
Joanna Plenzler
Tomas Pucik
Maria Putsay
Ryan Sobash
Stanisław Staśko
Sławomir Sulik
Małgorzata Szelachowska
Ákos J. Varga
Marcin Wdowikowski